Modeling of directional solidification of multicrystalline silicon in a traveling magnetic field

Von der Fakultät für Chemie und Physik

der Technischen Universität Bergakademie Freiberg

genehmigte

DISSERTATION

zur Erlangung des akademischen Grades

doctor rerum naturalium

Dr. rer. nat.

vorgelegt

von **MSc. Phys. Kaspars Dadzis**

geboren am 19.02.1983 in Ventspils, Lettland

Gutachter: Prof. Dr. H. J. Möller, Freiberg

Prof. Dr. André Thess, Ilmenau

Tag der Verleihung: 30. November 2012

Abstract

Melt flow plays an important role in directional solidification of multicrystalline silicon influencing the temperature field and the crystallization interface as well as the transport of impurities. This work investigates the potential of a traveling magnetic field (TMF) for an active control of the melt flow. A system of 3D numerical models was developed and adapted based on open-source software for calculations of Lorentz force, melt flow, and related phenomena. Isothermal and non-isothermal model experiments with a square GaInSn melt were used to validate the numerical models by direct velocity measurements. Several new 3D flow structures of turbulent TMF flows were observed for different melt heights. Further numerical parameter studies carried out for silicon melts showed that already a weak TMF-induced Lorentz force can stir impurities near to the complete mixing limit. Simultaneously, the deformed temperature field leads to an increase of the deflection of crystallization interface, which may exhibit a distinct asymmetry. The numerical results of this work were implemented in a research-scale silicon crystallization furnace. Scaling laws for various phenomena were derived allowing a limited transfer of the results to the industrial scale.

Theses

1. Open-source libraries `GetDP`, `OpenFOAM`, and `Elmer` are well-suited for three-dimensional simulations of coupled thermal, electromagnetic, and convective phenomena during directional solidification of silicon in time-dependent magnetic fields.

2. Unsteady three-dimensional flow calculations on relatively rough grids with the number of elements on the order of 10^5 are able to model turbulent flows in a TMF also without explicit turbulence models, provided that grid sensitivity of the relevant results is routinely checked. Such simulations agree well with velocity measurements in GaInSn melts.

3. Flow structures induced by a TMF in a square melt in model experiments:

   3.1 At a melt height-to-width ratio of 0.25, the typical TMF-induced toroidal flow is constrained to the rim and arbitrary rotation appears in the central part.

   3.2 At a ratio of 1.0, a distinct three-dimensional asymmetry appears also in a geometrically symmetric system.

   3.3 At low Lorentz force densities or high temperature gradients, the buoyancy forces damp all vertical melt motion and tend to form horizontal vortex structures.

   3.4 At high Lorentz force densities or low temperature gradients, the temperature field is mixed and the role of buoyancy forces becomes negligible.

4. Global temperature field in a crystallization furnace:

   4.1 Mainly the thermal conductivities of the silicon and the crucible as well as the heating and cooling powers determine the temperature gradients in the melt and the crystallization interface.

   4.2 A vertical temperature gradient of 1 K/cm, a radial temperature gradient of 0.1 K/cm, and a crystallization velocity of 1 cm/h can be selected as typical values for a Generation 1 (22x22x18 cm^3 ingots) furnace.

5. Electromagnetic field with 3 phase-shifted inductors surrounding the melt at the side:

   5.1 An increase of the melt width or of the current frequency reduces the vertical Lorentz force component and thus the efficiency of the TMF.

   5.2 With realistic inductor parameters, a Lorentz force angle with the horizontal plane of about 30° and a maximum force density of about 15 $\mathrm{N/m}^3$ can be reached in a Generation 1 melt.

   5.3 The square geometry of the melt leads to smaller Lorentz force densities in the corners.

6. Combination of a Lorentz force density of 15 $\mathrm{N/m}^3$ and a vertical temperature gradient of 1 K/cm in a Generation 1 melt:

   6.1 The temperature isolines are visibly deformed by the flow (with a velocity of 0.6 cm/s), and the influence on the crystallization interface deflection is up to about 8 mm.

    6.2 The bulk conditions of the concentration of such impurities as carbon and nitrogen correspond nearly to the analytical limit of a complete melt mixing, but the distribution along the crystallization interface still shows some sensitivity to the exact details of the velocity field.
    6.3 With a higher Lorentz force density by about a factor of 2, the relatively small asymmetry caused by the inductor current supplies leads to a very asymmetric interface shape in case of a downward TMF.
    6.4 An upward TMF does not show such effects and is also able to transport the impurities to the more favorable location at the melt rim over both a concave and a convex crystallization interface.
    6.5 The melt flow at high Lorentz force densities exhibits large oscillations of the temperature and concentration gradients at the interface, which may cause constitutional supercooling despite of the strong melt mixing effect.

7. Modification of the classical inductor geometry and implementation in a research-scale furnace using heaters supplied with an alternating current:
    7.1 The splitting of each side inductor into 4 separate segments gives significantly more freedom in the choice of the melt flow pattern beyond the classical toroidal structure.
    7.2 An asymmetric magnetic field configuration is able to enhance the mixing of impurities, while a periodic rotation of the asymmetry along the melt sides symmetrizes the impact on the crystallization interface.
    7.3 The control of the magnetic field can be achieved by changing the phase shift between the heaters, which allows for a relatively simple 50 Hz power source.
    7.4 First solidified multicrystalline silicon ingots seem to confirm several conclusions from numerical studies: a strong melt mixing can reduce the amount of inclusions in the crystal, but it may also have a large and asymmetric influence on the interface shape.

8. A precise up-scaling of the phenomena related to the melt flow from smaller (research-scale) to larger (industrial-scale) systems is limited by the high exponents in the scaling laws and by the same parameters in different dimensionless numbers. Nevertheless, the Lorentz-force-dominated flow regime could be transferred to 2...8 times larger systems in a realistic way. The up-scaling of the coupled phenomena of melt flow, crystallization interface, and species transport in the melt is also theoretically possible in this flow regime.

Contents

Chapter 1

Introduction

This chapter gives motivation for the current work and introduces to its topic from a physicist's viewpoint involving solid state physics, fluid mechanics, and other disciplines. Main goals are defined after a summary of the state of the art and a literature review.

1.1. Photovoltaics and multi-crystalline silicon

1.1.1. World energy consumption

Energy in the sense of mechanics can be described as the ability to do work, i.e., to cause motion. This very simplified perspective gives the correct indication that most processes not only in the nature but also in the human civilization depend on the availability of energy. If we consider only the current amount of electric energy consumed by the human population of almost 7 billion, we arrive at a number of $1.7 \cdot 10^4$ TWh per year, which is about 17% from the total energy consumption [IEAEnergyStatistics, 2010]. The laws of physics state that the total amount of energy is a conserved quantity, which makes such topics as *lack of energy* or *energy crisis* physically nonsensical. However, a deeper thermodynamic insight reveals that we should indeed care about qualitative sources of energy in order not to end up in the so-called *entropy crisis* where the energy is still there but available only in forms which do not allow an efficient conversion to work.

Current sources of world energy consumption are summarized in Tab. 1.1. More than two thirds of the total energy supply are based on coal, oil, and natural gas. The first alarming fact about these data is that we can assign to each of these sources an estimate of the final date when the current proved reserves will be depleted or, at least, when further usage will require intense search for new reserves and/or significant technological investments. In most cases, this point will be reached in the next 50 to 150 years. The second alarming fact is that energy consumption has not been very gentle to the environment, both in a global and a local sense. Although there is still an intense debate in the scientific world about the human factor and the overall impact for global phenomena like global warming or ozone layer decrease, local phenomena like air pollution with exhaust gases or nuclear plant disasters are very clear both regarding the causes and the consequences.

There is a clear motivation for the search for new energy sources that primarily are renewable and non-depletable. From a physical viewpoint, there is and has been only one ultimate

Source	Total, %	Electrical, %	Reserves, years
Coal	27	41	118
Oil	33	5.5	46
Natural gas	21	21	59
Nuclear	5.8	14	

Table 1.1.: World energy sources for total and electrical energy with an estimate for the proved reserves remaining at the current consumption rate. [BPEnergyStatistics, 2011; IEAEnergyStatistics, 2010].

external energy source for the planet of Earth – namely the Sun. The coal has developed during millions of years from plants on the Earth, which continued to grow thanks to the energy received from the Sun, and each 1 m^2 of Earth's surface still receives between 1000 and 2000 kWh of energy per year. A coverage of an area of 85000 km^2, equal to 1% of that of the Sahara desert, assuming a conversion efficiency of 10%, would be sufficient to cover the entire world consumption of electrical energy. The challenging question remains: how can we collect and distribute this energy. An important part of the answer can be summarized in the term of *photovoltaics* (PV) – the direct conversion of light into electrical energy. Other parts, including the decentralization of power generation and, of course, changes in the attitude to energy usage and environment, has been the subject of several visionary works, e.g., [Asbeck, 2009].

Leaving the physics of photovolaics for the following section, let us briefly describe today's PV industry. The total worldwide capacity of installed PV systems has grown from 1.4 GW in 2000 to 23 GW in 2009 following an almost exponential rule [EPIAreport, 2011]. There are several scenarios predicting an increase of up to 4669 GW until 2050, which could increase the share in the electricity generation from the current value of 0.2% up to even 21%. A deciding factor will be the costs of PV systems so that the electricity from PV is competitive with other sources. This sets major constrains on the technology and the processes along the entire production chain of solar cells.

1.1.2. Solar cell technology

The *photovoltaic effect* was first observed in 1839 by the French physicist A. E. Becquerel when he produced a current by exposing a silver electrode to illumination in an electrolyte [Goetzberger et al., 1997]. However, the explanation of these observations required almost a century and a deep understanding, based on quantum physics, of the electronic structure of metals and of the formation of bands and band gaps in metals and semiconductors. The first working solar cell was produced on silicon basis in 1954 at Bell Laboratories by Chapin et al. [1954] and had a conversion efficiency up to 6%. Today's understanding of the photovoltaic effect and its usage in solar cells is shortly summarized in the following text after [Goetzberger et al., 1997]; see Fig. 1.1.

In a semiconducting material with a band gap E_g, sunlight with an energy (typically $1 \ldots 3$ eV) higher than E_g can induce an electron transition from the valence band to the conduction band, leaving a hole behind in the valence band. This is the so-called *generation* process. If there is an electric field in the crystal, for example, in a space charge region generated by different doping levels (the p-n junction), electrons and holes are pushed in different directions and are separated from each other, once they have reached this region, for example, due to thermal diffusion. Now, a voltage can be measured on both sides of the space charge region, and an electric current would flow in a closed outer circuit. The sunlight has been converted to electricity.

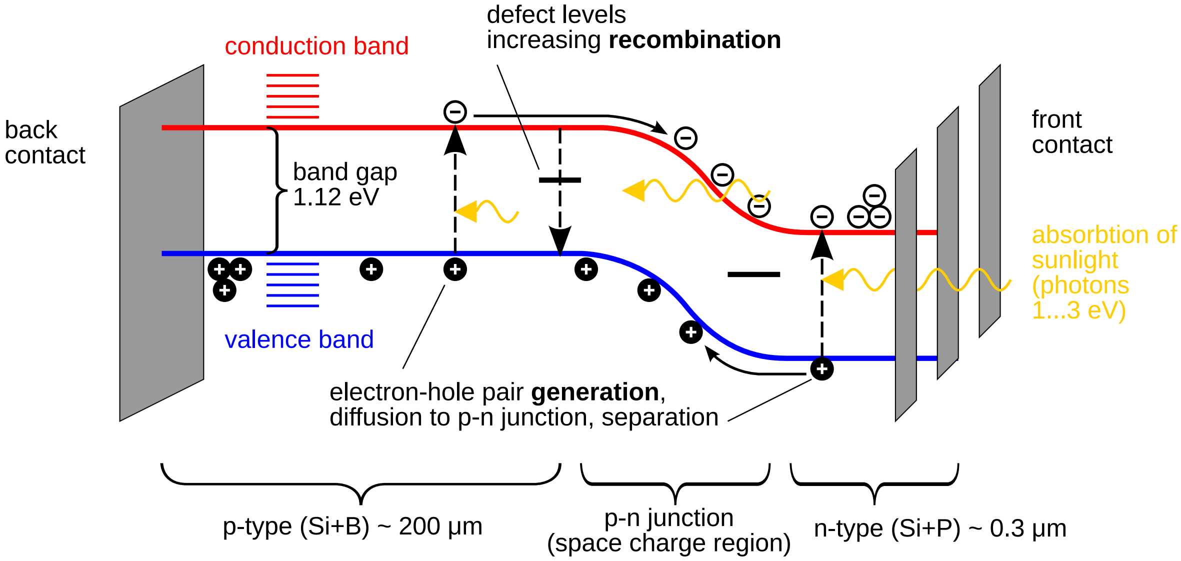

Figure 1.1.: Illustration of the photovoltaic effect in a silicon solar cell, including the role of material defects.

The basic photovoltaic principle can be realized on the basis of different materials and their combinations. In most cases, in a thin semiconductor plate (wafer) with a base doping, a large-area p-n junction is produced by adding a second dopant. Adding contacts on both sides (in the form of a grid on the front side to let the light through) gives a solar cell. Several cells are connected together in a solar module to reach the required electrical voltage and power.

There are many different solar cell technologies based on various materials, but the market is dominated by crystalline silicon, which reached a share of more than 80% in 2010 [EPIAreport, 2011]. This is not surprising because silicon is the second most abundant element in Earth's crust after the oxygen. Crystalline silicon solar cells are produced in a roughly equal proportion from *monocrystalline* and *multicrystalline* material. The latter is characterized in the bulk by the presence of grain boundaries that separate regions (grains) with different crystallographic orientations. The ultimate property of the final product is the conversion efficiency, which is currently 16. . . 22% for monocrystalline material and 14. . . 18% for multicrystalline silicon in commercial technologies [EPIAreport, 2011]. Both values are still below the theoretical limit of about 30% for idealized silicon solar cells [Shockley and Queisser, 1961]. Particularly the difference between monocrystalline and multicrystalline silicon cells and the continuous improvements over time place the question – what are the factors determining the efficiency on the wafer material level.

As for many other optical and electronic properties of solid materials, defects in the material play a decisive role. There is a probability that after the *lifetime* period electrons fall back to the valence band in the so-called *recombination* process and do not reach the space charge region where they get separated (see Fig. 1.1). It turns out that these recombination times are significantly smaller in the reality than in the theory due to the presence of defects in semiconductor crystals. These may be intrinsic or impurity defects, grain boundaries, dislocations, clusters, and different combinations of these; see, e.g., [Möller, 1993, Ch. 4, 5]. It is obvious that the first origin of structural defects is the crystallization process, which naturally influences also the distribution of impurities in the grown crystal. The directional solidification of multicrystalline silicon – the topic of this work – is described in the following section.

1.2. State of the art in the industrial directional solidification of multicrystalline silicon

1.2.1. Crystallization furnace

The production of multi-crystalline silicon (mc-Si) typically occurs in a crystallization furnace as shown in Fig. 1.2. The method known as *directional solidification* (DS) combines ideas from the *Bridgman technique*, the *heat exchanger method*, and the *vertical-gradient-freeze* (VGF) technique [Wilke and Bohm, 1988, Ch. 3]. The main difference between these methods lies in the primary approach for thermal control of crystallization, which is achieved by moving the crucible downward, cooling the crucible from the bottom, or producing a moving vertical temperature gradient through the use of heaters, respectively. From the various modifications of directional solidification applied to multicrystalline PV silicon starting from mid-1970s (see, e.g., [Helmreich, 1987], [Narayanan and Ciszek, 2010], and references therein), the SOPLIN (SOlidification by PLanar INterface) process [Koch et al., 1997; Franke, 2000] developed by Bayer AG is similar to the systems used today. Today, furnaces for directional solidification of silicon for photovoltaic applications are available commercially in mass production from a variety of suppliers; see, e.g., [Chunduri, 2011a].

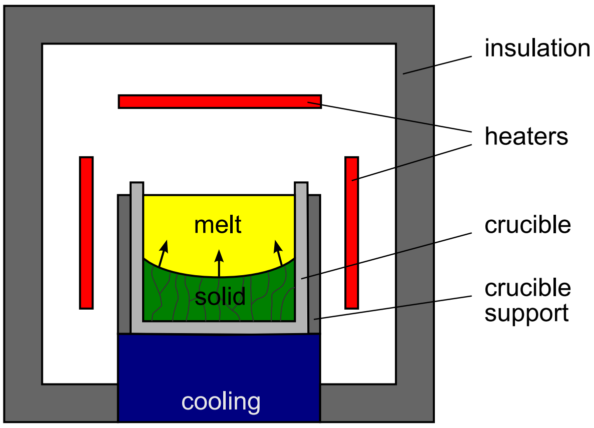

Figure 1.2.: Furncace for directional solidification of multicrystalline silicon.

At the start of the directional solidification process, the silicon feedstock (for example, polycrystalline chunks with the dimensions of a few centimeters) is placed in a square crucible. The crucibles used in the solar industry are made from fused silica (SiO_2) and contain a Si_3N_4 coating on the inside to prevent sticking of the solidified silicon. Such crucibles are used only once and are broken apart to remove the grown crystal because SiO_2 undergoes a phase transformation during the temperature process. The crucibles become soft at high temperatures; therefore, additional mechanical supports are used on the sides to withstand the load.

The horizontal crucible dimensions are approximately multiples of the standard size of a solar wafer, which is 156×156 mm^2, with the pre-factors called generations (Gen). Today, the industry has reached Gen5, with typical ingot dimensions of 84×84×26 cm^3 and a typical weight of 450 kg, but the transition to Gen6, with ingot dimensions of 100×100×34 cm^3 and a weight of 800 kg, is in progress [Chunduri, 2011a]. Note that in both cases, the crucible, with the typical height of 48 cm, is taller than the ingot to accommodate the less dense feedstock material. On the research scale, Gen1 ingots with dimensions of 22×22×13 cm^3 and a weight of 15 kg are still used.

The crucible is placed on a base plate and surrounded by a cooling system at the bottom and heaters at the sides and the top. The heaters are typically resistance heaters supplied with the standard (e.g., 50 Hz) AC current, but induction heating with water-cooled coils can be also applied. Two principal technologies can be used for the cooling system:

- Radiation from the parts under the crucible, which is controlled by the visible area of the heat sinks (cooled vessel of the furnace or dedicated installations)
- Convective cooling by the controlled flow of a cooling medium in a heat exchanger under the crucible

Additional control can be obtained in both cases by the adjustment of the vertical position of the crucible or insulation with respect to the heaters or by a heater in the bottom part of the furnace. The heaters are surrounded by heat insulation, which separates the so-called hot zone from the rest of the furnace. Most furnace parts are made of various graphite materials, e.g., isostatically pressed graphite or graphite felts. The insulation is surrounded by a hermetic water-cooled vessel that confines the furnace atmosphere – mostly argon with controlled pressure and inflow/outflow conditions.

The process starts with the melting of the polycrystalline silicon, with most heaters running at high power and without cooling. The melting phase is followed by crystallization with a controlled heat extraction from the crucible bottom. The growth may start at arbitrary positions on the bottom where the conditions for the nucleation are reached, which results in many crystallites (grains) competing with each other and, finally, in a multicrystalline structure. The typical bulk growth velocities are on the order of 1 cm/s. The heaters must ensure that the top part of the silicon remains liquid, i.e. that the silicon solidifies directionally from the bottom to the top. Because the density of solid silicon is lower than the density of liquid silicon, liquid trapped under or within solid silicon will expand and will cause cracks. After the crystallization, the silicon crystal is cooled down to the room temperature and removed from the furnace. The further production of silicon wafers includes sawing the ingot into vertical bricks using wire or band saws. Afterward, the bricks are wire sawed into wafers with typical thicknesses of 180 µm.

Note that directional solidification belongs to a larger group of methods for the melt growth of bulk crystals. Two other methods that are used for silicon and that are repeatedly mentioned in this work are the *Czocharlski* (CZ) and *float-zone* (FZ) techniques [Wilke and Bohm, 1988, Ch. 3]. In the Czochralski method, silicon feedstock is melted in a silica crucible; a seed crystal then touches the free surface and initiates crystallization. By pulling the seed crystal upward, a cylindrical single crystal (monocrystal) with a diameter up to 300 mm can be obtained. The float-zone method is crucible-free and requires a polycrystalline feedrod. The rod is moved from above vertically toward a pancake-form inductor and melted, while a cylindrical crystal is pulled downward out of the molten zone below the inductor. High-purity single crystals with diameters up to 200 mm can be produced. Although both of these techniques allow better material qualities than directional solidification due to less interaction with a crucible, the production costs are significantly higher.

1.2.2. Physical phenomena, their role and interactions

In the following paragraphs, the main physical processes in an industrial solidification furnace are summarized according to Fig. 1.3. The current state of knowledge in the literature is reflected.

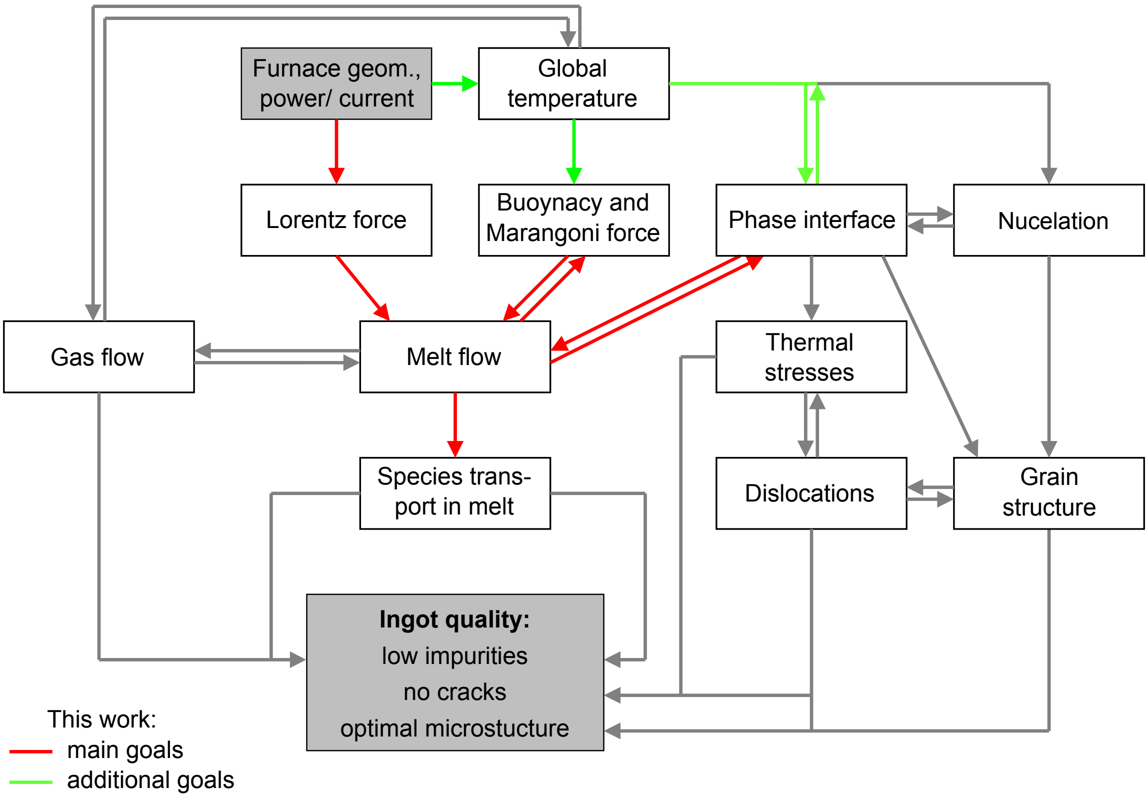

Figure 1.3.: Physical processes in an industrial solidification furnace. Processes investigated in the current work are indicated for further reference.

The **global heat transfer** in the furnace is in a root position determined primarily by the furnace geometry and the power of the heaters and coolers. Heat radiation plays a major role due to the high temperatures (above the 1412 °C melting point of silicon) for the heat transfer from and to the silicon as well as between various furnace parts. Heat conduction occurs in all furnace parts, with the largest temperature gradients occurring in the materials with the smallest thermal conductivity: the crucible and the insulation. Note that the global heat transfer has a highly nonlinear character due to the temperature dependences of the thermal conductivities and radiation heat fluxes, which are proportional to the 4th powers of the surface temperatures.

The temperature field in silicon determines the crystallization process, i.e., the macroscopic motion and shape of the **crystallization interface**. From a macroscopic point of view, the crystallization interface is simply determined by the local heat balance:

$$\boxed{\text{Cooling at the crystal side}} - \boxed{\text{Heating at the melt side}} = \boxed{\text{Crystallization velocity and release of latent heat}}$$

Because the solidification primarily occurs in the vertical direction, the velocity is determined by the vertical temperature gradients. The lateral temperature gradients influence the deflection of the interface, which becomes concave when losing heat at the crucible's sides and convex when receiving heat; this deflection can be adjusted by the furnace design [Franke, 2000]. A planar solidification interface has been considered optimal due to reduced thermal stresses in the crystal [Häßler et al., 1999].

Although the temperature field in the liquid silicon is stably stratified (cold at the bottom), it is impossible to avoid all lateral temperature gradients. As a consequence, **motion in the liquid silicon** can arise due to buoyancy forces in the bulk and Marangoni forces (related to the temperature dependence of the surface tension) at the free melt surface [Vizman et al., 2007; Dropka et al., 2010]. Furthermore, Vizman et al. [2007] shows that the melt motion is tightly coupled with the shape of the phase interface in both directions because the melt flow can change the heat flow to the crystallization interface but depends on the shape of the interface.

If the heaters are supplied with an alternating current, they produce a **time-dependent magnetic field**, which can induce a Lorentz force in electrically conducting bodies and additionally drive the melt motion. Several examples for industrial furnaces exist in the patent literature [Dietrich et al., 2007; Julsrud and Rudshaug, 2007]. The Lorentz force effect has been utilized in the KristMAG concept, which attempts the goal to develop a system with a flexible magnetic field, a traveling magnetic field in particular, generated by the heaters in crystal growth furnaces, including directional solidification of multicrystalline silicon [Rudolph, 2008]. The possibility to influence the flow pattern in industrial systems has been demonstrated in 3D numerical simulations [Dropka et al., 2010].

As previously mentioned, the furnace components also contain chemical elements other than silicon, for example, carbon, oxygen, and nitrogen. Additional **impurities**, such as the metals Fe, Al, and Cu, in the furnace parts as well as in silicon feedstock are also unavoidable. The principal sources of contamination and the reactions during the crystallization have been investigated by Reimann et al. [2010]; Reimann [2010].

The possibility that these impurities are built into the crystal is relevant. This situation can only occur in two ways – in-diffusion at the contact of the crystal with the crucible and segregation at the solid-liquid interface, where a specific fraction of the impurities available at the interface is incorporated into the crystal. The segregation process depends on the species distribution in the melt, which is significantly influenced by any melt motion, including the buoyancy flow as shown in a numerical simulation by Teng et al. [2010]. If the melt mixing is too low, impurities can start to precipitate if the solubility limit in the melt is exceeded; impurities can then be built into the crystal at the crystallization interface [Möller et al., 1999; Liu et al., 2008]. Such SiC or Si_3N_4 inclusions can cause shunts in solar cells [Breitenstein et al., 2004] and problems during sawing due to changes of the mechanical properties of silicon. In addition, the concentration of the dissolved impurities, Fe in particular, has been shown to have a strong correlation with solar cell efficiency [Coletti et al., 2008; Hofstetter et al., 2011].

Convection in the gas atmosphere can arise due to the inflow and outflow conditions as well as due to the large thermal differences between various furnace parts. Several designs for the inflow of gas have been proposed previously [Reimann, 2010; Chen et al., 2011], but little has been published about the conditions in industrial furnaces. Gas convection plays an important role for species transport at the free melt surface for evaporating species like oxygen; it is also responsible for the reactions involving the graphite parts. These effects have been extensively investigated numerically in small-scale silicon furnaces [Li et al., 2011c]. The gas flow effect on the heat transport in the furnace is probably much smaller than that of the radiation, but this effect can be relevant under specific conditions [Li et al., 2011b]. The same can be said about the influence of the gas flow on the melt flow (the momentum exchange) in comparison to the other forces driving the melt flow [Liu et al., 2011b].

Although the global temperature field determines the macroscopic movement and shape of the crystal, microscopic and kinetic effects are important for the formation of the **grain structure and structural defects**. The main origin of the multi-crystallinity lies in the availability of nucleation sites along the crucible bottom as well as on the side walls. Several techniques have been introduced to optimize this process toward large grains [Nakajima et al., 2008] or even monocrystalline materials [Stoddard et al., 2008]. A tight control of the global and local temperature distributions seems to play a key role [Chunduri, 2011b]. The link to the thermal conditions in silicon and the shape and velocity of the crystallization interface is even more pronounced for the dislocation generation and multiplication [Franke, 2000] as well as for the interaction between different grains [Yeh et al., 2010]. There is much experimental evidence that structural defects interact with each other (dislocation clusters) or with impurities (grain boundaries and dislocations aggregate impurities), decreasing the cell efficiency significantly [Möller, 1993, Ch. 5].

In summary, we can conclude that melt convection sits in a central position in the physical scheme of the directional solidification of multicrystalline silicon, interacting directly or indirectly with nearly every other phenomenon (see Fig. 1.3). Although melt convection is not the primary effect in most cases, it could typically be considered the most important second-order effect. However, there are no available detailed data about the flow conditions in industrial furnaces and no additional tools for a dedicated control have been extensively tested and described in the literature.

1.2.3. Methods for experimental investigation

The methods for the experimental investigation of directional solidification of silicon can be divided into techniques for the characterization of the solidified ingots and into measurements in the furnace to investigate the conditions during the growth. A brief summary is given below with an aim to give an impression what experimental data are available and, more important, what are not available.

The methods for the characterization of the solidified silicon ingots in order to investigate the influence of the melt flow (see, e.g., [Reimann, 2010; Würzner et al., 2010] and references therein):

- Measurements of the macroscopic distribution of impurities and dopants. The concentration of carbon, nitrogen, and oxygen can be determined using the Fourier Transformation Infrared Spectroscopy (FTIR) methods. The dopant concentration can be determined from the measurements of the resistivity.

- Analysis of the location, the type and the number of various impurity precipitates or inclusions is possible using the Infrared Transmission Microscopy (IR-TM) methods.

- Measurements of the microscopic resistivity variations (related to the dopant concentration variations), which allow a visualization of the interface shape at various stages during the growth, by the Lateral Photovoltage Scanning (LPS) technique.

A limitation of microscopy methods is that only a small sample of the entire ingot usually can be analyzed. The absence or presence of impurities, inclusions, or of a specific type of structural defects may not be typical for the entire ingot in three dimensions. On the other hand, spectroscopic methods for impurity concentration usually detect only the impurities occurring in a specific form, e.g., as interstitial defects or as precipitates.

Due to the high temperature and the chemical aggressiveness of liquid silicon, there are only a few methods available for in-situ measurements during the growth process:

- Temperature measurements in various furnace parts using thermocouples or pyrometers. These measurements are also needed for the process control, i.e., to adjust the heating and cooling powers.

- Measurements of the vertical position of the crystallization interface by means of mechanical sensing. For example, a rod of, e.g., quartz is immersed into silicon; or the exact position of the free surface is measured and the approximate solidified part is calculated [Müller et al., 2004]. First tests for the detection of the interface position by ultrasonic methods have been presented in [Azizi et al., 2010].

- Measurements of the temperature and its fluctuations in the liquid silicon using encapsulated thermocouples or optical measuring systems have been performed for other silicon growth processes [Gräbner et al., 2000], but no applications to industrial DS furnaces have been reported in the literature.

- Soiland [2004] describes a method for taking samples from the silicon melt during the growth process by sucking the liquid into a quartz tube that is immersed into the melt. These samples can be used for further analysis of the impurity contents.

There are only a few known examples of direct flow measurements in liquid silicon; e.g., Kakimoto et al. [1988] observed the motion of tracer particles by X-ray radiography in a small Czochralski furnace. Consequently, only indirect data about the flow conditions in DS furnaces is available. The macroscopic species distribution may show the impact of melt flow on the mixing of the species. The shape and velocity of the crystallization interface or temperature measurements in the melt may contain some hints about the impact of the flow on the temperature field in the melt. However, such indirect data require a coupled analysis where also, e.g., the initial species concentrations, mutual reactions, and the global temperature field are considered. Therefore, numerical models are very useful tools for such analysis. Another tool is the so-called model experiment, which attempts to reproduce the relevant aspects in experimental setups that are better accessible for measurements.

1.2.4. Review of numerical modeling

Much of the knowledge about the processes in silicon furnaces has been acquired with a significant support of numerical simulations. This section gives an overview of main research groups and their results with regard to numerical modeling of directional solidification of multicrystalline silicon. Due to the large amount and variety of studies, a summary is given as a table Tab. 1.2 and the main conclusions are outlined in the following paragraphs. The following research groups are considered:

- ACCESS: ACCESS e.V., Aachen, Germany
- EPM: Laboratory Electromagnetic Processing of Materials, Saint-Martin-d'Hères Cedex, France
- CGL: Department of Crystal Growth, Fraunhofer Institute IISB, Erlangen, Germany
- UVT: Faculty of Physics, West University of Timisoara, Romania
- IKZ: Leibniz Institute for Crystal Growth, Berlin, Germany
- Kyushu: Research Institute for Applied Mechanics, Kyushu University, Kasuga, Fukuoka, Japan
- NCU: National Central University, Jhongli City, Taiwan, R.O.C
- SINTEF: SINTEF Materials and Chemistry, Trondheim, Norway
- NTNU: Department of Materials Science and Engineering, Norwegian University of Science and Technology, Trondheim, Norway

2D global thermal calculations are carried out on a routine basis for optimizations of furnace design and heater control [Saitoh et al., 2005; Meese and Westermoen, 2007; Wu et al., 2008; Bellmann et al., 2008, 2009; Teng et al., 2009; Wei et al., 2009; Syvertsen et al., 2010; Bellmann et al., 2011b]. Generally, these calculations show a good agreement with the measured temperature profiles and with the experimentally determined crystallization velocity, after the model calibration, e.g., [Meese and Westermoen, 2007; Wei et al., 2009]. 3D global calculations are very time consuming and mostly the melt with the surroundings alone is calculated in 3D [Liu et al., 2007; Kuliev et al., 2007] or a 4-fold symmetry of the geometry is assumed [Bähr et al., 2007; Franke, 2000; Franke et al., 2002; Barvinschi et al., 2003; Delannoy et al., 2007; Wu and Clark, 2011]. These calculations allow one to obtain realistic temperature conditions in the melt corners, which can be important for further local models.

The coupled melt flow and species transport has been extensively investigated only in a 2D approximation. Several studies have been devoted to the behavior of carbon, nitrogen, and oxygen and the formation of SiC and Si_3N_4 precipitates in particular [Arens, 2007; Reimann et al., 2008; Reimann, 2010; Trempa et al., 2010; Liu et al., 2008; Bellmann et al., 2010; Teng et al., 2010]. It was shown that melt convection, e.g., due to buoyancy forces can influence both the absolute level and the distribution of the impurities in the ingot. A forced convection caused by a steady or accelerating crucible rotation of a cylindrical melt was found to decrease the level of melt mixing in several cases [Bellmann et al., 2011a; Bellmann and Meese, 2011]. Similar studies have been carried out for the distribution of dopants such as boron [Bellmann et al., 2010; Kakimoto et al., 2006; Bellmann et al., 2010; Ellingsen et al., 2010] or gallium [Kakimoto et al., 2006] as well as for metallic impurities such as iron [Kakimoto et al., 2006; Liu et al., 2006; Boulfrad et al., 2010]. The transport of oxygen is the primary focus in [Matsuo et al., 2008a,b; Hisamatsu et al., 2009; Matsuo et al., 2009; Nakano et al., 2009; Gao et al., 2010; Teng et al., 2011].

Research group/ References	Glob. temp.	Melt flow	Mag. fields	Species	Gas flow	Stress/ Disloc.	Crys. size	Sim. soft.
ACCESS: [Franke, 2000; Franke et al., 2002; Steinbach et al., 2002; Bähr et al., 2007; Behnken, 2009]	3D					3D/3D	Gen4	CASTS, Abaqus
EPM: [Barvinschi et al., 2003; Delannoy et al., 2007]	3D	3D					Gen4	ANSYS Fluent
CGL+UVT: [Arens, 2007; Reimann et al., 2008, 2010; Reimann, 2010; Trempa et al., 2010]	2D	2D		2D	(2D)		6cm	CrysMAS, OpenFOAM
[Vizman et al., 2007; Tanasie et al., 2011]		3D	3D				Gen4	STHAMAS3D
IKZ: [Menzel, 2008; Dropka et al., 2010, 2011]	(3D)	3D	3D				Gen4	ANSYS CFX
Kyushu: [Kakimoto et al., 2006; Liu et al., 2006; Chen et al., 2008; Liu et al., 2008; Matsuo et al., 2008a,b; Hisamatsu et al., 2009; Matsuo et al., 2009; Nakano et al., 2009; Gao et al., 2010; Li et al., 2011a,b]	2D	2D		2D	2D	2D	10cm	In-house
[Liu et al., 2007; Miyazawa et al., 2008a,b; Chen et al., 2010a]	3D	3D				3D/ 3D	10cm	In-house
NCU: [Teng et al., 2009, 2010, 2011]	2D	2D		2D	2D		Gen4	CGSim
SINTEF+NTNU: [Meese and Westermoen, 2007; Bellmann et al., 2008, 2009; M'Hamdi and Gouttebroze, 2009; Bellmann et al., 2010; Boulfrad et al., 2010; Ellingsen et al., 2010; Syvertsen et al., 2010; Bellmann et al., 2011b,a; Bellmann and Meese, 2011]	2D	2D		2D		2D/ 2D	25 cm	ANSYS Fluent, COMSOL
Various 2D: [Saitoh et al., 2005; Wei et al., 2009; Wu et al., 2008]	2D						Gen4	PHOENICS, CFD-ACE
Various 3D: [Kuliev et al., 2007; Kaden et al., 2008; Wu and Clark, 2011]	3D	3D		3D			Gen1 Gen4	CGSim, ANSYS Fluent, ProCAST

Table 1.2.: Overview of numerical modeling for directional solidification of multicrystalline silicon. Designations: () – not published; 2D/ 3D – simulation model. For crystal size, either the generation (Gen) of the square ingot or the diameter of the cylindrical crystal is given. Last column names the used simulation software for future reference.

The 2D approximation turns out to be sufficient to model the overall mixing level of impurities such as carbon for both cylindrical and square ingots – the calculated concentration profiles in the crystal show a good agreement with the experiment; e.g., [Bellmann et al., 2010; Teng et al., 2010]. However, several studies in 3D have clearly shown that also pure buoyancy forces lead to a three-dimensional flow structure in square systems [Vizman et al., 2007; Kuliev et al., 2007; Miyazawa et al., 2008b; Menzel, 2008; Dropka et al., 2010]. Three-dimensionality gains further importance if small tilts of the gravity vector are introduced into the calculations [Vizman et al., 2007; Miyazawa et al., 2008a]. An additional time-dependent magnetic field leads to a complex interaction with the buoyancy forces [Dropka et al., 2010, 2011], whereas a steady magnetic field damps flow oscillations [Tanasie et al., 2011].

Simulations of the gas flow and its influence on species and heat transport have been addressed in [Li et al., 2011b,c; Teng et al., 2011], but only in a 2D approximation. Considering the variety and complexity of the interactions between the physical processes, this approach allows one to carry out parameter studies and gain physical understanding in reasonable time. Selected 3D calculations for specific phenomena remains a topic for future research.

The situation is similar for the calculation of thermal stresses and dislocations in the ingot. Qualitative correlations between thermal process parameters and stresses/dislocations can be easily extracted from 2D calculations as performed in [Chen et al., 2008; Bellmann et al., 2009]. 3D calculations show that the stresses and dislocation densities have local extrema in the corners; e.g., [Chen et al., 2010a]. Nevertheless, most of these calculations should be considered only qualitative because the Alexander-Haasen continuum model is used for the dislocation motion and the multi-crystalline structure is neglected. First attempts to take the microstructure into account were shown in [Behnken, 2009].

In summary, there are almost no published 3D numerical studies about the influence of magnetic fields on the melt flow, species transport, and interface shape during directional solidification of silicon in large melts.

1.3. Melt flow control by magnetic fields

1.3.1. Types of magnetic fields used in crystal growth

The control of melt motion during crystal growth has to meet several challenges: high temperatures, hermetically sealed furnace containers, and high requirements for purity. Following the review by Rudolph and Kakimoto [2009], the methods can be divided into categories based on mechanical, electrical, and magnetic force fields. Mechanical and magnetic methods are widely used in crystal growth, both on a research and an industrial scale.

Mechanical methods include various schemes for crucible (and/or crystal) rotation, such as steady, periodically revered, or accelerated rotation. Vibrations in the range from a few Hz to several MHz can be introduced into the melt by vibrating the crucible or by using a submerged transducer. Although the mechanical methods can be used for all melts independently of their electrical and magnetic properties, their application to very large square melt volumes is not trivial, and no results for industrial directional solidification of silicon are known.

The use of external magnetic fields in crystal growth is motivated by the fact that most molten semiconductors behave as liquid metals; in particular, their electrical conductivity is on the level of liquid metals [Glazov et al., 1967]. This allows two principally different interactions with magnetic fields: for a static or a time-dependent magnetic field. The following paragraphs give a short summary of the various magnetic field types; see the reviews [Hurle and Series, 1994; Moreau, 1999; Davidson, 1999; Friedrich, 2007; Muiznieks et al., 2007; Rudolph, 2008; Rudolph and Kakimoto, 2009] and references therein.

A static (direct current) magnetic field on the order of several tens of mT generally damps the melt motion. In various crystal growth processes various DC field configurations have been used: vertical, horizontal, or the so-called CUSP field (generated by two axial coils with opposite currents). A decrease of temperature fluctuations and oscillations of dopant concentration, a stabilization of melt flow by increasing the instability threshold have been observed. The application of a steady magnetic field to multicrystalline silicon is less interesting because most findings currently indicate a need for a better mixing of the melt. Furthermore, ferromagnetic cores – which can not be used at the high temperatures inside the furnace – may be necessary due to the relatively high magnetic flux densities.

A time-dependent magnetic field induces potential differences and consequently eddy-currents in an electrically conductive melt according to Farady's law. The product of the eddy current density and the external magnetic field defines the Lorentz force acting on a melt volume. The resulting flow pattern is largely dependent on the (time-average) Lorentz force distribution. Three main types of time-dependent magnetic fields can be distinguished according to the inductor geometry and the phase shifts: alternating, rotating, and traveling magnetic fields, as summarized in the following paragraphs; see also Fig. 1.4.

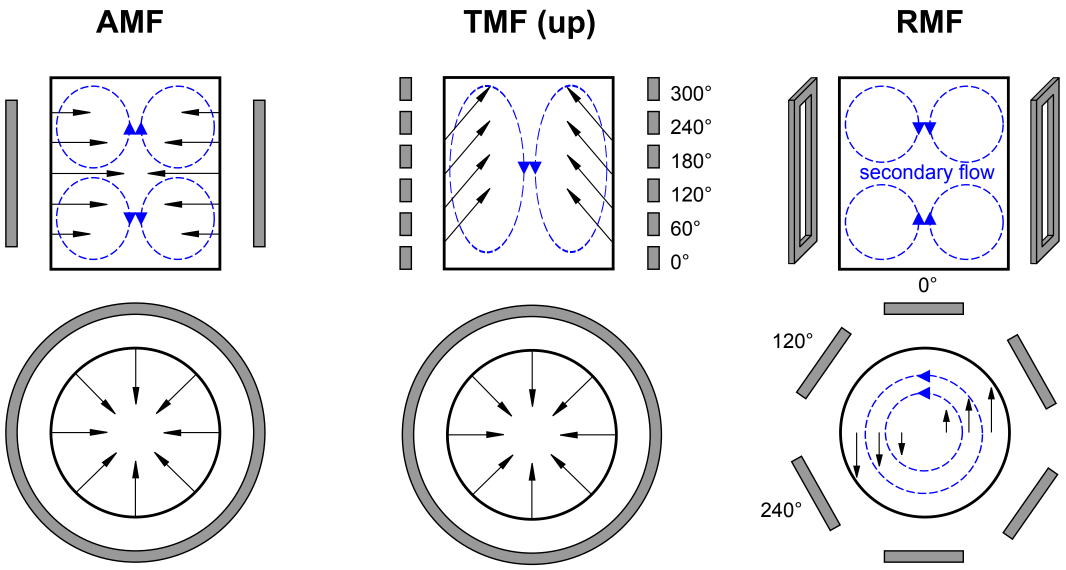

Figure 1.4.: Types of time-dependent magnetic fields used in crystal growth. Black arrows describe the time-average Lorentz force distribution, blue streamlines describe the typical flow structure. The numbers show the typical phase shifts between inductor currents.

A rotating magnetic field (RMF) can be generated by three azimuthally displaced coil pairs with a phase shift of 120 degrees. It is often described in an idealized way as a magnetic induction vector that is rotating in the horizontal plane with the current frequency. The resulting force is directed azimuthally and drives a primary azimuthal flow. A secondary structure consisting of two tori appears in the meridional plane due to the boundary layers at the top and bottom surfaces. A RMF has been applied to control the shape of the crystallization interface and the thermal stresses or to achieve a better dopant distribution or mixing in different crystal growth systems.

A traveling magnetic field (TMF) can be generated with several displaced and phase-shifted coils that are arranged vertically at the side of the melt in the classical configuration. The Lorentz force acting in the meridional plane has a vertical component. The direction of the force can be reversed up or down by the phase shift between the coils. A toroidal flow pattern is typically generated in the melt. The main objectives for the use in crystal growth are similar to that of a RMF.

An alternating magnetic field (AMF) can be considered a special case of a TMF where the phase shift is set to zero. Of course, a single inductor can be used in this case. This simplification eliminates the force direction and makes the Lorentz force perpendicular to the side surface. The corresponding flow structure consists of two tori. AMFs with frequencies of several kHz are used in induction furnaces, where they also provide an induction heating. Due to the high Lorentz force density, the flow usually is turbulent. The magnetic field generated by the induction coil in the float-zone technique with a frequency of several MHz also can be considered a AMF. In addition to heating and stirring, it contributes to the stabilization of the liquid meniscus.

Various **combinations** of all these fields have been also investigated and may lead to striking flow patterns, such as a liquid metal tornado for the combination of a RMF and a TMF [Grants et al., 2008]. Another variation is a time-modulation of the fields by generating pulses [Eckert et al., 2009], reversing the force direction [Wang et al., 2009], or superimposing two different frequencies [Dropka et al., 2011]. This allows one to generate further flow structures in both space and time.

The basic effects of the action of different magnetic fields on liquid metals, such as the typical flow patterns and the transition between steady and unsteady flows, have been understood on a fundamental fluid mechanics level; see, e.g., [Grants and Gerbeth, 2001, 2002]. The group at HZDR has developed a coil system that allows arbitrary configurations and combinations of the various fields and proposes the principle: describe the flow pattern, and we will find out how to generate it [Pal et al., 2009]. The difficulty of the requirement in the first part of the quote should not be underestimated – how to determine the optimal flow pattern for a specific process.

For a better melt flow control in the industrial directional solidification, a low-frequency (Hz range) TMF seems to be the most promising option from the time-dependent magnetic fields. It offers the following advantages in comparison to other fields (see also [Rudolph, 2008]):

- Requires relatively low flux densities achievable without ferromagnetic cores
- Can be generated also by the heaters inside a furnace

- Has a flexible flow direction (vs. RMF, AMF)
- A negligible heat generation and a large skin layer are possible (vs. high-frequency AMF)

1.3.2. Review of the use of traveling magnetic fields

Due to the advantages of a TMF outlined in the previous section, an overview of the main research groups and their results is given here with regard to the use of a TMF in DS and similar growth processes. Again, due to the large amount and variety of studies, a summary is given as a table Tab. 1.3 for the scientific literature and Tab. 1.4 for the patent literature. Here, we are mainly interested in scientific results in the form of experiments or simulations included in patent publications, which often are the only publicly available information for industrially relevant contributions. Moreover, the patent literature not only contains a vast amount of technical knowledge that cannot be found elsewhere but also can be used for the evaluation of the current state and trends of a specific technology; see e.g. [Liu et al., 2011a]. The following research groups and companies are considered:

- CGL: Department of Crystal Growth, Fraunhofer Institute IISB, Erlangen, Germany
- EPM: Laboratory Electromagnetic Processing of Materials, Saint-Martin-d'Hères Cedex, France
- HZDR: Magnetohydrodynamics Department, Helmholtz-Zentrum Dresden-Rossendorf, Germany
- IKZ: Leibniz Institute for Crystal Growth, Berlin, Germany
- NASA: NASA Marshall Space Flight Center, Huntsville, Alabama, USA
- Riga: Faculty of Physics and Mathematics, University of Latvia, Riga, Latvia
- IPUL: Institute of Physics, University of Latvia, Salaspils, Latvia
- TUBA: Institut für NE-Metallurgie und Reinststoffe, Technische Universität Bergakademie Freiberg, Germany
- TUD: Institute of Fluid Mechanics, Technische Universität Dresden, Germany
- IKZ: Leibniz Institute for Crystal Growth, Berlin, Germany
- DeutscheSolar: Deutsche Solar AG, Freiberg, Germany
- REC: REC SCANWAFER AS, Porsgrunn, Norway
- Siltronic: Siltronic AG, München, Germany
- CGS: Crystal Growing Systems GmbH, Aßlar, Germany

With regard to the methodology, the studies about the TMF can be divided in two groups:

- Application of a TMF to real crystal growth processes such as DS, VGF, or CZ for various materials (Si, Ge, GaAs, etc.). Characterization of the influence of a TMF using the grown crystal (resistivity distribution, striation intensity, shape of the crystallization interface, etc.) or simulations for a specific furnace.
- Application of a TMF to the so-called model experiments that resemble a real growth process but simplify the geometry and/or boundary conditions. The analysis is carried out by means of general numerical simulations (often using dimensionless variables) or by direct velocity measurements in low-melting-point melts (Ga, GaInSn, Hg).

Research group/ References	Method	Material	Melt size	TMF	Melt flow	Flow regime	Species
CGL: [Dagner et al., 2003; Iuga, 2003; Socoliuc et al., 2003; Schwesig et al., 2004; Hainke et al., 2005]	VGF, (VGF)	InP,AlSi, (Ga)	4mm.. 2in	SE, 2D	2D, Exp.	Lam.	
EPM: [Zaidat et al., 2005; Zaidat, 2005; Zaidat et al., 2007; Noeppel et al., 2009]	DS	AlNi	8mm	SE	2D	Lam.	2D
HZDR: [Cramer et al., 2004a,b; Grants and Gerbeth, 2004; Cramer et al., 2007b; Grants and Gerbeth, 2008; Grants et al., 2009a; Cramer et al., 2011]	(VGF)	(GaInSn)	4..14cm	Id.	2D, Exp.	Lam., Turb.	2D
IKZ: [Frank-Rotsch et al., 2008; Kasjanow et al., 2008; Rudolph, 2008; Frank-Rotsch and Rudolph, 2009; Rudolph et al., 2009a; Dropka et al., 2010, 2011; Rudolph et al., 2011; Miller et al., 2011]	DS, VGF	Si, Ge	3in.. Gen1	SE, 2D	2D, 3D	Lam., Turb.	Exp.
[Lechner et al., 2007; Klein et al., 2008, 2009; Nacke et al., 2009; Rudolph et al., 2009b]	CZ	Si, GaAs	3in	SE, 2D	2D, 3D	Lam., Turb.	Exp.
NASA: [Ramachandran et al., 2000; Mazuruk, 2002; Volz and Mazuruk, 2004; Yesilyurt et al., 2004]	VGF, (VGF)	Ge, (Hg)	2.. 3cm	SE, 2D	2D, Exp.	Lam.	
Riga: [Krauze et al., 2004; Krauze, 2005; Krauze et al., 2008, 2009, 2010]	(CZ)	(GaInSn)	20in	SE, 2D	2D,3D, Exp.	Turb.	
IPUL: [Gelfgat et al., 1999, 2001; Abricka et al., 2002; Gelfgat et al., 2003a,b; Gelfgat, 2005; Gelfgat and Kit, 2005]	(VGF)	-	-	SE, 2D	2D	Lam.	
TUBA: [Lantzsch et al., 2006; Galindo et al., 2007; Lantzsch et al., 2007, 2008; Lantzsch, 2009; Niemietz et al., 2011]	VGF, (VGF)	Ge, GaAs, (GaInSn)	3in, 9cm	2D	2D, Exp.	Lam., Turb.	Exp.
TUD: [Stiller et al., 2006, 2008; Koal et al., 2009; Stiller and Koal, 2009; Koal, 2011]	(VGF)	-	-	Id.	3D	Turb.	3D
Various VGF: [Lyubimova et al., 2004]	VGF	GaAs	1in	SE, 2D	2D	Lam.	2D
Various CZ: [Ono and Trapaga, 1997]	CZ	Si	44cm	SE, 2D		Lam.	2D

Table 1.3.: Overview of the use of a TMF in DS and similar crystal growth processes (scientific literature). Designations: DS, VGF, and CZ denote crystal growth processes, where brackets mean dedicated model experiments; Exp. denotes experimental and 2D/3D denotes numerical investigations for the Lorentz force, melt flow, or species transport; a TMF can be with a distinct skin effect (SE) or idealized (Id.); the melt flow can be either in the laminar (Lam.) or in the turbulent (Turb.) regime. The melt size is given if experiments or simulations without dimensionless variables are performed.

Group/ References	Method	Ideas	Results
IKZ: [Ziem et al., 2009; Lange et al., 2009; Frank-Rotsch et al., 2009a; Jockel et al., 2009; Frank-Rotsch et al., 2009b; Frank-Rotsch and Rudolph, 2010; Ziem et al., 2010; Büllesfeld et al., 2010; Czupalla et al., 2011; Lange et al., 2011]	CZ, VGF, DS	Heater-magnet modules with decoupled AC (for TMF) and DC (for heating) parts at the side, top, or bottom of the melt	2D simulations for Lorentz force
DeutscheSolar: [Dietrich et al., 2007]	DS	AC heaters with variable phase shifts and frequencies	Exp. with mc-Si for various phase shifts
REC: [Julsrud and Rudshaug, 2007]	DS	AC coils outside the hot-zone	Exp. with Gen4 Si
Siltronic: [Ammon et al., 2002, 2008]	CZ for Si	TMF inducotors in a CZ furance; asymmetric shielding of magnetic field	Exp. with 10in crystal
CGS: [Mühe et al., 2005]	VGF	Coupled heaters and TMF coils	

Table 1.4.: Overview of the use of TMF in DS and similar crystal growth processes (patent literature).

One of the first application of a TMF to a specific crystal growth system was the work by Ono and Trapaga [1997]. They performed 2D numerical simulations for the continuous double-crucible CZ growth of 160 mm silicon crystals. A decrease of oxygen concentration at the crystallization interface was observed in a limited range of inductor frequency due to an optimal stirring. More recently, the IKZ research group has applied a TMF generated by a coupled inductor-heater system to the CZ growth of GaAs and Si [Lechner et al., 2007; Klein et al., 2008; Kasjanow et al., 2008; Klein et al., 2009; Nacke et al., 2009; Rudolph et al., 2009b,a]. An unexpected effect was observed with a strong flow induced by superimposed upward and downward TMF fields – a growth of silicon crystals with a nearly quadratic cross section due to low radial temperature gradients was observed [Rudolph et al., 2011; Miller et al., 2011]. However, in general, it should be noted that the melt flow in a CZ system significantly differs from the DS and VGF processes due to the unstable temperature profile and crystal/crucible rotation. The same differences occur also in model experiments and simulations presented in [Krauze et al., 2004; Krauze, 2005; Krauze et al., 2008, 2009, 2010].

Only a few research groups have performed real growth experiments for the VGF process with a TMF. The works [Zaidat et al., 2005; Zaidat, 2005; Zaidat et al., 2007; Noeppel et al., 2009] investigated the combined effect of natural convection and a TMF on the microstructure (the transition between columnar and equiaxed grain structure) and segregation in AlNi crystals with a diameter of 8 mm. The research group at IKZ has found that the application of an optimized downward TMF to Ge crystals with a diameter of 110 mm allows to obtain a favorable flattened interface shape [Frank-Rotsch et al., 2008; Frank-Rotsch and Rudolph, 2009; Rudolph et al., 2009a]. With a carefully adjusted inductor frequency and current, the convection-induced temperature fluctuations can be damped, and nearly striation-free crystals are obtained. Similar results have been obtained by Lantzsch et al. [2008] and Lantzsch [2009] for Ge and GaAs crystals with a diameter of 75 mm – they observed a smaller interface deflection with an downward TMF and a higher deflection with an upward TMF than in the case without a magnetic field. Additional application of a DC field to damp the flow oscillations causing striations was suggested. For the axial macrosegregation, the melt was considered completely mixed also without magnetic fields, and no significant influence of magnetic fields was observed. The results from growth experiments mostly agree well with the conclusions from numerical simulations for the effects on the interface shape and flow oscillations.

From the research groups, only IKZ has applied a TMF to directional solidification of silicon with square crystals. Experiments in a Gen1 furnace have been presented very recently [Kiessling et al., 2011; Kiessling, 2011; Kiessling et al., 2012]. Under optimized TMF conditions, it was possible to avoid SiC and Si_3N_4 inclusions in a silicon ingot. A downward TMF allowed to obtain a convex interface shape. Numerical simulations for a Gen4 melt [Dropka et al., 2010, 2011] illustrate the possibility to obtain various flow structures depending on the TMF strength and direction. The industrial experience for the use of time-dependent magnetic fields has not been discussed actively. The contribution in the patent literature by Dietrich et al. [2007] states that the phase shift of a TMF has a significant influence on the yield, and the work by Julsrud and Rudshaug [2007] indicates that a time-dependent magnetic field can increase the melt mixing and can help avoid inclusions in industrial Gen4 furnaces.

There are many numerical and experimental studies for VGF-like model experiments, see Tab. 1.3. Usually, a small cylindrical container with a diameter up to 14 cm containing a low-melting-point liquid metal is considered. The early works by Ramachandran et al. [2000] and Mazuruk [2002] investigated the stability of a TMF flow in a liquid mercury column by an anemometer at the free surface. [Cramer et al., 2004a,b, 2007a] demonstrated the capability of ultrasonic methods to resolve complex unsteady flow structures. This technique was further applied by [Lantzsch et al., 2006; Galindo et al., 2007; Lantzsch et al., 2007] to optimize the conditions in VGF crystal growth. The instability threshold of the TMF flow was analyzed in detail. The additional influence of a vertical temperature gradient in model experiments has been investigated for an unstable stratification in [Socoliuc et al., 2003] and for a stable stratification in [Klyukin et al., 2008; Niemietz et al., 2011]. In the case of the stable temperature configuration, the buoyancy exhibits a stabilization effect in comparison with an isothermal TMF flow.

Several numerical studies have been devoted to cylindrical melts under an idealized low-frequency TMF with a negligible skin effect. The works [Grants and Gerbeth, 2004, 2008; Grants et al., 2009a] investigated the flow instability and the transition to a time-dependent flow for different melt aspect ratios for the laminar flow regime. The laminar flow regime has been addressed also in several early numerical works [Gelfgat et al., 1999, 2001; Abricka et al., 2002; Gelfgat et al., 2003a,b; Gelfgat, 2005; Gelfgat and Kit, 2005]. The unsteady turbulent melt flow for an idealized TMF has been investigated numerically by [Stiller et al., 2006, 2008; Koal et al., 2009; Stiller and Koal, 2009; Koal, 2011] and demonstrated an efficient melt mixing. Cramer et al. [2011] pointed out that the flow structure is very sensitive to small displacements of the melt axis in this flow regime.

Various specific crystal growth processes in a TMF have been analyzed numerically in [Yesilyurt et al., 2004; Lyubimova et al., 2004; Dagner et al., 2003; Iuga, 2003; Schwesig et al., 2004; Hainke et al., 2005].

In summary, it can be concluded that there is a lack of studies about the unsteady turbulent melt flow in square melts with realistic TMF inductors. Neither isothermal melts nor melts with vertical temperature gradients have been investigated in the literature.

1.4. Contents and goals of this work

1.4.1. Main goals

It was shown in the introduction that directional solidification of multicrystalline silicon is one of the main technologies for industrial production of PV silicon. Structural and impurity defects in the silicon wafer material incorporated during the growth process play a decisive role for the resulting solar cell efficiency. Melt flow during the growth is involved in complex interactions with nearly every other physical phenomena. The melt flow could be controlled efficiently by a time-dependent TMF, which could conveniently be analyzed by numerical simulations as has been done for many other aspects of the growth process. Despite of that, the influence of magnetic fields in large silicon furnaces has not been investigated extensively in the literature. The main goals of the current work are set as follows:

1. Development and adaptation of tools of 3D numerical modeling for the TMF influence on melt flow during industrial mc-Si growth. Evaluation of the potential of open-source software. Derivation of analytical solutions and realization of model experiments to verify and validate the models.

2. Investigation of the possibilities for the application of a TMF in industrial mc-Si growth. Parameter studies for the Lorentz force, melt flow, and species mixing to determine the optimal parameter ranges for the standard TMF geometry. Analysis of correlations and derivation of scaling laws to transfer the results between different parameter ranges.

3. Development of a TMF concept for a research scale mc-Si furnace. Investigation of various TMF inductor geometries with respect to the Lorentz force and melt flow. Evaluation of the options of using TMF inductors inside a growth furnace.

1.4.2. Contents and overview of model systems

After this introductory chapter, theoretical physical and mathematical foundations in **Chapter 2** are described. This is followed by an introduction to the numerical tools, which are applied in this work, in **Chapter 3**. The logical structure of the further content is summarized in Fig. 1.5, the model systems are described in Tab. 1.5.

In the beginning, we consider an industrial problem – in this case, the optimization of melt flow in directional solidification of multicrystalline silicon by using traveling magnetic fields. As discussed previously, numerical simulations are very useful, in particular, in the case of very limited experimental measurement methods. The first step (step 1 in Fig. 1.5) is the development of a physical model of the process, i.e., the geometrical approximations, physical equations and boundary conditions. Since the problem cannot be solved analytically

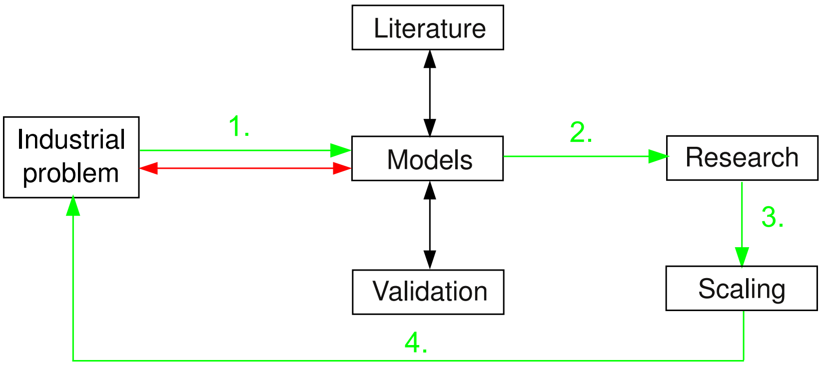

Figure 1.5.: Contents of this work. Red path: optimization and modeling is done directly on the industrial scale. Green path (this work): it is done on the research scale, and the results are transferred to the industry by scaling.

in most cases, appropriate numerical methods must be selected and verified. This step requires a thorough analysis of the industrial system, including the experience in the literature, etc.

An important part of model development is the model validation by using experimental data. This is the topic of **Chapters 4 and 5** dealing with Models I and II (in Tab. 1.5). Model I is a new experimental setup for small-scale model experiments with a low-melting-point liquid metal (GaInSn) in a TMF. An additional vertical temperature gradient is considered in a further system denoted as Model II. Magnetic field measurements within the TMF coils are used for the validation of the electromagnetic calculations, direct velocity and temperature measurements in the melt allow the validation of the flow calculations.

After the model development, it is possible to apply the model to an industrial system and carry out the optimization using simulations and experiments complementary. However, the research on the industrial scale is related to high costs. Considering only the costs for the silicon feedstock for a single run in a Gen1 (15 kg) furnace and in a Gen5 (450 kg) furnace, gives 750 Euro and 22500 Euro, respectively, with an approximate solar-grade polysilicon price of 50 Euro/kg. Of course, the costs of the operation, service as well as material characterization would also be much higher on the industrial scale. Therefore, this work proposes a strategy to focus the investigations on the research scale (step 2), but simultaneously developing scaling laws and concepts (step 3) for the transfer of the results back to the industrial scale (step 4).

The numerical studies start with a global thermal model for an idealized furnace geometry (Model III and **Chapter 6**). Although the reference case is a Gen1 furnace, the effect of increasing dimensions dimensions is considered. The influence of key furnace parameters on the crystallization velocity and temperature gradients in silicon is investigated to find an appropriate parameter range for further local models.

The next numerical parameter study deals with the calculation of Lorentz forces for a simplified system, which consists of a Gen1 silicon melt surrounded by several side inductors for the TMF generation (Model IV and **Chapter 7**). This is the classical TMF configuration, which still has many degrees of freedom, such as the current amplitude, current frequency, number of inductors, which all influence the resulting Lorentz force distribution.

The results of parameter studies for the global temperature field and Lorentz force provide input data for local melt flow calculations in **Chapter 8**. Model V in the reference configuration is a Gen1 melt with an optional crystal part in a TMF field of side inductors. The melt

No	System	Description	Numerical models	Results	Chap.
I	Local model for small-scale isothermal model experiments	Model experiments with GaInSn melt: L=10 cm, H=2.5, 5, 7.5 cm; side TMF inductors	3D GetDP, 3D OpenFOAM	Lorentz force and melt flow	4
II	Local model for small-scale non-isothermal model experiments	Model experiments with GaInSn melt: L=10 cm, H=2.5, 5, 10 cm; side TMF inductors, heater at the top and cooler at the bottom	3D GetDP, 3D OpenFOAM	Lorentz force, melt flow and temperature	5
III	Global thermal model	Variation of geometric and material parameters for a simplified furnace geometry	2D and 3D Elmer	Temperature distribution, crystallization velocity	6
IV	Local model of melt and TMF inductors	Variation of geometric and current parameters	2D and 3D GetDP	Lorentz force	7
V	Local small-scale model of melt, crystal, and TMF inductors	System with L=22 cm, H=11 cm (melt) and several TMF inductor geometries	2D and 3D GetDP, 2D and 3D OpenFOAM	Lorentz force, melt flow and temperature, species concentration, interface shape	8, 9
VI	Local large-scale model of melt and inductors	Variation of melt size: L=10, 20, 40, 80 cm, H/L=1/6, 1/3, 2/3, side TMF inductors	3D GetDP, 3D OpenFOAM	Lorentz force, melt flow and temperature	8

Table 1.5.: Overview of model systems used in this work. Height H and side length L of the melt is given. Software used for numerical modeling is given for future reference.

flow and temperature field are investigated for several TMF parameters with a fixed crystallization interface. The influence of melt flow on species mixing is investigated for short time intervals with a prescribed crystallization interface movement to take into account the segregation effect. The approximate models for the crystallization interface are validated in several fully coupled calculations of the flow, temperature, and species transport, as well as crystallization interface. Finally, local melt flow and temperature calculations are performed for systems with various dimensions defined as Model VI to determine and test the scaling laws.

Results of all numerical studies in the previous chapters are accumulated in **Chapter 9**, where a concept for a research scale furnace with a TMF is formulated. On the basis of Model V, several modified inductor geometries with bottom and top inductors and segmented side inductors are analyzed. The coupling of such inductors with heaters in the hot-zone of a furnace is briefly discussed. Finally, the implementation of this concept in a crystallization furnace and the first experimental results are presented.

Part I.

Basics

Chapter 2

Theoretical foundations

The fundamental physical equations and the relevant approximations for the current work are summarized in this chapter. In addition to well known fundamentals, several new analytical models are derived to obtain simple analytical relationships, which will support the later numerical analysis. Since this work has a distinct interdisciplinary character and makes use of the knowledge from various areas of physics, a short introduction to the basics highlighting the most relevant aspects is given, which will be helpful for the further analysis. It should be noted that all fundamental theories discussed here, such as Maxwell's equations or Navier-Stokes equations, belong to classical physics and are more than a century old. Nevertheless, the application of these theories to practical problems is not trivial.

2.1. Electromagnetic fields

2.1.1. Maxwell's equations

All electromagnetic phenomena are described by the Maxwell's equations[1], which are valid for all reference frames regardless of their relative velocity. Maxwell's equations are [Hughes and Young, 1989, Ch. 2]:

$$\operatorname{rot}\vec{E} = -\frac{\partial \vec{B}}{\partial t}, \tag{2.1}$$

$$\operatorname{div}\vec{B} = 0, \tag{2.2}$$

$$\operatorname{rot}\vec{H} = \vec{j} + \frac{\partial \vec{D}}{\partial t}, \tag{2.3}$$

$$\operatorname{div}\vec{D} = \rho_e, \tag{2.4}$$

where $\vec{E}$ is the electric field intensity [V/m], $\vec{D}$ is the electric induction or electric flux density [C/m^2], $\vec{B}$ is the magnetic induction of magnetic flux density [T], and $\vec{H}$ is the magnetic field intensity [A/m]. $\vec{j}$ denotes the conduction current density [A/m^2] and ρ_e denotes the

---

[1] Discovered by J. C. Maxwell (Scottish physicist, 1831–1879) in 1861/62.

electric charge density [C/m^3]. t is the time. For a complete set of equations, the so-called constitutive relations or material equations are required to connect $\vec{D}$ and $\vec{E}$, $\vec{H}$ and $\vec{B}$, $\vec{j}$ and $\vec{E}$. In moving media, these relations have a complicated form that is not independent of the relative velocity of the reference frame even in the non-relativistic approximation. Significant simplifications are possible in the case of liquid metals – usually denoted as the non-relativistic magnetohydrodynamic (MHD) approximation. A rigorous derivation is discussed by Hughes and Young [1989] and leads for linear isotropic media to a system of equations given in Tab. 2.1 (cf. [Moreau, 1990; Davidson, 2001])[2].

In the same approximation, we additionally have the Ohm's law for isotropic moving media, which gives an expression for the current density:

$$\vec{j} = \sigma\left(\vec{E} + \vec{u} \times \vec{B}\right), \tag{2.5}$$

where σ is the electrical conductivity and $\vec{u}$ is the motion velocity. Each volume element of an electrically conducting body experiences the so-called Lorentz force with a force density [N/m^3] given as

$$\vec{F}_L = \vec{j} \times \vec{B}. \tag{2.6}$$

Name	Differential form	Integral form
Faraday's law	$\mathrm{rot}\,\vec{E} = -\dfrac{\partial \vec{B}}{\partial t}$ (2.7)	$\oint\limits_{\partial S} \vec{E} \cdot d\vec{l} = -\dfrac{\partial}{\partial t} \iint\limits_{S} \vec{B} \cdot d\vec{S}$ (2.8)
No mag. monopoles	$\mathrm{div}\,\vec{B} = 0$ (2.9)	$\oiint\limits_{\partial V} \vec{B} \cdot d\vec{A} = 0$ (2.10)
Ampere's law	$\mathrm{rot}\,\dfrac{\vec{B}}{\mu\mu_0} = \vec{j}$ (2.11)	$\oint\limits_{\partial S} \dfrac{\vec{B}}{\mu\mu_0} \cdot d\vec{l} = \iint\limits_{S} \vec{j} \cdot d\vec{S}$ (2.12)
Current conserv.	$\mathrm{div}\,\vec{j} = 0$ (2.13)	$\oiint\limits_{\partial V} \vec{j} \cdot d\vec{S} = 0$ (2.14)

Table 2.1.: Maxwell's equations in the MHD approximation in differential and integral form: μ_0 and μ are the permeabilities of vacuum and isotropic media, respectively; symbols S, V, ∂ denote an arbitrary surface, volume, its boundary, respectively.

2.1.2. The time-harmonic formulation

In practical applications, electric and magnetic fields are often generated by harmonic sources described by an amplitude and frequency. In such cases, the so-called time-harmonic formulation is very useful. It can be formulated in several ways, but a simple notation is obtained when using complex numbers[3]. Each time-harmonic variable is substituted with a complex amplitude multiplied by a complex exponent (shown here for the magnetic induc-

---

[2] These equations have been used in many applications to crystal growth and related processes; e.g., [Baumgartl, 1992; Kaiser, 1998; Krauze, 2005; Fischer, 2001; Kirpo, 2008].

[3] This is usually called the phasor notation. An alternative method is used in, e.g., [Gresho and Derby, 1987].

tion $\vec{B}$):

$$\vec{B}(t) \to \vec{B}_C \exp(i\omega t), \quad \vec{B}_C = \vec{B}_{CRe} + i\vec{B}_{CIm}. \tag{2.15}$$

If the equation system is linear, exponents with time-dependencies cancel out, and only the equations for the complex amplitudes must be solved. The time-dependent field (as the real part of the complex amplitude) can be reconstructed as

$$\begin{aligned}\vec{B}(t) &= \mathfrak{Re}[\vec{B}_C \exp(i\omega t)] = \mathfrak{Re}[(\vec{B}_{CRe} + i\vec{B}_{CIm}) \cdot (\cos\omega t + i\sin\omega t)] = \\ &= \mathfrak{Re}[\vec{B}_{CRe}\cos\omega t - \vec{B}_{CIm}\sin\omega t + i\ldots] = \vec{B}_{CRe}\cos\omega t - \vec{B}_{CIm}\sin\omega t = \ldots = \\ &= \vec{B}_0 \cos(\omega t + \phi),\end{aligned} \tag{2.16}$$

where $\vec{B}_0$ and ϕ are the amplitude and the phase of the real-valued field, respectively. The conversion between these variables and the complex amplitude is possible through the use of transformations between the trigonometric and algebraic forms of complex numbers [Bronstein et al., 2008, Sec. 1.5.2.3]:

$$\begin{aligned}&\vec{B}_{CRe} = \vec{B}_0\cos\phi, \quad \vec{B}_{CIm} = \vec{B}_0\sin\phi; \\ &B_{0k} = \sqrt{B_{CRek}^2 + B_{CImk}^2}, \quad \phi = \arctan\frac{B_{CIm}}{B_{CRe}}, \quad k = x, y, z.\end{aligned} \tag{2.17}$$

where the phase ϕ is defined in the interval (-180°,180°].

Care must be taken when calculating the Lorentz force as the cross product of the current density and the magnetic field because it is not a linear operation. We must calculate the real parts before the vector product:

$$\begin{aligned}\vec{F}_L(t) &= \vec{j} \times \vec{B} = \mathfrak{Re}[\vec{j}_C \exp(i\omega t)] \times \mathfrak{Re}[\vec{B}_C \exp(i\omega t)] = \\ &= [\vec{j}_{CRe}\cos\omega t - \vec{j}_{CIm}\sin\omega t] \times [\vec{B}_{CRe}\cos\omega t - \vec{B}_{CIm}\sin\omega t] = \\ &= \vec{j}_{CRe} \times \vec{B}_{CRe}\cos^2\omega t + \vec{j}_{CIm} \times \vec{B}_{CIm}\sin^2\omega t - \\ &- \vec{j}_{CRe} \times \vec{B}_{CIm}\cos\omega t \sin\omega t - \vec{j}_{CIm} \times \vec{B}_{CRe}\sin\omega t\cos\omega t.\end{aligned}$$

Because $\sin^2\omega t$ and $\cos^2\omega t$ are always greater than zero and $sin\omega t\cos\omega t = 0.5\sin 2\omega t$, the Lorentz force has a non-zero time-average component and the oscillations contain a component with the double frequency 2ω. The time-average value can be calculated by an integration of the trigonometric functions (see [Bronstein et al., 2008, Sec. 21.7.3]) over one period $t_p = 2\pi/\omega$:

$$\vec{F}_{Lav} = \frac{1}{t_p}\int_0^{t_p} \vec{F}_L(t)dt = \frac{\vec{j}_{CRe} \times \vec{B}_{CRe} + \vec{j}_{CIm} \times \vec{B}_{CIm}}{2}. \tag{2.18}$$

The induced heat can be calculated in a similar way. The time-dependent power density (in W/m^3) in each volume element is $Q_{ind}(t) = |\vec{j}(t)|^2/\sigma = \vec{j} \cdot \vec{j}/\sigma$. The time-average value can be obtained identically as the expression (2.18) when $\vec{B}$ is replaced with $\vec{j}$ and the cross product is replaced with the dot product:

$$Q_{ind\,av} = \frac{\vec{j}_{CRe} \cdot \vec{j}_{CRe} + \vec{j}_{CIm} \cdot \vec{j}_{CIm}}{2\sigma} = \frac{|\vec{j}_{CRe}|^2 + |\vec{j}_{CIm}|^2}{2\sigma} = \frac{|\vec{j}_C|^2}{2\sigma}. \tag{2.19}$$

2.1.3. Subject of magnetohydrodynamics

The Lorentz force derived in the previous section can be included in the equations for fluid flow as a body source. However, a question arises whether the flow velocity does not influence the external magnetic field due the term containing the velocity in eq. (2.5) and how to handle the coupled problem in this case.

We can distinguish two cases with regard to the time-dependence of the magnetic field $\vec{B}$. First, if the field is time-dependent (AC), both terms in eq. (2.5) are active because an eddy electric field $\vec{E}$ is induced and a magnetic field $\vec{B}$ is present. In this case, we can neglect the influence of the velocity on the electromagnetic problem if

$$|\sigma\vec{E}| \gg |\sigma\vec{u}\times\vec{B}| \;\Rightarrow\; |\vec{j}| \approx |\sigma\vec{E}| \;\Rightarrow\; |\vec{j}| \gg |\sigma\vec{u}\times\vec{B}| \;\Rightarrow\; \left|\frac{1}{\mu_0}\mathrm{rot}\vec{B}\right| \gg |\sigma\vec{u}\times\vec{B}| \;\Rightarrow$$
$$\frac{1}{\mu_0}\frac{B}{L_0} \gg \sigma u_0 B \;\Rightarrow\; \mu_0\sigma u_0 L_0 \equiv Rm \ll 1, \tag{2.20}$$

where eq. (2.11) was applied and characteristic values for the length L_0 and velocity u_0 were introduced. The obtained dimensionless parameter Rm is known as the magnetic Reynolds number. The characteristic length here actually is the penetration depth of the magnetic field δ_{em}, which may be several times smaller than the melt size. We can estimate that for liquid silicon with $\delta_{em} \sim 0.1$ m the flow velocity must be smaller than 0.8 m/s to obtain $Rm < 0.1$. These conditions are met in the current work.

In the second case, we consider a steady (DC) field $\vec{B}$. Because there is no induced electric field, the second term in eq. (2.5) must be always taken into account. The question remains whether the influence of this term on the flow velocity is significant. This can be answered only by a comparison of the electromagnetic force to other forces in the melt. To account for the velocity term in eq. (2.5), the equation for the current density $\vec{j}$ must be solved in a coupled system with the fluid motion equations; see, e.g., [Krauze, 2005; Kumar, 2005]. In this work, we consider only time-dependent fields.

For the AC and DC cases, the electromagnetic force can be roughly estimated as (cf. [Muiznieks et al., 2007])

$$\vec{F}_{LAC} = \vec{j}\times\vec{B} \;\Rightarrow\; \frac{1}{\mu_0}\mathrm{rot}\vec{B}\times\vec{B} \;\Rightarrow\; \frac{B_0^2}{\delta_{em}\mu_0}, \tag{2.21}$$
$$\vec{F}_{LDC} = \vec{j}\times\vec{B} \;\Rightarrow\; (\sigma\vec{u}\times\vec{B})\times\vec{B} \;\Rightarrow\; \sigma u_0 B_0^2. \tag{2.22}$$

2.1.4. Equations for magnetic and electric potentials

Maxwell's equations and the previously introduced simplifications allow for a more advantageous form for numerical calculations. While the original 4 equations contain 6 unknown components of the vectors $\vec{E}$ and $\vec{B}$, the so-called potential formulations can reduce the number of equations to 1…2 and the number of unknowns to 1…4 depending on the electrical and magnetic properties in various domains of the actual problem. From the various possibilities available for the choice of the potentials [Holmberg, 1998], the so-called $A-V$ formulation has been frequently used and is also adopted in the current work.

The magnetic vector potential $\vec{A}$ and the electric scalar potential V are defined according to the equations

$$\vec{B} = \operatorname{rot}\vec{A}, \quad \vec{E} = -\frac{\partial \vec{A}}{\partial t} - \operatorname{grad} V. \tag{2.23}$$

In this way, the equations (2.7) and (2.9) are satisfied automatically:

$$\operatorname{div}\operatorname{rot}\vec{A} = 0, \quad \operatorname{rot}\vec{E} = -\frac{\partial}{\partial t}\operatorname{rot}\vec{A} - \operatorname{rot}\operatorname{grad} V = -\frac{\partial \vec{B}}{\partial t} - 0.$$

The substitution of potential definitions into the two remaining equations (assuming $\vec{u} \times \vec{B} \approx 0$ in eq. (2.5) according to the estimation $Rm \ll 1$) gives two equations for the calculation:

$$\operatorname{rot}\left(\frac{1}{\mu\mu_0}\operatorname{rot}\vec{A}\right) = \vec{j} = \sigma\left(-\frac{\partial \vec{A}}{\partial t} - \operatorname{grad} V\right) + \vec{j}_S, \quad \operatorname{div}\left(-\sigma\frac{\partial \vec{A}}{\partial t} - \sigma \operatorname{grad} V\right) = 0, \tag{2.24}$$

where $\vec{j}_S$ in the first equation denotes an additional source current. The potential equations (2.24) can be rewritten also in the time-harmonic form:

$$\operatorname{rot}\left(\frac{1}{\mu\mu_0}\operatorname{rot}\vec{A}\right) = \vec{j} = \sigma\left(-i\omega\vec{A} - \operatorname{grad} V\right) + \vec{j}_S, \quad \operatorname{div}\left(-i\sigma\omega\vec{A} - \sigma \operatorname{grad} V\right) = 0, \tag{2.25}$$

where the index C for the complex amplitudes $\vec{A}_C$, V_C, and $\vec{j}_C$ was omitted.

2.1.5. Analytical models for traveling magnetic fields

A traveling magnetic field can be described in an idealized way as a traveling wave with z component of the magnetic induction defined as

$$B_z(t,z) = B_0 \cos(\omega t - \alpha \cdot z), \tag{2.26}$$

where $\omega = 2\pi f$ is the cyclic frequency, B_0 is the amplitude, and α is the TMF wave number; see Fig. 2.1. The question what inductor systems can approximate well such an idealized TMF wave better is not trivial. This topic will be discussed later. If we have a given magnetic field $\vec{B} = (B_x, B_y, B_z)$ in the complex notation, the TMF parameters B_{z0} and α for a sinusoidal wave in z direction can be locally calculated as follows:

$$B_{z0} = \sqrt{B_{zRe}^2 + B_{zIm}^2}, \tag{2.27}$$

$$\phi(z) = \arctan\frac{B_{zIm}}{B_{zRe}} \quad \Rightarrow \quad \alpha \approx -\frac{\partial \phi}{\partial z} = -\frac{\frac{\partial B_{zIm}}{\partial z} B_{zRe} - B_{zIm}\frac{\partial B_{zRe}}{\partial z}}{B_{zRe}^2 + B_{zIm}^2}, \tag{2.28}$$

where the expressions (2.17) were used and the expression for α was obtained from a linear approximation $\phi(z) \approx -\alpha \cdot z$ for a small z interval.

The idealization of a TMF field as a sinusoidal wave allows one to obtain analytical solutions for the induced Lorentz force. Despite the wide capabilities of numerical calculations available today, similar analytical solutions are still used, for example, in cases where very small geometric changes have to be computed with a high precision [Cramer et al., 2011]. Analytical solutions for a TMF with the skin effect taken into account have been rigorously derived in the monographs [Krumin, 1969, 1983]. We consider the solution for the induced

Lorentz force in a long cylindrical body and in a semi-infinite body (2D) as shown in Fig. 2.1. The induced Lorentz force distributions for both cases are as follows:

$$\text{Cyl.:}\quad F_{Lr} = -\frac{\omega\sigma B_0^2}{2|\gamma|^2}\frac{\Im\mathrm{m}[\gamma \mathrm{I}_0(\gamma r)\mathrm{I}_1(\gamma^* r)]}{|\mathrm{I}_0(\gamma R)|^2}, \qquad F_{Lz} = \frac{\alpha\omega\sigma B_0^2}{2|\gamma|^2}\left|\frac{\mathrm{I}_1(\gamma r)}{\mathrm{I}_0(\gamma R)}\right|^2; \tag{2.29}$$

$$\text{2D:}\quad F_{Lx} = -\frac{\omega\sigma B_0^2}{2}\Im\mathrm{m}\left[\frac{\exp[-(\gamma+\gamma^*)x]}{\gamma}\right], \qquad F_{Lz} = \frac{\alpha\omega\sigma B_0^2}{2|\gamma|^2}\exp[-(\gamma+\gamma^*)x], \tag{2.30}$$

with

$$\gamma = \sqrt{\alpha^2 + i\sigma\mu_0\omega} \tag{2.31}$$

and γ^* – the complex conjugate. I_0 and I_1 denote Bessel functions.

The skin depth of the magnetic field in the material for the 2D case can be estimated as

$$\delta_{TMF} = \frac{2}{\gamma+\gamma^*} = \sqrt{\frac{2}{\sqrt{\alpha^4+(\mu_0\sigma\omega)^2}+\alpha^2}}. \tag{2.32}$$

With $\alpha = 0$, we obtain the solution for a simple alternating field. The skin depth of the magnetic field is $\delta_{em} = \sqrt{2}/\sqrt{\mu_0\sigma\omega}$. The skin depth of the Lorentz force is 2 times smaller than the skin depth of the magnetic field in both cases.

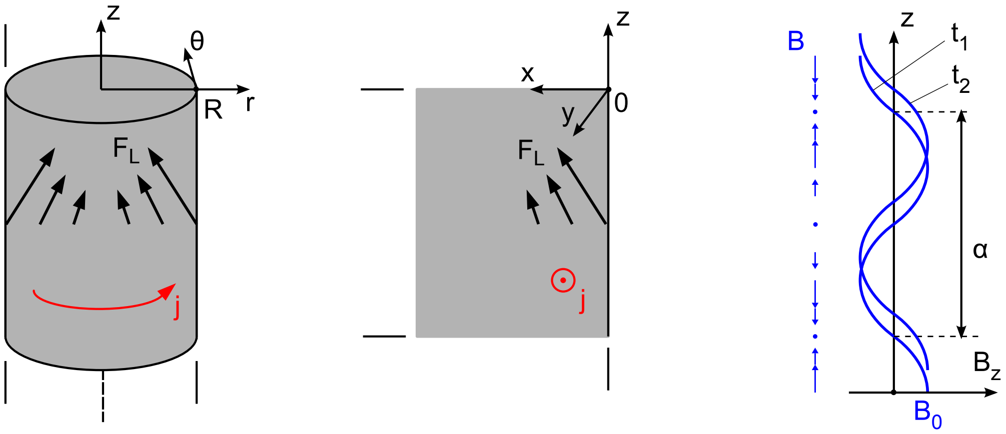

Figure 2.1.: Analytical solutions for a TMF idealized as a sinusoidal wave in z direction.

A frequently used approximation in the literature for the axisymmetric case is obtained under the conditions of a long TMF wavelength ($2\pi/\alpha \gg R$) and a negligible skin-effect ($2R^2/\delta_{em}^2 \ll 1$) [Grants and Gerbeth, 2004]. It follows that

$$F_{Lr} = 0, \qquad F_{Lz} = \frac{\sigma\omega\alpha B_0^2}{8}r^2, \tag{2.33}$$

i.e., the Lorentz force is purely axial. For the opposite case with a distinct skin effect, a simple approximation can be derived for the 2D case. However, if the skin depth is much smaller than the radius, this approximation can be also applied to the axisymmetric case. The derivation for the conditions $\delta_{em} \ll L_0$ and $\delta_{em} \ll 1/\alpha$ is given in Sec. C.1 and yields the expression for $x = 0$:

$$F_{Lxm} = \frac{B_0^2}{2\mu_0} \cdot \frac{1}{\delta_{em}}, \quad F_{Lzm} = \frac{B_0^2}{2\mu_0} \cdot \alpha, \quad \delta_{em} = \frac{1}{\sqrt{\pi \mu_0 \sigma f}}, \tag{2.34}$$

with an exponential dependence in the skin layer according to $F_L(x) \sim \exp(-2x/\delta_{em})$.

2.2. Incompressible fluid flow

2.2.1. Conservation laws and equations for fluid motion

We consider a flow of incompressible liquid metals. Generally, The assumption of incompressibility holds if the ratio of the flow velocity to the speed of sound (the Mach number) is much smaller than unity. The speed of sound in liquid silicon is about 3900 m/s [Yoshimoto et al., 1996], and this requirement is fulfilled in all practical applications[4]. The governing equations can be directly derived from the fundamental conservation laws; see, e.g., [Versteeg and Malalasekera, 2007, Ch. 2], [Ferziger and Peric, 2002, Ch. 1]. The **conservation of mass** leads to the continuity equation

$$\operatorname{div} \vec{u} = 0 \quad \text{or} \quad \frac{\partial u_x}{\partial x} + \frac{\partial u_y}{\partial y} + \frac{\partial u_z}{\partial z} = 0. \tag{2.35}$$

The **conservation of momentum** follows from the application of Newton's second law to fluids. It can be written for a fluid element $\rho \vec{u}$ in the Eulerian reference frame (connected to a fixed point in space and time) using tensorial notation as

$$\rho \frac{\partial u_i}{\partial t} + \rho \frac{\partial (u_j u_i)}{\partial x_j} = -\frac{\partial p}{\partial x_i} + \frac{\partial \tau_{ij}}{\partial x_j} + F_i, \tag{2.36}$$

where p is the pressure, the tensor τ_{ij} represents viscous forces acting on a fluid element (stress components act in the j-direction on a surface that is normal to the i-direction), F_i is a body force. In a so-called Newtonian fluid, the shear (viscous) stresses are assumed to be proportional to the rates of deformations according to the expression

$$\tau_{ij} = \eta \left(\frac{\partial u_i}{\partial x_j} + \frac{\partial u_j}{\partial x_i} \right), \tag{2.37}$$

where the dynamic viscosity η was introduced. The **conservation of angular momentum** places constraints on the symmetry of the stress tensor τ_{ij}. A combination of both expressions leads to the Navier–Stokes equation[5], which can be written in the conservative

---

[4] The applicability of the incompressible model to non-isothermal flows is discussed in Sec. 2.2.3.

[5] Discovered by C.-L. Navier (French physicist, 1785–1836) in 1822 and by G. G. Stokes (English physicist, 1819–1903) in 1845.

(divergence) and vectorial forms as follows:

$$\rho\frac{\partial u_i}{\partial t}+\rho\,\mathrm{div}(u_i\vec{u}) = -\frac{\partial p}{\partial x_i}+\mathrm{div}(\eta\,\mathrm{grad}\,u_i)+F_i, \quad i\to x,y,z, \tag{2.38}$$

$$\rho\left[\frac{\partial\vec{u}}{\partial t}+(\vec{u}\cdot\nabla)\vec{u}\right] = -\,\mathrm{grad}\,p+\eta\Delta\vec{u}+\vec{F}. \tag{2.39}$$

In this work, the body force $\vec{F}$ contains components due to Lorentz forces $\vec{F_L}$ and due to buoyancy forces $\vec{F}_{buoy}$ as discussed later.

Finally, we have the **conservation of energy**. The energy equation follows from the first law of thermodynamics, which states for a fluid particle that the *rate of change of energy* is equal to the *rate of heat addition* plus the *rate of work done on it*. The energy of a particle can be defined as the sum of internal (thermal) energy E_i and mechanical (kinetic) energy E_{kin} (the gravitational force is regarded as a body force doing work on the particle). For an incompressible fluid, we can write:

$$E_i = cT, \quad E_{kin} = |\vec{u}|^2/2, \tag{2.40}$$

where c is the heat capacity. The heat flux q is related to the temperature field according to Fourier's law of heat conduction[6]

$$q = -\lambda\,\mathrm{grad}\,T, \tag{2.41}$$

where λ is the thermal conductivity. Now it is possible to formulate a conservation law for the internal energy of the fluid (see [Versteeg and Malalasekera, 2007, Ch. 2] for a derivation):

$$\rho c\frac{\partial T}{\partial t}+\rho c\,\mathrm{div}(T\vec{u}) = \mathrm{div}(\lambda\,\mathrm{grad}\,T)+\Phi, \tag{2.42}$$

$$\Phi = \eta\left[2\left(\frac{\partial u_x}{\partial x}\right)^2+2\left(\frac{\partial u_y}{\partial y}\right)^2+2\left(\frac{\partial u_z}{\partial z}\right)^2+\right. \tag{2.43}$$

$$\left.+\left(\frac{\partial u_x}{\partial y}+\frac{\partial u_y}{\partial x}\right)^2+\left(\frac{\partial u_x}{\partial z}+\frac{\partial u_z}{\partial x}\right)^2+\left(\frac{\partial u_y}{\partial z}+\frac{\partial u_z}{\partial y}\right)^2\right], \tag{2.44}$$

where Φ represents a heat source due to the viscous energy dissipation in the fluid. The dissipation plays the most important role in the regions with high velocity gradients, which usually appear at solid walls where the fluid sticks to the solid and the velocity falls to zero. We can consider the balance between heat conduction and heat dissipation in such a boundary layer of thickness δ_Φ:

$$\frac{\partial}{\partial x}\left(\lambda\frac{\partial T}{\partial x}\right)\sim\eta\left(\frac{\partial u}{\partial x}\right)^2 \quad\Rightarrow\quad \frac{\lambda\Delta T}{\delta_\Phi^2}\sim\eta\frac{u^2}{\delta_\Phi^2} \quad\Rightarrow\quad \Delta T\sim\frac{\eta u^2}{\lambda}. \tag{2.45}$$

With a velocity of 0.1 m/s, the expected temperature differences due to the dissipation in silicon are on the order of 10^{-7} K. Consequently, the dissipation effect can be neglected.

---

[6] Formulated by J. Fourier (French mathematician, 1768-1830) in 1822.

2.2.2. Turbulence modeling

It is widely accepted that the Navier-Stokes equation describes all possible phenomena in fluid flows.[7] However, this equation is time-dependent and nonlinear; solutions may be highly sensitive to small changes in the input parameters and may depend on the history of the flow (hysteresis effect). These properties are most evident in the phenomenon of turbulence – unsteady, irregular, three-dimensional fluid motion, observable in practically any (also initially steady) flow if the inertial forces start to dominate over the viscous forces. The ratio of both forces can be estimated from the Navier-Stokes equation and is known as the Reynolds number:

$$\frac{\rho\,\mathrm{div}(u\vec{u})}{\mathrm{div}(\eta\,\mathrm{grad}\,u)} \approx \frac{\rho u_0^2/L_0}{\eta u_0/L_0^2} = \frac{\rho u_0 L_0}{\eta} \equiv Re, \tag{2.46}$$

where u_0 is a characteristic flow velocity and L_0 is a characteristic length scale. Some of the most important properties of turbulent flows are the presence of motion on many different scales and the transfer of energy from the large scales (energy production by outer forces) to the small scales (energy dissipation). A simple dimensional analysis proposed by A. N. Kolmogorov allows to estimate the ratios between the largest (subscript 2) and smallest (subscript 1) scales of velocity, length, and time [Davidson, 2004, Sec. 1.6]:

$$u_1/u_2 = Re^{-1/4}, \quad L_1/L_2 = Re^{-3/4}, \quad t_1/t_2 = Re^{-1/2}. \tag{2.47}$$

Obviously, an unsteady 3D calculation would require at least $(Re^{3/4})^3 = Re^{9/4}$ grid points and $Re^{1/2}$ time steps. A more detailed analysis shows that the product of both values reaches $160 \cdot Re^3$ [Zikanov, 2010, Sec. 11.1.2]. Assuming 100 floating point operations (FLOP) per grid point and per time step, we obtain about $10^4 \cdot Re^3$ required FLOPs. Today, a small computing cluster with several tens of processors reaches about 10^{12} FLOPs per second and the most powerful supercomputers about 10^{16} FLOPs per second [TOP500, 2012]. With a calculation time of one week, this corresponds to a maximum Re number of $4 \cdot 10^4$ and $8 \cdot 10^5$, respectively. Calculations at these limits allow fundamental insights into turbulence properties and are called *Direct Numerical Simulations* (DNS). One of the largest DNS has been carried out on a supercomputer with more than 5000 processors and a grid with $4096^3 = 7 \cdot 10^{10}$ nodes [Kaneda and Ishihara, 2006]. According to the estimate given above, this corresponds to a fully resolved Reynolds number of 66000. A flow Reynolds number of 40000 was reported in the study.

It should be noted that the transition to turbulence and the properties of the turbulent flow strongly depend on the specific flow. A classification based on the Reynolds number alone is not possible. For example, if we consider the practical range of the Reynolds number between the development of three-dimensional instabilities and a fully turbulent flow, we observe $Re = 2300 \ldots 10^4$ for the flow in a pipe, $Re = 300 \ldots 3 \cdot 10^5$ for the flow around a cylinder, and $Re = 6 \cdot 10^4 \ldots 5 \cdot 10^5$ for the flow along a flat plate [Baehr and Stephan, 2010]. Furthermore, flow details such as the inlet geometry or the surface roughness play a great role – with a careful elimination of all flow disturbances, laminar flow in a pipe has been observed up to $Re = 10^5$.

There exists a frequently quoted result in Kolmogorov's theory of developed turbulence,

---

[7] It should be noted that the existence of smooth solutions of the Navier-Stokes equation in three dimensions is still one of the major unsolved problems in applied mathematics [MillenniumPrize, 2011].

which predicts a slope coefficient of 5/3 in the power spectrum of velocity oscillations in the so-called intertial subrange between the large and the small scales. However, this theory is strictly applicable only to homogeneous isotropic turbulence; there are no quantitative criteria for the transitional stages; slopes deviating from 5/3 and differences between the spectra of the velocity and passive scalars have been observed; e.g., [Danaila and Antonia, 2009]. Therefore, for practical applications it should be sufficient to determine whether the flow is steady and laminar or unsteady, fluctuating, and turbulent; and to devote the rest of the analysis to the classification of the parameters of interest, such as the level of melt mixing.

Most flows in practice are out of reach for DNS calculations, which has motivated the development of turbulence modeling, where the properties of turbulent flows are modeled rather than directly simulated. Two main approaches are the RANS (*Reynolds Averaged Navier Stokes*) and the LES (*Large Eddy Simulation*); see, e.g., [Ferziger and Peric, 2002, Ch. 9], [Versteeg and Malalasekera, 2007, Ch. 3], [Zikanov, 2010, Ch. 11].

The RANS approach decomposes the fluid flow velocity in mean and fluctuating components as $\vec{u}(t) = \bar{\vec{u}} + \vec{u}'$. A substitution back into the equations of fluid motion gives equations for the mean component, with new terms containing products of u'. These terms can be interpreted as new stresses (the turbulent or Reynolds stresses). Additional equations are required for these new terms to close the system of equations. The RANS approach suffers from the inability to analyze the time-dependent properties of the flow and from a large amount of modeling assumptions, which mostly have a limited range of applicability. The increase of the available computing power today has motivated an increasing popularity of the LES approach, which at least partly avoids these drawbacks.

In the LES approach, the three-dimensional, time-dependent motion equations are solved. In comparison to DNS, only the large scale motion (with the largest energy; playing the main role in transport processes) is calculated directly, i.e., resolved. The small scale motions are approximated (modeled) by filtering the velocity field $u_i,\ i = x,y,z$ through the use of a local average

$$\bar{u}_i(\vec{x},t) = \iiint G(\vec{x},\vec{x}',\Delta) u_i(\vec{x}',t) dx_1' dx_2' dx_3', \tag{2.48}$$

where G is a localized filter function with a cutoff width Δ (e.g., the function is zero outside a box with a side length Δ). The width Δ is typically chosen equal to the grid cell size: $\Delta = (\Delta x \Delta y \Delta z)^{1/3}$. It can be shown that a substitution of these expressions into the Navier-Stokes equation (2.38) gives identical equations now for the bared variables, but with an additional term on the right-hand side

$$-\frac{\partial \tau_{ij}^s}{\partial x_j}, \quad \tau_{ij}^s = -\rho(\overline{u_i u_j} - \bar{u}_i \bar{u}_j). \tag{2.49}$$

This term is called the subgrid-scale (actually, subfilter scale) Reynolds stress, which requires additional modeling approximations. The most commonly used subgrid-scale model is the Smagorinsky model, which introduces the relations [Ferziger and Peric, 2002, Sec. 9.3]

$$\tau_{ij}^s - \frac{1}{3}\tau_{kk}^s \delta_{ij} = 2\nu_t \bar{S}_{ij}, \quad \nu_t = C_S^2 \rho \Delta^2 \sqrt{\bar{S}_{ij} \cdot \bar{S}_{ij}}, \quad \bar{S}_{ij} = \frac{\partial \bar{u}_i}{\partial x_j} + \frac{\partial \bar{u}_j}{\partial x_i}, \tag{2.50}$$

where ν_t is the so-called eddy viscosity. It reflects the *Boussinesq eddy viscosity hypothesis* – that the turbulent transport by the turbulent eddies depends on the velocity field in a similar way as the molecular transport. C_s is the empirical Smagorinsky constant; a value of 0.13

was used in this work. To account for turbulence damping at the walls, the filter width is often artificially modified according to the van Driest damping method [Ferziger and Peric, 2002, Sec. 9.3]. A LES model as described here is used in the current work. Similar models have been adopted to magnetically-driven flows by several researchers, e.g., [Felten et al., 2004; Umbrashko et al., 2006; Krauze et al., 2010].

It should be noted that there is a new direction of LES simulations that is called ILES – implicit LES. It stems from the observation that most LES simulations are not independent of the numerical algorithms used in the calculation [Pope, 2004; Fröhlich, 2006; Drikakis et al., 2009]. The main practical conclusions is that in turbulence modeling, it is crucial to analyze not only the equations solved but also the numerical procedure as a whole, including, e.g., the discretization schemes. Often, such analysis cannot be generalized and must be repeated for each case with more or less different flow conditions.

2.2.3. Buoyancy and Marangoni forces

If a liquid metal is not isothermal, its density changes with temperature, which leads to a body force due to the buoyancy:

$$\vec{F}_{buoy} = \rho(T)\vec{g} = \rho_0\left[1-\beta(T-T_{ref})\right]\vec{g}, \tag{2.51}$$

with the linear expansion coefficient β, reference temperature T_{ref}, reference density ρ_0, and gravity $\vec{g}$. In this case, the fluid can not be considered incompressible even at low flow velocities. In the frequently used Boussinesq approximation, it is assumed that the density is temperature-dependent only in the body force term for the buoyancy but constant in all other terms, which allows one to retain the incompressible model. Furthermore, it is commonly assumed that the viscosity is temperature-independent and that viscous dissipation is negligible. Gray and Giorgini [1976] propose the following criteria for the validity of this approximation:

$$|\beta\Delta T| \le 0.1, \quad \left|\frac{1}{\eta}\frac{d\eta}{dT}\Delta T\right| \le 0.1, \quad \left|\frac{\beta g L_0 T_0}{c\Delta T}\right| \le 0.1, \quad \left|\frac{\beta g L_0 \eta}{\lambda}\right| \le 0.1, \tag{2.52}$$

where $T_0 \dots T_0+\Delta T$ is a characteristic temperature interval over a characteristic length L_0. The first two inequalities limit the temperature-dependence of the density and viscosity, while the last two inequalities describe the dissipation in the heat equation. With a characteristic length L_0 = 1 m, temperature T_0 = 1685 K, and physical properties of silicon given in Sec. B, we can estimate:

$$\Delta T \le 971K, \quad \Delta T \le 159K, \quad \Delta T \ge 0.02K, \quad 10^{-8} \le 0.1. \tag{2.53}$$

Consequently, the characteristic temperature difference should be in the interval 0.02. . . 159 K. In this work, these conditions are met and the equations for an incompressible fluid from Sec. 2.2.1 are used.

If a non-isothermal fluid has a free surface, the temperature-dependence of the surface tension leads to shear forces on the surface – the *Marangoni forces*. The tangential stress on the surface can be written as [Zeytounian, 2009, Sec. 4.2]

$$\sigma_\tau = Ma \cdot \mathrm{grad}_\tau T, \tag{2.54}$$

where *Ma* is the Marangoni coefficient; it is negative for silicon. Consequently, Marangoni forces depend on the temperature distribution on the surface and act along the surface from the hot to the cold regions.

2.2.4. Electromagnetic body forces

2.2.4.1. Role of time-average force distribution

A part of the Lorentz force term in the Navier-Stokes equation may not contribute effectively to the melt motion. A simple illustration of this effect offers the gravity force. It acts as $\rho\vec{g}$ on every fluid particle and can be estimated with ρ = 2000 kg/m^3 and g = 9.8 m^2/s as approximately 20000 N/m^3. Nevertheless, the fluid does not move in a homogeneous gravity field because this force is compensated by the pressure distribution. A general Lorentz force distribution can decomposed as follows [Davidson, 2001, p. 97]:

$$\vec{F}_L = \vec{j}\times\vec{B} = \frac{(\vec{B}\cdot\vec{\nabla})\vec{B}}{\mu_0} - \mathrm{grad}\left(\frac{B^2}{2\mu_0}\right). \tag{2.55}$$

The second term is a potential force and can be compensated by the pressure in an incompressible fluid, without any contribution to melt motion. The first term can be written as follows with the use of coordinates in normal and tangential directions to a surface $(\vec{n}, \vec{\tau}_1, \vec{\tau}_2)$:

$$\begin{aligned}(\vec{B}\cdot\vec{\nabla})\vec{B} =& B_{\tau1}\frac{\partial B_{\tau1}}{\partial\tau_1}\vec{\tau}_1 + B_{\tau2}\frac{\partial B_{\tau2}}{\partial\tau_2}\vec{\tau}_2 + B_n\frac{\partial B_n}{\partial n}\vec{n} = \\ =& \frac{1}{2}\frac{\partial(B_{\tau1}^2)}{\partial\tau_1}\vec{\tau}_1 + \frac{1}{2}\frac{\partial(B_{\tau2}^2)}{\partial\tau_2}\vec{\tau}_2 + \frac{1}{2}\frac{\partial(B_n^2)}{\partial n}\vec{n}.\end{aligned} \tag{2.56}$$

We can distinguish the following features of the magnetic field distribution (in addition to the amplitude itself), which determine the effective Lorentz force in the melt:

1. Variation of the squared tangential components in the tangential directions (dominated by the inductor–melt geometry).
2. Variation of the squared normal component in the normal direction (dominated by the skin effect).

The time-average Lorentz force is determined by the time-average of these properties.

2.2.4.2. Role of force oscillations

The time-averaged Lorentz force is a convenient approximation for flow calculations, but the question remains – what is the lowest frequency limit where this approximation is still applicable. The most simple qualitative answer would be that the characteristic flow reaction time must be larger than the force oscillation period: $t_r \gg t_{FL}$. The reaction time can be defined as the ratio of the characteristic length scale L_0 to the characteristic velocity u_0; in the sense that a fluid particle would experience changes of its state within this time interval. The largest time scale can be estimated from macroscopic flow properties, while Kolmogorov's analysis (2.47) gives the ratio to the smallest time scale as $Re^{-1/2}$. Hence, we obtain a criterion for the frequency

$$f_{FL} \gg \frac{u_0}{L_0} \ldots \frac{u_0}{L_0} Re^{1/2}. \tag{2.57}$$

With L_0 = 0.5 m and u_0 = 0.1 m/s (corresponding to $Re = 2{\cdot}10^5$ for silicon), we obtain $f_{FL} \gg 0.2\ldots90$ Hz. It is not trivial to investigate the influence on the smallest scales both in experiments (the frequency changes also the force distribution) and in simulations (a full DNS resolution would be required). Nevertheless, for frequencies f_{FL} that do not satisfy this criterion, it should be verified that force oscillations with the highest resolved frequency in the simulation $u_0/\Delta L$ (ΔL – grid size) do not significantly influence the results.

2.3. Heat and mass transport

2.3.1. General transport equation and boundaries

We have already derived the equation for heat conduction and convection in a fluid by applying Fourier's law in Sec. 2.2.1. The transport of mass is described by a similar equation for the concentration C, where Fick's law relates the mass flux and with the concentration gradients and the diffusion coefficient D. The equations for temperature, concentration, and velocity components can be written in a general form as a transport equation for a scalar quantity ψ [Versteeg and Malalasekera, 2007, Sec. 2.5]:

$$\begin{aligned} &\frac{\partial(\rho\psi)}{\partial t} + \mathrm{div}(\rho\psi\vec{u}) = \mathrm{div}(\Gamma\,\mathrm{grad}\,\psi) + S_\psi \qquad (2.58)\\ &\text{Temperature}: \quad \psi = cT,\ \Gamma = \lambda/c\\ &\text{Concentration}: \quad \psi = C,\ \Gamma = \rho D\\ &\text{Momentum}: \quad \psi = u_i,\ \Gamma = \eta \end{aligned}$$

where the four terms in the equation (from the left) describe the rate of increase in the fluid element, rate of flow out of the element, rate of increase due to diffusion, rate of increase due to sources inside the element. The coefficient Γ may also include the effect of turbulence. For the velocity field, the turbulent (eddy) viscosity is used instead of the molecular viscosity: $\Gamma = \eta_t$. For the temperature and concentration fields, the coefficient Γ is calculated according to the *Reynolds analogy* with the momentum transport: $\Gamma = \eta_t/Pr_t$, where Pr_t is the turbulent Prandtl number; $Pr_t = 0.85$ was used in this work.

The conditions on a boundary b of the transport quantity ψ can be divided into three main categories:

1. Dirichlet condition – given constant value: $\psi|_b$.
2. Neumann condition – given normal flux: $\Gamma\frac{\partial\psi}{\partial n}\big|_b$.
3. Poincare condition – normal flux depends on the value on the boundary with a reference value ψ_{ref} and coefficient p_ψ: $\Gamma\frac{\partial\psi}{\partial n}\big|_b = p_\psi(\psi|_b - \psi_{ref})$.

If there is a fluid flow along the boundary, and the value of the transport quantity on the boundary differs from the upstream value in the fluid, a steep gradient of the transport quantity may apper in a thin layer at the boundary – the *boundary layer*. To estimate the characteristic thickness of this layer, we may assume in (2.58) that the convection dominates in the direction τ parallel to the boundary, while the diffusion dominates in the direction n

normal to the boundary, and neglect all other terms:

$$\frac{\partial}{\partial \tau}(\rho \psi u) \sim \frac{\partial}{\partial n}\left(\Gamma \frac{\partial \psi}{\partial n}\right) \quad \Rightarrow \quad \frac{\rho \psi u}{L_\tau} \sim \frac{\Gamma \psi}{L_n^2} \quad \Rightarrow \quad L_n \sim \sqrt{L_\tau \frac{\Gamma}{\rho u}}, \tag{2.59}$$

where characteristic lengths in the normal L_n and tangential L_τ directions were introduced; u denotes the flow velocity far from the boundary. The final expression gives an estimation for the thickness of the boundary layer $\delta = L_n$ in dependence of the characteristic length in flow direction L_τ. It can be written for the transport of momentum (u), heat (T), or mass (C) according to eq. (2.58) as follows:

$$\delta_u \sim L_\tau \sqrt{\frac{\eta}{\rho u L_\tau}} = \frac{L_\tau}{\sqrt{Re}}, \quad \delta_T \sim L_\tau \sqrt{\frac{\lambda}{\rho c u L_\tau}} = \frac{L_\tau}{\sqrt{Pe}}, \quad \delta_C \sim L_\tau \sqrt{\frac{D}{u L_\tau}} = \frac{L_\tau}{\sqrt{Pe_S}}. \tag{2.60}$$

The dimensionless parameters Re, Pe, and Pe_S denote the Reynolds number, Peclet number, and solutal Peclet number, respectively. Such an estimation of the boundary layer thickness is helpful to determine the required spatial resolution in the calculations.

2.3.2. Phase change

In this work, we are dealing with silicon undergoing a phase change, containing small amounts of impurities. This process is described by thermodynamics and can be summarized in a phase diagram showing the dependence between composition and temperature. For silicon with carbon at small concentrations, the phase diagram is schematically shown in Fig. 2.2. Two important consequences can be identified and are described in the following subsections; see, e.g., [Wilke and Bohm, 1988, Sec. 1.3.1, 1.3.2].

2.3.2.1. Segregation

If we start cooling the system as shown in Fig. 2.2, the composition of the liquid and solid phases becomes different when the liquidus line $T_L(C_L)$ is reached. If the solidus $T_S(C_S)$ and liquidus lines can be approximated with straight lines, the ratio between the concentrations in the solid C_S and liquid C_L phase is independent of the composition. This constant is known as the equilibrium *segregation coefficient*:

$$k_0 = \frac{C_S}{C_L}. \tag{2.61}$$

For a moving phase interface, we observe an enrichment of concentration in the liquid phase if $k_0 < 1$ (e.g., carbon in silicon). If $k_0 > 1$ (e.g., oxygen in silicon), we observe a depletion in the liquid phase. These phenomena can be formulated mathematically in a boundary condition for the species transport equation at the phase interface [Wilke and Bohm, 1988, Sec. 1.3.1.3]:

$$D\frac{\partial C}{\partial n} = -(1 - k_0) v_n C, \tag{2.62}$$

where v_n is the normal interface velocity, with the normal vector pointing into the melt.

We can consider the segregation process locally at the phase interface and allow additional transport processes in the liquid and solid phases – convection and diffusion of the

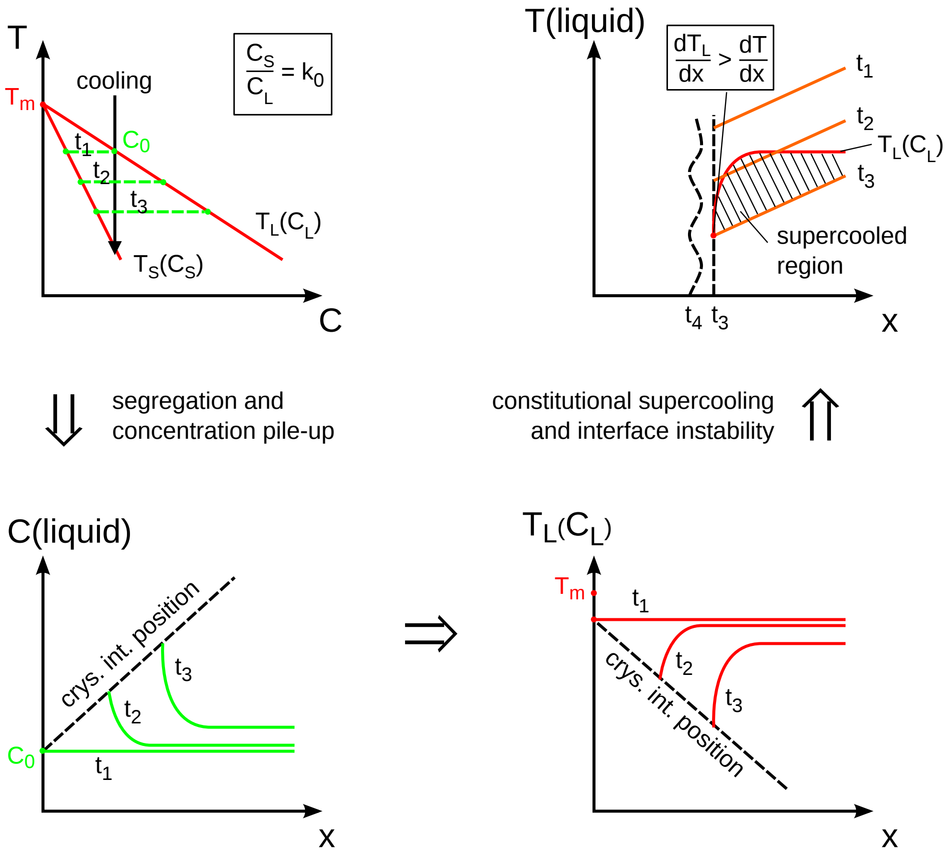

Figure 2.2.: Sketch of the phase diagram of silicon with carbon at small concentrations (top left) and the consequences: segregation and supercooling. t_i denote consecutive time instants. Further details are explained in the text.

impurities. In many practical applications, transport processes in the liquid phase are more important due to the possibility of convection and higher diffusion coefficients. For the two extreme cases – pure diffusion and complete convective mixing in the liquid phase – there are analytical solutions available, which are useful for both validation of calculations and better understanding. These solutions are summarized in Tab. 2.2. Note that for the solution with a pure diffusion, a steady state can be reached, where the concentration in the crystal does not increase any more and fulfills $C_S = k_0 C_L = C_0$.

Although several models for the intermediate states between a pure diffusion and complete mixing have been proposed, the most popular being the model by Burton et al. [1953] (BPS), these models may fail in specific cases and contain several parameters that are unknown or not accessible for a precise definition. For instance, it was shown by Priede and Gerbeth [2005] that the BPS solution breaks down in a radially converging flow.

Both analytical solutions in Tab. 2.2 suffer from the requirement of a closed (or infinite) system with no species flux over the boundaries. As already mentioned previously, oxygen is subjected to intensive evaporation from the melt. We can assume that this is not critical for the pure diffusive case because the evaporation initially affects only the top layer far away from the crystallization interface. But this boundary condition has a decisive role for a complete mixing. Fortunately, Scheil's law can be extended by an additional evaporation term of Poincare type:

$$D\frac{\partial C}{\partial n} = p_C(C - C_{ref}), \tag{2.65}$$

Name/Ref.	Assumptions	Expression
Scheil [Scheil, 1942]	Complete mixing in liquid, no diffusion in solid	$\frac{C_L}{C_0} = \left(1 - \frac{v_g t}{H}\right)^{k_0-1}$ (2.63)
Smith [Smith et al., 1955][a]	Pure diffusion in an infinite liquid, no diffusion in solid	$\frac{C_L}{C_0} = \frac{1}{2k_0}\Big\{1 + \operatorname{erf}\left[\frac{1}{2}\sqrt{xv_g/D}\right] + (2k_0-1)\exp\left[-k_0(1-k_0)xv_g/D\right] \cdot \cdot \operatorname{erfc}\left[\frac{1}{2}(2k_0-1)\sqrt{xv_g/D}\right]\Big\}$ (2.64)

[a] A popular approximation with 20% uncertainty is given by Tiller et al. [1953].

Table 2.2.: Analytical solutions for the segregation process. H is the melt height, x is the solidified length, and C_0 is the initial concentration in the liquid.

which gives for the distribution in the crystal:

$$\frac{C(p_C + v_g(1-k_0)) - p_C C_{ref}}{C_0(p_C + v_g(1-k_0)) - p_C C_{ref}} = \left(1 - \frac{v_g t}{H}\right)^{-p_C/v_g - 1 + k_0}. \tag{2.66}$$

The full derivation is given in Sec. C.2. A similar extension of Scheil's equation has been discussed by Eichler et al. [2003].

2.3.2.2. Supercooling and undercooling

The phase diagram in Fig. 2.2 clearly shows that the melting point depends on the composition of the melt. If the concentration locally increases due to segregation effects, the melting point locally decreases. If the spatial gradient of the melting point dT_L/dx is larger than the temperature gradient in the melt dT/dx, it is possible that a melt region at the crystallization interface becomes *supercooled* – its temperature is below the melting point but it is still in the liquid state. This situation is unstable, and the phase interface may develop a wave-like shape where the disturbances continue to grow.[8] If dT_L/dC is the slope of the liquidus line, the criterion for stability can be written as

$$\frac{dT_L}{dx} \leq \frac{dT}{dx} \quad \Rightarrow \quad \frac{dC}{dx}\frac{dT_L}{dC} \leq \frac{dT}{dx}. \tag{2.67}$$

In the case of complete mixing, dC/dx is zero, which ensures stability. Tiller et al. [1953] has derived an expression for the stability in the purely diffusive case:

$$\frac{dT/dx}{v_g} \geq \frac{dT_L}{dC}\frac{C_0}{D}\frac{1-k_0}{k_0}. \tag{2.68}$$

It should be noted that a similar critical value involving the temperature gradient in the crystal $v_g/(dT/dn|_S)$ plays an important role for the formation of interstitial point defects in the crystal [Chen et al., 2010b]. In the simulations in the current work, we will generally assume

---

[8] This model represents a simplified theory of the interface stability. A more exact model has been proposed by [Mullins and Sekerka, 1964]; see also [Coriell and McFadden, 1993] for a review.

that the phase interface has a smooth shape, but the possibility of a supercooling effect will be evaluated.

Another effect that must be mentioned in relation to crystallization dynamics is the so-called *undercooling*. To initiate the nucleation, an undercooling of the liquid below the equilibrium melting point is necessary, for example, up to 20 K for a nucleation of silicon on a Si_3N_4 coating [Appapillai and Sachs, 2010]. Furthermore, the further growth may also require a small amount of undercooling, which depends on the crystallographic orientation, presence of dislocations, and other factors [Beatty and Jackson, 2000]. In the simulations in the current work, we will assume that these effects can be neglected and that the solidification takes place exactly at the equilibrium melting point from the start.

2.3.2.3. Solidification

The phase change from the liquid to the crystalline state is accompanied by a release of latent heat. This can be seen in the temperature dependence of the enthalpy $H_e(T)$, which shows a jump at the melting point. This curve can be used for temperature calculations with the phase change considered automatically. If we define the specific enthalpy $h_e(T)$ [J/kg] (enthalpy is $H_e(T) = h_e(T)\rho(T)$) as [Kurz, 1998]

$$h_e(T) = \int\limits_0^T c(T')\,dT' + Q_l G(T), \tag{2.69}$$

we can solve an equation for h_e instead of the temperature equation (2.42):

$$\frac{\partial(\rho h_e)}{\partial t} = \operatorname{div}(\lambda \operatorname{grad} T). \tag{2.70}$$

The convection term was omitted here. Q_l denotes the latent heat, and $G(T)$ is a step function describing the $H_e(T)$ curve. For sake of calculation stability, this step is usually smoothed out over a finite temperature interval (the so-called mushy zone) even for substances with a well-defined melting point.

The jump of the enthalpy function can be mathematically formulated as an exact boundary condition for the temperature field at the phase interface – the Stefan condition:

$$\lambda_S \left.\frac{\partial T}{\partial n}\right|_S = \lambda_L \left.\frac{\partial T}{\partial n}\right|_L + Q_l \rho_S v_n, \tag{2.71}$$

where S denotes the solid, L denotes the liquid, and the normal vector points into the melt.[9] The Stefan condition merely states that the difference between the heat flows on both sides of the interface is identical to the released latent heat. An analytical solution in the 1D case is available [Alexiades and Solomon, 1993, Sec. 2.2, 2.4]. One end ($x = 0$) of an infinitely long bar ($x \geq 0$) initially at temperature T_i is hold at a constant temperature T_b. Under the assumption that the volume change due to the density jump can be neglected, we can obtain

---

[9] In the latent heat term, ρ_S should be used for the melting of an initially solid material and ρ_L for the solidification of an initially liquid material. However, if the geometric volume change is neglected in calculations, a proper choice is not obvious any more. In this work, ρ_S is used in the latent heat term.

for the interface position X ($T = T_m$) and velocity v_g:

$$X(t) = 2\Gamma\sqrt{\alpha_S t}, \quad v_g(t) = \Gamma\sqrt{\alpha_S/t}, \quad \alpha_L = \lambda_L/\rho_L c_L, \quad \alpha_S = \lambda_S/\rho_S c_S, \tag{2.72}$$

and for the temperature distribution:

$$\begin{aligned} T(x<X,t) &= T_b + (T_m - T_b)\frac{\operatorname{erf}\left[\frac{x}{2\sqrt{\alpha_S t}}\right]}{\operatorname{erf}\Gamma}, \\ T(x>X,t) &= T_i + (T_m - T_i)\frac{\operatorname{erfc}\left[\frac{x}{2\sqrt{\alpha_L t}}\right]}{\operatorname{erfc}(\Gamma\nu)}, \end{aligned} \tag{2.73}$$

where Γ is the solution of a transcendental equation (can be solved numerically)

$$\frac{c_S(T_m - T_b)}{Q_l}\frac{1}{\exp\Gamma^2 \operatorname{erf}\Gamma} - \frac{c_L(T_i - T_m)}{Q_l}\frac{1}{\nu\exp(\nu^2\Gamma^2)\operatorname{erfc}(\nu\Gamma)} = \Gamma\sqrt{\pi}, \quad \nu = \sqrt{\frac{\alpha_S}{\alpha_L}}. \tag{2.74}$$

This solution even describes supercooling if $T_i < T_m$.

2.3.3. Heat radiation in transparent media

Heat radiation means energy transport by electromagnetic radiation between surfaces at different temperatures. Here, we assume that all relevant media are either opaque or transparent, and describe the so-called surface-to-surface approach for the calculation of heat radiation (for an overview of methods see, e.g., [Versteeg and Malalasekera, 2007, Ch. 13]). A surface with a temperature T and emissivity ε (describing the properties of the surface in comparison to a black body) emits a heat flux density according to the Stefan-Boltzmann law

$$q = \sigma_{sb}\varepsilon T^4, \tag{2.75}$$

where $\sigma_{sb} = 5.67 \cdot 10^{-8}$ W/m^{2}K^4 is the Stefan-Boltzmann constant. An emissivity dependence of the temperature and a q dependence of the direction for specular surfaces (see [Guo et al., 1998] for an example with silicon) are possible. Such effects will be neglected in this work, and all radiation surfaces will be treated as diffuse. Furthermore, all materials will be considered either transparent or opaque, neglecting the possibility of semi-transparency.

The emitted power can be reflected or absorbed by another surface. We are interested in the equilibrium state between a set of such surfaces. First, we have to analyze what fraction of the radiation is received by a surface depending on its size and angle if it is not obstructed by another surface. This fraction is expressed in the *view factor* – a pre-factor for the heat flux density, which can be calculated by geometric integration [Baehr and Stephan, 2010, Sec. 5.5]:

$$W_{1\to 2} = \frac{1}{\pi A_1}\int\limits_{A_1}\int\limits_{A_2}\frac{\cos\beta_1\cos\beta_2}{r^2}\,dA_1\,dA_2, \tag{2.76}$$

where A_1, A_2 denote the surfaces and β_1, β_2 are the angles between surface normals and the line connecting both surfaces. There are many optimized algorithms for view factor calculations [Emery et al., 1991], such as the Hemicube method or the integration method for axisymmetric geometries [Dupret et al., 1990].

The exchange between many radiating and absorbing surfaces can be effectively solved by introducing a new variable – the radiosity H_i, which is defined as the total outgoing radiation flux [Baehr and Stephan, 2010, Sec. 5.5]. For $1\ldots m$ surfaces with given temperatures T_i and $m+1\ldots n$ surfaces with given heat fluxes Q_i, a system of algebraic equations is obtained:

$$\sum_{j=1}^{n}[\delta_{ij}-(1-\varepsilon_i)W_{ij}]H_j=\varepsilon_i\sigma T_i^4, \quad i=1...m \tag{2.77}$$

$$\sum_{j=1}^{n}[\delta_{ij}-W_{ij}]H_j=Q_i/A_i, \quad i=m+1...n \tag{2.78}$$

where δ_{ij} denotes the Kronecker delta. Q_i, T_i, and the radiosity H_i are connected by

$$Q_i=\frac{A_i\varepsilon_i}{1-\varepsilon_i}(\sigma T_i^4-H_i). \tag{2.79}$$

The system of equations for H_i can be solved iteratively as a linear system for fixed surface temperatures. An alternative approach is available in terms of the Gebhardt factors; they depend on the view factors and emissivities and can be obtained by a matrix inversion [Kurz, 1998]. In this case, for given Gerbhardt factors, the net heat fluxes Q_i are obtained directly, without solving a linear system.

In a frequently used approximation, the surface-to-surface radiation is replaced by a radiation from the surface to the ambient (an enclosing surface with $\varepsilon=1$ and $T=T_A$):

$$q=\sigma_{sb}\varepsilon(T^4-T_A^4). \tag{2.80}$$

2.4. Dimensionless numbers, model experiments, and scaling

The trivial assumption that physical laws should not depend on the chosen measurement units motivates a reduction to the so-called dimensionless form. Then, all variables are expressed as fractions of the corresponding characteristic values, and new dimensionless groups containing these characteristic values appear in the equation. This form of physical laws has the advantage that the number of variables needed to describe a specific system is reduced. Furthermore, we can scale the system by changing the characteristic values but keeping the dimensionless groups constant. In this way, we can carry out *model experiments*: perform the investigations in a system that is smaller, running at lower temperatures, etc. – better accessible to experimental investigations; scale the results to the target system.

There are several approaches how the relevant dimensionless groups can be obtained. In this work, we assume that we know all relevant governing equations with all relevant terms[10] and perform a straightforward **equation scaling** procedure. It is shown in the following sections for the relevant topics. A different source of dimensionless numbers is the so-called **dimensional analysis** [Ruzicka, 2008]. The definition of the relevant system parameters with their physical dimensions and the application of Buckingham's Pi-theorem [Gibbings, 2011] allows one to identify the dimensionless groups without even knowing the governing equations. However, this approach requires good physical intuition and does not necessarily

---

[10] See the work by Zeytounian [2009] for a discussion of this non-trivial topic on the basis of Rayleigh-Benard convection.

lead to dimensionless groups with a clear physical meaning. This is exactly where a yet another approach to dimensionless numbers starts: the **theory of similitude** first analyzes the geometric, kinematic (velocity), and dynamic (forces) similarity between two different systems [Gibbings, 2011]. In any case, the physical meaning of dimensionless numbers should not be overestimated – they provide not more than the order of magnitude of, e.g., ratios between different forces and depend on the definition of characteristic values.

It should be noted that sometimes dimensionless groups are introduced quite arbitrarily, without taking reference to the equations, and then used in all correlations. For example, we could take the 'TMF number' used in literature for a low-frequency TMF [Grants and Gerbeth, 2004], add a factor H/R_0 as it was done in [Lantzsch et al., 2007], and add a factor $\cos\phi$ to describe the influence of the phase shift ϕ. This would still be a valid dimensionless group containing parameters relevant to the problem. We could use it for correlations, for example: flow conditions vs. value of 'TMF number'. However, this presentation may give a completely wrong picture of the influence of the arbitrarily added $\cos\phi$. If the dimensionless number contains a product $I_0^2\cos\phi$, one may think that the effect of a two times increased $\cos\phi$ can be compensated by a $\sqrt{2}$ times smaller current I_0. This may not be true at all.

In this work, we are interested in a precise scaling of results and follow the concept: if we cannot introduce a relevant parameter like $\cos\phi$ by scaling the equations, then we consider different values of $\cos\phi$ as different cases each of which requires a separate analysis of correlations, etc. The calculations are performed and presented in a dimensional form for a specific case, and the generalization, i.e., scaling is treated as a separate topic in the corresponding chapters. The general scaling laws are validated with calculation examples.

2.4.1. Scaling of fluid flow and temperature

We introduce new scales for the length $L = L_0 L'$, velocity $u = u_0 u'$, time $t = t_0 t' = (u_0/L_0)t'$, pressure $p = p_0 p' = (\rho u_0^2)p'$, Lorentz force $\vec{F}_L = F_{L0}\vec{F}_L'$, and temperature $T = T_1 + (T_0 - T_1)T'$. Substitution into eqns. (2.39) and (2.42) gives

$$\begin{aligned}
&\frac{\partial \vec{u}'}{\partial t'} + (\vec{u}'\nabla')\vec{u}' = -\operatorname{grad}' p' + \frac{1}{Re}\Delta'\vec{u}' + \frac{Gr}{Re^2}T'\vec{u}' + \frac{F_{em}}{Re^2}\vec{F}_L', \\
&\frac{\partial T'}{\partial t'} + (\vec{u}'\nabla')T' = \frac{1}{Pe}\Delta' T'
\end{aligned} \tag{2.81}$$

with

$$Re = \frac{u_0 L_0 \rho}{\eta}, \quad Gr = \frac{\rho^2 g\beta(T_0 - T_1)L_0^3}{\eta^2}, \quad F_{em} = F_{L0}\frac{L_0^3\rho}{\eta^2}, \quad Pe = \frac{\rho c L_0 u_0}{\lambda} = Re\frac{c\eta}{\lambda}. \tag{2.82}$$

The dimensionless numbers are the Reynolds number, Grashof number, forcing parameter, and Peclet number, respectively. They describe per definition the approximate ratios of convective to viscous forces, convective to buoyancy forces, electromagnetic to convective forces, heat convection to heat conduction, respectively. The Prandtl number $Pr = Pe/Re$ can be used instead of the Peclet number. Through the scales for the unsteady and pressure terms we choose that their ratios to the convective term are on the order of unity. This is not important for the dimensionless form of equations, but it must be considered when analyzing the role of various terms in the equation.

The convective species transport is described by an equation that is identical to the temperature equation, with species concentration instead of temperature and the solutal Peclet number $Pe_S = u_0 L_0/D$ instead of Pe.

Note that most of the dimensionless numbers can not be calculated from the known system parameters and require a numerical calculation to obtain the values of u_0, $T_0 - T_1$, and F_{L0}. Once the characteristic values are found, they can be used to present the results in a general dimensionless form, e.g., as Re, Gr, Pe = function of (F_{em}, boundary conditions). The coupling between the Gr number and flow conditions does not allow to treat it as an independent variable. Note that in the literature, the F_{em} number is often defined using the analytical Lorentz force expression for F_{L0} from (2.33). This is not possible for a 3D geometry with a distinct skin effect.

2.4.2. Scaling of magnetic field and Lorentz force

We introduce new scales for the length $L = L_0 L'$, magnetic vector potential $\vec{A} = A_0 \vec{A}'$, electric scalar potential $V = V_0 V'$, and source current $\vec{j}_S = j_{S0} \vec{j}'_S$. The second eq. (2.25) gives a relation between the scales as $V_0 = \omega A_0 L_0$. The induction effects are usually neglected in source current regions, and the first equation (2.25) contains only the source term on the right-hand side. We obtain another relation between the scales: $A_0 = \mu_0 j_{S0} L_0^2$. We can also introduce an inductor current I_0 with $j_{S0} = I_0/L_0^2$. It follows for both equations (2.25):

$$\mathrm{rot}'\,\mathrm{rot}'\vec{A}' = S_{em}\left(-i\vec{A}' - \mathrm{grad}'V'\right) + \vec{j}'_S, \quad \mathrm{div}'\left(-i\vec{A}' - \mathrm{grad}'V'\right) = 0, \tag{2.83}$$

with

$$S_{em} = \mu_0 \sigma \omega L_0^2. \tag{2.84}$$

Here, rot′, etc., denote operators with dimensionless coordinates: $x = L_0 x'$, etc. The S_{em} number is known as the shielding parameter because it is directly related to the electromagnetic skin depth: $S_{em} = 2L_0^2/\delta_{em}^2$. The expression for the S_{em} number with L_0 replaced by the radius is often used in the literature for low-frequency TMF calculations.

The Lorentz force can be expressed in terms of variables $\vec{A}$ and V using eqns. (2.6) and (2.23). The previously defined scales and a scale $\vec{F}_L = F_{L0}\vec{F}'_L$ leads to

$$\vec{F}'_L = F_{I0}\left(-i\vec{A}' - \mathrm{grad}'V'\right) \times \mathrm{rot}'\vec{A}', \tag{2.85}$$

where

$$F_{I0} = \frac{1}{F_{L0}}\frac{A_0^2\sigma\omega}{L_0} = \frac{1}{F_{L0}}\frac{\mu_0^2 I_0^2 \sigma\omega}{L_0} = \frac{1}{F_{L0}}\frac{\mu_0 I_0^2}{L_0^3} S_{em} \tag{2.86}$$

describes the Lorentz force magnitude. Obviously, with a constant S_{em} number, the dimensionless Lorentz force F'_L is proportional to I_0^2/L_0^3.

Note that this derivation is valid for any time-dependent magnetic field and is not limited to a TMF. However, we have introduced a significant restriction with the assumption that the entire system is described by a single scale of inductor current I_0 or density j_{S0}. The currents in different inductors may still have different amplitudes and phase angles, but the amplitude must be changed proportionally in all inductors and the phase angles must remain constant for this derivation to be valid.

2.4.3. Scaling of heat transport

2.4.3.1. Global heat radiation

We consider here the global heat transfer in a furnace in the approximation where only heat conduction and radiation are relevant. The main equations and boundary conditions can be summarized as follows:

1. Heat radiation from a surface element with a temperature T_s belonging to a body with steady-state heat conduction described by a thermal conductivity λ. The radiation conditions are determined by an ambient temperature T_a and view factor W.

2. Heat radiation from a heater surface element with a temperature T_s, with a prescribed power Q on a surface S. The radiation conditions are determined by an ambient temperature T_a and view factor W.

3. Heat conduction from a surface with a prescribed heat flux density q belonging to a body with steady-state heat conduction described by a thermal conductivity λ.

The corresponding equations follow from Sec. 2.3.1 and their dimensionless forms are obtained using the scales $T = T'T_0$ (it is useful to set the reference temperature to zero because we are dealing with heat radiation), $L = L'L_0$, $S = S'L_0^2$, $Q = Q'Q_0$, and $q = q'q_0$:

$$1. \quad \lambda\frac{dT}{dn} = W\sigma_{sb}(T_s^4 - T_a^4) \quad \Rightarrow \quad \frac{dT'}{dn'} = R_1(T_s'^4 - T_a'^4), \quad R_1 = \frac{W\sigma_{sb}L_0T_0^3}{\lambda}; \tag{2.87}$$

$$2. \quad \frac{Q}{S} = W\sigma_{sb}(T_s^4 - T_a^4) \quad \Rightarrow \quad Q' = R_2(T_s'^4 - T_a'^4), \quad R_2 = \frac{W\sigma_{sb}L_0^2T_0^4}{Q_0}; \tag{2.88}$$

$$3. \quad q = \lambda\frac{dT}{dn} \quad \Rightarrow \quad q' = R_3\frac{dT'}{dn'}, \quad R_3 = \frac{\lambda T_0}{q_0L_0}. \tag{2.89}$$

If we change the scales L_0, T_0, etc., but keep the dimensionless groups R_1, R_2, and R_3 constant, dimensionless variables like T' remain constant. Let us consider the case where only R_1 and R_2 are relevant (adjustment of R_3 by q_0 is trivial). Fixing the ratio of the length scales for the reference (1) and target (2) systems, leaves us with one additional free ratio from λ_0, T_0, or Q_0. Tab. 2.3 summarizes the scaling laws for the remaining ratios as well as for the temperature gradient G. Special cases of scaling with a constant absolute temperature or constant temperature gradients are given as well. It can be seen that a precise furnace scaling for dominating heat conduction and radiation is generally possible.

2.4.3.2. Local transient heat conduction

Phase change in a local domain of a crystallization furnace requires additional equations to be considered. The time-dependent heat equation in a solid material (2.42) transforms with scales $T = T_1 + (T_0 - T_1)T'$, $L = L'L_0$, and $t = t'L_0/v_0$ to

$$\frac{dT'}{dt'} = \frac{1}{Pe_v}\triangle'T', \quad Pe_v = \frac{\rho c v_0 L_0}{\lambda}, \tag{2.90}$$

where the velocity scale in Pe_v can be related to the crystallization velocity.

Case	L_{02}/L_{01}	λ_2/λ_1	Q_{02}/Q_{01}	T_{02}/T_{01}	G_2/G_1
A	$\boldsymbol{a}$	$\boldsymbol{b}$	$a^{2/3}b^{4/3}$	$a^{-1/3}b^{1/3}$	$a^{-4/3}b^{1/3}$
B	$\boldsymbol{a}$	ab^3	a^2b^4	$\boldsymbol{b}$	$a^{-1}b$
C	$\boldsymbol{a}$	$a^{-1/2}b^{3/4}$	$\boldsymbol{b}$	$a^{-1/2}b^{1/4}$	$a^{-3/2}b^{1/4}$
A1	$\boldsymbol{a}$	$\mathbf{1}$	$a^{2/3}$	$a^{-1/3}$	$a^{-4/3}$
B1	$\boldsymbol{a}$	a	a^2	$\mathbf{1}$	a^{-1}
B2	$\boldsymbol{a}$	a^4	a^6	a	$\mathbf{1}$
C1	$\boldsymbol{a}$	$a^{-1/2}$	$\mathbf{1}$	$a^{-1/2}$	$a^{-3/2}$

Table 2.3.: Scaling of the global temperature for given ratios a and b. Scaling with a constant temperature in B1 and constant temperature gradients in B2. Note that per definition $T_{02}/T_{01} = T_2/T_1$.

Relevant boundary conditions include the Stefan condition (2.71) and heat radiation from the free surface (2.80). The dimensionless form of the radiation condition is identical to (2.87); the Stefan condition can be written in a dimensionless form as

$$J_S \left.\frac{dT'}{dn'}\right|_S = J_L \left.\frac{dT'}{dn'}\right|_L + v'_g, \quad J_{S/L} = \lambda_{S/L} \frac{T_0 - T_1}{Q_l \rho_s} \frac{1}{L_0 v_0}, \tag{2.91}$$

with new dimensionless parameters J_S and J_L.

2.4.4. Scaling of a crystallization furnace

The dimensionless numbers from the previous sections are summarized in Tab. 2.4, and typical values for this work are given in Tab. 2.5. It is obvious that all phenomena can not be independently scaled to different conditions at the same time because the dimensionless numbers share several parameters. In practice, the scaling may be limited due to the requirement of precise geometry scaling and due to high exponents present in the dimensionless groups leading to very large parameter changes. Therefore, one of the goals of this work is to develop approximate scaling laws useful for practice through the use of geometric parameters in particular.

Magnetic field	Melt flow	Global temperature
$S_{em} = \mu_0 \sigma \omega L_0^2,$	$Re = \frac{u_0 L_0 \rho}{\eta}$	$R_1 = \frac{W \sigma_{sb} L_0 T_0^3}{\lambda}$
$F_{I0} = \frac{1}{F_{L0}} \frac{\mu_0 I_0^2}{L_0^3} S_{em}$	$Gr = \frac{\rho^2 g \beta (T_0 - T_1) L_0^3}{\eta^2}$	$R_2 = \frac{W \sigma_{sb} L_0^2 T_0^4}{Q_0}$
	$F_{em} = F_{L0} \frac{L_0^3 \rho}{\eta^2}$	$R_3 = \frac{\lambda T_0}{q_0 L_0}$
	$Pe = \frac{\rho c L_0 u_0}{\lambda}$	$Pe_v = \frac{\rho c L_0 v_0}{\lambda}$
	$Pe_S = \frac{L_0 u_0}{D}$	$J_{S/L} = \lambda_{S/L} \frac{T_0 - T_1}{Q_l \rho_S} \frac{1}{L_0 v_0}$

Table 2.4.: Summary of dimensionless numbers for the scaling of a crystallization furnace.

System →	I (GaInSn)	II (GaInSn)	V (Si)	VI (Si)
Chapters →	4	5	8, 9	8
Parameters ↓				
S_{em}	28	3.2	4.8	1.0…63
Re	$7 \cdot 10^3$	$2 \cdot 10^3$	$2 \cdot 10^3$ $(0.7 \ldots 16 \cdot 10^3)$	$3 \cdot 10^3 \ldots 1 \cdot 10^5$
F_{em}	$1 \cdot 10^8$	$1.3 \cdot 10^7$	$8 \cdot 10^7$ $(2 \ldots 41 \cdot 10^7)$	$3 \cdot 10^7 \ldots 4 \cdot 10^{10}$
Gr	–	$7 \cdot 10^6$	$2 \cdot 10^8$	$6 \cdot 10^6 \ldots 3 \cdot 10^{10}$
Pe	–	43	25 (8…184)	$37 \ldots 1.3 \cdot 10^3$
L_0, m	0.05	0.05	0.11	0.05…0.4
δ_{em}, cm	1.3	4.0	7.1	7.1
δ_u, mm	0.6	1.1	2.3 (4.1…0.9)	0.9…1.2
δ_T, mm	–	7.6	22 (39…8)	8…11

Table 2.5.: Typical values (reference cases and/or typical parameter studies) of dimensionless numbers (see Sec. 2.4) and related parameters (see Sec. 2.3.1) in the calculations in this work. Model systems correspond to Tab. 1.5.

Chapter 3

Numerical modeling

This chapter describes the numerical software tools used in the current work. The description of the underlying numerical methods is held on the level needed for the adjustment of relevant numerical parameters, evaluation of calculation precision, and further software development on the basis of general numerical libraries. Nevertheless, several technical details, especially about the use of the open source software, are also included because the adaptation and testing of these tools was a significant part of this work and such details may help other users of these tools.

3.1. Introduction

3.1.1. Choice of software tools

One of the goals of this work was to evaluate the possibility to use open source software. It has an advantage of no license costs and a freely available source code, which allows both a better understanding of the algorithms and a possibility to introduce any modifications. The main disadvantage lies in a steep learning curve because of the often lacking documentation, limited support, and no comfortable user interface. These aspects are addressed by specialized commercial tools, but typically with a price of 10000…30000 Euro per year for industrial usage and limited insights into the algorithms leading partly to a black-box-type usage. The main question before choosing between these possibilities is what open source and commercial tools are available for the specific topic and what are their capabilities.

Tab. 3.1 summarizes commercial and open source alternatives for the topics relevant for the current work. These results are based on a series of discussions with software vendors about product capabilities as well as on benchmark calculations for several industrially relevant test cases[1]. Of course, only a part of the available tools is considered here; the choice is motivated by applications to similar topics in the literature and a still active software development. The following software vendors/developers have been considered:

- Fraunhofer IISB, Germany (CrysMAS): `http://www.iisb.fraunhofer.de/de/abteilungen/kristallzuechtung/crysmas.html`

---

[1] This evaluation was carried out in the framework of a benchmarking project managed by the author and with contributions from several other colleagues at SolarWorld.

- FemagSoft S.A., Belgium: `http://www.femagsoft.com`
- STR Group Ltd., Russia: `http://www.str-soft.com`
- ANSYS, Inc., United States: `http://www.ansys.com`
- COMSOL AB, Sweden: `http://www.comsol.com`
- ESI Group, France (CFD-ACE+): `http://www.esi-group.com`
- Cobham CTS Limited, United Kingdom (Opera): `http://www.cobham.com/about-cobham/aerospace-and-security/about-us/antenna-systems/aurora/products/opera-3d.aspx`
- CSC - IT Center for Science Ltd., Finland (Elmer, open source): `http://www.csc.fi/english/pages/elmer`
- OpenCFD Ltd. (SGI), United Kingdom (OpenFOAM, open source): `http://www.openfoam.com`
- GetDP (open source): `http://www.geuz.org/getdp`
- Gmsh (open source): `http://www.geuz.org/gmsh`
- NETGEN (open source): `http://www.sourceforge.net/projects/netgen-mesher`

Two main groups of simulation software packages can be distinguished in Tab. 3.1:

1. Specialized ready-to-use tools for crystallization furnace simulation, including models for the global heat transfer, phase change, species transport, etc. First evaluation indicated that these tools usually have no or only limited 3D capabilities.

2. General 3D program packages that can be applied to the missing features in the specialized crystallization furnace simulation tools. The emphasis in Tab. 3.1 is on 3D multi-physics packages to allow efficient coupling between various processes.

Note that the summary in Tab. 3.1 uses several numerical concepts that will be introduced only later in this chapter. It can be seen that a complete 3D model for crystallization furnaces is not available. The most complete solution is currently offered by STR, but it lacks the capabilities for 3D heat radiation and magnetic fields. We can find an actively developed open source tool for each topic, but with the already mentioned general limitations. However, if the choice is between further model development on the basis of open source or general commercial software, the former has clear advantages. Therefore, this work sets the goal to develop and adapt models based on the open source software for crystallization furnace simulation with alternating magnetic fields. The main software tools and main development topics are summarized in Tab. 3.2.[2]

To model coupled phenomena in a crystallization furnace, data between the separate simulation modules must be exchanged using additional interpolation routines, etc. Furthermore, various scripts are required for an automated pre-processing of calculations and post-processing, i.e., analysis of the calculation results. The entire work flow is depicted in Fig. 3.1 and should provide only the keywords for the following description. Basic methods for electromagnetic calculations, melt flow calculations, and global thermal modeling are described in this chapter. Appendix D presents the methods for grid generation as well as various additional software utilities.

---

[2] The `GetDP` and `OpenFOAM` solvers developed previously at Fraunhofer IISB were provided by Dr. Thomas Jung. They have been published only to a very limited extent, e.g., [Jung and Friedrich, 2007].

Name	Main capabilities	Main limitations
Global coupled furnace simulation		
CrysMAS	2D global thermal, 2D local flow/species calculations. Various 2D magnetic fields.	Only 2D. No segregation. Fixed triple point when melt flow active.
FEMAG-DS 2D & 3D	2D global thermal, 2D local flow/species calculations	3D still in development. No alternating magnetic fields.
STR CGSim & FlowModule	2D global thermal and 2D/3D local flow/species calculations	No 3D radiation. No alternating magnetic fields.
Elmer (open source)	2D and 3D global thermal calculations and solidification. Other solvers also available.	Use in text-mode.
3D heat/ flow/ species		
ANSYS Fluent	FVM for transport processes including 3D radiation.	No moving grid methods for crystallization and segregation.
COMSOL Multiphysics + modules	3D global thermal calculations. Other solvers also available.	FEM not optimal for convection processes.
CFD-ACE+ + modules	FVM for transport processes including 3D radiation.	No moving grid methods for crystallization and segregation.
OpenFOAM (open source)	General FVM package for transport processes.	Limited heat radiation models. Solvers must be programmed by the user. Use in text-mode.
3D magnetic field		
Opera Elektra	$A-V$ with linear edge elements and very efficient solver. Built-in basic CAD and meshing utility	Limited grid control, no import. Separate tool for 2D required.
COMSOL AC/DC module	$A-V$ with arbitrary-order edge elements in 2D and 3D.	Requires Comsol Multiphysics. High memory requirements.
CFD-ACE+ Magnetic module	$A-V$ with linear node elements.	Requires CFD-ACE+ Base. Only node elements.
ANSYS Emag module	$A-V$ with linear edge elements in 2D and 3D.	Requires ANSYS Mechanical. Heavy scripting needed due to lacking integration in the Workbench interface.
GetDP (open source)	General framework allowing also $A-V$ edge elements in 2D and 3D.	Solvers must be programmed by the user. Use in text-mode.
3D mesh generator		
ANSYS DesignModeler & Meshing	Simple CAD tool. Hex and tet meshes.	Limited mesh control
ANSYS ICEM CFD	3D tet and hex meshes with many controls.	No CAD tool.
Gmsh (open source)	Text-mode CAD tool. 2D tri and quad meshes, 3D tet meshes.	No solid operations for CAD.
NETGEN (open source)	Text-mode CAD tool including 3D solid operations. 3D tet meshes.	No CAD tool for 2D.

Table 3.1.: Main features of selected commercial and open source simulation packages. Abbreviations: FEM – Finite Element Method, FVM – Finite Volume Method, CAD – Computer Aided Design; meshes types: (tet)rahedrons, (hex)ahedrons, (tri)angles, (quad)rangles.

Topic	Software	Current state	Development goals in this work
3D global thermal	Elmer	Available solver (HeatSolve) for 2D/3D radiation including solidification	
3D flow/ species	OpenFOAM	One-domain solver with fixed phase interface shape developed at Fraunhofer IISB	Crystal domain and moving phase interface coupled with melt flow. Time-dependent Lorentz force distribution.
3D magnetic field	GetDP	$A-V$ 2D and 3D solvers developed at Fraunhofer IISB	Time-harmonic Lorentz force calculation. Higher-order elements.
3D mesh generator	Gmsh	Graphical and text-mode scripting for geometry definition and mesh generation	Scripts for definition of complex geometries.

Table 3.2.: Goals for open source software development in the current work. Extensive model testing and validation is not explicitly mentioned here as an obligatory part of model development.

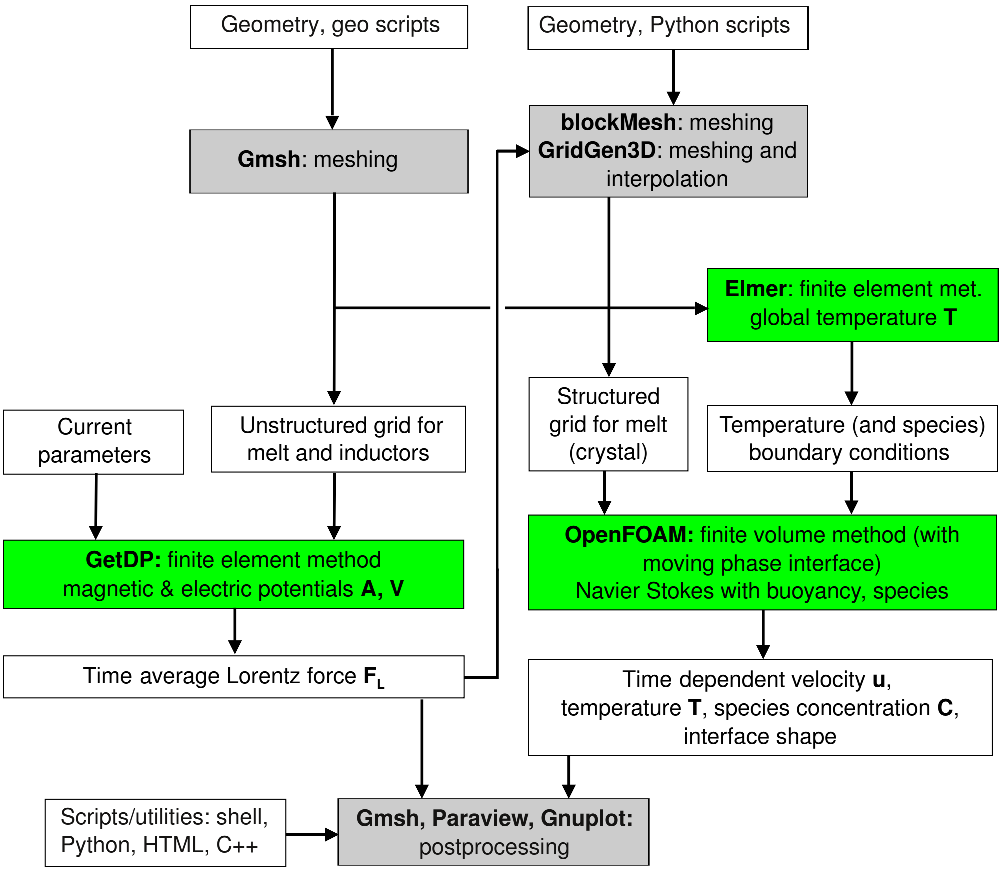

Figure 3.1.: Work flow and main software tools (green background for calculation, gray background for pre- and post-processing) for numerical calculations in this work.

3.1.2. Verification and validation

An essential part of the development of numerical software is verification and validation. According to Hatton [1997], even commercially released scientific software contains 8...12 serious faults per 1000 executable code lines. Even when working with well-tested software, there are still many input parameters prone to errors or sub-optimal values if the software is new to the user or if a new model is being developed. We follow the definition by Roache [1998] where *verification* is defined as *solving the equations right* and *validation* means *solving the right equations*. In the ideal case, verification should involve only mathematical analysis in the form of analytical solutions, etc., so that a comparison with an arbitrary precision is possible that is not disturbed by experimental uncertainties. The following validation shows whether the *correctly solved equations* can reproduce the experimental data well.

Verification of the models used in the current work is presented in this chapter; mainly analytical solutions or well-known benchmark calculations are applied. Validation is the topic of the following chapters, which are devoted to model experiments.

3.2. Electromagnetic calculations with `GetDP`

We consider the following general electromagnetic problem illustrated in Fig. 3.2:

- The system consists of several inductor coils and several conducting bodies surrounded by a non-conducting gas.
- Either a time-dependent voltage is prescribed at the outer ends of inductor supplies or a time-dependent current density in the inductors is given. In both cases, the skin effect in the inductors is considered negligible either due to low electrical conductivities or due to special coil designs with thin wire windings.
- Inductors produce a time-dependent magnetic field in the surrounding region. The magnetic field is assumed to be contained in this region, with magnetic field lines not crossing domain boundaries.
- The time-dependent magnetic field induces eddy currents in the conducting bodies. The interaction between the eddy-currents and the magnetic field leads to a Lorentz force acting in the bulk of the conducting bodies.

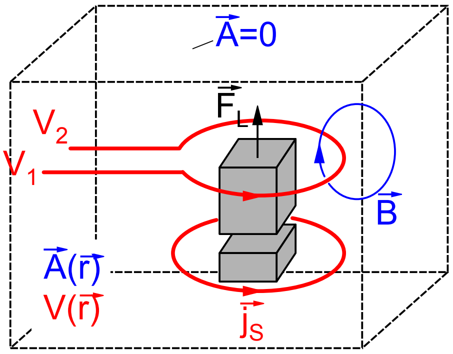

Figure 3.2.: General electromagnetic problem.

This problem is described by the equations for the magnetic vector potential $\vec{A}$ and electric scalar potential V (2.24). The current density can be set in inductor's volume with $\vec{j}_s$ or voltage can be set on the outer supply surfaces with V. On the outer boundary, we set $\vec{A}=0$, which means that all vector components are zero and that their derivatives in tangential directions to the boundary are zero as well. The resulting condition for $\vec{B}$ follows from the consideration of a local coordinate system on the boundary $(\vec{n},\vec{\tau}_1,\vec{\tau}_2)$:

$$\vec{B}=\mathrm{rot}\vec{A}=\vec{n}\left(\frac{\partial A_{\tau 2}}{\partial \tau_1}-\frac{\partial A_{\tau 1}}{\partial \tau_2}\right)+\vec{\tau}_1(\ldots)+\vec{\tau}_2(\ldots) \quad \Rightarrow \quad B_n=0,$$

which shows that magnetic field lines do not cross the boundary. For the electric potential, the normal derivative on the boundary is set to zero, $\partial V/\partial n=0$. Together with $\vec{A}=0$, this implies no current flow over the boundary according to (2.5) and (2.23).

For an 2D or axisymmetric case in the plane (x,y) with the third coordinate z, magnetic and electric fields have the form $\vec{B}=(B_x,B_y,0)$ and $\vec{E}=(0,0,E_z)$, respectively, due to the symmetry considerations for the equations (2.7) and (2.11). It follows from (2.23) that $\vec{A}=(0,0,A_z)$ and $\mathrm{grad}V=(0,0,\partial V/\partial z)$ (or $V=const$ in the (x,y) plane). Consequently, only a single equation for A_z must be solved, with the inductor current most conveniently set using $\vec{j}_s=(0,0,j_{sz})$.

3.2.1. The finite element method

The boundary-value problem for 4 partial differential equations with 4 unknown variables A_x, A_y, A_z, and V can be solved for an arbitrary 2D or 3D geometry using the *finite element method* (FEM). We follow the Galerkin's technique[3] for the derivation of the FEM equations; see, e.g., [Jin, 2002, Ch. 2, 8], [Bondeson et al., 2005, Ch. 6]. The first step is to fill the entire domain with mesh elements. The approximate distribution of the unknown variable is described by discrete values at specific mesh locations such as nodes and interpolated between them. Symbolically this can be written for $\vec{A}$ and V as

$$V(\vec{r})=\sum_{j=1}^{N_n}V_j n_j(\vec{r}), \quad \vec{A}(\vec{r})=\sum_{j=1}^{N_e}A_j\vec{N}_j(\vec{r}), \tag{3.1}$$

where n_j, $\vec{N}_j$ are local expansion functions related to the mesh nodes and edges, respectively, and V_j, A_j are the corresponding coefficients, i.e., the unknown values of V at the nodes and of the tangential component of $\vec{A}$ on the edges, respectively. This is the so-called edge element formulation for the magnetic potential. If the vector $\vec{A}$ is described simply by nodal elements for its three components, spurious nonphysical solutions may appear. Edge elements ensure continuous tangential components across element borders.

In the second step, the so-called weak form of the equation is derived. It follows from the original equation multiplied with a weighting or test function, which is identical to the expansion function in the Galerkin's method, and integrated over the whole calculation domain. For both time-dependent potential equations[4], we obtain (integration volume is denoted by

---

[3] An alternative technique is the variational method, which allows a physical interpretation of the FEM equations as conditions, e.g., for the energy minimum, but it involves more complex mathematical operations.

[4] Derivation for the time-harmonic case is identical – not influenced by the complex character of some quantities.

V' to avoid a confusion with the scalar potential):

$$\int_{V'} \left[\mathrm{rot} \left(\frac{1}{\mu_0 \mu} \mathrm{rot} \vec{A} \right) + \sigma \frac{\partial \vec{A}}{\partial t} + \sigma \,\mathrm{grad}\, V - \vec{j}_s \right] \vec{N}_i \, dV' = 0,$$

$$\int_{V'} \mathrm{div} \left(-\sigma \frac{\partial \vec{A}}{\partial t} - \sigma \,\mathrm{grad}\, V \right) n_i \, dV' = 0.$$

It is a common practice to transform these integrals to avoid second-order derivatives of the unknown functions $\vec{A}$ and V. Using general identities for arbitrary vectors $\vec{a}$ and $\vec{b}$ as well as a scalar s [Bronstein et al., 2008, Sec. 13.2.4.3]

$$\mathrm{div}(\vec{a} \times \vec{b}) = \vec{b}\, \mathrm{rot}\, \vec{a} - \vec{a}\, \mathrm{rot}\, \vec{b}, \quad \vec{a} \to \vec{N}_i, \quad \vec{b} \to \frac{1}{\mu_0 \mu} \mathrm{rot} \vec{A}, \tag{3.2}$$

$$\mathrm{div}(s\vec{a}) = \vec{a}\, \mathrm{grad}\, s + s\, \mathrm{div}\, \vec{a}, \quad s \to n_i, \quad \vec{a} \to -\sigma \frac{\partial \vec{A}}{\partial t} - \sigma \,\mathrm{grad}\, V, \tag{3.3}$$

and Gauss's theorem in the form

$$\int_{V'} \mathrm{div}\, \vec{a}\, dV' = \oiint_S \vec{a} \vec{n}\, dS, \tag{3.4}$$

we arrive at

$$\begin{aligned} -\oiint_S \left[\vec{N}_i \times \frac{1}{\mu_0 \mu} \mathrm{rot} \vec{A} \right] \vec{n}\, dS + \int_{V'} \frac{1}{\mu_0 \mu} \mathrm{rot} \vec{A}\, \mathrm{rot} \vec{N}_i \, dV' + \int_{V'} \vec{N}_i \sigma \frac{\partial \vec{A}}{\partial t} dV' + \\ + \int_{V'} \vec{N}_i \sigma \,\mathrm{grad}\, V \, dV' - \int_{V'} \vec{N}_i \vec{j}_s \, dV' = 0, \end{aligned} \tag{3.5}$$

$$\oiint_S \left[-\sigma \frac{\partial \vec{A}}{\partial t} - \sigma \,\mathrm{grad}\, V \right] n_i \vec{n}\, dS + \int_{V'} \sigma \frac{\partial \vec{A}}{\partial t} \mathrm{grad}\, n_i \, dV' + \int_{V'} \sigma \,\mathrm{grad}\, V \,\mathrm{grad}\, n_i \, dV' = 0. \tag{3.6}$$

Now, only first-order derivatives of the unknown function are needed. The surface integral over the domain boundary in the first equation is irrelevant if $\vec{A}$ is given on this boundary – the corresponding functions $\vec{N}_i$ are not used. For the surface integral in the second equation, two cases must be distinguished. On an insulating boundary with $\vec{A} = 0$ and $\partial V / \partial n = 0$, this integral vanishes. On a boundary with current flow where $\vec{A}$ and V are given, this integral becomes irrelevant again.

In the third step, the expressions (3.1) are substituted into equations (3.5) and (3.6). As the index i is varied over all edges and nodes, respectively, we obtain N_e equations for the unknown A_j values on the edges and N_n equations for the unknown V_j values at the nodes. Note that the expansion functions are local and the integration is performed only locally around the corresponding mesh element. As a result of this so-called global assembly process, a system of linear equations is obtained. Further technical discussion is out of scope of this work – `GetDP` is an already available finite element library.

3.2.2. Implementation in `GetDP`

`GetDP` is a general finite element library, and the solver is defined in a special PRO file containing commands in a special syntax on a high level of mathematical abstraction; see [Dular and Geuzaine, 2011; Geuzaine, 2001]. First, geometric regions, material properties, source currents, etc., are defined using the objects *Group/Region* and *Function*. For example, a constant current density in a circular 3D coil can be defined with:

```
Function {
  js0[Region[786]] = Complex[ jh*Cos[+4*Pi/3],jh*Sin[+4*Pi/3] ];
  jsource[DomainS_Mag] = js0[]*Vector[-Y[]/Sqrt[X[]*X[]+Y[]*Y[]+1e-15],
                                      X[]/Sqrt[X[]*X[]+Y[]*Y[]+1e-15], 0];
  }
```

The object *FunctionSpace* defines the expansion functions of the unknown fields, whereas the boundary conditions are set using the *Constraint* object. The central part of the solver is contained in the *Formulation* object, which contains equations in the weak form. For the 3D solver used in this work, the code resembles the equations (3.5) and (3.6) closely:

```
Equation {
  //Magnetic vector potential
  Galerkin { [ nu[] * Dof{d a} , {d a} ]; In Domain_Mag; Jacobian Vol; Integration Int; }
  Galerkin { DtDof [ sigma[] * Dof{a} , {a} ]; In DomainC_Mag; Jacobian Vol; Integration Int; }
  Galerkin { [ sigma[] * Dof{d v} , {a} ]; In DomainC_Mag; Jacobian Vol; Integration Int; }

  //Source current
  Galerkin { [ - jsource[] , {a} ]; In DomainS_Mag; Jacobian Vol; Integration Int; }

  //Electric scalar potential
  Galerkin { [ sigma[] * Dof{d v} , {d v} ]; In DomainC_Mag; Jacobian Vol; Integration Int; }
  Galerkin { DtDof [ sigma[] * Dof{a} , {d v} ]; In DomainC_Mag; Jacobian Vol; Integration Int; }
  }
```

In addition to Galerkin's integral expression (the scalar product of expressions separated by a comma in [] is integrated over the calculation domain), the domain for each term (*In*), coordinate transformations (*Jacobian*) and integration methods (*Integration*) are specified. For example:

```
Jacobian {
  { Name Vol; Case { { Region All; Jacobian Vol; } } } // 2D planar or 3D
  { Name VolAxi; Case { { Region All; Jacobian VolAxiSqu; } } } // 2D axisymmetric
  }
```

The *Resolution* object defines the solution method (e.g., time-dependent, time-harmonic, etc.) for each formulation. The methods for solving the linear system are defined in a separate PAR file. The iterative GMRS method with preconditioning from the `Sparsekit` library and the direct MUMPS method from the `PETSc` library was applied in this work within `GetDP`. Finally, the *PostProcessing* and *PostOperation* objects allow one to calculate various quantities from calculation results and write them to files in various forms, respectively. The following code shows the expressions to calculate the integral induced current and integral induced heat power for the axisymmetric case as well as the time-averaged Lorentz force for the time-harmonic 3D case:

```
Quantity {
  { Name Im;  Value { Integral { [ (1/(X[]+1e-15))*(-sigma[]*Dt[{a}]) ];
    In Melt;  Jacobian VolAxi; Integration Int; } } }

  { Name Qm;  Value { Integral { [2*Pi*0.5*sigma[]*SquNorm[Dt[{a}]]];
    In Melt;  Jacobian VolAxi; Integration Int; } } }
```

```
  { Name FL_avr; Value { Local { [ 0.5*Cross[ Re[-sigma[]*(Dt[{a}]+{d v})], Re[{d a}] ] +
                                   0.5*Cross[ Im[-sigma[]*(Dt[{a}]+{d v})], Im[{d a}] ] ];
    In Melt;  Jacobian Vol; Integration Int; } } }
  }
```

We point to the previously mentioned references for further technical details, but one aspect of the solver must be emphasized. As can be seen from the basic equations, the potentials $\vec{A}$ and V in 3D calculations are not uniquely determined without an additional gauge condition. An efficient way of gauging is the cotree method, where $\vec{A}$ is set to zero on a tree of edges. In this manner, the number of unknowns is reduced as well. This type of gauging can be implemented in `GetDP` using the *Constraint* object:

```
Constraint {
  { Name Gauge; Type Assign;  Case { { Region Domain_Mag; SubRegion OuterBoundary; Value 0.0; }  }  }
  }

FunctionSpace {
  { Name Hcurl_a_Mag_3D; Type Form1;
  // BasisFunction { ... }
  Constraint {
    { NameOfCoef ae; EntityType EdgesOf; NameOfConstraint a; }
    { NameOfCoef ae; EntityType EdgesOfTreeIn; EntitySubType StartingOn; NameOfConstraint Gauge; }
    }
  } }
```

3.2.3. Verification

For a precise verification we use the analytical solution for a long cylinder in a TMF from Sec. 2.1.5. This solution contains an ideal traveling magnetic wave that can be generated by a real finite inductor only approximately, without a clear relation between the wave parameters the inductor inductor. Therefore, the validation consists of two steps:

1. The vertical magnetic field component on the surface of the cylinder is analyzed to determine the parameters α and B_0 of the TMF wave according to (2.27).
2. The TMF parameters are used in (2.29) to calculate the analytical Lorentz force distribution. This is compared with the numerical result.

The geometric and current parameters chosen for the calculation are given in in Fig. 3.3. The parameters of the TMF wave are evaluated from the 2D calculation because it has a higher numerical accuracy. For a point on the cylinder surface at mid height: $B_{z0} = 4.073$ mT and $\alpha = 9.7$ 1/m. These parameters were relatively constant over the height indicating that the inductor approximates an idealized wave well; however, we cannot exclude an inaccuracy of at least a few percent here.

The meshes used in 2D and 3D calculations are depicted in Fig. 3.5, the calculated Lorentz force distribution in Fig. 3.4. A comparison with the analytical solution shows a good agreement for the 2D case with quadratic elements, which ensure a high numerical accuracy. The case with linear elements in 2D clearly emphasizes the need to use spatial averaging of the force distribution to obtain a smooth profile. The same is true for the 3D calculation. Both the 2D and 3D results show that a rough grid at the surface with linear elements may introduce an error with an underestimated force density by approx. 20%. The force angle agrees well with the analytical solution in the 2D and 3D calculation; the accuracy is better at the surface but shows large deviations near the axis in most cases. However, the force density near the axis is practically zero and not relevant.

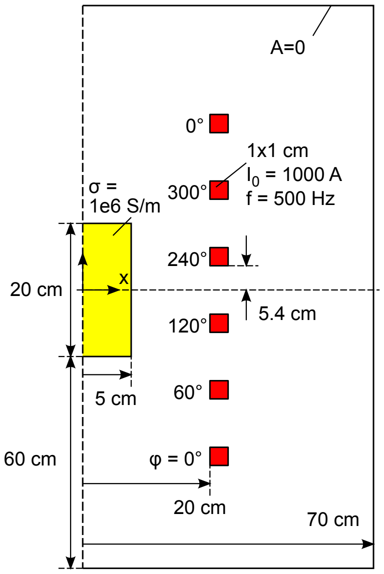

Figure 3.3.: Verification of Lorentz force calculations. Geometric and current parameters for a system consisting of a long conducting cylinder and 6 inductor coils. An upward TMF is generated with a distinct skin effect due to the high frequency.

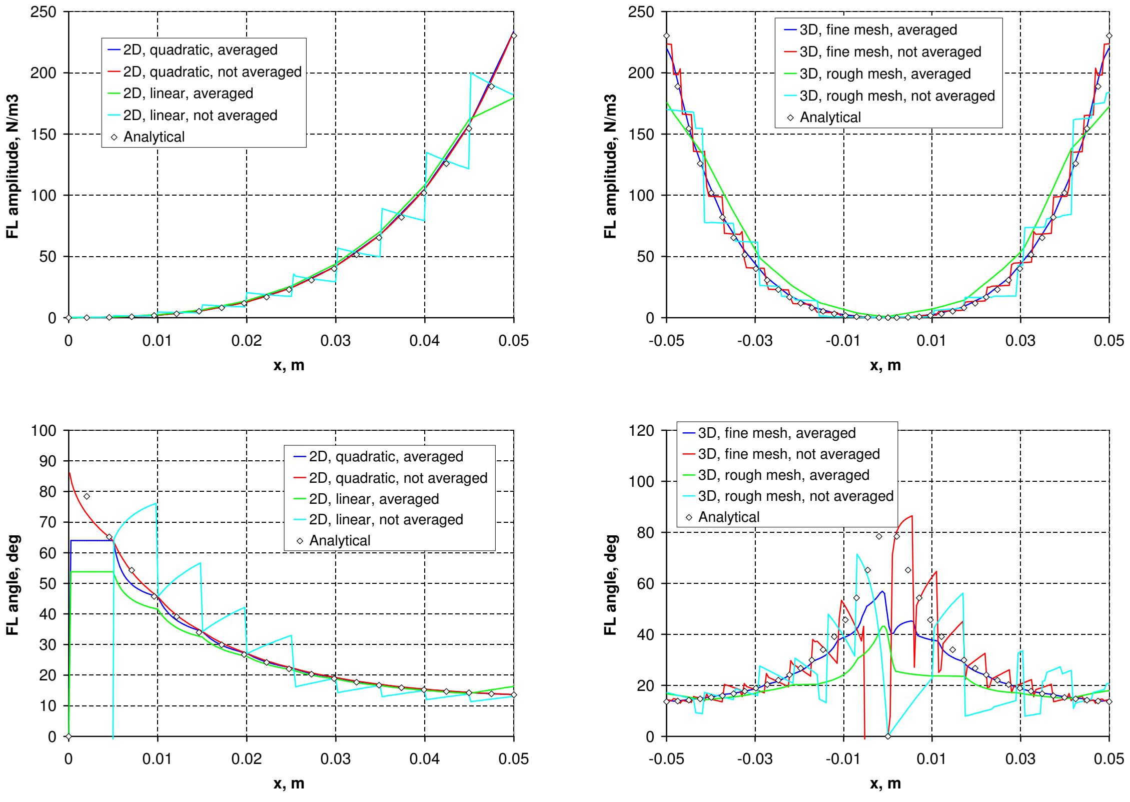

(a) 2D (b) 3D

Figure 3.4.: Verification of Lorentz force calculations. Calculated distribution of the Lorentz force density (top) and angle (bottom) over the cylinder radius at mid height for the 2D (a) and 3D (b) case. The angle is measured from the vertical direction. Results with and without spatial averaging of the Lorentz force are used. In the 2D case, a comparison between linear and quadratic elements is given.

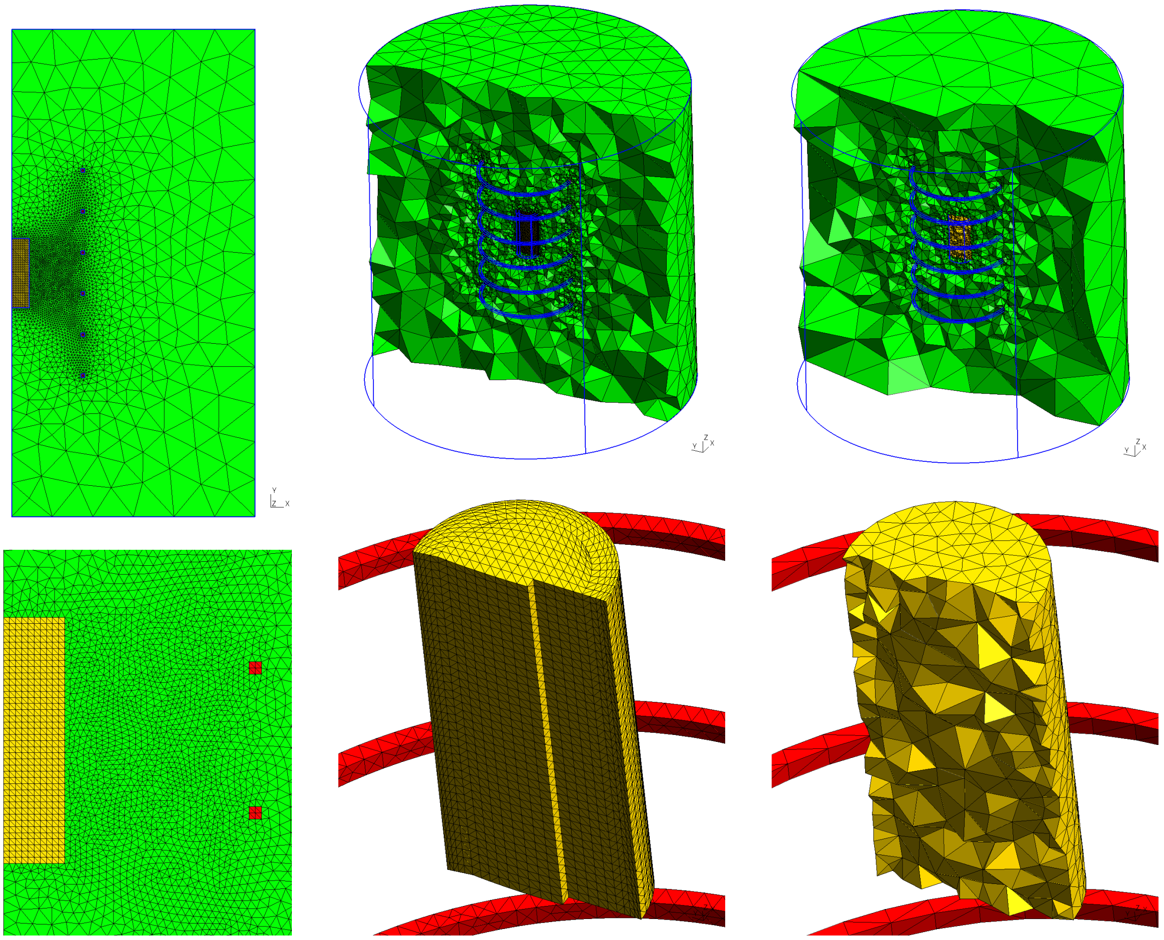

(a) 2D (b) 3D, fine grid (c) 3D, rough grid

Figure 3.5.: Verification of Lorentz force calculations. Grid generated using `Gmsh` for the entire domain showing also geometry lines (top); zoomed-in to the melt domain (bottom): (a) 2D case (6759 triangles; size in melt 5 mm); (b) 3D case with a fine grid (406652 tetrahedrons; size in melt 1...5 mm); (c) 3D case with a rough grid (77077 tetrahedrons; size in melt 9 mm). Note that the volumes are clipped.

3.3. Calculations of melt flow, phase interface, and species transport with `OpenFOAM`

We consider the following coupled fluid mechanics problem illustrated in Fig. 3.6:

- The system consists of a crystal domain and a melt domain with a moving solidification interface between them.
- Temperature field in both domains is considered, with local boundary conditions on the outer surfaces. These are: fixed temperature, fixed heat flux, heat flux due to radiation to an ambient temperature or due to convection (Poincare-type).
- Fixed temperature is assumed on the phase interface. The interface is assumed either stationary or moving with a prescribed velocity, or moving according to the local heat balance.

- Melt motion is driven by a prescribed Lorentz volume force as well as by buoyancy and Marangoni forces due to temperature gradients.
- Concentration field of several types of impurities is considered in the melt. Local boundary conditions are set on melt surfaces. These are: fixed concentration, fixed mass flux, mass flux due to segregation or due to dissolution/ chemical reactions (Poincare-type).

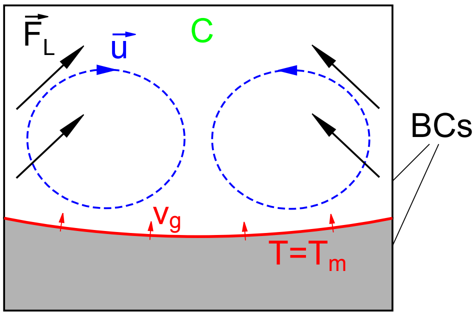

Figure 3.6.: General coupled fluid mechanics problem. Boundary conditions (BCs) are further discussed in the text.

This problem is described by the equations for incompressible fluid flow (2.38), including source terms for Lorentz forces and buoyancy forces in the Boussinesq approximation, transport equations (2.58) for temperature and species concentration. Melt motion may require turbulence models as described in Sec. 2.2.2. The motion of the crystallization interface obeys the heat balance equation (2.71).

3.3.1. The finite volume method

The finite volume method starts with the integration of transport equations over the basic mesh volume – the *control volume* (CV). For the actual problem, we have transport equations for velocity components $\vec{u}$, temperature T, and species concentration C. The equation for a general transport variable ψ (2.58) is integrated as follows [Versteeg and Malalasekera, 2007, Sec. 8.1]:

$$\int\limits_{CV} \frac{\partial(\rho\psi)}{\partial t}\,dV + \int\limits_{CV} \mathrm{div}(\rho\psi\vec{u})\,dV = \int\limits_{CV} \mathrm{div}(\Gamma\,\mathrm{grad}\,\psi)\,dV + \int\limits_{CV} S_\psi\,dV.$$

Application of Gauss's theorem (3.4) and integration over a time step Δt yields finally an integral conservation equation[5] for ψ:

$$\int\limits_{CV} \rho(\psi_{t+\Delta t} - \psi_t)\,dV + \int\limits_{\Delta t}\int\limits_{S} (\rho\psi\vec{u})\vec{n}\,dS\,dt = \int\limits_{\Delta t}\int\limits_{S} (\Gamma\,\mathrm{grad}\,\psi)\vec{n}\,dS\,dt + \int\limits_{\Delta t}\int\limits_{CV} S_\psi\,dV\,dt. \tag{3.7}$$

Turbulence modeling in this work is performed by adjusting the transport coefficient Γ, see section 2.3.1. External forces for the momentum equation are included in the source term S_ψ.

In the second step, the integral equation is applied to each control volume of the mesh to obtain an equation for the unknown value at the center of the control volume (assumed

---

[5] The integral form can be considered an alternative exact form of the transport equation (2.58), see [Zikanov, 2010, Sec. 2.8].

constant over the CV). This approach has a clear physical interpretation – in principle, we are dealing with a local conservation law for each CV, where the rate of change in a CV is balanced by diffusive and convective fluxes over the boundary S. In this manner, the finite volume method fulfills the conservation laws on a base numerical level.

Several numerical aspects are crucial for an efficient implementation of the finite volume method. The first is the discretization scheme: we need the values of the unknown variable ψ and its gradient $\operatorname{grad}\psi$ on the faces of the CV (surface S); we have to apply also a time-discretization scheme. The second aspect is the continuity requirement $\operatorname{div}\vec{u} = 0$, i.e., the calculation of the pressure field.

3.3.1.1. Pressure–velocity coupling

Because there is no separate equation for the pressure field in an incompressible flow, an iterative strategy is usually applied to find a pressure field that ensures the continuity of the resulting velocity field. The two most popular algorithms are known under the names SIMPLE (semi-implicit method for pressure-linked equations) and PISO (pressure-implicit split-operator). The main steps in these algorithms are as follows ([Versteeg and Malalasekera, 2007, Ch. 6, Sec. 8.7], [Jasak, 1996]):

1. Initial guesses for pressure and velocity fields.
2. Solve momentum equation to obtain intermediate velocity field $\vec{u}^*$ (predictor step).
3. Solve pressure correction equation, deduced from the continuity equation, to obtain a pressure correction field p'. This equation may require several iterations on non-orthogonal grids.
4. Correct the velocity and pressure fields (corrector step). Calculate the new face fluxes.
5. In case of PISO, repeat previous two steps for a prescribed number of corrector steps.
6. Solve all other transport equation using the obtained face fluxes.
7. Repeat the loop until convergence in each time step is reached in case of SIMPLE or go to the next time step in case of PISO. Relaxation can be applied for SIMPLE, but not for PISO (only one complete iteration per time step).

`OpenFOAM` offers also a merged SIMPLE–PISO algorithm – PIMPLE, where a PISO loop is included in a outer SIMPLE loop. Both the PIMPLE algorithm (in Sec. 8.5, 8.6) and the PISO algorithm (in other parts) were used in this work. Typically, at least 4 PISO or SIMPLE/PISO iterations were calculated in each time step.

If both the velocity and the pressure are stored at the centers of control volumes (collocated grid), checker-board type oscillations may appear in the solution [Versteeg and Malalasekera, 2007, Sec. 6.2]. A well known remedy is to store pressure on the faces (staggered grid). However, this approach becomes complicated on non-structured grids. In this case, the so-called Rhie-Chow correction is often applied when interpolating the velocity on the faces [Versteeg and Malalasekera, 2007, Sec. 11.14]. Although this correction is not explicitly applied in `OpenFOAM`, the numerical algorithms are implemented in the spirit of Rhie-Chow [Kärrholm, 2006].

3.3.1.2. Discretization schemes

To express an unknown variable on the cell face ψ_e in terms of values in parent and neighbor cells, several approximations or differencing schemes may be applied. The most common schemes are shortly described below following [Ferziger and Peric, 2002, Ch. 4] and [Versteeg and Malalasekera, 2007, Ch. 5]:

- The central differencing scheme (CDS) uses linear interpolation between the two nearest nodes. It is second-order accurate but may produce oscillatory solutions if the cell Peclet number $Pe_{cell} = \rho u \Delta x / \Gamma > 2$. The CDS (denotation in `OpenFOAM`: 'Gauss linear') is used in this work for the convective term in the momentum equation.
- The upwind differencing scheme (UDS) approximates ψ_e by its value at its upstream node. This scheme is the only one which never yields oscillatory solutions, but it has only first-order accuracy and introduces numerical (artificial, false) diffusion. Second-order accuracy is achieved in the linear upwind scheme (LUDS) where two upstream nodes are used. The LUDS ('Gauss linearUpwind Gauss') is used in this work for the convective term in the concentration equation.
- The QUICK scheme (quadratic upwind interpolation for convective kinetics) assumes a parabolic profile between the neighbor nodes; two nodes are taken from the upstream side. This scheme is third-order accurate on a uniform mesh. The QUICK scheme ('QUICK') is used in this work for the convective term in the temperature equation.

The gradients in the diffusive term of transport equation (3.7) can be calculated by assuming a linear profile between the two neighbor nodes as in the CDS. This method has second-order accuracy and is the default method used in this work. It is denoted in `OpenFOAM` as 'Gauss linear corrected'.

The time integral of transport equation (3.7) can be approximated using values of the variable ψ at several time instants. For two time points:

$$\int_{t}^{t+\Delta t} \psi \, dt \approx \left[\theta \psi_{t+\Delta t} + (1-\theta)\psi_t\right] \Delta t. \tag{3.8}$$

Three cases are shortly described below:

- Explicit scheme (explicit Euler scheme) with $\theta = 0$ has first-order accuracy and sets a limit on the maximum time step for stability. For the case with dominating convection, the Courant number must fulfill: $Co = \Delta t \, u / \Delta x < 1$. This scheme has not been implemented in `OpenFOAM`.
- Crank-Nicolson scheme with $\theta = 0.5$ is second-order accurate and unconditionally stable.
- Fully implicit scheme (implicit Euler scheme) with $\theta = 1$ is first-order accurate and unconditionally stable. This is the default method used in this work. It is denoted in `OpenFOAM` as 'Euler'.

Note that the stability conditions are mostly derived for simple 1D (steady) cases. In practice, the limit for the Courant number may be relevant also for the implicit time scheme due to the nonlinearities in the equations. In this work, the time step is usually adjusted automatically to fulfill $Co < 0.5$ in all control volumes. The CDS scheme may remain stable also at cell Peclet numbers up to 100 [Villiers, 2006].

3.3.2. Implementation in `OpenFOAM`

`OpenFOAM` is a general finite volume library for arbitrary polyhedral meshes [OpenFOAM, 2011]. The library is based on the object oriented C++ programming language. A solver in `OpenFOAM` is defined using C++ syntax and then compiled to an application. Many examples are included in the `OpenFOAM` installation or can be found in user forums. The standard solvers `buoyantBoussinesqPimpleFoam` and `pimpleDyMFoam` are most similar to this work. Nevertheless, reading the raw source code and its automated description generated by `Doxygen` cannot be avoided in the development of new applications.

The first step in an `OpenFOAM` solver is to define the mesh using *dynamicFvMesh* or similar classes and the fields using *volScalarField, volVectorField*, or similar classes. Various parameters and switches typically are read from predefined or new *dictionaries* as *dimensionedScalar, scalar, label*, or other types. After these initialization steps, the main solver loop can be started. Its central part contains the equations and the corresponding solution algorithms. The code fragment below shows the definition of the momentum equation and the main part of the PISO loop.

```
fvc::makeRelative(phi, U);

fvVectorMatrix UEqn (
                    fvm::ddt(U)
                    + fvm::div(phi, U)
                    + turbulence->divDevReff(U)
                    //- fvm::laplacian(nu, U) //laminar model only
                    + beta*(T - TRef)*g //buoyancy force
                    - FL/rho0 //Lorentz force
                    );

solve(UEqn == -fvc::grad(p)); // momentum predictor step

for (int corr=0; corr<nCorr; corr++) // PISO loop
   {
   rAU = 1.0/UEqn.A();
   U =  rAU*UEqn.H();
   phi = (fvc::interpolate(U) & mesh.Sf());

   // solve for pressure field - loop of non-orthogonality coorections
   for (int nonOrth=0; nonOrth<=nNonOrthCorr; nonOrth++)
      {
      fvScalarMatrix pEqn ( fvm::laplacian( rAU, p) == fvc::div(phi) );
      pEqn.setReference(pRefCell, pRefValue);
      pEqn.solve();
      if (nonOrth == nNonOrthCorr) { phi -= pEqn.flux(); }
      }

   fvc::makeRelative(phi, U);
   #include "continuityErrs.H"
   U -=rAU*(fvc::grad(p)); // momentum corrector step
   U.correctBoundaryConditions();
   }

turbulence->correct();
```

The momentum equation contains an external Lorentz force as well as the buoyancy force. If the phase boundary is moving, the Lorentz force may change with the melt height. Therefore, the following option has been implemented: Lorentz force distributions for several melt heights are imported and a simple interpolated distribution is used as the mesh moves (without topology changes). Additionally, a 3D Lorentz force distribution can be easily defined with an analytical expression, such us the equation (2.33):

```
vector forcedir = ForceAnalyticTMF/mag(ForceAnalyticTMF);
```

```
forAll(mesh.cells(), cellsi)
    {
    vector p = mesh.C()[cellsi];
    // project point radius vector onto the plane normal to the force
    vector r = p - (p & forcedir) * forcedir;
    FL[cellsi] = ForceAnalyticTMF * magSqr(r);
    }

forAll(FL.boundaryField(), patchesi)
    {
    forAll(FL.boundaryField()[patchesi], facesi)
        {
        vector p = mesh.Cf().boundaryField()[patchesi][facesi];
        vector r = p - (p & forcedir) * forcedir;
        FL.boundaryField()[patchesi][facesi] = ForceAnalyticTMF * magSqr(r);
        }
    }
```

The face flux field (*phi*) obtained from the calculated velocity field is used for the temperature and species concentration equations. The example below shows the code for the temperature:

```
volScalarField kappaEff
(
    "kappaEff",
    turbulence->nu()/Pr + turbulence->nut()/Prt
);

fvScalarMatrix TEqn
(
    fvm::ddt(T)
  + fvm::div(phi, T)
  - fvm::laplacian(kappaEff, T)
);
```

In the final part of the time loop, routines to save the results are usually called and additional quantities are written to text files. In this work, the time-average properties of the flow are often needed. The time-averaged velocity, the corresponding standard deviation, as well as the mean, turbulent, and total (instantaneous) kinetic energy (both the distribution and the integral value) can be calculated recursively as follows:

```
avstep++;
KUVmean = ( KUVmean*(avstep-1) + U )/avstep;
KUx2 = ( KUx2*(avstep-1) + sqr( U.component(0) ) )/avstep; //KUy2 = .., KUz2 = ..
KUxdev = sqrt(mag( KUx2 - sqr( KUVmean.component(0) ) ));  //KUydev = .., KUzdev = ..
KKtot = 0.5*( U & U );
KKmean = 0.5*( KUVmean & KUVmean );
KKturb = 0.5*( mag( KUx2 - sqr( KUVmean.component(0) ) ) +
               mag( KUy2 - sqr( KUVmean.component(1) ) ) +
               mag( KUz2 - sqr( KUVmean.component(2) ) )
             );
KKtotvol = ( fvc::domainIntegrate(KKtot) ).value(); //KKmeanvol = .., KKturbvol = ..
```

In addition to the solver, boundary conditions must be defined. In the current work, only the flux-based Poincary-type boundary conditions for thermal radiation, convective cooling, and species segregation required additional implementation. For example, the segregation condition contains the following lines of code:

```
fvsPatchField<scalar> phip = patch().patchField<surfaceScalarField, scalar>(phi);
gradient() = (k0_-1)/D_ * (*this) * phip / patch().magSf();
```

When an OpenFOAM application is called, it requires a definite directory/file structure – the *case*. In addition to the geometry, it contains also main parameters for the discretization of the equations and for the solution of the linear systems in parameter files *fvSchemes* and *fvSolution*, respectively. In the current work, mainly the GAMG (geometric-algebraic multi-grid) and PBiCG (preconditioned bi-conjugate gradient) linear system solvers were applied. Both allow parallel calculations if the calculation domain has been *decomposed* before.

3.3.2.1. Crystal domain with a moving phase boundary

The previous section described a typical OpenFOAM solver with a single calculation domain. Although a moving mesh is supported in OpenFOAM, addition of several calculation domains and data exchange between them are relatively complex. In the current work, a new solver for two meshes corresponding to one liquid and one solid domain has been developed. The two surfaces (*patches*) corresponding to the phase boundary are moved at the beginning of each time step according to the thermal balance. The thermal balance is evaluated in the following way:

1. Calculation of temperature gradients at face centers of the phase boundary patch in the solid and fluid domains. Interpolation of the values from the solid mesh to the fluid mesh. For coinciding points, a more stable manual 'interpolation' can be applied.
2. Calculation of the crystallization velocity normal to the phase boundary from thermal balance (2.71) (see code below) and interpolation of the values from face centers to nodes.
3. Transformation of the normal crystallization velocity $\vec{v}_n$ so that the nodes move only in vertical direction $\vec{e}_z$ to avoid node collisions. The approximation for the vertical velocity: $\vec{v}_z = (|\vec{v}_n|^2/\vec{v}_n\vec{e}_z)\vec{e}_z$. Nodes on the triple-point line can be frozen if required.
4. Interpolation of velocities from fluid mesh nodes to solid mesh nodes and application of the mesh motion as $\Delta z = v_z \cdot \Delta t$. Saving of monitored quantities such us phase boundary coordinates, heat fluxes at predefined points, etc.

```
Unormal = MotionVelocCoeff * ( AddSolidifRate +
            (
            - lambdasolid.value() * TsnGradsolid_interp
            - lambda.value() * TsnGrad
            )
            / rhosolid.value() / q0solid.value()
          );
```

Additionally, an algorithm has been implemented to obtain a steady-state shape of the crystallization interface. It is assumed that the entire interface moves with a prescribed velocity v_{n0} (the velocity offset *AddSolidifRate* in the code above) and the latent heat is released at the entire interface according to $Q_l\rho_s v_{n0}$. In each time step of the unsteady calculation, the value of v_{n0} is adjusted so that a prescribed point of the crystallization interface (e.g., at the interface center) does not move, i.e., remains at its initial position. Because only the steady-state is needed, the movement of the interface can be accelerated by multiplying its velocity with an acceleration factor (*MotionVelocCoeff* in the code above); values in the range 50…100 are usually used. The physical interpretation of such steady-state interface shapes is discussed later in Sec. 8.7.1.

To evaluate the heat balance at the crystallization interface, the unsteady temperature field in the crystal must be calculated. An equation very similar to the temperature equation for the melt is solved, with a convective term to account for mesh deformation:

```
fvc::makeRelative(phisolid, Usolid);

fvScalarMatrix TsolidEqn
(
   fvm::ddt(Tsolid)
 + fvm::div(phisolid, Tsolid)
 - fvm::laplacian(DTsolid, Tsolid)
);
```

The motion of mesh nodes in the bulk can be calculated automatically, but the available algorithms fail for large mesh deformations. A FEM-based algorithm suitable for large deformations [Tukovic and Jasak, 2007] is available only in an alternative `OpenFOAM` version. Therefore, a simple manual method has been implemented, where the points of a structured mesh are moved by compressing/extending the vertical line between the moving phase boundary and the opposite stationary surface. Note that this algorithm as well as the entire velocity calculation is not easily compatible with parallelized calculations containing several fluid mesh parts.

3.3.3. Verification

Test cases for the most important aspects of `OpenFOAM` solvers are presented in the following sections.

3.3.3.1. Lid-driven cavity with and without buoyancy

For the verification of the fluid flow, we have to accept an exception and use a numerical/experimental result for comparison because analytical solutions exist only for simple, open flow geometries. The so-called lid-driven cavity is the most popular benchmark case in fluid dynamics literature. It consists of an incompressible fluid in a 2D square cavity (width and height L_0) with a moving lid, e.g., a specified horizontal velocity component u_{lid} on the top wall. There are various modifications with included buoyancy effects available in the literature. The configuration closest to our case is a stable temperature gradient with fixed temperatures on the top and bottom walls (temperature difference ΔT), with the other walls insulated. This problem can be fully described by three dimensionless numbers: the Reynolds, Grashof and Prandtl number (only Re in the isothermal case), which we define and choose as follows:

$$Re = \frac{\rho u_{lid} L_0}{\eta} = 1000, \quad Gr = \frac{\rho^2 g \beta L_0^3 \Delta T}{\eta^2} = 10^6, \quad Pr = \frac{\eta}{\rho}\frac{\rho c}{\lambda} = 0.71.$$

Although the exact material properties are irrelevant, the values for air at 20 °C are used [VDI-Waermeatlas, 2006] and the values of u_{lid} and ΔT are adjusted. The material and geometry parameters are shown in Fig. 3.7. `OpenFOAM` calculations are carried unsteady (starting from zero fields) until a steady-state is reached. The comparison of calculation results in Fig. 3.7 with reference results from the literature – [Botella and Peyret, 1998] for the isothermal case and [Iwatsu et al., 1993; Agrawal et al., 2001] for the non-isothermal case – shows a good agreement that clearly becomes better if the grid is refined.

3.3.3.2. 1D time-dependent diffusion and segregation

We use the analytical solution (2.64) for an exact verification of diffusion and segregation calculations. Carbon impurities in a silicon melt are considered; system parameters are given

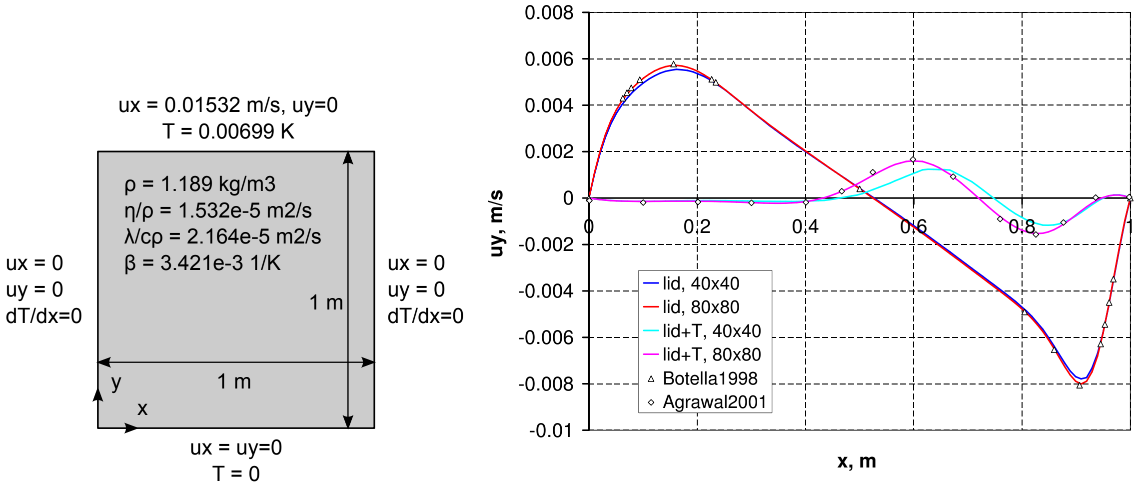

(a)

(b)

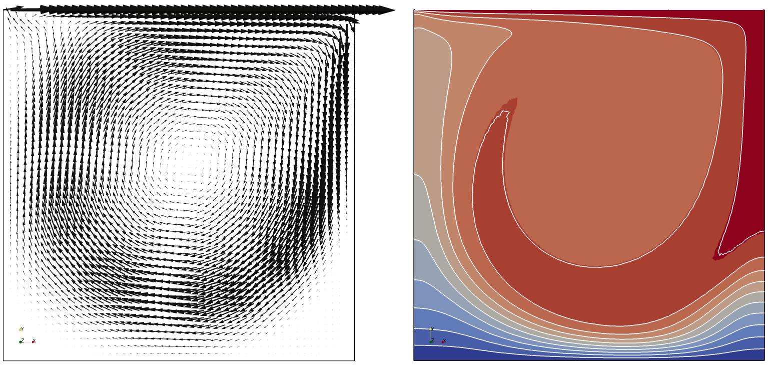

(c) isothermal case

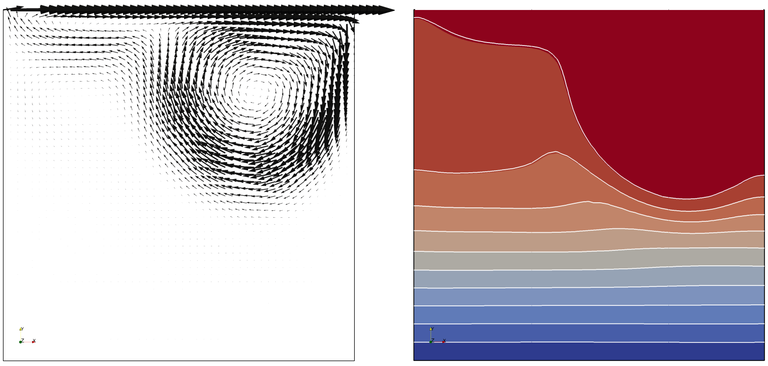

(d) non-isothermal case

Figure 3.7.: Verification of flow calculations: (a) system parameters; (b) comparison of the velocity profile on a horizontal line through the center between the literature and a calculation on a rough grid with 40×40 elements and a fine grid with 80×80 elements; (c) velocity vectors and temperature distribution (as a passive scalar) for the isothermal case on the fine grid; (d) the same for the non-isothermal case with buoyancy forces. In both cases, the maximum velocity is 0.0151 m/s and the temperature lies in the range 0…0.00699 K.

in Fig. 3.8. The grid consists of 1×1 element in the horizontal directions and of uniformly sized elements in the vertical direction. Species concentration on the phase boundary moving with a constant velocity of 1 cm/h in dependence of time is compared between the numerical calculation and analytical solution in Fig. 3.8. It can be seen that the solution on the finest grid with 0.01 mm deviates only by 0.03%, whereas the solution on the rough grid with 1 mm deviates by approximately 3%. This test gives an important hint that for a proper resolution of the carbon segregation boundary layer, element sizes smaller than 1 mm might be necessary. The steady-state size of this layer can be estimated from the derivation in [Smith et al., 1955] – it describes the concentration distribution in the melt ahead of the crystallization interface with an exponent $\exp(-v_g x/D)$. The boundary layer size can be estimated as D/v_g, which gives for our case 7.2 mm. Note that the boundary layer can be much smaller in the transient initial stage; we do not reach the steady-state within 10 h because the concentration continues to increase.

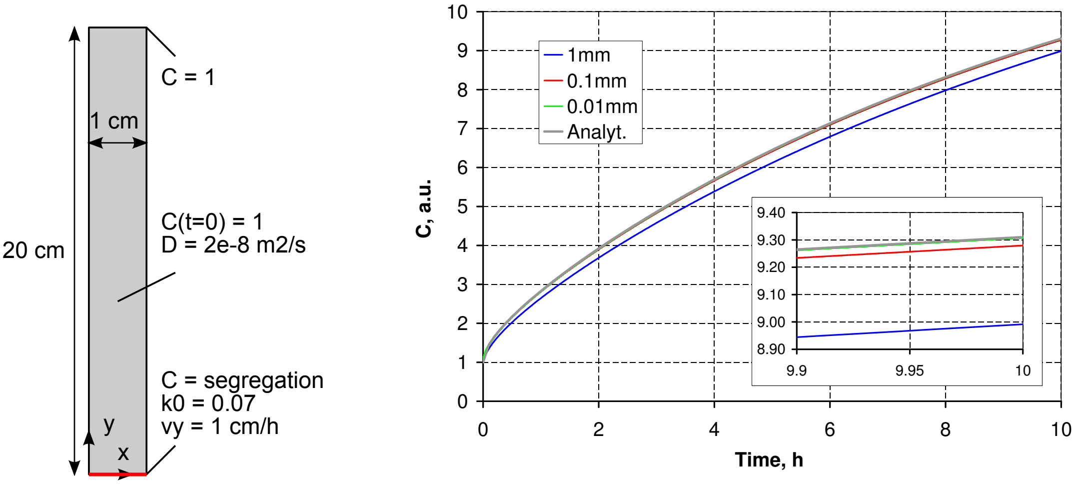

(a) (b)

Figure 3.8.: Verification of segregation calculations: (a) system parameters; (b) comparison of the concentration on the interface with the analytical solution for various grid element sizes.

3.3.3.3. 1D time-dependent solidification

We use the analytical solution from Sec. 2.3.2.3 for an exact verification of the solidification in 1D. The system parameters are given in Fig. 3.9. The grid consists of 1×1 element in the horizontal direction and of elements refined at the crystallization interface in the vertical direction. Note that we cannot start from zero crystal length here because the mesh topology cannot change in the current implementation of the `OpenFOAM` solver. This introduces a small deviation from the analytical solution; however, we can simply use the analytical solution from a time instant of 0.079 h where the crystal has reached a length of 1 cm. The differences in the initial temperature distributions are negligible because the pre-defined 1 cm long crystal is cooled down from the initial temperature within a few seconds. Another important note is that the melt height has to be very large because it extends to infinity in the analytical solution. If we use a zero flux condition in the calculation, we must check that the temperature during the calculation remains at its initial value. It can be estimated that the melt height must be 4 m for the temperature decrease to be smaller than 0.5% from the maximum temperature difference in the system for the current case. The comparison of the time-dependence of the crystallization interface position with the analytical solution in Fig. 3.9 shows a very good agreement.

In practical applications, 2D and 3D effects of the movement of the crystallization interface may play an important role. Since analytical solutions for phase change in 2D and 3D geometries are complicated, the verification was carried out in a simplified manner. Identical material properties were set for the melt and crystal domains; the latent heat was set to zero. Thermal boundary conditions were chosen so that a steady state could be reached. The final steady-state shape of the moving boundary was compared to the 2D isoline or 3D isosurface obtained in a heat conduction calculation by the `OpenFOAM` solver `laplacianFoam`. Good agreement was observed in both 2D and 3D cases.

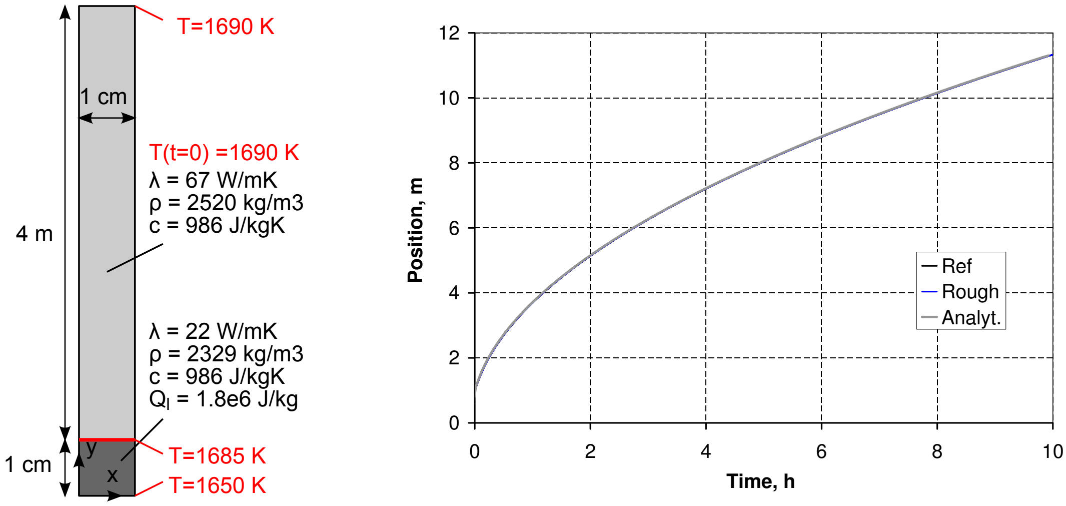

(a) (b)

Figure 3.9.: Verification of solidification calculations with a moving grid: (a) system parameters; (b) comparison of the interface position for the reference grid (20/400 elements in crystal/melt) and for a rough grid (10/200 elements) with the analytical solution.

3.4. Global thermal modeling with `Elmer`

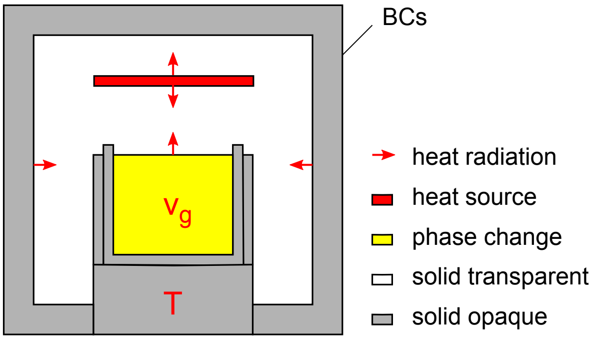

Figure 3.10.: General global thermal problem (example of a crystallization furnace). Boundary conditions (BCs) are further discussed in the text.

We consider the following 2D, 2D-axisymmetric, or 3D global thermal problem illustrated in Fig. 3.10:

- The system consists of an arbitrary number of domains which can be either solid or partly solid/liquid with a phase boundary. The solid domains (including a stationary gas) can be either opaque or fully transparent to heat radiation.
- Time-dependent heat conduction is considered in all domains. The thermal properties – density, heat capacity, emissivity, and thermal conductivity – can be functions of temperature.
- In phase change domains, movement of the phase boundary that separates the solid and liquid parts with different material properties and release/absorption of latent heat are considered.
- Heat exchange by radiation occurs between boundary surfaces of the transparent domains.
- The type of boundary conditions on the outer boundary can be Dirichlet, Neumann, or Poincare as described in Sec. 2.3.1. Internal domains may contain additional time-dependent volume heat sources.

This problem is described by the transport equation for temperature (2.58). The effect of phase change is included in temperature-dependent material properties, and the effect of radiation is included in local boundary conditions. These aspects are both discussed in the following section. The convective term in equation (2.58) is not needed if we do not consider moving domains or convection.

Although global multi-domain solvers can be implemented also in `OpenFOAM`, the segregated approach where the equations are solved sequentially for all domains has a limited efficiency and the parallelization is not fully supported. Furthermore, the algorithms for heat radiation are still in active development, and there are no built-in methods for phase-change calculations. The finite element library `Elmer` [Elmer, 2011] offers a ready-to-use 2D and 3D solver `HeatSolve` for conductive and radiative heat transfer. Other solvers for magnetic fields or melt flows are also available, but they are less developed than `GetDP` and `OpenFOAM`. Because the global temperature calculation in the current work is needed primarily to obtain approximate boundary conditions for a local melt analysis, we can use `HeatSolve` separately for such investigations.

3.4.1. Numerical algorithms

For temperature calculations, `Elmer` uses the finite element method. It is applied to the temperature equation in a very similar manner as to electric potential in Sec. 3.2.1. If we repeat the integration procedure to obtain the weak form of the temperature equation, we arrive at

$$\int_V \left(\rho c \frac{\partial T}{\partial t} - \operatorname{div}(\lambda \operatorname{grad} T) - S_T \right) n_i \, dV = 0 \quad \Rightarrow$$

$$\int_V n_i \rho c \frac{\partial T}{\partial t} dV - \oiint_S (\lambda \operatorname{grad} T)\, n_i \vec{n}\, dS + \int_V \lambda \operatorname{grad} T \operatorname{grad} n_i \, dV - \int_V n_i S_T \, dV = 0. \tag{3.9}$$

The surface integral in the second term requires a special treatment. This integral is obviously determined by the heat flux over the domain boundary: $\lambda \partial T / \partial n$. The integral is irrelevant if temperature is specified on the boundary; it is zero if the boundary is insulating; it has a definite value if the heat flux is specified on the boundary. The Poincare boundary condition needs a similar treatment.

Heat radiation in `Elmer` is calculated using the Gebhardt factor method as described in Sec. 2.3.3. View factors and Gebhardt factors are calculated only at the beginning of the calculation (recalculation may be required if, e.g., emissivities depend on the temperature). An important step is the renormation of view factors so that their sum equals unity in a closed cavity. In this way, the numerical error in the view factor calculation is distributed over all view factors.

Each time step in an unsteady calculation is divided in several sub-steps. In each sub-step, radiation heat fluxes on surface elements of the boundaries of transparent domains are linearized and set as Poincare-type boundary conditions using surface temperatures from the previous step. The temperature field due to heat conduction is calculated using these boundary conditions. The implicit Poincare-type condition gives a better convergence than an approach with constant heat fluxes calculated from the temperatures in the previous time step.

As an example of phase change calculation on a fixed grid, the enthalpy method was mentioned in 2.3.2.3. There are several similar alternatives available [Voller et al., 1990], from which `Elmer` uses the apparent heat capacity method. The apparent heat capacity is defined as

$$c_A = \frac{dh_e}{dT}. \tag{3.10}$$

It can be seen that this substitution transforms the enthalpy equation (2.70) to the usual transport equation for temperature (2.3.1) where c is replaced by c_A. If the function $h(T)$ is approximated with a mushy zone in the region $T_1 \ldots T_2$, then in this region $c_A = Q_l/(T_2 - T_1)$ according to (2.69). In practice, the application of this method requires some kind of averaging to ensure numerical stability [Voller et al., 1990]. From several possibilities in `Elmer`, the spatial averaging technique (denoted as ‘Phase Change Model = Spatial 2’) was selected due to better stability properties. In this case, c_A is calculated according to

$$c_A = \sqrt{\frac{\operatorname{grad} h_e \cdot \operatorname{grad} h_e}{\operatorname{grad} T \cdot \operatorname{grad} T}}. \tag{3.11}$$

In each time step, the distribution of $h_e(T)$ is calculated using a given tabular dependence and the corresponding c_A distribution is obtained. Note that for this c_A definition to work, the temperature gradient $\operatorname{grad} T$ in the entire phase change must be non-zero.

An important aspect in global thermal calculations is the presence of many domains. During the assembly of the linear system of equations, each domain has to be processed separately because we may need also flux boundary conditions on the internal boundaries between several domains (e.g., for heat radiation). Nevertheless, all equations form a single coupled system and are solved simultaneously.

3.4.2. Verification

3.4.2.1. Heat radiation between two spherical shells

We consider a system containing two spherical shells of finite thickness. The inner shell (heater) contains a volume heat source P; heat is radiated to an ambient temperature T_a from the outer surface of the outer shell (insulation). This problem not only can be calculated as an axisymmetric or full 3D problem but also can be solved fully analytically as shown in Sec. C.3. System parameters and the 2D and 3D grids are given in Fig. 3.11 (a,b). The mesh was generated using `Gmsh`. The comparison of the calculated temperature distributions on the radius with the analytical solution in Fig. 3.11 (c) shows considerable deviations only for the largest element size in 3D. This is not a surprise because there is only one element over the thickness, which cannot describe the curved temperature profile in case of linear finite elements. It should be noted that in 3D, a refinement of the grid increased the calculation time from 1 hour to 50 hours. The largest amount of time was needed for an iterative calculation of the Gebhardt matrix. Heat radiation was calculated in both cavities, without setting the heat flux on the inside of the heater to zero. The number of surface elements participating in radiation was 3512 for the rough mesh and 13830 for the fine mesh in 3D.

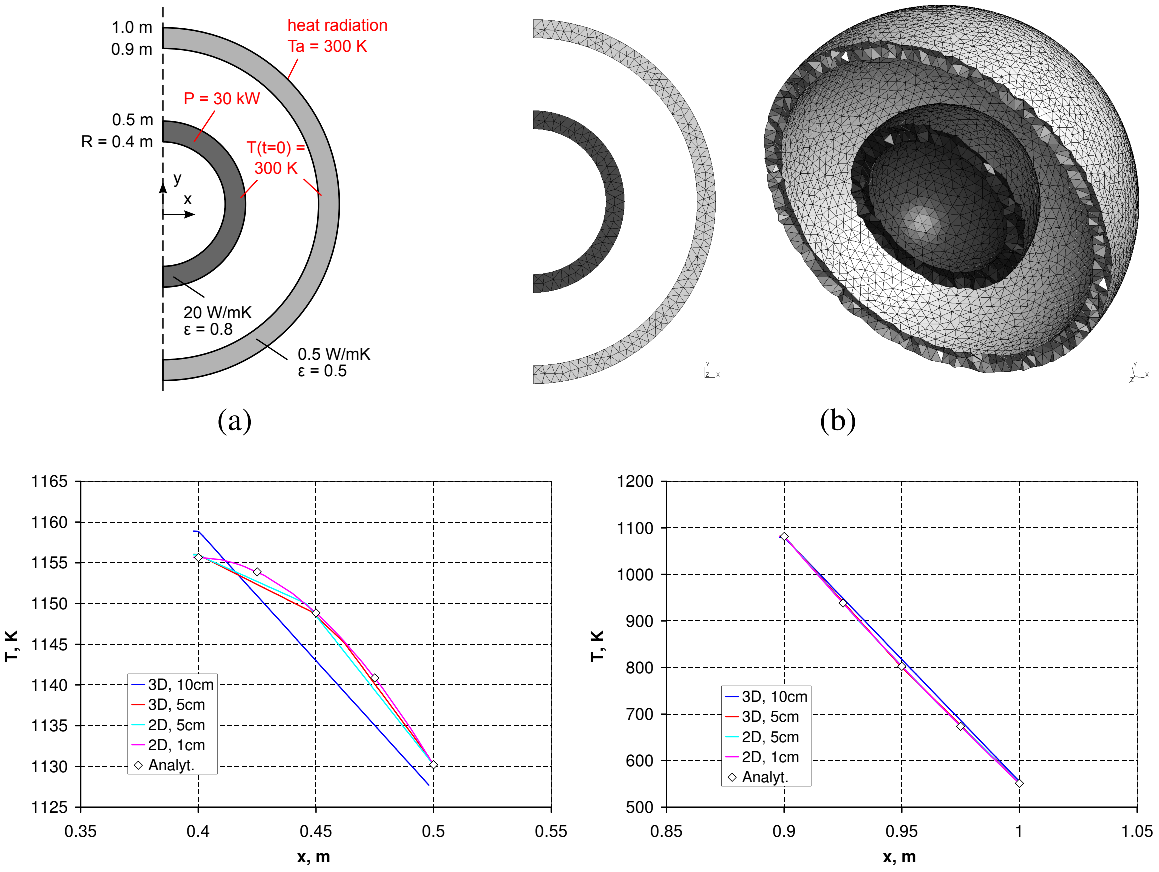

(a) (b)

(c)

Figure 3.11.: Verification of heat radiation calculations: (a) system parameters; (b) example of the 2D (400 triangles; element size 5 cm) and 3D grid (77145 tetrahedrons; element size 5 cm); (c) comparision of temperature profiles in the heater and insulation for different mesh element sizes in 2D and 3D.

3.4.2.2. 1D time-dependent solidification

We use the same test case as in Sec. 3.3.3.3. However, the fixed-grid method in `Elmer` requires a definition of the enthalpy as a function of temperature. By introducing a small mushy zone T_2 =1684.8 K... T_3 =1685.2 K as discussed in Sec. 2.3.2.3, the enthalpy function in the temperature range T_1 =300 K... T_4 =1800 K was defined as follows (with linear interpolation between the points):

$$H_e(T) = \begin{cases} T_1, & H_{e1} = 0 \\ T_2, & H_{e2} = (T_2 - T_1)\rho_S c_S \\ T_3, & H_{e3} = H_{e2} + (T_3 - T_2)\rho_S c_S + \rho_S Q_l \\ T_4, & H_{e4} = H_{e3} + (T_4 - T_3)\rho_L c_L \end{cases} \tag{3.12}$$

where the subscripts S and L denote properties of the solid and liquid, respectively. The same temperature-dependence with a mushy zone was also used for the density and thermal conductivity. The enthalpy definition in `HeatSolve` reads:

```
Enthalpy = Variable Temperature
Real
  300.0   0.0
  1684.8  3.1800e9
  1685.2  7.3732e9
  1800.0  7.6584e9
End
Phase Change Intervals(2,1) = 1684.8  1685.2
```

Calculations with various grid sizes and time step sizes are summarized in Fig. 3.12. The time step has a rather small influence on the solidification, a large jump at the beginning is observed only with the largest time step of 4 min. A similar effect can be seen for different mesh sizes, where the largest deviations also appear at the start of the solidification. A perfect agreement with the analytical solution is not achieved mainly due to this jump. The slope of interface position on the time axis (the crystallization velocity) in later stages of the growth agrees well between all calculations, with oscillations appearing only on the roughest meshes. The observed sensitivity to mesh size and time step is a disadvantage of the fixed-grid method in comparison to the moving-grid method. On the other hand, the fixed-grid method allows any crystallization front geometry.

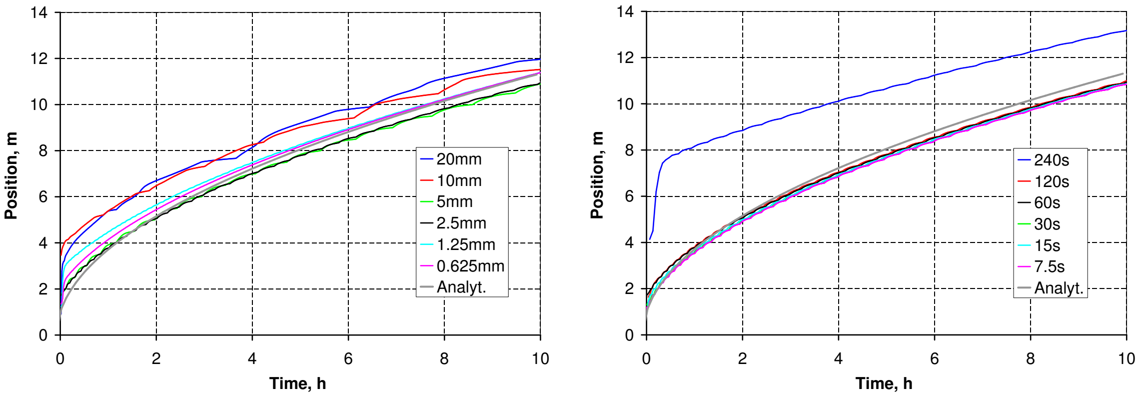

(b) (b)

Figure 3.12.: Verification of solidification calculations with a fixed grid: Comparison of the interface position for various grid element sizes (a) and various time steps (b) with the analytical solution.

Part II.

Model experiments

Chapter 4

Isothermal melt

This chapter describes model experiments with a low-melting-point liquid metal in a square container where a flow can be generated by a TMF in the same way as in a silicon melt. The low melting point allows direct flow measurements, which are not possible in silicon. Complementary use of experiments and simulations facilitates a precise validation of the numerical tools and also gives detailed insights into the flow structure, revealing several new important properties of TMF flows.

4.1. Experimental setup

The generation of a flow in a silicon melt by a TMF can be exactly reproduced also in low-melting-point liquid metals if the inductor and melt geometries are preserved and the dimensionless parameters are adjusted. However, a large liquid metal melt would lead to a complex and expensive setup, and correct scaling between small and large systems is, in general, limited as discussed in Sec. 2.4. Therefore, an existing small-scale TMF setup at the Institut für Nichteisen-Metallurgie und Reinststoffe (INEMET), TU Bergakademie Freiberg [Lantzsch et al., 2007] is used here, but it is extended with a square container instead of a cylindrical one.[1] This is the first step in the investigation of directional solidification of silicon using model experiments, and the transfer of the results is a part of the discussion.

The eutectic GaInSn alloy ($Ga^{68}In^{20}Sn^{12}$), which is liquid at room temperature, is used as a model fluid. The model experiments are carried out under isothermal conditions at about 20 °C. The relevant material properties of GaInSn are given in Tab. 4.1 in comparison to silicon; see also Appendix B. The melt container with a square horizontal inner cross-section ($10{\times}10$ cm^2) made of Plexiglas plates (with the thickness of 6 mm) is placed in the center of a coil system for the generation of the TMF as shown in Fig. 4.1. The coil system consists of 6 axisymmetric circular coils of 36 windings each with an inner radius of 15 cm, cross section of $3{\times}3$ cm^2, and a constant spacing of 9.1 cm between midpoints. The coils are fed by a sinusoidal current from a AC current supply *(EAAT)* with an amplitude in one winding $I_0 = 0 \ldots 16.3$ A, a frequency $f = 20 \ldots 800$ Hz, and a fixed phase shift between adjacent coils $\phi = 60°$. An upward or downward TMF with an induction amplitude B up to approximately

---

[1] The assembly of the new setup as well as the experimental measurements described later were carried out by Kathrin Niemietz, Jan Ehrig, and several technical assistants at INEMET under the supervision by Dr. Olf Pätzold. Several colleagues from Fraunhofer THM were involved in various electrical measurements.

3 mT can be generated. A detailed description of the TMF system can be found in [Lantzsch et al., 2007].

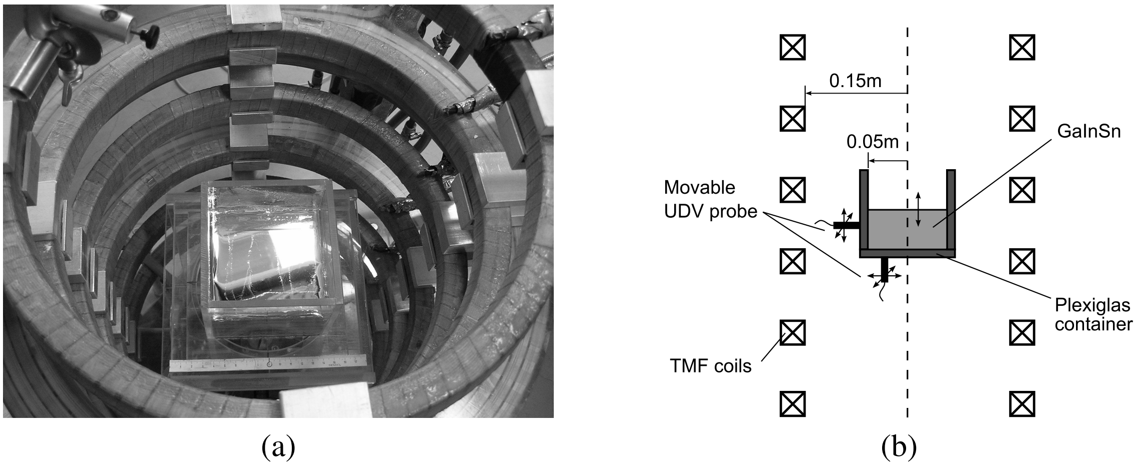

(a) (b)

Figure 4.1.: Experimental setup: (a) photo of TMF coil system and container filled with GaInSn; (b) sketch of the setup with a movable UDV probe. For further reference: the center of the coil system in the calculations is located at a vertical coordinate $z = 0.025$ m, the bottom of the melt is located at $z = 0$.

Property	Symb.	GaInSn	Silicon
Density, kg/m^3	ρ	6360	2520
Viscosity, Pa·s	η	$2.16 \cdot 10^{-3}$	$7.6 \cdot 10^{-4}$
El. conductivity, S/m	σ	$3.2 \cdot 10^{6}$	$1 \cdot 10^{6}$

Table 4.1.: Relevant material properties: GaInSn (at room temperature) [Lantzsch et al., 2007] in comparison with liquid silicon (near the melting point of 1685 K).

4.1.1. Current and magnetic field measurements

Numerical simulations of the Lorentz force induced by a TMF require exact values of the inductor current. The readings of the current supply were verified using additional current measurements in supply cables and directly at the TMF coils. Calibrated commercial Rogowski coils were applied as current sensors. Such a sensor consists of a toroidal coil with N windings, which is closed around the current. According to Maxwell's equation (2.12), integral of the magnetic field along any (!) closed path L_p around the current I_0 is proportional to the current:

$$\mu_0 I_0 = \oint\limits_{L_p} \vec{B}\, d\vec{l} \approx L_p \sum_{i=1}^{N} B_i, \tag{4.1}$$

where B_i is the magnetic field in the i-th winding of the coil if the path coincides with the centerline of the toroidal coil. The magnetic field induces a voltage U_i in each winding of the toroidal coil according to (2.8), the total voltage U is proportional to the current I_0:

$$U = \sum_{i=1}^{N} U_i \sim \sum_{i=1}^{N} B_i \approx \mu_0 I_0 / L_p. \tag{4.2}$$

Using this simple physical principle, we can measure the current independently of the exact position or shape of the Rogowski coil around the current. The Rogowski coils were connected to a digital 4-channel oscilloscope *TDS2024B (Tektronix)* for the analysis of possible deviations from an ideal sinusoidal signal and for the verification of phase shifts between the TMF coils.

The validation of electromagnetic calculations can be performed with magnetic field measurements. There is a variety of commercial magnetic field sensors available. In the current work, a commercial 3-channel Gaussmeter *Model 460 (LakeShore)* showing the effective (RMS) magnetic field measured by a 3-axis probe was used for a routine control of the magnetic field inside the TMF coils. Additionally, characterization of the time-dependent magnetic field was performed using a special Hall probe (developed at Fraunhofer THM) connected to a digital oscilloscope. Both sensors were re-calibrated using a simple circular coil with a radius R = 0.055 m and height H = 0.129 m, containing N = 230 windings. The magnetic field in the center of a short coil can be calculated analytically using the expression (see Sec. D.2.1)

$$B_z = \frac{\mu_0 N I_0}{\sqrt{H^2 + 4R^2}}, \tag{4.3}$$

where the current I_0 was precisely measured with a multimeter. This allowed to correct the commercial Gaussmeter with $+3\%$ and the in-house sensor with -6% at a magnetic field induction of about 2 mT [ExpTHMelectric, 2010].

4.1.2. Velocity measurements

There are several methods for measuring flow velocities in opaque liquid metals; see, e.g., the review [Eckert et al., 2007]. However, only two of them are non-invasive methods that are able to capture complex flow structures: contact-less inductive flow tomography (CIFT) and ultrasonic Doppler velocimetry (UDV). Both methods seem to have a potential to be applied to high-temperature liquid silicon flows in the future. The conventional UDV can be used up to about 200 °C. Measurements up to 750 °C have been demonstrated but usually require different sensor materials or acoustic waveguides [Eckert et al., 2007]. From CIFT and UDV, only UDV is available commercially, and it is applied in the current work.

The basic principles of UDV are described in [SignalProcessingUDV, 2011] on a popular level; see also [Cramer et al., 2004a] and references therein. A special probe containing a piezoelectric ultrasonic transducer and receiver is acoustically contacted with the fluid. It emits bursts or pulses of ultrasound that are reflected back by moving particles (e.g., originating from the oxide layer at the contact surface between GaInSn and air) in the fluid and detected by the receiver. If the speed of ultrasound in the fluid is known, the distance between the particles and the probe can be calculated from the time delay between the burst and the echo. By analyzing the shift in the distribution pattern between several successive bursts and echoes, the velocity of the particles distributed along the ultrasound beam can be calculated. Note that the word *Doppler* in the name of the method is rather misleading because the Doppler effect (frequency change due to the relative movement of a wave source and an observer) is not involved here. The main physical limitation of this technique restricts the maximum velocity u_{max} and the measurement depth d_{max} [DOP2000Manual, 2006]:

$$u_{max} = \frac{c_u}{4T_{\mathrm{prf}} f_e}, \quad d_{max} = \frac{T_{\mathrm{prf}} c_u}{2}, \tag{4.4}$$

where c_u is the speed of ultrasound in the fluid, T_{prf} is the time interval between two ultrasound pulses, and f_e is the emitting ultrasound frequency. With f_e of 8 MHz, c_u in GaInSn of 2750 m/s, and T_{prf} in the range 64 $\mu s \ldots 0.1$ s, we obtain a maximum velocity range of 1.3 m/s…0.9 mm/s and a maximum depth range of 9 cm…138 m. Furthermore, the velocity resolution with a fixed maximum amount of 256 discrete values leads to an error $\Delta u = u_{max}/256$, which is obviously related to the temporal resolution. To measure velocities up to 1 cm/s, the value of T_{prf} according to (4.4) must be about 9 ms, which corresponds to a sampling frequency of 116 Hz. A smaller value of T_{prf} would increase not only the maximum velocity u_{max} but also the velocity error Δu. Of course, there are also several practical and technical difficulties of UDV measurements as discussed in the following sections.

In the current work, the commercial UDV measurement system *DOP2000 (Signal Processing SA)* was used. It is equipped with an 8 MHz ultrasound transducer probe *TR0805LS (Signal Processing SA)* and provides the profile of the velocity component parallel to the normal direction of the probe face. Negative (positive) velocities indicate melt flow towards (away from) the transducer. The UDV probe was mounted at different positions on the bottom wall or the sidewalls of the container as shown in Fig. 4.1 (b) to detect vertical and horizontal velocity profiles, respectively. The measurements were performed through the Plexiglas walls, without a direct contact between the probe and the melt.

4.2. Magnetic field and Lorentz force

4.2.1. Magnetic field validation

Results of the measured current amplitudes in TMF coils are given in Fig. 4.2, which contains also the corresponding time-dependencies. The measured amplitudes can be compared with the readings of the generator, I_{eff}, according to the formula

$$I_{0N} = \frac{\sqrt{2}}{\sqrt{3}} N I_{\mathrm{eff}} = 0.816 \cdot N I_{\mathrm{eff}}, \tag{4.5}$$

where N = 36 is the number of windings in a single TMF coil, the factor $\sqrt{2}$ appears due to conversion from effective values to amplitudes, the factor $\sqrt{3}$ appears due to the connection between 6 TMF coils and 3 generator phases. It can be seen that the measured current amplitudes can be up to 14% higher than the values calculated from the generator readings. Furthermore, the time-dependent current shows high-frequency oscillations with an amplitude up to 7%, and there are differences between different TMF coils up to 6%. Consequently, generator readings can be used for the characterization of the experiments with an uncertainty in the current amplitude of about 10%. For a higher precision, current measurements in each TMF coil would be required on a routine basis.

Magnetic field measurements were performed on several vertical lines of the coil system. A comparison with 3D calculations is shown in Fig. 4.3. The agreement is not better than approximately 10%, which can be caused by inaccuracies in current readings as well as deviations in the coil geometry from the numerical model. For example, the presence of current supplies, ferromagnetic screws at the outside, or additional DC coils is not considered in the model. In the experiment, DC coils were disconnected to interrupt the current loop but not disassembled. A closed DC loop may decrease the TMF amplitude by about 35% [Lantzsch, 2009], but this effect does not occur if the loop is open.

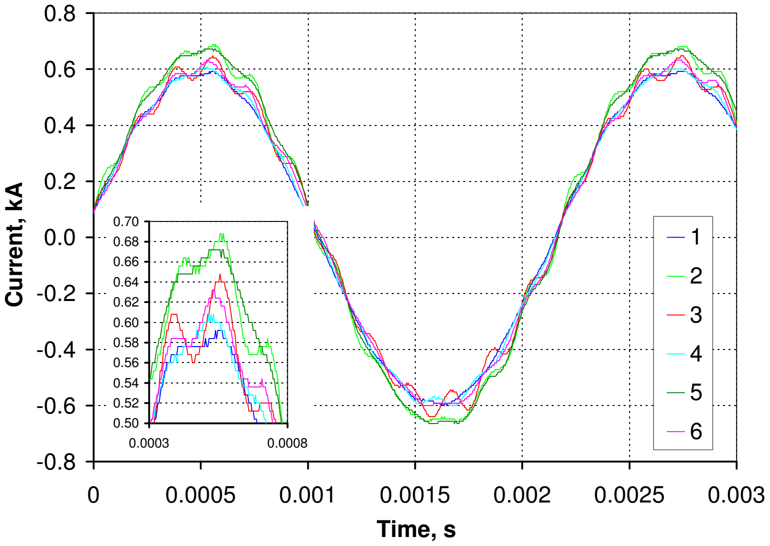

(a)

Coil	I_{0N}, A
1	597
2	670
3	610
4	600
5	672
6	610

(b)

Figure 4.2.: Current measurements with Rogowski coils: (a) time-dependence of the current in the TMF coils 1 (top)...6 (bottom); (b) calculated current amplitude (from the integral effective value). The built-in current sensor showed $I_{\mathrm{eff}} = 20$ A, which allows to estimate the current amplitude as $I_{0N} = 587$ A in all coils. [ExpTHMelectric, 2010]

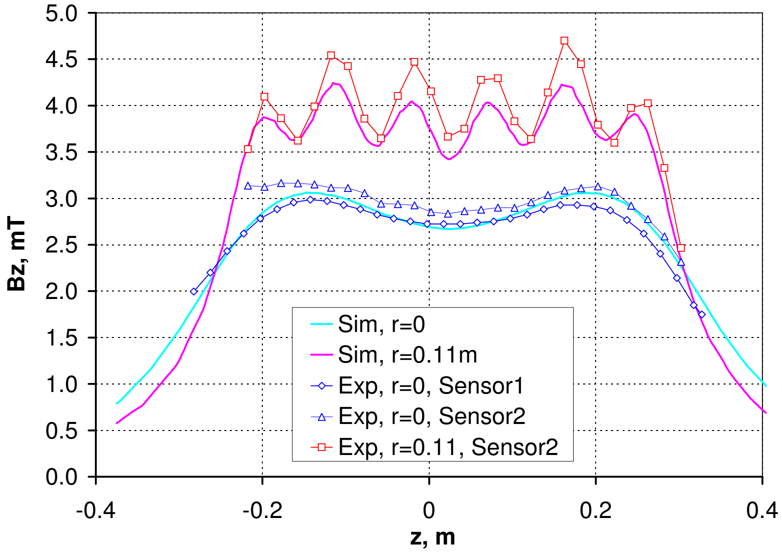

Figure 4.3.: Comparison of measured (Exp) and calculated (Sim) vertical magnetic field components on the axis of the coil system (coil system center at $r = 0$, $z = 0.025$ m) and near the coils ($r = 0.11$ m) without the melt for $I_{\mathrm{eff}} = 20$ A. Results from a commercial Gaussmeter (Sensor1) and an in-house system (Sensor2) after recalibration are shown. The calculation is carried out in 3D as described in the next section. [ExpTHMelectric, 2010; ExpINEMET, 2010]

4.2.2. Lorentz force calculations

For the TMF parameter range considered in the current study, analytical solutions for a TMF force with a neglected skin effect often used in literature are not valid and 3D calculations due to the square shape of the melt are necessary. The mesh for the melt, coils, and the surrounding air was generated by `Gmsh`, and the electromagnetic calculations were carried out using `GetDP`.

The melt height for the reference case was set to 5 cm giving an aspect ratio $H/L = 0.5$ (melt height H to side length L of the container). The TMF parameters were set to obtain the maximum possible Lorentz force density considering the generator limits: frequency $f = 450$ Hz and current amplitude coil $I_0 = 16.3$ A per winding. Fig. 4.4 shows the 3D geometry and grid used for Lorentz force calculation as well as the calculated Lorentz force distribution. It can be seen that the force is present only in the skin layer near the container wall with a thickness of about 1.3 cm as it can be estimated by $\sqrt{\pi\mu_0\sigma f}$. For a proper resolution, the grid element size was set to 1 mm and 5 mm at the sidewalls and in the bulk, respectively. The horizontal force component is relatively large. The force density is smaller in the corners of the melt despite the obviously smaller distance to the coils because of the resulting eddy current distribution in the horizontal cross-section. The maximum Lorentz force density at 16.3 A reaches 664 N/m^3.

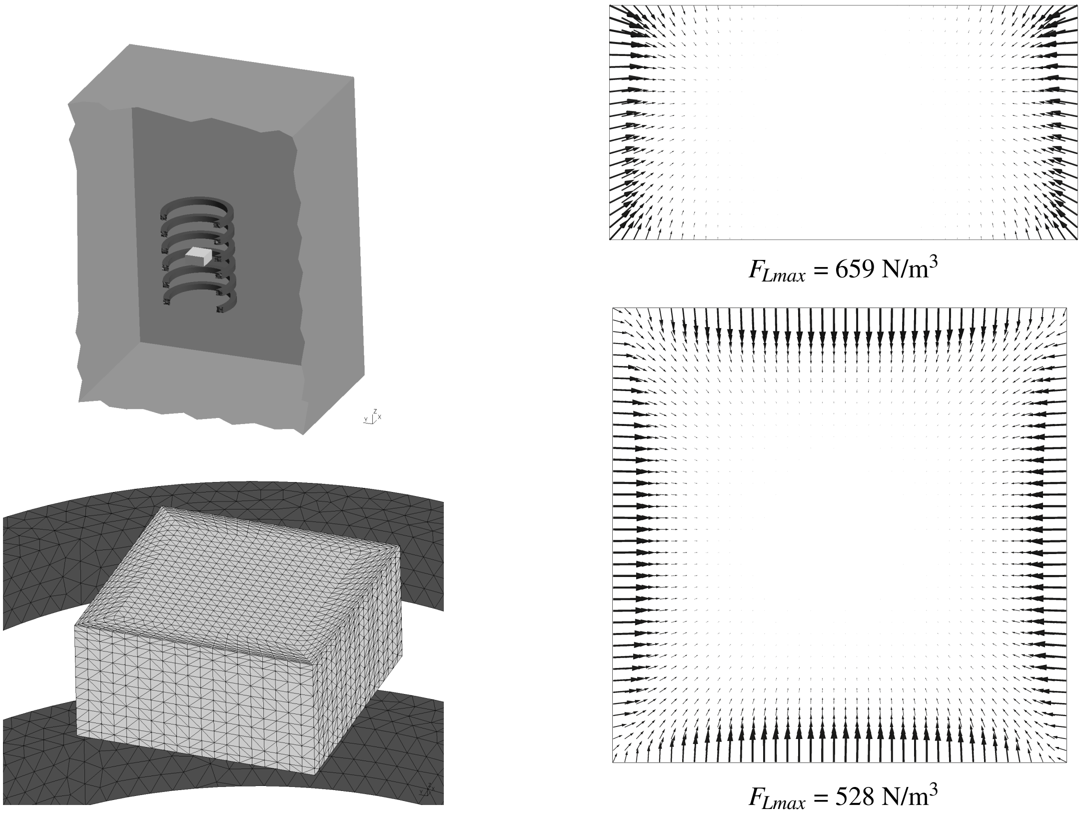

(a) (b)

Figure 4.4.: Reference case with $H = 5$ cm, $I_0 = 16.3$ A, $f = 450$ Hz, TMF up: (a) Geometry (melt, clipped coil volumes and outer boundary) and grid (401602 tetrahedrons; air volume elements not shown here) for Lorentz force calculations; (b) Lorentz force density distribution (maximum in melt – 664 N/m^3) in a horizontal (below) and vertical (above) cut through the melt center perpendicular to the side wall.

The role of melt corners for the Lorentz force distribution can be determined by comparing the Lorentz forces in a cylindrical and a square melt placed in an identical external magnetic field. Fig. 4.5 shows the Lorentz force in a vertical cut for a cylindrical melt and further variations of the square melt geometry: smaller and larger melt height and shifted melt axis. It can be seen that the maximum Lorentz force density significantly increases at the melt height of 2.5 cm. A local increase can be also achieved by an asymmetric placement of the melt. The corresponding melt flows are investigated in the following sections.

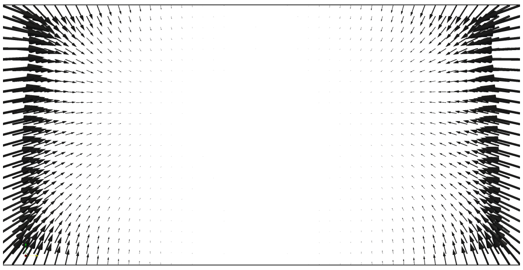

F_{Lmax} = 459 N/m^3

(a) H = 5 cm, cylinder

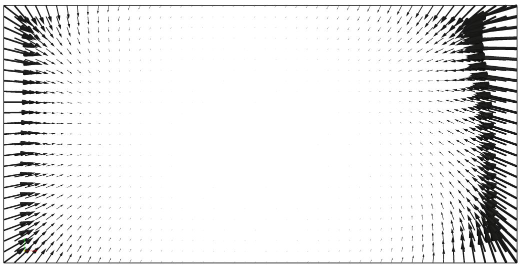

F_{Lmax} = 959 N/m^3

(b) H = 5 cm, shifted

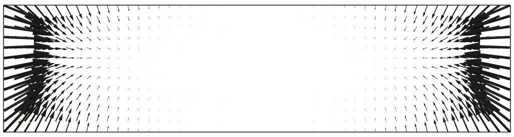

F_{Lmax} = 810 N/m^3

(c) H = 2.5 cm

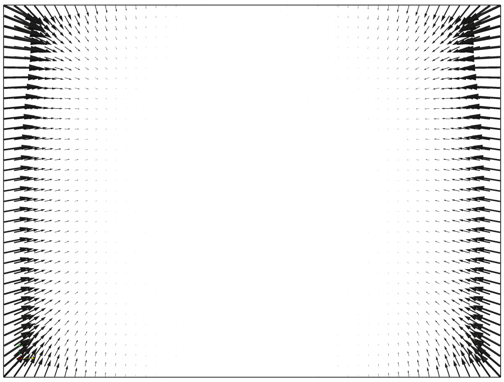

F_{Lmax} = 645 N/m^3

(d) H = 7.5 cm

Figure 4.5.: Calculated Lorentz force distribution in a vertical cut through the melt center perpendicular to the side wall. Cases with f = 450 Hz, I_0 = 16.3 A, TMF up: (a) H = 5 cm, but with a cylindrical form with $R = H$; (b) H = 5 cm, but with the melt shifted 4 cm from the axis (in the plane showed here); (c) H = 2.5 cm; (d) H = 7.5 cm.

4.3. Fluid flow

The Lorentz force computed with `GetDP` was used for further calculations of the melt flow using `OpenFOAM`. Only the melt domain was considered, typically located with the bottom at $z = 0$ (see Fig. 4.4). The no-slip condition for the velocity was considered on all melt surfaces in contact to the container wall. As GaInSn is effectively oxidized under ambient conditions, no-slip was assumed for the top surface, too.

4.3.1. Reference case

The calculated time-averaged 3D flow pattern is depicted in Fig. 4.6 (a) using 3D streamlines and velocity vectors in a vertical cut. The typical toroidal flow structure already known from cylindrical melts [Gelfgat et al., 1999] is observed, with some extension into the melt corners. Fig. 4.6 (b) gives a comparison of the calculated and measured vertical distribution of the vertical velocity component in the center, at the rim, and in the corner of the melt. Numerical and experimental results are averaged over 200 s and at least 600 s, respectively, ensuring stable time-averaged velocity profiles.

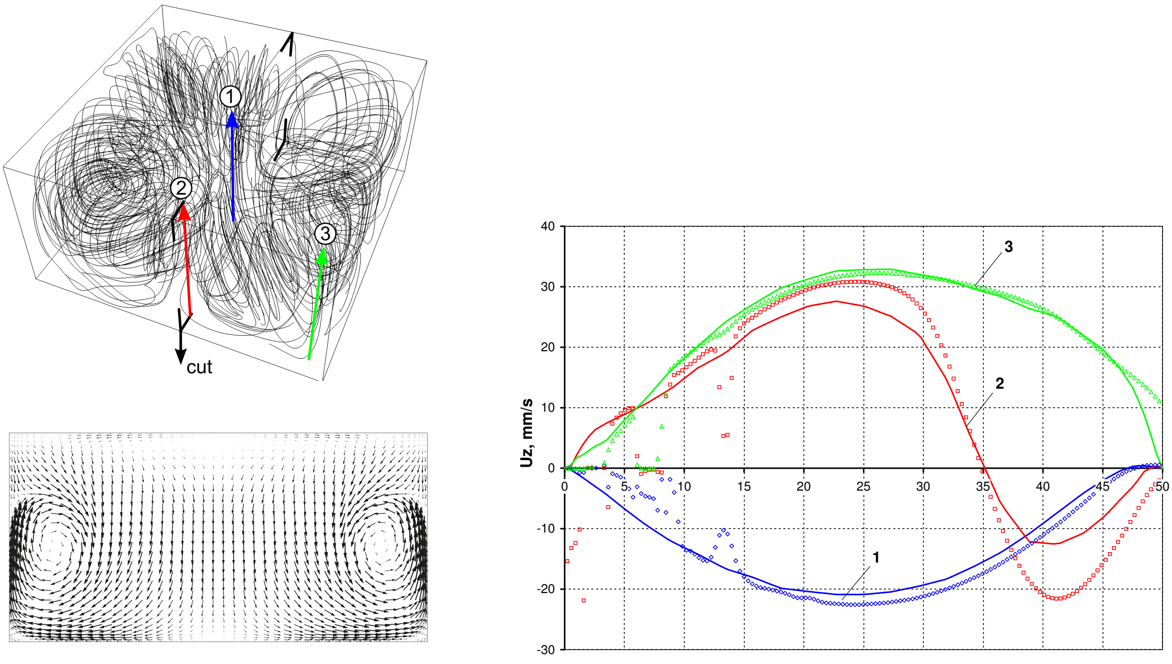

u_{max} = 4.3 cm/s

(a)

(b)

Figure 4.6.: Reference case with H = 5 cm, I_0 = 16.3 A, f = 450 Hz, TMF up: (a) calculated time-averaged 3D streamlines and velocity vectors (maximum in melt – 4.6 cm/s) in a vertical cut through the melt center perpendicular to the side wall; (b) comparison of calculated (lines) and measured (symbols) time-averaged vertical velocity profiles (1: melt center, 2: 5 mm from side wall, 3: 5 mm from both side walls in the corner). [ExpINEMET, 2010]

Calculated and measured velocity profiles in Fig. 4.6 (b) show a good qualitative agreement. The spurious scattering of experimental values detected in the near-wall regions can be mainly attributed to resonance effects when measuring through the container walls. The offset between the experimental and numerical profiles near the container side walls can be attributed to ultrasound reflections from the wall and some spreading of the beam over the horizontally inhomogeneous velocity distribution in the boundary region [Messer and Aidun, 2009]. The deviations in the velocity magnitude may be related to changing slip conditions at melt surfaces due to incomplete and/or time-varying oxidation and wetting conditions. Measurements for the reference case were carried out with an additional Plexiglas plate on the top of the melt, however, its influence on the velocity profiles was not significant. The overall experimental accuracy can be estimated as not better than 10% on the basis of a series of velocity measurements under identical conditions.

4.3.2. Influence of numerical parameters and turbulence

Possible uncertainties in the simulation can be detected by varying relevant numerical parameters. The influence of the grid size, velocity interpolation scheme, and time discretization

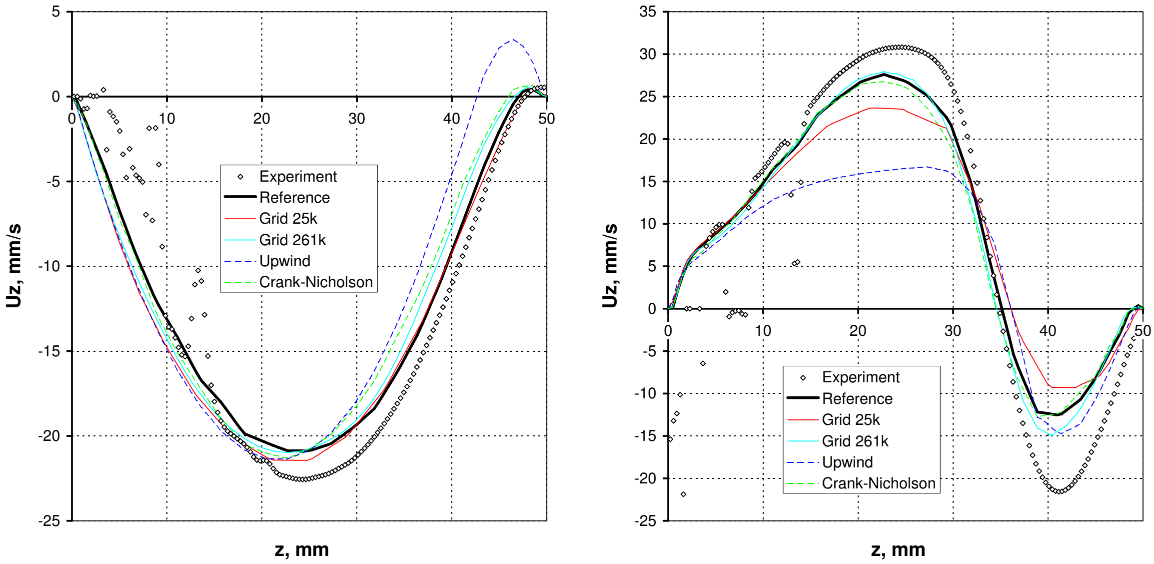

(a) In melt center (b) At side wall

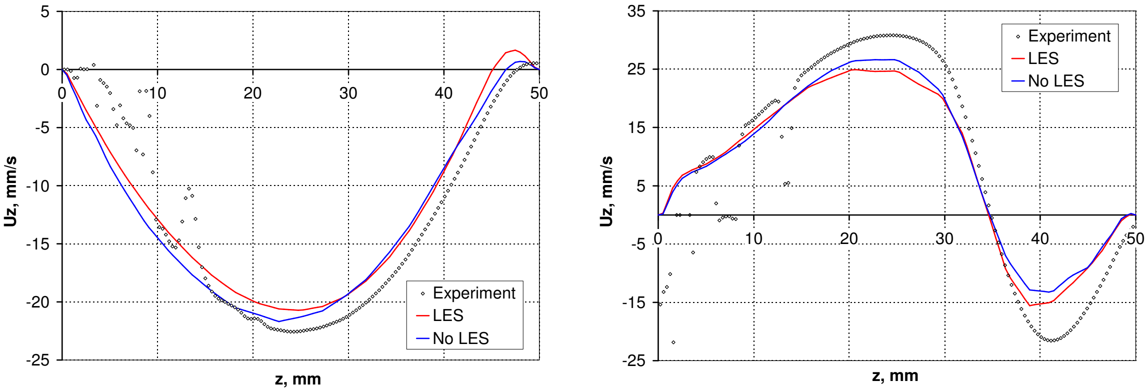

(c) In melt center (d) At side wall

Figure 4.7.: Influence of numerical parameters on the time-averaged velocity profile in the melt center (a,c) and 5 mm from the side wall (b,d) from Fig. 4.6 (b): 25400, 80600 (reference), and 261000 grid cells corresponding to a bulk element size of 4.3 mm, 2.5 mm, and 1.5 mm, respectively (smallest element at the wall: 0.2 mm for the reference case; scaled proportionally to the bulk size); time discretization with Euler (reference) and Crank-Nicholson scheme; velocity interpolation with linear (reference) and upwind scheme; without turbulence modeling or with a Smagorinsky LES model with van Driest damping. [ExpINEMET, 2010]

scheme on the time-averaged velocity profile is shown in Fig. 4.7 (a,b). An upwind scheme leads to a larger deviation from experiments, which could be explained by the additional numerical diffusion. A rough grid introduces a larger error at the side wall due to the limited resolution of the boundary layer. The more accurate Crank-Nicolson time scheme and the finest grid lead to rather small deviations from the reference case; some part of the deviations might be related to the limited averaging time and the highly unsteady flow.

It can be concluded that for the present system, calculations without explicit turbulence models lead to a reasonable agreement with experiments. In the literature, very often turbulence models are employed for similar systems with a TMF, such as the k-omega-SST model

[Dropka et al., 2010; Niemietz et al., 2011] or various LES models [Krauze et al., 2010]. Therefore, we also performed LES calculations for the reference case. Fig. 4.7 (c,d) compares the vertical velocity profiles. Because of some slight differences between `OpenFOAM` solvers, the calculations were carried out with the same solver, with the LES model switched on or off to obtain an exact comparison. It can be seen that for the reference case, there are practically no differences between the calculations with and without a LES model.

Fig. 4.8 depicts the distribution of the turbulence viscosity in the LES calculation for the reference case as well as for a smaller inductor current. With both inductor currents, it is 2 to 7 times higher than the molecular kinematic viscosity of $3 \cdot 10^{-7}$ m^2/s. However, this is not necessarily an indication of a large influence of the turbulent viscosity on the flow. It is possible that other terms in the equations motion are still significantly larger that the viscous term. The `OpenFOAM` solver was modified to calculate the time-average value of the various terms in the momentum equation (2.38). Their distributions are given in Fig. 4.9. Indeed, the viscous term is about 100 times smaller than the convective term in most parts of the melt, and it is relevant mainly in a thin skin-layer at the no-slip walls.

The simplest explanation for the nearly negligible role of the turbulence model (NOT: of the role of turbulence) could be the fact that every time-dependent three-dimensional direct flow calculation is capable of capturing basic turbulent flow properties to some extent. Of course, the contents of such a statement depends on exact definitions of the turbulence and the turbulent melt state. A simple method is to define the oscillating part of the velocity, i.e., the corresponding kinetic energy as the turbulent energy. This can be compared with the kinetic energy related to the steady part of the flow in a time-average sense. The following expressions were used in `OpenFOAM` to evaluate the mean and turbulent part of the integral kinetic energy from the velocity field $\vec{u}(x,y,z)$:

$$\bar{E}_{kinmean} = \frac{1}{2} \int\limits_V \left(\bar{\vec{u}} \cdot \bar{\vec{u}} \right) dV, \tag{4.6}$$

$$\bar{E}_{kinturb} = \frac{1}{2} \int\limits_V \left(\overline{u_x'^2} + \overline{u_y'^2} + \overline{u_z'^2} \right) dV = \frac{1}{2} \int\limits_V \left(\left| \overline{u_x^2} - \overline{u_x}^2 \right| + \left| \overline{u_y^2} - \overline{u_y}^2 \right| + \left| \overline{u_z^2} - \overline{u_z}^2 \right| \right) dV, \tag{4.7}$$

where a bar denotes time-average values over all time steps in the considered time interval. The kinetic energy for the reference case is plotted in dependence of time in Fig. 4.10. It can be seen that the turbulent part reaches about 25% from the total kinetic energy. While the reference grid size has a relatively small influence on the mean kinetic energy, a finer grid increases the turbulent kinetic energy by approximately 10%.

To sum up, we were able to show that a definite part of the turbulence can be modeled by a straightforward time-dependent three-dimensional simulation. The addition of a turbulence model such as LES does not lead to significant changes in the calculated velocity field; therefore, there is no obvious reason for the use of a turbulence model in our case. Of course, the decisive question is what are the limitations of this approach: for what types of flows and up to which velocities it can be applied. Probably, there is no general answer. These limits would probably depend also on the exact details of numerical algorithms such as the discretization schemes. Therefore, the only reliable method is to perform a grid-independence test *of the calculation results of interest.* It is possible that various flow characteristics, such as time-average velocity, fluctuation amplitude, velocity gradients, have various requirements regarding the mesh resolution. Only if the required mesh size becomes too large, it is worthwhile to consider the use of turbulence models. However, such models

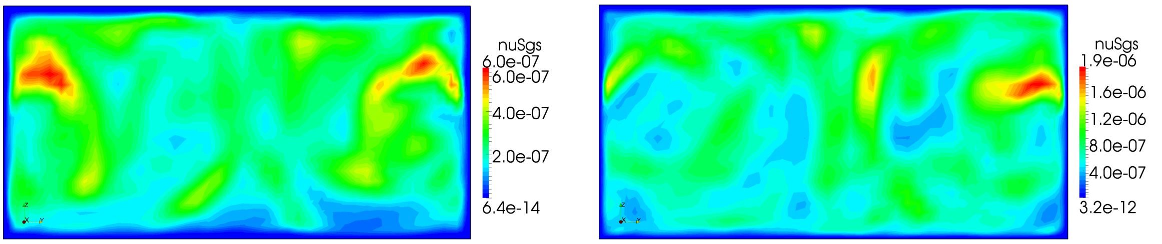

(a) I_0 = 6.5 A (b) I_0 = 16.3 A

Figure 4.8.: Case with H = 5 cm, f = 450 Hz, TMF up. Turbulent kinematic viscosity [m^2/s] distribution in LES calculations in a vertical cut through the melt center perpendicular to the side wall after 300 s for I_0 = 6.5 A (a) and I_0 = 16.3 A (b).

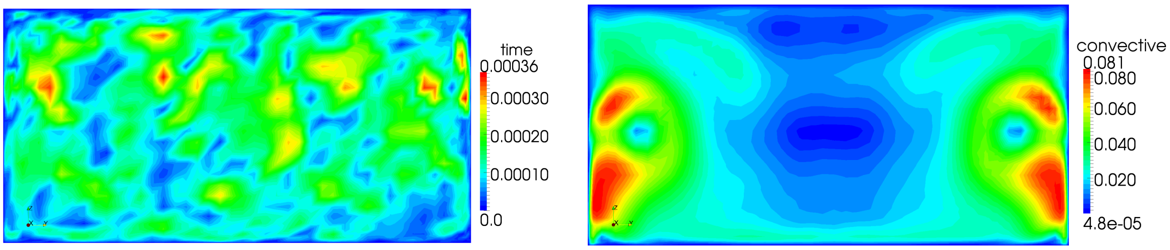

(a) Unsteady term (b) Convective term

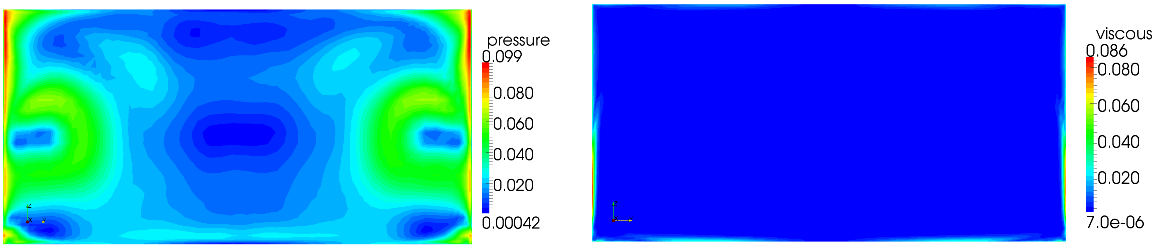

(c) Pressure term (d) Viscous term

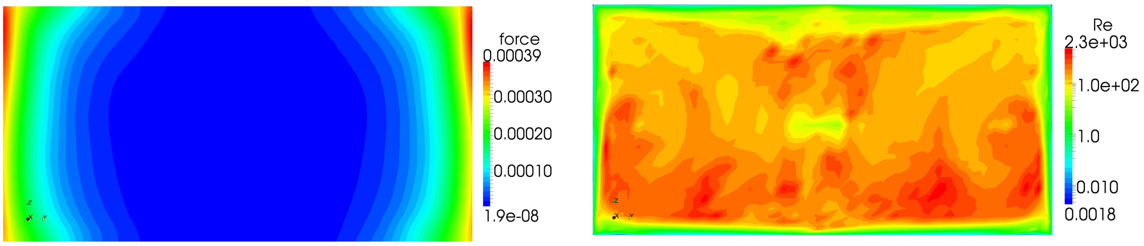

(e) Lorentz force term (f) Convective/viscous term

Figure 4.9.: Reference case with H = 5 cm, I_0 = 16.3 A, f = 450 Hz, TMF up. Time-average (100...300 s) distributions of terms in the momentum equation (2.38) given in [m/s^2] in a vertical cut through the melt center perpendicular to the side wall: unsteady (a), convective (b), pressure (c), viscous (d), and Lorentz force (e) terms, as well as the ratio between the convective and viscous terms, which defines the Reynolds number, in a logarithmic color scale (f).

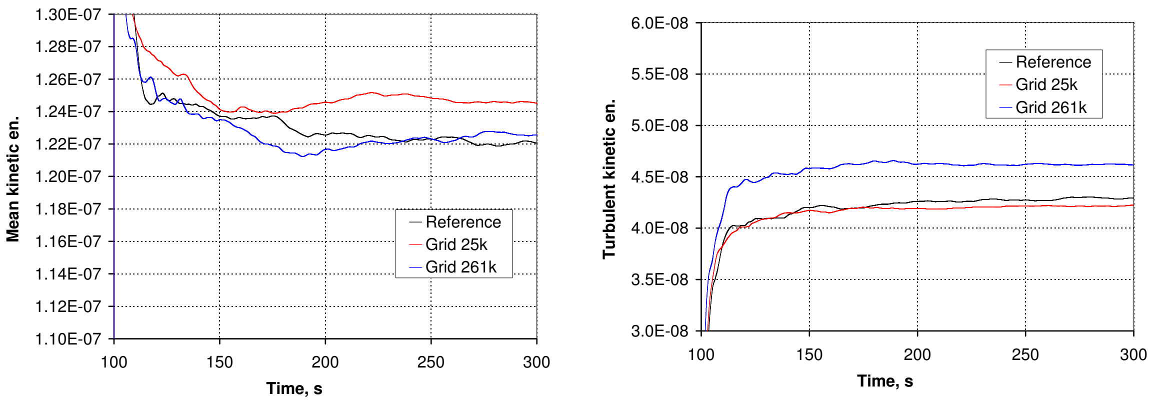

(a) (b)

Figure 4.10.: Reference case with H = 5 cm, I_0 = 16.3 A, f = 450 Hz, TMF up. Integral mean (a) and turbulent (b) kinetic energy in [$\text{m}^3 \cdot \text{m}^2/\text{s}^2$] for different grid sizes (cf. Fig. 4.7).

have to be validated for the specific case because there is no single optimal turbulence model for all flows.

4.3.3. Influence of current amplitude

The current amplitude in the coils is probably the simplest way of setting the Lorentz force level in the melt. Most experiments in the present work were performed for at least 6 different coil currents to check the reproducibility of the measured time-averaged velocity profiles. The sequential experimental profiles for the reference case configuration are shown in Fig. 4.11 (a). With a decreasing current amplitude, the characteristic flow velocity becomes smaller, while the toroidal flow pattern is essentially preserved. The maximum time-average velocity in the melt center at z = 25 mm is plotted as a function of the inductor current I_0 in Fig. 4.11 (b). An approximately linear dependence is found in both simulations and experiments.

The comparison of the time-dependence of the velocity in the melt center is given in Fig. 4.12 (a). Qualitative agreement between simulations and experiments can be seen. The time step in the simulation was adjusted according to the Courant criterion leading to approximately 0.01 s for the case with 16.3 A. First evaluation of the velocity oscillations spectra showed that the usual Fast Fourier Transform is not sufficient to filter out the noise and make reliable comparisons between numerical and experimental results. Instead, special algorithms as described, e.g., by Krauze et al. [2010] are required for a detailed analysis of velocity oscillations.

Fig. 4.12 (b) shows the standard deviation of velocity (vertical component) oscillations around the mean value at a monitor point in the melt center for different inductor currents. It can be seen that the oscillations start already at about 3.3 A and then increase linearly with the current amplitude. Because the mean velocity behaves similarly, the ratio of the standard deviation to the mean value remains approximately constant at about 30% between 3.3 A and 16.3 A.

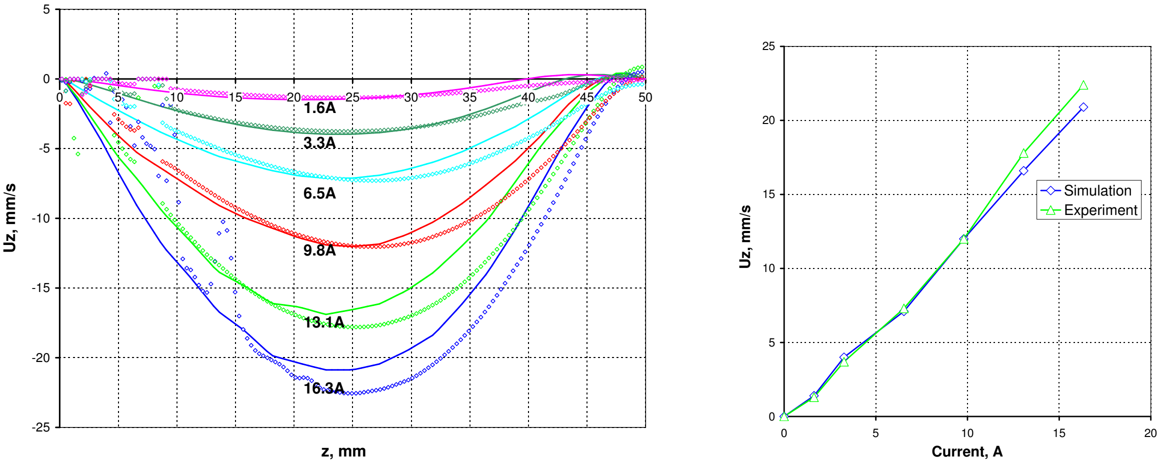

(a) (b)

Figure 4.11.: Reference case configuration (cf. Fig. 4.6 (b)) with different inductor currents: (a) calculated (lines) and measured (symbols) time-averaged vertical velocity profiles in the melt center; (b) magnitude of time-averaged vertical velocity in the melt center at $z = 25$ mm. [ExpINEMET, 2010]

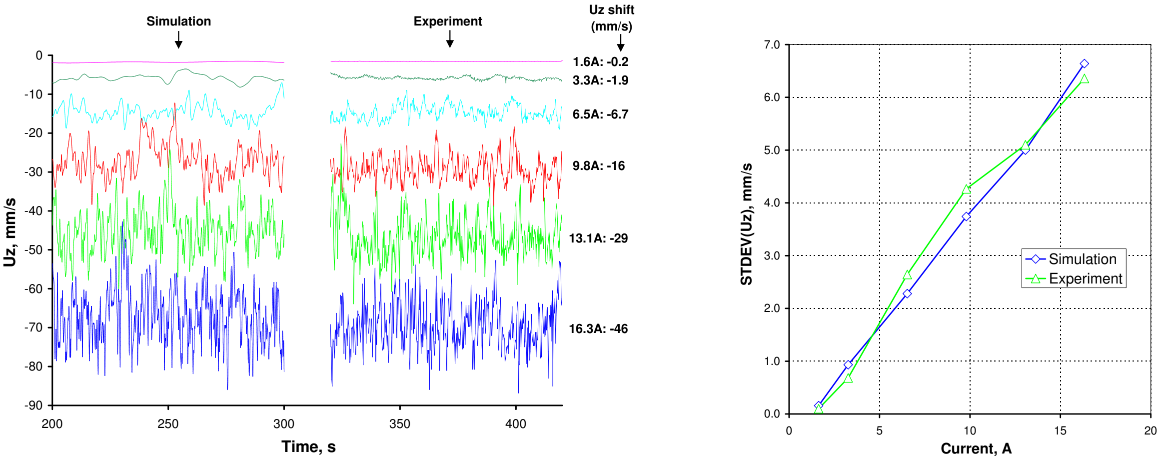

(a) (b)

Figure 4.12.: Reference case configuration (cf. Fig. 4.6 (b)) with different inductor currents: (a) fragments of vertical velocity oscillations (resolution of about 5 Hz in the experiment) exactly in the melt center (profiles are vertically shifted by an interval indicated at the right side of the figure (Uz shift) to avoid overlapping); (b) the corresponding standard deviation for the usual averaging time intervals. [ExpINEMET, 2010]

4.3.4. Influence of melt axis shift

Results of simulations and experiments in the previous section indicate that the toroidal flow structure is preserved over a wide range of inductor currents also for a square melt. Changes in the flow pattern can be expected if the melt or TMF geometries are significantly altered. The effect of shifting a cylindrical melt from the axis of the TMF coil system has been recently addressed by Cramer et al. [2011], where a significant influence of shifts of even less than 2% of the melt diameter was observed. In the current study, the melt was shifted horizontally by 4 cm perpendicular to one of the side surfaces. The resulting Lorentz forces calculated at the centers of the corresponding opposite sidewalls were 684 N/m^3 and 475 N/m^3 for the container wall closer and farther from the coils, respectively. The maximum Lorentz force in the melt was 980 N/m^3. Since the magnetic field falls off with the inverse distance from the inductor, the Lorentz force has a steep quadratic dependence of the inductor–melt distance.

The calculated flow streamlines and velocity vectors are shown in Fig. 4.13 (a). It can be seen that the axial flow symmetry is broken and that the toroidal flow pattern is preserved only along three melt sides, forming a kind of incomplete, open torus that ends at the fourth side. Measurements of the vertical velocity profiles were performed at two sidewalls and in the melt center. A comparison of numerical and experimental results is given in Fig. 4.13 (b). A better agreement between the calculated and measured profiles at the sidewalls can be achieved with a spatial averaging of the simulation results over the horizontal extension of the UDV probe (note also the large velocity gradients at the wall in Fig. 4.13 (a)).

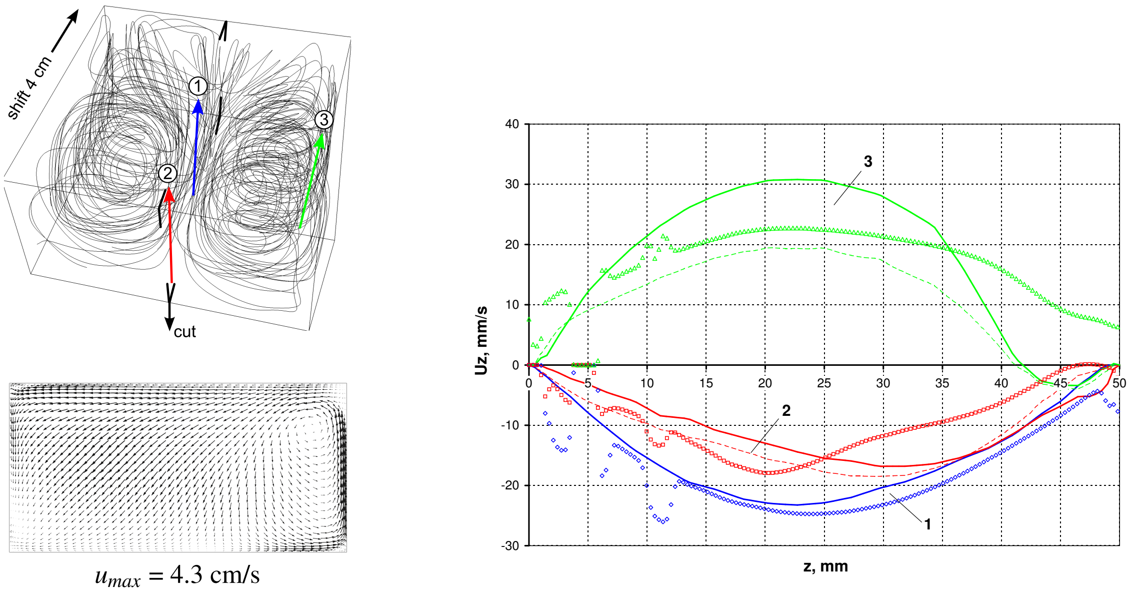

(a) (b)

Figure 4.13.: System with the melt shifted 4 cm from coil system axis, H = 5 cm, I_0 = 16.3 A, f = 450 Hz, TMF up: (a) calculated time-averaged 3D streamlines and velocity vectors (maximum in melt – 5.0 cm/s) in a vertical cut through the melt center containing profiles 1 and 2; (b) comparison of calculated (solid lines – without spatial averaging, dashed lines – with spatial averaging over a horizontal region of 5×5 mm^2 with 5 points) and measured (symbols) time-averaged vertical velocity profiles (1: melt center, 2: 9 mm from the sidewall far from coils, 3: 9 mm from the sidewall at standard distance to coils). [ExpINEMET, 2010]

4.3.5. Influence of melt height

To investigate a possible influence of the melt height on the flow, experiments and simulations with the container in the central position were performed also for melt heights of 2.5 cm (H/L = 0.25) and 7.5 cm (H/L = 0.75). While no significant differences in the toroidal flow structure were observed between 5 cm and 7.5 cm, the smaller melt height of 2.5 cm caused drastic changes of the time-averaged flow pattern. The results of numerical calculations in

Fig. 4.14 (a) give clear evidence that a distinct horizontal vortex dominates in the central part. The ordinary TMF torus is constrained at the rim of the melt and obtains a distinct helical component. The existence of the central vortex is experimentally confirmed by horizontal velocity profiles measured from the sidewall 1 cm below the melt surface at different lateral positions, i.e., the center of the sidewall and 1 cm to the left/right; see Fig. 4.14 (b). Experimental as well as numerical profiles through the center reveal an extended range of very low lateral velocities, which just represents the “eye” of the central vortex.

It should be noted that also the Lorentz force shows a dependence of the melt height at a constant inductor current. The maximum force densities with melt heights of 7.5 cm and 2.5 cm were 657 N/m^3 and 817 N/m^3, respectively.

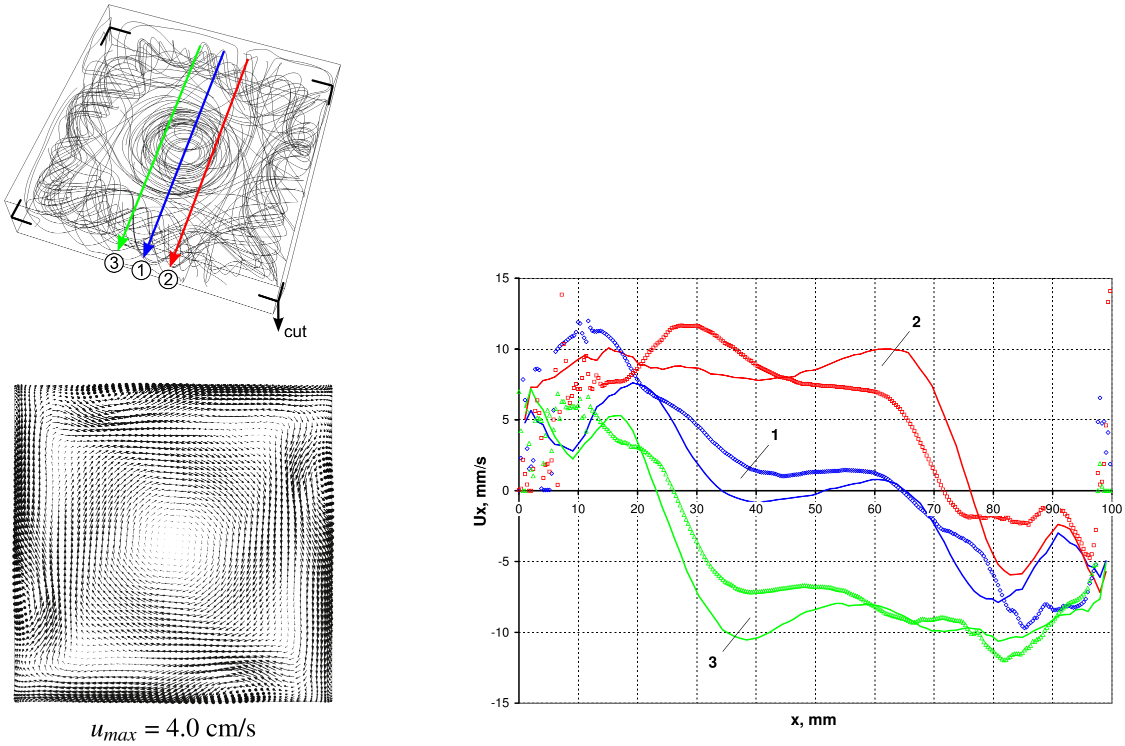

u_{max} = 4.0 cm/s

(a)

(b)

Figure 4.14.: System with H = 2.5 cm, I_0 = 16.3 A, f = 450 Hz, TMF up: (a) calculated time-averaged 3D streamlines and velocity vectors (maximum in melt – 4.0 cm/s) in a horizontal cut through the melt center; (b) comparison of calculated (lines) and measured (dense symbols) time-averaged horizontal velocity profiles 1 cm below the melt surface (1: wall center, 2: 1 cm to the left, 3: 1 cm to the right). [ExpINEMET, 2010]

To determine the inductor and geometrical parameters influencing the appearance of this new flow pattern, several additional studies were performed. The results can be summarized as follows:

1. No net Lorentz force component was found to act in the azimuthal direction.

2. Under a downward TMF, experiments indicated an opposite rotation of the central vortex than with an upward TMF, whereas the rotation direction in numerical simulations depended only on initial velocity conditions (perturbed in a definite rotation direction).

3. Simulations showed that, when started from a zero velocity field, the rotation direction fluctuated for the first 30 s, whereas a dominating rotation direction appeared afterward.

4. With an inductor current of I_0 = 1.6 A resulting in a stationary melt flow, the central vortex was still present in the simulation, but it was less distinct. A different flow pattern with a smaller inner torus developed if the flow viscosity was increased by a factor of 2.

5. Simulation with similar Lorentz force densities in a cylindrical melt with the same diameter showed no central vortex.

A similar flow pattern has been shown by Dropka et al. [2010], but without further discussion. Swirl accumulation due to a superposition of traveling and rotating magnetic fields has been investigated by Grants et al. [2008, 2009b], therein referred to as the “liquid metal tornado”. However, the effect observed in the current study is substantially different because no force is acting in the azimuthal direction.

Regarding the mechanism of the appearance of the central vortex at small melt heights, the importance of the square shape clearly hints to a relation with the 3D flow structure in the melt corners. The importance of an unsteady flow and the random character of the rotation direction may hint to a flow instability. These conclusions let us propose the following explanation.

At small melt aspect ratios, the typical TMF torus is more concentrated at the rim. As a consequence, the flow in the central melt part becomes less defined through the TMF forces directly. Comparison of the torus shape in round and square melts obviously shows upward streamlines converging at the top surface in the corners of the square melt. Deviations from the diagonal direction may appear at the melt top, especially for high and fluctuating flow velocities. If these deviations in different corners point at some time in the same direction, an azimuthal rotation may be initiated. As a result, a spontaneous swirl generation in a converging flow with a small aspect ratio can be observed.

4.4. Discussion

4.4.1. Scaling

As discussed in Sec. 2.4, an isothermal melt in a TMF can be described by three dimensionless parameters – the Reynolds number, the TMF forcing parameter, and the shielding parameter:

$$Re = \frac{\rho u_0 L_0}{\eta}, \quad F_{em} = F_{L0}\frac{\rho L_0^3}{\eta^2}, \quad S_{em} = 2\pi f \sigma \mu_0 L_0^2. \tag{4.8}$$

Let us consider a simple example of transferring the results from the current study to the research scale (Gen1) and industrial scale (Gen5) silicon melts. Complete geometrical similarity of TMF inductors and the melt is assumed. By choosing the characteristic, i.e., maximum values for the force density F_{L0} and velocity u_0 from the reference case in Sec. 4.3.1 and by setting $L_0 = L/2$, we can calculate the dimensionless numbers as $Re = 7 \cdot 10^3$, $F_{em} = 10^8$, and $S_{em} = 28$. Requiring that these numbers remain constant for the both target cases, we obtain the corresponding F_{L0}, f, and u_0 values as summarized in Tab. 4.2.

L, cm	L_0, cm	F_{L0}, N/m^3	f, Hz	u_0, cm/s
10 (this study, GaInSn)	5	664	450	4.6
20 (Gen1, Si)	10	26	360	2.04
80 (Gen5, Si)	40	0.4	23	0.51

Table 4.2.: Example for scaling the results of model experiments in the present work to larger TMF systems with silicon melts.

The inductor frequency and Lorentz force density for the up-scaling to the research scale are realistic (e.g., [Frank-Rotsch et al., 2008]); the corresponding inductor current follows from the $F_{L0} \sim I_0^2/L_0^3$ scaling discussed in Sec. 2.4 and is in both target cases 56% from the reference value. For the industrial scale, the scaled Lorentz force becomes rather weak, resulting also in relatively small flow velocities of about 1 cm/s. In practice, such weak Lorentz forces may often be dominated by buoyancy forces. This force balance has been analyzed for an idealized TMF by Grants et al. [2009a].

The scaling between the first two cases in Tab. 4.2 is illustrated with 3D simulations in Fig. 4.15. The meshes for the Lorentz force and flow calculations were not regenerated, but up-scaled. It can be seen that the flow pattern is exactly transferred between both systems, the velocity and time scales transform according to the constant dimensionless numbers (4.8). Note that the time-dependence of the velocity at the monitor point is not identical in both cases, which can be caused by rounding errors, e.g., in the interpolation of the Lorentz force.

4.4.2. Application to directional solidification of silicon

The numerical tools, which will be applied for the simulation of silicon flows in the present work, have been validated for an isothermal TMF flow. The approach for turbulence modeling can be summarized as follows:

- A blind use of standard turbulence models only because the flow seems to be in an unsteady turbulent regime should be avoided. If the computational resources allow only 2D calculations or calculations of a time-average flow, a method for the determination and validation of the optimal turbulence model should be defined.

- If the computational resources allow unsteady three-dimensional calculations, a grid-independence test for the flow characteristics of interest is carried out. If a full grid refinement of at least 2 times in all directions has no significant influence on the results, then the resolution can be considered as sufficient.

One of the goals of using a TMF in directional solidification is the possibility to control the melt stirring level. For a strong stirring, the flow should be in the unsteady flow regime. For the present system, this transition occurs in the current range $I_0 = 1.6 \ldots 3.3$ A (see Section 4.3.3), which corresponds to the forcing parameter range $F_{em} = 1 \cdot 10^6 \ldots 4 \cdot 10^6$. These values are comparable to the instability threshold of $F_{em} = 4 \cdot 10^5$ at $S_{em} = 20$, reported in the literature for axisymmetric systems [Lantzsch et al., 2007]. Above the threshold, the standard deviation of velocity fluctuations could be used as a simple criterion to estimate the relative mixing or turbulence level of the melt; see the analysis in Section 4.3.3.

The shifting of the melt position discussed in Section 4.3.4 may be important for practical applications due to the changes in the flow pattern and the high sensitivity already at very

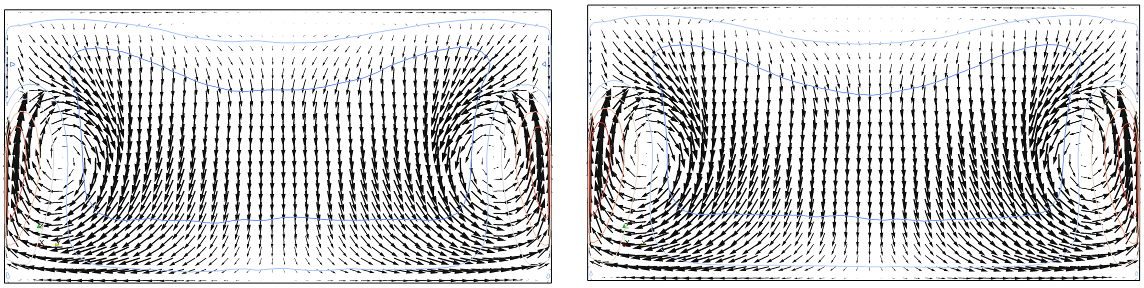

$u_{max} = 4.34$, $u_z = 2.65 \ldots 4.34$ cm/s

(a) GaInSn, $L = 10$ cm,
$f = 450$ Hz, $I_{0N} = 587$ A

$u_{max} = 1.91$, $u_z = -1.23 \ldots 1.91$ cm/s

(b) Si, $L = 20$ cm,
$f = 360$ Hz, $I_{0N} = 329$ A

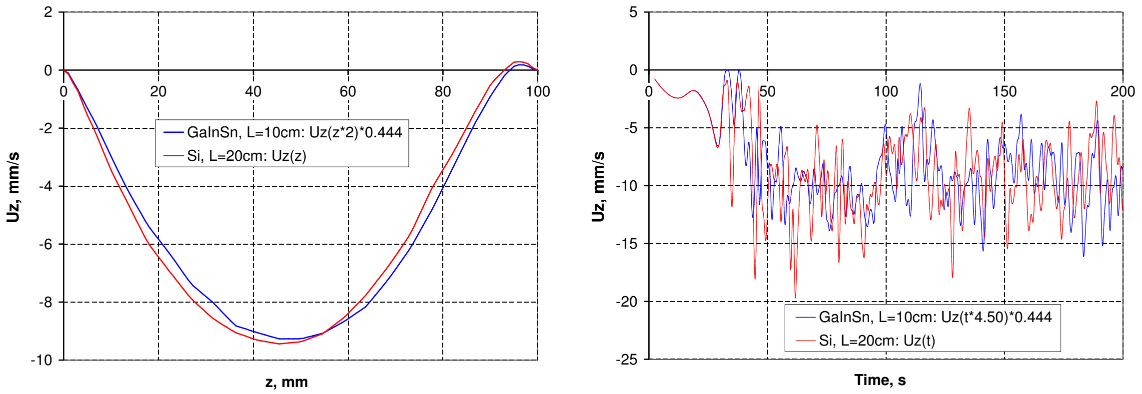

(c)

(d)

Figure 4.15.: Example for scaling the results of model experiments (GaInSn, $L = 10$ cm) to larger TMF systems with silicon ($L = 20$ cm) according to Tab. 4.2: (a,b) calculated time-averaged velocity vectors and isolines of u_z field in a vertical cut through the melt center; (c) calculated time-averaged vertical velocity profiles through the melt center; (d) calculated velocity oscillations in the melt center. For the sake of comparison, the values for the small system are transformed according to the scaling laws as indicated in the diagrams.

small shifts. Qualitatively similar effects on the flow pattern can be expected also from typical 3D features of the inductors, such as the current supplies at one side of the coils. A gap between the current supplies would also lead to a weaker Lorentz force at the corresponding side of the melt.

During the directional solidification; the melt height inevitably decreases from the initial value to zero crossing also the range with the possibility of occurrence of the swirling motion in the melt center as shown in Section 4.3.5. While the “liquid metal tornado” [Grants et al., 2008, 2009b] has been assumed to be beneficial for intensive melt mixing especially in the vertical direction, the swirl generation in the present work would rather lead to a region with a poor mixing in the central melt part. An increase of the overall melt mixing, e.g., by adjusting the inductor current might be necessary at a definite range of melt height.

Chapter 5

Non-isothermal melt

A new experimental setup for small-scale model experiments with a low-melting-point liquid metal is developed that, in contrast to the previous chapter, allows cooling at the bottom and heating at the top of the melt. Such a stable vertical temperature gradient is always present in silicon furnaces and can significantly influence the TMF-induced flow. Again, the complementary use of simulations and experiments allows the validation of the numerical tools and gives detailed insights into the flow properties. The described experience in the construction of the new experimental setup offers an useful insight into the practical difficulties with model experiments of this type.

5.1. Experimental setup

We continue with small-scale model experiments as described in the previous chapter, but now a vertical temperature gradient is introduced in the melt. There are only a few studies in the literature where liquid metal model melts with thermal gradients, in alternating magnetic fields have been investigated experimentally; see the literature review in Sec. 1.3.2. Closest to the current work is the system presented in [Grants et al., 2009a] and [Klyukin et al., 2008]. The flow of gallium in a cylindrical container with a diameter and height equal to 14 cm was investigated under a TMF and a varying vertical temperature gradient imposed with isothermal top and bottom walls. It was experimentally confirmed that a stable temperature stratification delays the TMF-driven flow instability, but no further studies of the turbulent flow regime were performed.

5.1.1. Design and construction

The same system of TMF coils as in the previous chapter was used to generate a Lorentz force in a square GaInSn melt with dimensions up to 10×10×10 cm^3. A completely new setup for the melt was developed[1], which contains a container with a cooler at the bottom and heater at the top, as shown in Fig. 5.1. The container consists of four Makrolon side

---

[1] The assembly of the new setup as well as the experimental measurements described later were carried out by Kathrin Niemietz, Jan Ehrig, and several technical assistants at INEMET under the supervision by Dr. Olf Pätzold. Several colleagues from Fraunhofer THM were involved in various electrical measurements.

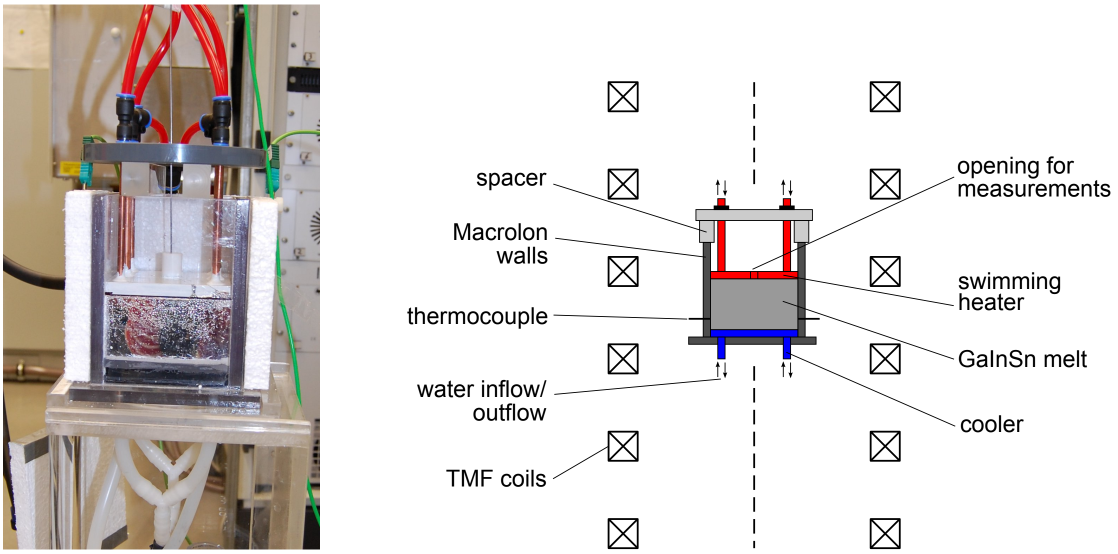

(a) (b)

Figure 5.1.: Experimental setup: (a) photo of the container filled with GaInSn (outside of TMF coils); (b) sketch of the setup.

walls with thicknesses of 1 cm. Makrolon was chosen due to its mechanical stability, which is better than that of than Plexiglas at temperatures over 60 °C. Makrolon's low temperature conductivity[2] of approximately 0.2 W/mK ensures good thermal insulation at the side walls, which helps to reduce the lateral temperature gradients and to achieve more exact (adiabatic) thermal conditions. Additional polystyrene insulation at the outside of the side wall did not show any significant effect on the temperature conditions in the melt.

In the vertical direction, we want to impose a temperature gradient up to 5 K/cm on the melt. This gradient corresponds to a temperature difference of 50 K for a melt height of 10 cm or to a vertical heat flux density of 19500 W/m^2. This heat flux density puts significant constraints on the thermal conductivity of the materials for the bottom and top walls to keep the temperature difference between the cooling and heating systems low. A Makrolon wall at the top and bottom would lead to a temperature difference of 100 K per 1 mm, which is not realistic. Therefore, both the heater and the cooler were made of copper (thermal conductivity of 401 W/mK) directly attached to the melt. The Makrolon side walls of the container were permanently bond to the cooler with glue to avoid melt leakage. The heater is swimming on the melt, which allows the melt height to be freely adjusted. Both the heater and the cooler were made from two separate rectangular tanks (the wall thickness is approximately 5 mm at the melt side and approximately 2 mm at the opposite side), which were glued together.

The horizontal cross section of the melt, which is 10×10 cm^2, defines the heating and cooling power required to achieve the desired temperature gradient. For the heat flux density given above, we obtain a heating and cooling power of 195 W. The experimental setup was designed for cooling and heating with water, which significantly reduces the setup's complexity. One liter (or 1 kg) of water releases 4180 J of heat when cooled down by 1 K. Therefore, a discharge of 1 liter/min produces a heating power of 4180 J/min or 70 W. To reach 195 W, we would need a temperature difference of approximately 3 K between the in-

---

[2] Material properties used in this section are taken mainly from [VDI-Waermeatlas, 2006]. The properties of GaInSn are summarized in Tab. 5.1; see also Appendix B.

let and the outlet. To reduce the produced lateral temperature inhomogeneity, several parallel inlets and outlets can be used. Therefore, both the heater and the cooler are equipped with two inlets at the central part of the side and four outlets in the corner. This outlet distribution also ensures a more homogeneous heat exchange over the entire wall. The heater and the cooler were connected to two low-temperature thermostats *(LAUDA)* running with water and enabling a temperature range from the temperature of the supply water to above 90 °C. Typical discharges of 0.9 liter/min for the heater and 1.4 liter/min for the cooler were used in the experiments. An increase of the discharge showed no significant effect on the thermal conditions in the melt. Therefore, the lower discharge was kept to reduce the risk of water leakage.

The high thermal conductivity of copper is related to a high electrical conductivity ($6 \cdot 10^7$ S/m), which leads to a small skin depth of the AC magnetic field and a strong shielding effect. For a frequency of 450 Hz, which was used in the isothermal setup, the skin depth is about 3 mm. Therefore, the frequency was reduced to 50 Hz, which increases the skin depth to 9 mm. The dimensions of the copper parts were kept as small as possible, especially avoiding extension in the lateral direction. Furthermore, an electrical contact of the copper parts with the melt could lead to a complex interaction. Therefore, the surfaces of the heater and cooler were covered with an electrically insulating layer of acrylic varnish with a thickness of approximately 0.2 mm.

Property	Symbol	GaInSn	Silicon
Density, kg/m^3	ρ	6360	2520
Viscosity, Pa·s	η	$2.16 \cdot 10^{-3}$	$7.6 \cdot 10^{-4}$
Electrical conductivity, S/m	σ	$3.2 \cdot 10^6$	$1 \cdot 10^6$
Thermal conductivity, W/mK	λ	39	67
Heat capacity, J/kgK	c	361	986
Linear expansion coefficient, 1/K	β	$1.32 \cdot 10^{-4}$	$1.44 \cdot 10^{-4}$

Table 5.1.: Relevant material properties: GaInSn (at room temperature) in comparison with liquid silicon (near the melting point of 1685 K).

5.1.2. Measurement methods

The UDV technique already described in the previous chapter is applied for direct velocity measurements. Although special high-temperature probes are available for the present UDV device, these probes produced a higher noise and more interference effects in the velocity signal. Therefore, the standard UDV probe as in the previous chapter was used. The measurements of the vertical profiles were performed from the melt top through a special opening in the heater (see Fig. 5.1). Measurements of the horizontal profiles could not be performed through the Makrolon side walls. In contrast to Plexiglas, a (very weak) velocity signal could be obtained through the Makrolon side walls only with a high ultrasound power; no significant improvements were observed for thinner walls down to a few mm. The reasons are not yet understood. Probes permanently installed in a hole in the wall (with direct contact to the melt) were successfully tested, but these probes would require more complex mechanical solutions for routine use.

Vertical temperature profiles were also measured through the opening in the heater. An encapsulated *Type K* thermocouple connected to an *Almemo 2590 (Ahlborn)* analyzing device was vertically shifted. This system allows also time-dependent temperature measurements but only with 3 significant numbers, i.e., with a precision of 0.1 K. Therefore, this system was used to obtain the instantaneous temperature in a steady regime and the approximate time-averaged temperature in an oscillating regime, where the average value is estimated from the minimum and maximum values over a characteristic time interval. Additional temperature readings were obtained from two permanently installed thermocouples in two opposite walls, with a direct contact to the melt.

For time-resolved measurements of the temperature oscillations, the thermocouple in the melt center was attached to a high-precision *Keithley 2700* voltmeter. It enables single-channel measurements with a frequency over 100 Hz. However, it turned out that it is crucial to use an averaging filter to filter out the noise induced by the environment or the device itself or by the magnetic field of the TMF coils in the thermocouple wires. The thermo-voltage measured with this system is approximately 0.05 mV/°C. A magnetic field with a frequency f and amplitude B_0 induces a voltage $U \approx 2\pi f B_0 S$ in a wire loop with a surface S according to Faraday's law (2.8). Assuming S = 50×1 cm^2, B_0 = 3 mT, f = 50 Hz, we obtain $U \sim 5$ mV. The averaging filter downgraded the measurement frequency to approximately 10 Hz. A higher resolution could be probably achieved with sophisticated shielding and grounding techniques, which were not applied in this work.

5.2. Thermal model

The thermal conditions in the experimental setup were characterized by various temperature measurements. The heater was put into an upright position, with a thick aluminum plate on it containing small holes. Temperature measurements with a thermocouple on the heater surface were performed through the holes to avoid a direct influence of air convection. A good agreement with the thermostat temperature and a very uniform distribution over the entire surface were observed. The results for the cooler were similar. The heater and cooler in the air atmosphere as well as various parts of the setup were also inspected by thermographic imaging. However, only qualitative results could be obtained in this way because the emissivities were not known, the properties of the surfaces were not uniform, and the metallic surfaces showed very strong reflection effects.

In a further test, the container was filled with GaInSn and the vertical temperature profile in the center was measured with the thermocouple for various melt heights and thermostat temperatures. When the TMF was switched off, there was no significant flow in the melt. Even under these conditions, temperature measurements showed considerable deviations between thermostat temperatures and the temperatures on the heater and cooler surfaces (measured temperature profiles without a melt flow are given in the following sections). The origin of this deviation is assumed to be the thermal resistance of the acrylic varnish layer, as will be explained in the following.

We consider a thermal serial connection of the varnish layer at the top, the melt, and the varnish layer at the bottom. The thermal conductivity of the layers are λ_a, λ, and λ_a, respectively, and the thicknesses are d, H, and d, respectively. The temperature of the heater T_h and that of the cooler T_c is given by the thermostats. We are interested in the temperatures T_t and T_b at the top and bottom, respectively, of the melt. The expression for the heat flux density through this type of series connection reads [Baehr and Stephan, 2010] as follows:

$$q = \frac{T_h - T_c}{d/\lambda_a + H/\lambda + d/\lambda_a} = \frac{T_t - T_b}{H/\lambda} = \frac{T_h - T_t}{d/\lambda_a} = \frac{T_b - T_c}{d/\lambda_a}. \tag{5.1}$$

This expression allows one to obtain the unknown thermal properties of the varnish layer from temperature measurements in the following way:

$$\frac{T_t - T_b}{T_h - T_c} = k = \frac{H/\lambda}{d/\lambda_a + H/\lambda + d/\lambda_a} \quad \Rightarrow \quad \frac{d}{\lambda_a} = \frac{H}{\lambda}\frac{1-k}{2k}. \tag{5.2}$$

The ratio of temperature intervals k was found to be constant at $k = 0.5$ in a wide temperature range. It follows that the thermal resistance of the varnish layer is $d/\lambda_a = 0.5H/\lambda = 0.00064$ $\mathrm{m^2K/W}$. With an estimated thickness of 0.2 mm, we obtain a realistic value for the thermal conductivity of $\lambda_a = 0.3$ W/mK.

For numerical modeling, it is useful to set a thermal boundary condition directly on the surfaces of the melt so that only one calculation domain must be considered. The model described above can be formulated in a Poincare-type boundary condition on the top surface of the melt as follows:

$$\lambda \frac{\partial T}{\partial n} = p_T(T - T_h), \quad p_T = \lambda_a/d = 1563\ \mathrm{W/m^2K}. \tag{5.3}$$

dT/dn denotes the temperature gradient in the normal direction. In the expression for the cooler at the bottom surface of the melt, the reference temperature T_h is replaced by T_c.

5.3. Magnetic field and Lorentz force

The calculation of the Lorentz force is more complicated than for the isothermal setup due to the presence of copper parts with distinct skin effects at the bottom and top of the melt. It would be very complicated to model the entire system in three dimensions with a submillimeter gap between the copper and the melt and a three-dimensional shape of the copper parts. Therefore, both the heater and the cooler were replaced in the electromagnetic calculation by a solid rectangular copper plate with an effective thickness of 6 mm and with an effective distance to the melt of 2 mm. This model showed a good agreement with the vertical profile of the magnetic field on the axis measured at 50 Hz without the melt, as shown in Fig. 5.2 (a). The precision of 3D calculations was tested in a comparison with 3D results for an axisymmetric geometry.

The Lorentz force distributions (calculated with `GetDP`) for the various melt heights considered in this study are shown in Fig. 5.3 for an inductor frequency $f = 50$ Hz and current $I_0 = 19.6$ A. The typical size of the elements of the tetrahedral mesh in the melt ranges from 5 mm to 1 cm; see Fig. 5.2 (b). In the former isothermal setup with an upward TMF, the Lorentz force density in a vertical cut always showed an more upward-directed force in the bottom corners and a more downward-directed force in the top corners (see Fig. 4.5). For the new setup, the copper parts have obviously reversed this boundary effect for all melt heights – the force density becomes even more upward in the top corner and becomes almost downward in the bottom corner. This effect leads to a qualitatively different force distribution in comparison to that in the former isothermal setup. The horizontal cut in Fig. 5.3 is shown only for the melt height of 2.5 cm, but the distributions were also very similar also for other

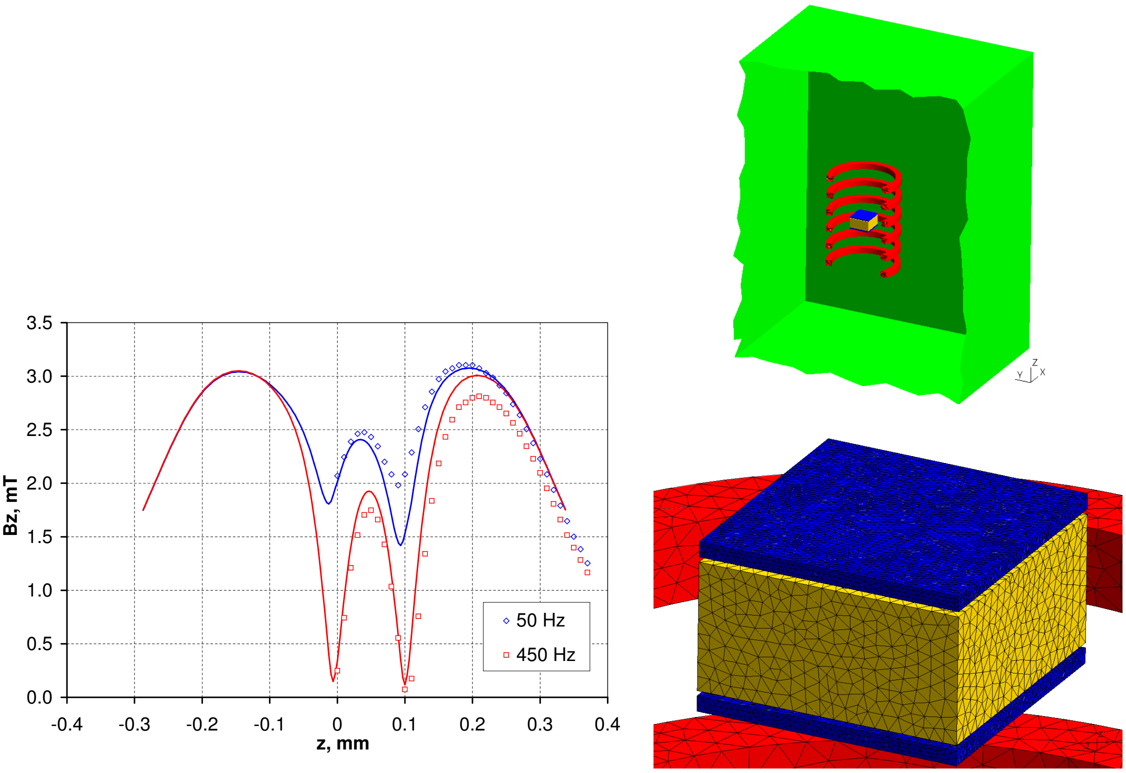

(a) (b)

Figure 5.2.: (a) Comparison of the vertical magnetic field component on the coil system axis in 2D calculations (lines) and in measurements (symbols) with a commercial Gaussmeter (see Sec. 4.1.1) for I_0 = 16.3 A. The top surface of the cooler is located at z = 0, the heater bottom is located at z = 10 cm, there is no melt in the container. (b) Example of the geometry and mesh (533492 tetrahedrons; air volume elements not shown here) used for 3D Lorentz force calculations with a melt height of 5 cm. [ExpINEMET, 2010]

melt heights. The skin depth is significantly larger than in the former investigations with the isothermal setup, where a higher frequency (450 Hz) was used.

Although, the reference inductor current was increased from 16.3 A in the isothermal setup to 19.6 A in the new setup, the level of the Lorentz force density has significantly decreased – from the typical value of 660 N/m^3 to 70 N/m^3. This decrease is caused primarily by the 9 times lower frequency as well as by the shielding effect from the copper parts. However, several tests showed that a higher flow velocity can be achieved in the new setup with a frequency of 50 Hz than with 450 Hz. This effect obviously results from the combined effects of the changes in the Lorentz force distribution, the skin depth in the melt, and the shielding by the copper parts.

5.4. Fluid flow and temperature field

The following sections present the results from 3D `OpenFOAM` calculations that include the effects of the Lorentz and buoyancy forces. The Poincare boundary condition for the temperature is set on the top and bottom walls of the melt, and the side walls are assumed to be thermally insulated. A no-slip condition is prescribed on all walls for the velocity. The results of calculations are compared to measurements of the temperature and velocity. Both the

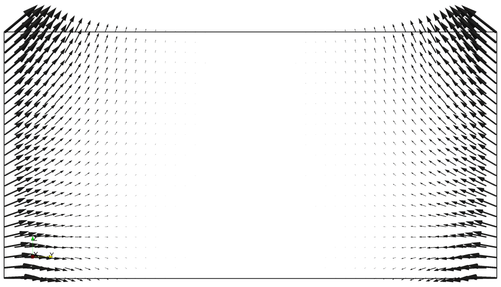

F_{Lmax} = 77 N/m^3

(a) H = 5 cm, TMF up

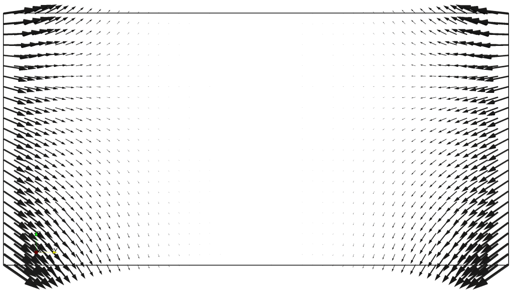

F_{Lmax} = 74 N/m^3

(b) H = 5 cm, TMF down

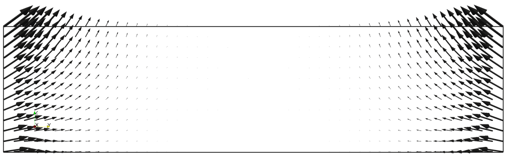

F_{Lmax} = 70 N/m^3

(c) H = 2.5 cm, TMF up

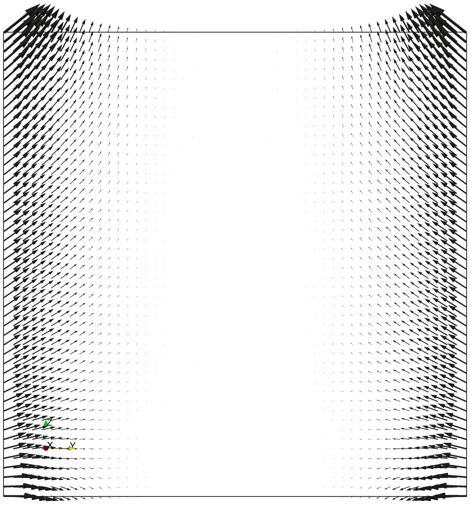

F_{Lmax} = 87 N/m^3

(d) H = 10 cm, TMF up

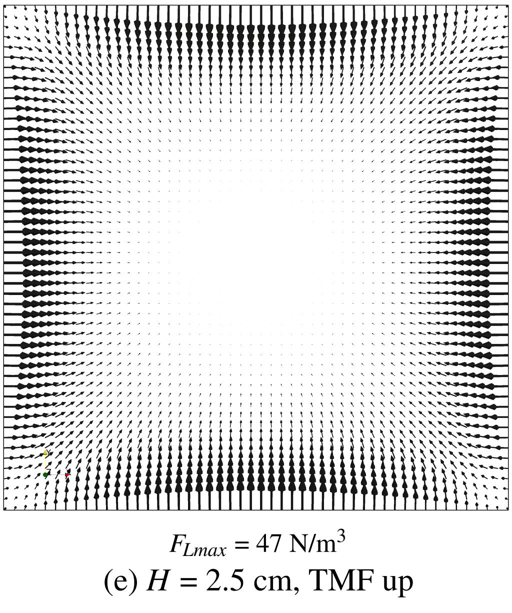

F_{Lmax} = 47 N/m^3

(e) H = 2.5 cm, TMF up

Figure 5.3.: Calculated Lorentz force distribution in a vertical cut (a–d) and a horizontal cut (e) through the melt center perpendicular to the side wall. Cases with f = 50 Hz, I_0 = 19.6 A: (a) H = 5 cm, TMF up; (b) H = 5 cm, TMF down; (c,e) H = 2.5 cm, TMF up; (d) H = 10 cm, TMF up. The maximum value of the Lorentz force density F_{Lmax} in the cut is given for each case.

time-average fields and the oscillations at fixed points are analyzed for various melt heights. Cases with and without a vertical temperature gradient are considered because the differences in the Lorentz force distribution do not allow a direct comparison of the results in the former isothermal setup and the new setup.

The fields in the simulation were averaged over at least 200 s, starting from the time instant at 100 s. In the experiment, the averaging of the velocity profiles was performed over at least 600 s to to obtain reproducible time-average values. The time-averaged temperature was estimated from the minimum and maximum values.

5.4.1. Reference case

For the reference case, a melt height of 5 cm is chosen. Other reference parameters are: an upward TMF, an inductor current I_0 = 19.6 A, and cooler/heater temperatures T_c/T_h = 25/35 °C. All results of the measurements of the time-averaged temperature and velocity fields are summarized in Fig. 5.4. for isothermal conditions (T_c/T_h = 25/25 °C) and for two different vertical temperature gradients (T_c/T_h = 25/35, 25/45 °C). In the isothermal case at room temperature, we observe the typical toroidal flow pattern, which is very similar to the result in the former isothermal setup at 450 Hz except the flow velocity approximately 3 times lower.

A vertical temperature gradient in the melt of 1 K/cm without a TMF can be imposed if the heater thermostat temperature is increased to 35 °C. The measurements of the vertical temperature profiles without a TMF shows a temperature of 27.1 °C at the melt bottom and 32 °C at the melt top. These results agree well with the calculation using the Poincare boundary conditions as described previously in Sec. 5.2. A vertical temperature gradient in the melt of 2 K/cm without a TMF requires a heater temperature of 45 °C.

Without a TMF, there is no melt motion regardless of the vertical temperature profile as long as the temperature increases linearly in vertical direction and there are no significant lateral gradients. The measured and calculated velocity profiles in Fig. 5.4 show the effect of the combination of a TMF and a vertical temperature gradient. The velocity becomes significantly smaller with an increasing temperature gradient in both the simulation and the experiment. Although for a temperature gradient of 2 K/cm the flow velocity is smaller by a factor of 2 in the experiment, the simulation shows an almost complete elimination of the flow with respect to the isothermal case. A closer examination of the simulated flow pattern, however, reveals that the torus is pressed into the top corners of the melt, while a second torus appears at the bottom of the melt. Consequently, the velocity in the central part becomes smaller by an order of magnitude, while the maximum velocity in the entire melt decreases by less than a factor of 2. A distinct secondary flow structure in the horizontal plane appears in the case of a high temperature gradient. This effect is further elucidated in a Fig. 5.5. With the smaller temperature gradient, the melt basically moves upward in the corners and at the sides and moves downward in the central part. With a high temperature gradient, the circular trajectories of the torus are tilted from the vertical plane, and eight horizontal vortices appear in the corners.

The temperature distributions in a vertical cut and the temperature profiles in Fig. 5.4 (b) show a strong mixing of the temperature field with respect to the case without a TMF (constant vertical temperature gradient in the entire melt). In the case with 1 K/cm, the temperature distribution in the central part becomes almost homogeneous. The weak flow with 2 K/cm is unable to stir the melt, and the imposed temperature gradient is more or less pre-

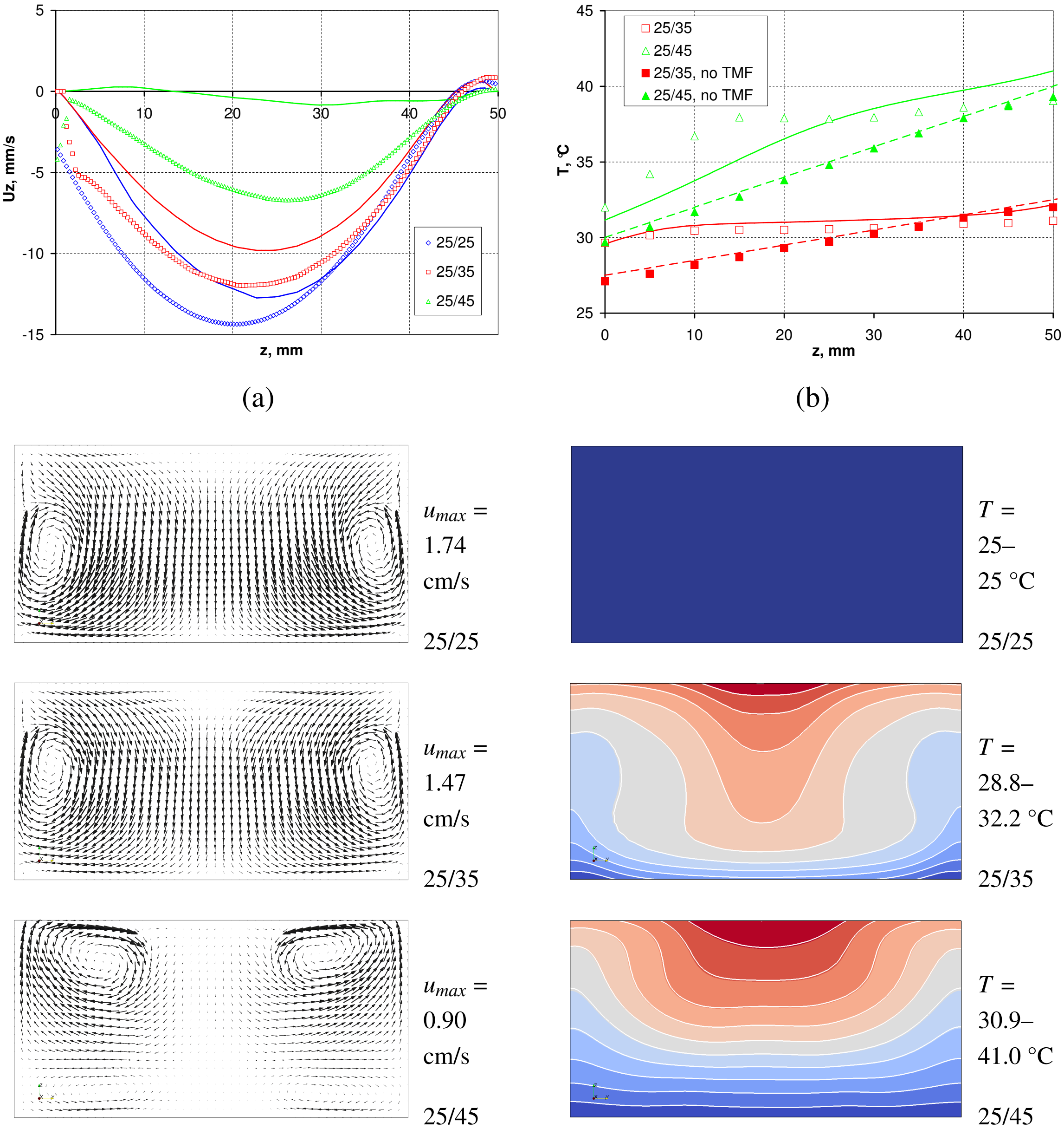

(a) (b)

(c) (d)

Figure 5.4.: Case with $H = 5$ cm, TMF up, $I_0 = 19.6$ A, $T_c/T_h = 25/25, 25/35, 25/45$ °C: (a) comparison of calculated (lines) and measured (symbols) time-averaged vertical velocity profiles in the melt center; (b) the corresponding temperature profiles; (c) calculated time-averaged velocity in a vertical cut through the melt center perpendicular to the side wall; (d) the corresponding temperature field. [ExpINEMET, 2010]

served. It must be emphasized that the interaction of the velocity and temperature fields essentially depends on the thermal (boundary) conditions at the heater and cooler surfaces. If the temperatures were fixed, we would rather see a distinct local increase of the temperature gradient. However, it is an open question how realistic such a boundary condition is. High cooling and heating powers with good homogeneity along the entire cooler and heater surface would be required to supply the convection-enhanced heat transport.

All velocity profiles in Fig. 5.4 show a lower velocity in the simulation than in the experiment. A similar trend was already observed in the former isothermal setup, where it was attributed to experimental uncertainties such as deviations from the no-slip condition on container boundaries or imprecision of the measured inductor current. These factors apply also for the new setup in the cases without a temperature gradient and with a gradient of 1 K/cm. The discrepancy between the simulation and the experiment is much larger in the case with 2 K/cm. This can be explained by the transitional character of the flow as discussed later in Sec. 5.4.5.

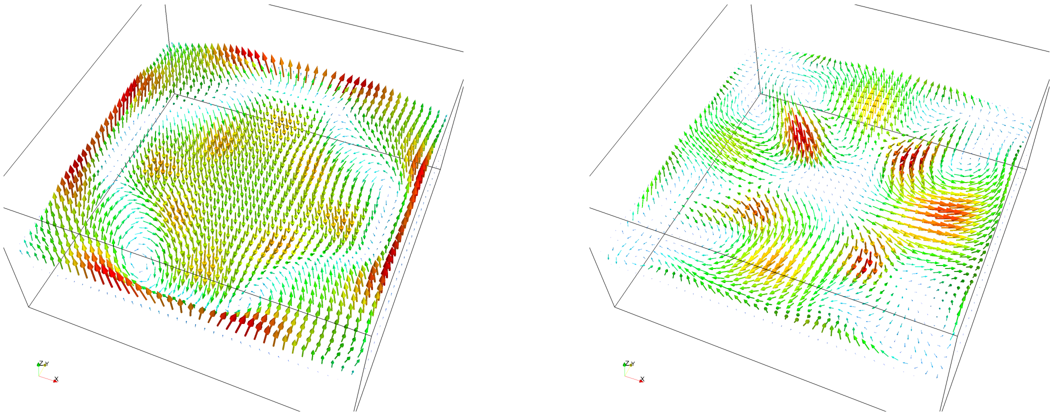

u_{max} = 1.56 cm/s

(a) T_c/T_h = 25/35 °C

u_{max} = 0.57 cm/s

(b) T_c/T_h = 25/45 °C

Figure 5.5.: Case with H = 5 cm, TMF up, I_0 = 19.6 A. Calculated time-averaged velocity distribution in a horizontal cut through the melt center with T_c/T_h = 25/35 °C (a) and 25/45 °C (b).

5.4.2. Influence of numerical parameters

It was shown for the former isothermal setup that the time-averaged velocity distribution in the calculation is not influenced by further refinement of the grid or by more accurate discretization schemes. Some of these tests were repeated with the additional buoyancy force in the melt. Fig. 5.6 shows, for example, the influence of the mesh size for a melt height H = 5 cm, an upward TMF, an inductor current I_0 = 19.6 A, and cooler/heater temperatures T_c/T_h = 25/35 °C. Qualitatively, the simulated and measured velocity profiles agree well. However, there is a deviation of approximately 20%. No improvement can be achieved even when the mesh size is increased from the reference case with 80 thousand elements to 1.6 million elements.

The discrepancy between the experimental and numerical results might arise, in addition to other factors, from the fact that the flow is in an unsteady regime. It is nearly impossible that the exact time-dependent velocity at a fixed position is reproduced in the simulation.

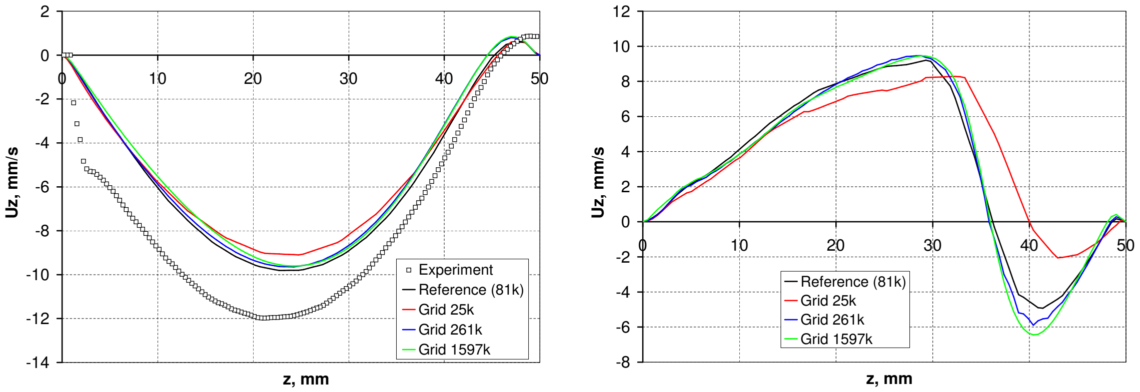

(a) In melt center

(b) At side wall

Figure 5.6.: Case with $H = 5$ cm, TMF up, $I_0 = 19.6$ A, $T_c/T_h = 25/35$ °C. Comparison of calculated (lines) and measured (symbols) time-averaged vertical velocity profiles in the melt center (a) and 5 mm from the center of the side wall (b). Grids with 25400, 80600 (reference), 261000, and 1597000 cells are considered. [ExpINEMET, 2010]

The time-averaged velocities should generally show an exact agreement but may not agree for an average performed at a fixed position or, especially, for a fixed velocity component. An unsteady flow exhibits strong fluctuations in both space and time. Therefore, a better comparison would be possible for the entire velocity vector at a fixed position or for the distribution of a velocity component in two or three dimensions. A technique for UDV measurements of the velocity distribution in a 2D plane has been developed recently [Franke et al., 2010]. However, the dynamics of the UDV measurement in a highly unsteady flow has not been discussed extensively in the literature.

5.4.3. Influence of TMF direction

Because the gravity and the buoyancy forces possess a definite direction, there may be differences in the interaction with a TMF directed downward or upward. The calculated and measured velocity and temperature fields in the isothermal case and with a temperature gradient of 1 K/cm, but now with a downward TMF, are shown in Fig. 5.7. A comparison with the results in Fig. 5.4 reveals that the temperature and velocity fields show the same essential effects, except the distributions are turned upside down because the direction of the velocity is reversed.

The interaction of a forced convection with a buoyancy force in a stabilizing temperature gradient has been already investigated in the literature. A lid-driven cavity with a vertical temperature gradient [Iwatsu et al., 1993] (see also Sec. 3.3.3.1) shows that the temperature gradient damps the forced convection and suppresses its vertical extension. In the case of our model system with a TMF, the velocity value is not explicitly specified by the moving lid, and a reduction of the maximum flow velocity can be observed at higher temperature gradients. We also observe that the motion is forced from the vertical plane to the horizontal plane, leading to a complex 3D flow pattern. The formation of 3D structures has been also observed for the well-known lid-driven cavity case [Iwatsu and Hyun, 1995]. This general effect has a simple physical explanation: a horizontal vortex does not mix a vertically stratified temperature field, i.e., the temperature fields prevents in this way itself from mixing.

The stabilizing effect of the temperature field on the TMF flow can also be explained

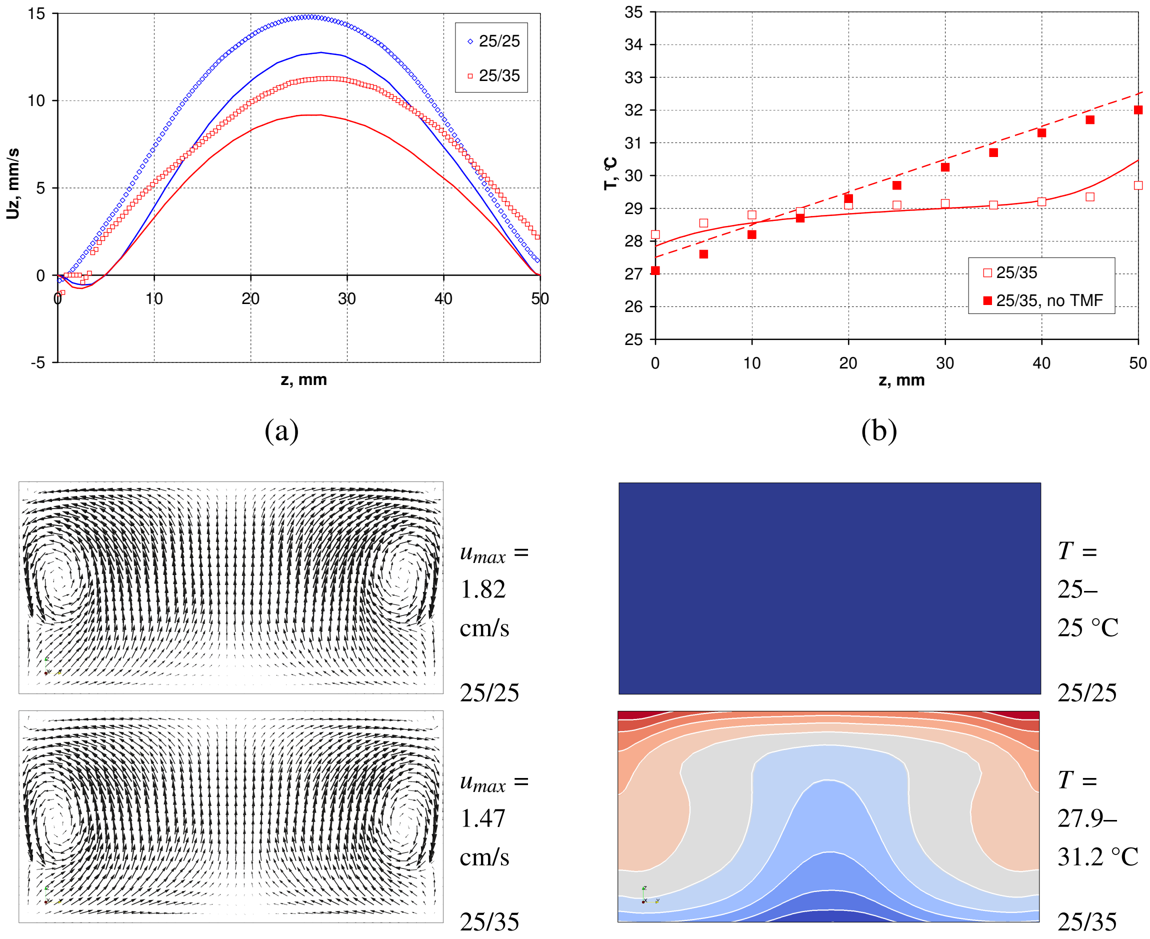

(a) (b)

(c) (d)

Figure 5.7.: Case with H = 5 cm, TMF down, I_0 = 19.6 A, T_c/T_h = 25/25, 25/35 °C: (a) comparison of calculated (lines) and measured (symbols) time-averaged vertical velocity profiles in the melt center; (b) the corresponding temperature profiles; (c) calculated time-averaged velocity in a vertical cut through the melt center perpendicular to the side wall; (d) the corresponding temperature field. [ExpINEMET, 2010]

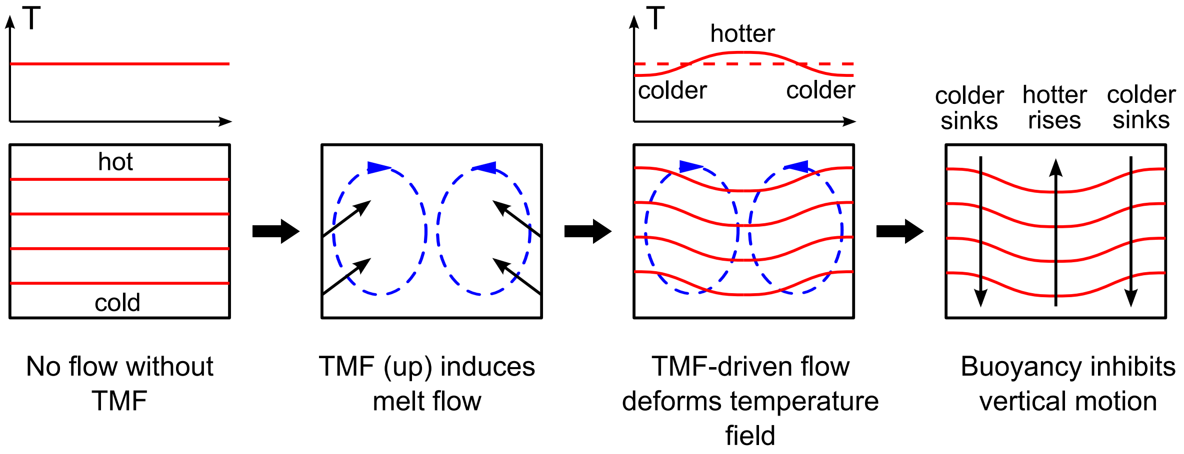

Figure 5.8.: Qualitative explanation of the suppression of a TMF-induced flow due to the buoyancy.

qualitatively as shown in Fig. 5.8. We consider a melt without a TMF, with a vertical temperature gradient, where the temperature increases in the vertical direction. If we add an upward TMF, the melt flows up at the walls and down in the central part. The cold melt from the melt bottom is transported upward along the wall, and the hot melt from the melt top is transported downward in the central part. Hence, we produce a lateral temperature gradient where the temperature decreases from the melt center to the side walls. This temperature distribution produces a buoyancy force that acts downward at the wall because the colder melt has a higher density that its neighborhood and tends to sink. This force is directed opposite to the Lorentz force from the upward TMF. A downward TMF would obviously lead to an upward buoyancy force, which would damp the flow in the same way.

5.4.4. Influence of melt height

In the former isothermal setup, a new flow pattern with a horizontal vortex was observed for a small melt height. Considering the relevance of the melt height for the directional solidification, where the melt height decreases to zero during the growth process, we investigated, in addition to the reference case with an aspect ratio of 0.5, also the flow for a 2-times-smaller and 2-times-larger aspect ratio. The results are given in Fig. 5.9 for a melt height of 2.5 cm and in Fig. 5.10 for a melt height of 10 cm.

The isothermal flow with a melt height of 2.5 cm shows the same flow pattern with a horizontal vortex as observed in the former setup. In the current case, a small but reproducible vertical velocity (value smaller than 4 mm/s) could be measured in the center. Note that the obtained velocity is approximately 5-times-smaller than that for a melt height of 5 cm (see Fig. 5.4 (a)), which hints at significant changes in the flow structure. Under the conditions of a vertical temperature gradient of 1 K/cm, the simulation shows a decrease of the vertical velocity profile and the formation of the 8 horizontal vortices, which were previously observed for a melt height of 5 cm and a temperature gradient of 2 K/cm (see Fig. 5.5 (b)). The comparison of the calculated and measured velocity profiles in the melt center shows some discrepancies. As previously observed, the calculated flow velocity is smaller. The temperature profile in the melt center shows a higher temperature gradient in the simulation.

To test some possible experimental uncertainties, isothermal calculations were performed with an initially perturbed velocity to initiate a horizontal rotation in the opposite direction. The opposite rotation did not significantly change the shape of the velocity profile (see Fig. 5.9 (a) profile named ‘opposite direction’) but increased the velocity in the center by 40%, reaching the level measured in the experiments. In general, it is also possible that the weak secondary flow in the melt center is very sensitive to various small deviations and inhomogeneities in the experimental setup.

The increase of the melt height to 10 cm initially showed a velocity in the experiment that was less than a half of that in the simulation, with good reproducibility; see Fig. 5.10 (a). Variation of various parameters in the simulation revealed that for the isothermal case a new flow pattern with an asymmetric 3D torus is observed if the melt height in the flow calculation is increased from H = 10 cm to 12.5 cm (the Lorentz force distribution is not recalculated, only deformed). The details of the new flow structure are shown in Fig. 5.11. In this new flow regime, the agreement of the calculated velocity profile with the measurements is much better. Obviously, there is a transition between two flow regimes if the melt height exceeds H = 10 cm under the given conditions. This transition may occur at somewhat smaller melt heights in the experiment than in the simulation. With an additional temperature gradient of

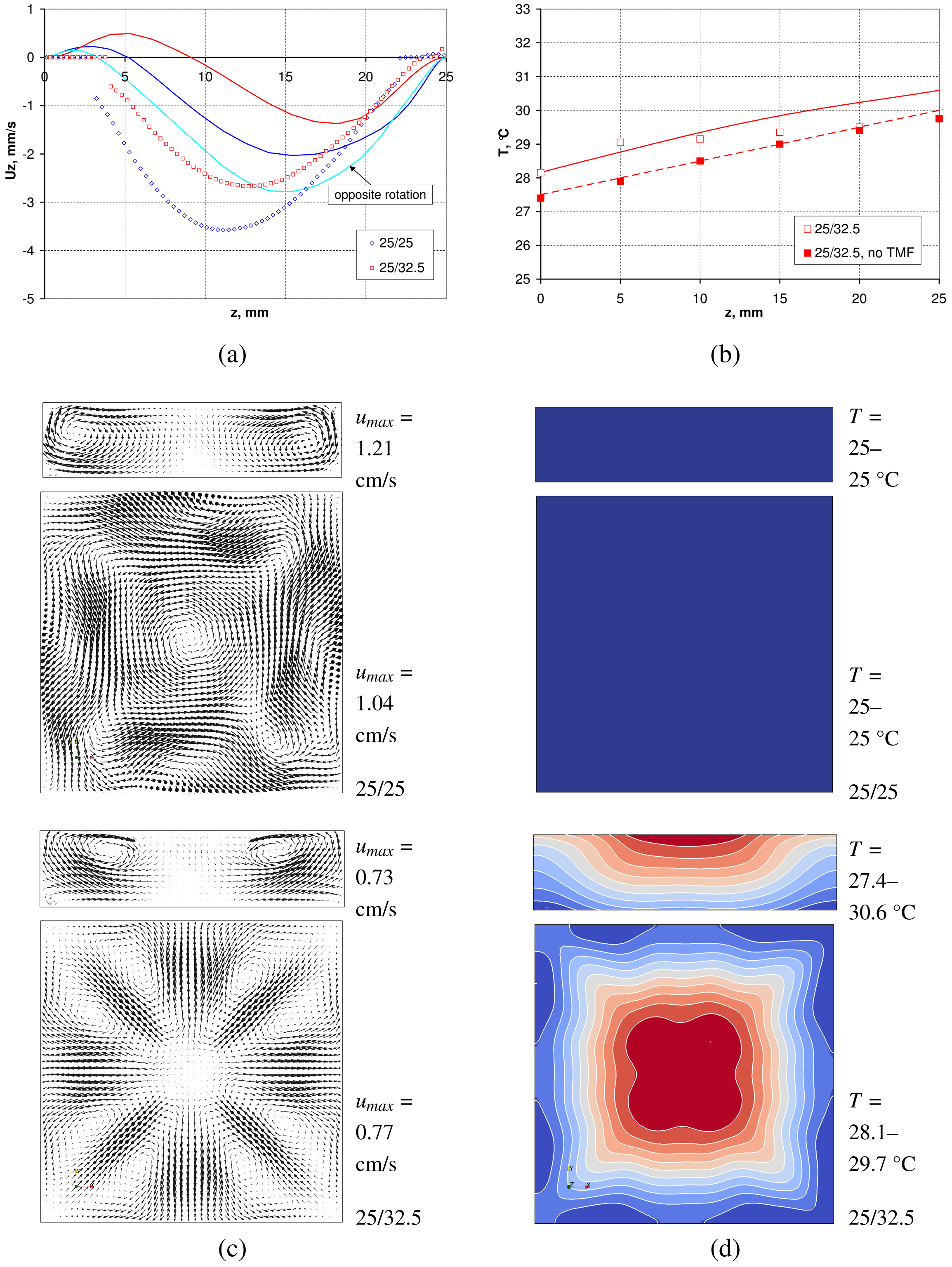

Figure 5.9.: Case with H = 2.5 cm, TMF up, I_0 = 19.6 A, T_c/T_h = 25/25, 25/32.5 °C: (a) comparison of calculated (lines) and measured (symbols) time-averaged vertical velocity profiles in the melt center; (b) the corresponding temperature profiles; (c) calculated time-averaged velocity in a vertical and horizontal cut through the melt center perpendicular to the side wall; (d) the corresponding temperature field. [ExpINEMET, 2010]

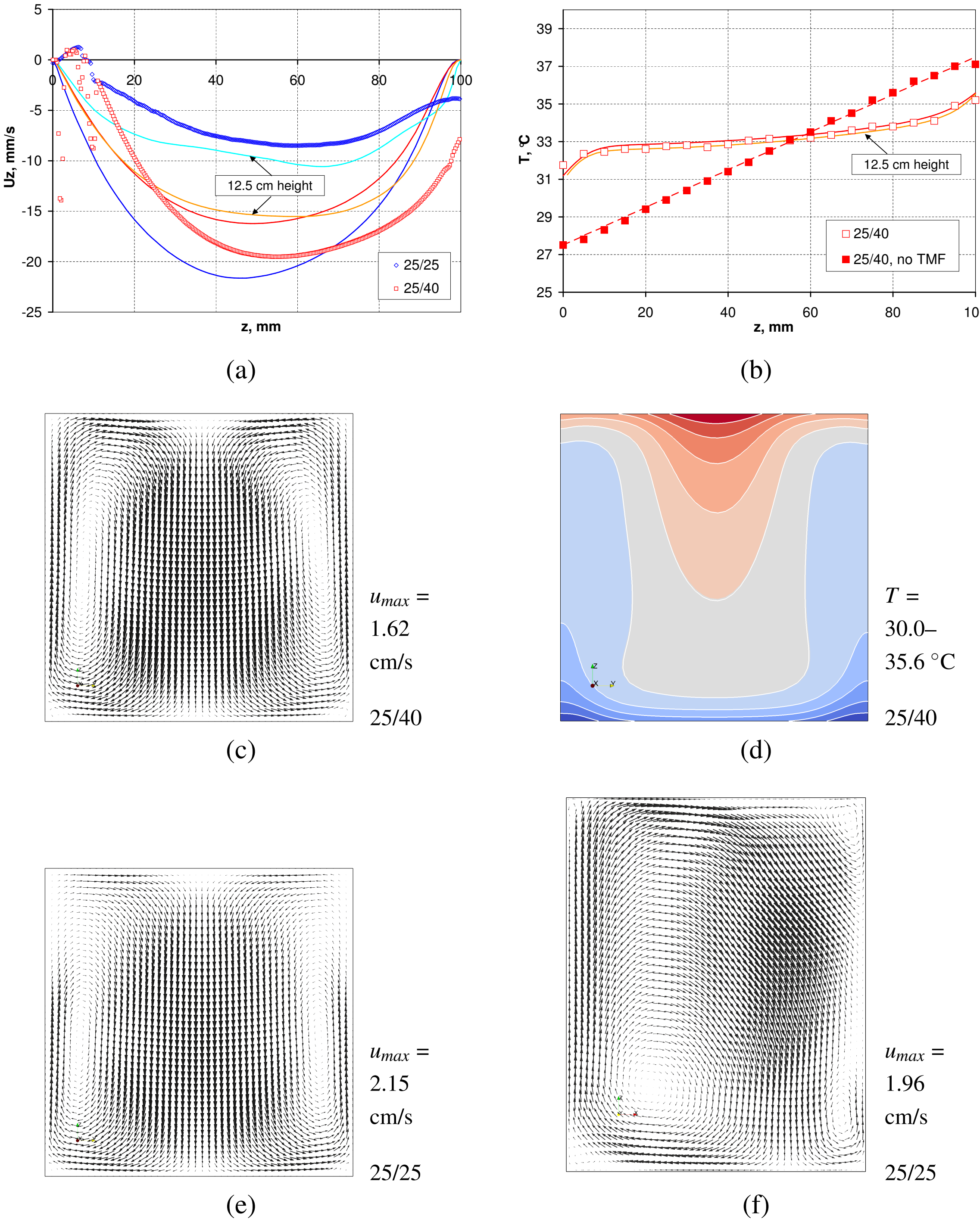

Figure 5.10.: Case with H = 10 cm, TMF up, I_0 = 19.6 A, T_c/T_h = 25/25, 25/40 °C: (a) comparison of calculated (lines) and measured (symbols) time-averaged vertical velocity profiles in the melt center; (b) the corresponding temperature profiles; calculated time-averaged velocity (c) and temperature (d) in a vertical cut through the melt center perpendicular to the side wall for the non-isothermal case; calculated time-averaged velocity in the same vertical cut for the isothermal case with a melt height of 10 cm (e) and deformed to 12.5 cm (f) in flow calculations. Results with a melt height of 12.5 cm are also given for comparison in (a) and (b). [ExpINEMET, 2010]

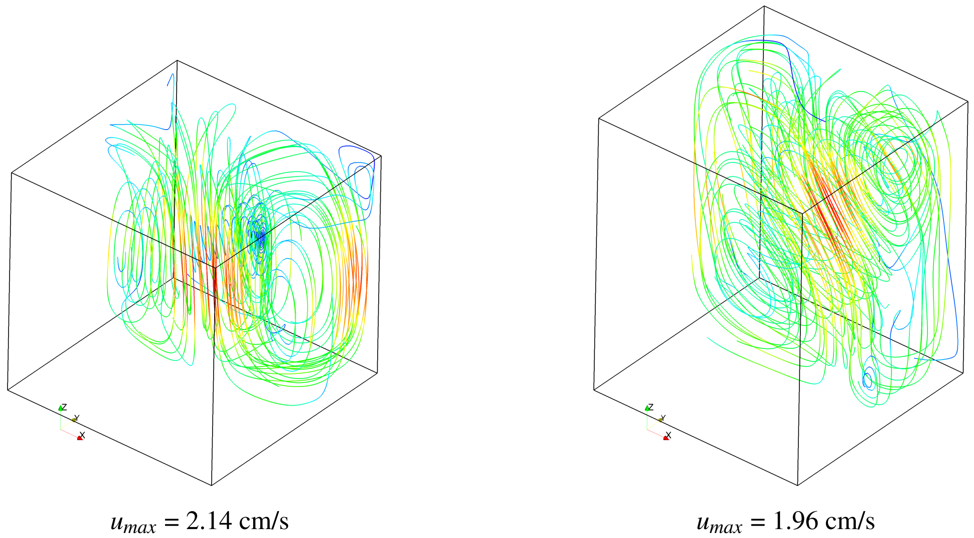

(a) H = 10 cm (b) H = 12.5 cm

Figure 5.11.: Case with TMF up, I_0 = 19.6 A, T_c/T_h = 25/25 °C: comparison of the calculated time-averaged 3D streamines for a melt height of 10 cm (a) and deformed to 12.5 cm (b) in the flow calculations. Only half of the melt is shown with a cut on a vertical mirror plane in both cases.

1 K/cm, the typical symmetric torus reappears in both simulations and experiments at a melt height of 10 cm. The velocity in the central part of the melt becomes significantly higher than in the isothermal case (see Fig. 5.10 (a)), causing a strong deformation of the temperature isolines (see Fig. 5.10 (d)). However, such a deformation is not necessarily accompanied by a significant increase of the absolute temperature gradients because the maximum melt temperature may decrease; see Fig. 5.10 (b).

5.4.5. Velocity and temperature oscillations

Fluctuations of the convective heat and mass transport have long been an important topic in crystal growth because these fluctuations cause unwanted oscillations of the growth velocity and dopant concentration, which leads to striations. Here, we focus on the unsteady flow regime to optimize the stirring in directional solidification, where flow fluctuations are an indicator for the mixing level in the melt.

The velocity oscillations in the melt center for different melt heights in Fig. 5.12 show an amplitude increase at melt heights that are both higher and lower than 5 cm for the isothermal case. For a melt height H = 2.5 cm, the amplitude is up to twice higher than the average value, which could be one of the reasons for the previously analyzed discrepancies between the simulation and the experiment. For the melt height of 10 cm in the asymmetric flow regime (observed in the simulation at H = 12.5 cm as discussed in the previous section), the same tendency appears; see Fig. 5.12 (e). An additional temperature gradient of 1 K/cm tends to decrease the amplitude of the oscillations in most cases, but the effect is not very distinct. Note that all measured velocity signals seem to have some noise when compared to calculations.

The velocity oscillations are directly coupled with temperature oscillations, and we observe an increase for a melt height of 10 cm (see Fig. 5.12 (c)). If we compare the ratio of

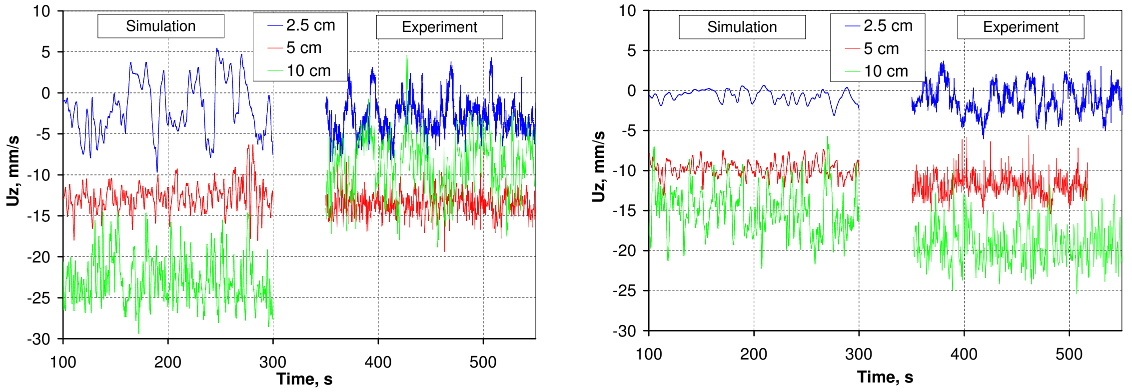

(a) Isothermal

(b) Non-isothermal

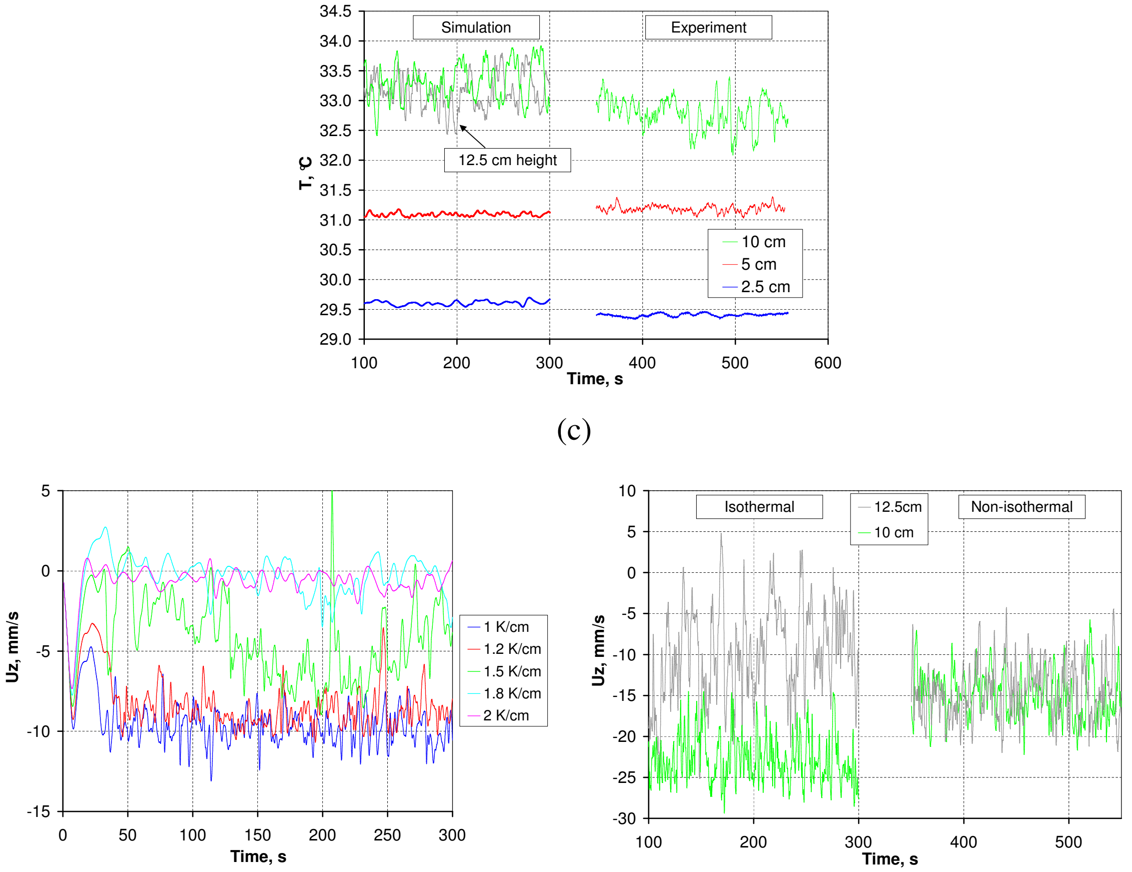

(c)

(d)

(e)

Figure 5.12.: Case with TMF up, $I_0 = 19.6$ A: calculated and measured oscillations of the vertical velocity (a,b) and temperature (c) in the melt center for melt heights $H = 2.5$, 5, and 10 cm in the isothermal (a) and non-isothermal (b,c) regimes (with temperature conditions $T_c/T_h = 25/32.5$, 25/35, and 25/40 °C, respectively); calculated vertical velocity oscillations for $H = 5$ cm with various temperature gradients in the melt (d); a comparison of the calculated velocity oscillations for $H = 10$ cm and 12.5 cm (e). [ExpINEMET, 2010]

the standard deviation of the calculated temperature oscillations to the mean value, we obtain 0.9% for 10 cm and 0.1% for both other cases – an increase by a factor of 9. The ratio of the maximum temperature difference between melt heights of 5 cm and 10 cm is only 2 because the temperature gradient in both cases is 1 K/cm. The typical largest period of temperature oscillations for the cases with 1 K/cm is approximately 20 s.

Numerical calculations for a melt height of 5 cm were additionally performed with further temperature gradients of 1.2, 1.5, and 1.8 K/cm. The velocity and its oscillations in the melt center were similar for the cases with 1 and 1.2 K/cm and those with 1.8 and 2 K/cm; see Fig. 5.12 (d). At the gradient of 1.5 K/cm, the average velocity value was in the middle between the other cases; however, the amplitude of the long-period oscillations was significantly larger, indicating that the flow actually oscillated between the state of dominating Lorentz forces ($dT/dz \leq 1.2$ K/cm) and dominating buoyancy forces ($dT/dz \geq 1.8$ K/cm). Therefore, the transitional stage between both regimes should be considered as a new flow regime, where new physical effects may appear.

5.4.6. Influence of inductor current

All results in the previous sections were obtained at the maximum inductor current of I_0 = 19.6 A. However, the interaction between the Lorentz and buoyancy forces depends not only on the temperature gradient but also on the Lorentz force density, which is proportional to the square of the inductor current. Fig. 5.13 summarizes the effect of the inductor current on the measured maximum velocity in the melt center and the measured maximum temperature difference. In the isothermal case, the velocity increases approximately linearly with the inductor current, which was previously ascertained in the former isothermal setup. Different melt heights lead to different slopes of the profiles, which need not cross the origin (0,0) because the linear function would probably not hold in the laminar regime at small flow velocities.

In the case of an additional temperature gradient of 1 K/cm, the velocity rapidly decreases with respect to the isothermal cases at a critical inductor current. The number of measurement points does not allow us to determine this point precisely. The critical current lies in the range I_0 = 13...16.3 A for a melt height of 5 cm. The critical current can be seen more clearly in the change of the maximum melt temperature difference. For all values of the melt height, the temperature difference drops approximately by a factor of 2 in the current range I_0 = 13...16.3 A. It can be clearly seen again that the transition between the flow regimes with dominating buoyancy and dominating Lorentz forces has a critical character.

5.5. Discussion

5.5.1. Scaling

The scaling of the fluid flow including the buoyancy force was discussed for a general case in Sec. 2.4. For the current system, the Poincare boundary conditions for the temperature must also be considered. If we introduce new scales for the length L_0 and for the temperature as $T = (T_h - T_c)T' + T_c$, the Poincare boundary conditions for the top and bottom of the melt transform to

$$\frac{\partial T'}{\partial n} = P_c(T'-0),\ P_c = \frac{p_T L_0}{\lambda} \quad \text{and} \quad \frac{\partial T'}{\partial n} = P_h(T'-1),\ P_h = \frac{p_T L_0}{\lambda}. \tag{5.4}$$

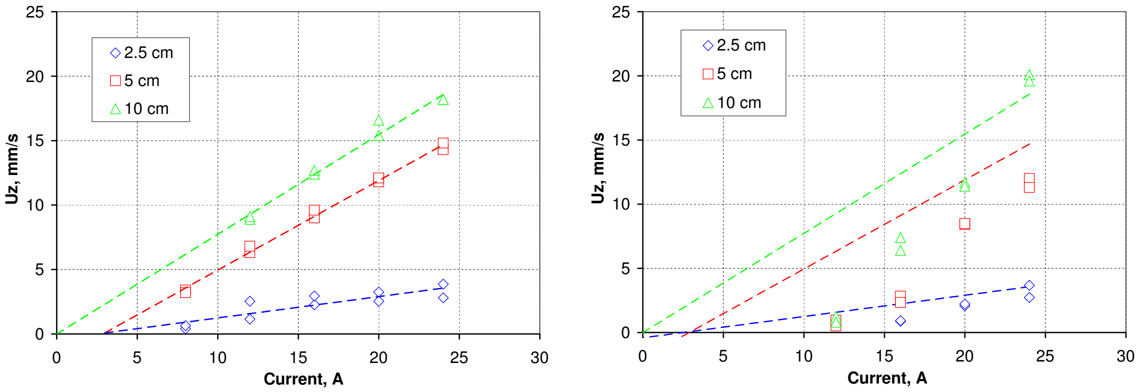

(a) Isothermal (b) Non-isothermal

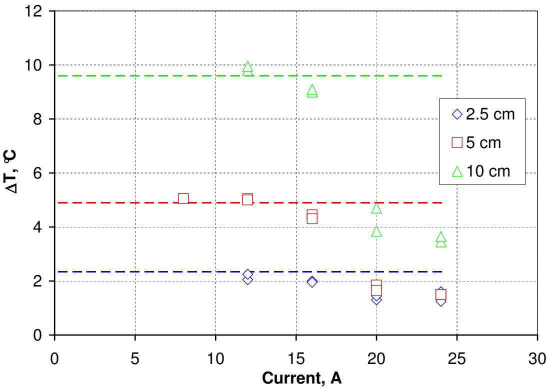

(c) Non-isothermal

Figure 5.13.: Influence of the inductor current: maximum measured time-averaged vertical velocity component in the melt center for the isothermal (a) and non-isothermal (b) cases; (c) maximum measured time-average difference between the temperatures at the melt top and bottom for the non-isothermal cases. A linear approximation is included for the velocity in the isothermal case. For the temperature in the non-isothermal case, the value without a TMF is given. For melt heights $H = 2.5$, 5, and 10 cm, temperature regimes $T_c/T_h =$ 25/32.5, 25/35, and 25/40 °C are considered, respectively. Results with TMF down are also included. The generator current I_{eff} is given here, where $I_0 = I_{\text{eff}}\sqrt{2/3}$. [ExpINEMET, 2010]

The system is now described by 7 dimensionless numbers – the Reynolds number Re, the TMF forcing parameter F_{em}, the shielding parameter S_{em}, the Grashof number Gr, the Prandtl number Pr, and the dimensionless numbers describing the heat transfer at the top and bottom of the melt $P_{h/c}$:

$$Re = \frac{\rho u_0 L_0}{\eta}, \quad F_{em} = F_{L0}\frac{\rho L_0^3}{\eta^2}, \quad S_{em} = 2\pi f \sigma \mu_0 L_0^2,$$
$$Gr = \frac{\rho^2 \beta g (T_h - T_c) L_0^3}{\eta^2}, \quad Pr = \frac{c\eta}{\lambda}, \quad P_{h/c} = \frac{p_T L_0}{\lambda}. \tag{5.5}$$

If the geometry is perfectly scaled and the numbers F_{em}, S_{em}, Gr, Pr, and $P_{h/c}$ remain constant, the value of Re also remains constant, and the distribution of the velocity and temperature is transferred perfectly.

Let us consider a simple example of transferring the results from the current study to the research scale (Gen1 silicon melt) and industrial scale (Gen5 silicon melt). We use the reference case from Sec. 5.4.1 with a melt height of 5 cm and with a temperature gradient of 1 K/cm. By choosing the characteristic vales, i.e., the maximum values for the force density F_{L0} and the velocity u_0, and by setting L_0 to half melt width as $L_0 = L/2$, we can calculate the dimensionless numbers as $Re = 2160$, $F_{em} = 1.3 \cdot 10^7$, $S_{em} = 3$, $Gr = 1.4 \cdot 10^7$, $Pr = 0.02$, and $P_{h/c} = 2$. For the transfer between GaInSn and silicon, we must neglect the difference of the Prandtl number, which is a material constant. The difference from $Pr = 0.011$ for silicon is not very large. Regarding the other parameters, F_{em} can be adjusted with the force density F_{L0} (i.e., with the inductor current), S_{em} can be adjusted with the frequency f, Gr can be adjusted with the temperature difference $T_h - T_c$, and $P_{h/c}$ can be adjusted with the Poincare coefficient p_T. The values of the adjusted parameters are summarized in Tab. 5.2.

L, cm	L_0, cm	F_{L0}, N/m^3	f, Hz	$T_h - T_c$, K	p_T, W/m^{2}K	u_0, cm/s
10 (GaInSn)	5	77	50	10	1563	1.5
20 (Gen1, Si)	10	3	40	0.9	1343	0.65
80 (Gen5, Si)	40	0.05	2.5	0.014	336	0.16

Table 5.2.: Example for scaling the results of model experiments in the present work to larger TMF systems with silicon.

It can be seen that up-scaling is complicated due to the high exponent in the Grashof number: $Gr \sim L_0^3$. If the only possibility is the adjustment of the temperature difference $T_h - T_c$, then this difference must be decreased to 0.7 K in the Gen1 melt and to 0.01 K in the Gen5 melt. The latter value is not realistic because temperatures cannot be controlled with this precision (in the sense of precise scaling, the melt still cannot be considered as isothermal). The same exponent in the forcing parameter $F_{em} \sim L_0^3$ leads to very weak Lorentz forces required in the larger system; however, these forces may still be realistic in some special cases.

The Poincare coefficient p_T, and the reference temperature $T_{ref} = T_{h/c}$ require physical interpretations in a real silicon furnace without any heater directly attached to the melt. At least two possibilities can be considered here:

- Heat conduction due to a contact with a body having a thermal conductivity λ_b and a fixed temperature T_b at a distance d_b from the contact. This case corresponds to the model experiments; hence $p_T = \lambda_b/d_b$, and $T_{ref} = T_b$.

- Heat radiation to an ambient temperature T_b from a surface with an emissivity ε and a view factor W. The radiation heat flux density out of the melt can be linearized for small temperature differences $T - T_b$ as follows:

$$\lambda \frac{\partial T}{\partial n} = \sigma_{sb} \varepsilon W (T^4 - T_b^4) \approx 4 T_b^3 \sigma_{sb} \varepsilon W (T - T_b). \tag{5.6}$$

  Here, we can assume $p_T = 4T_b^3 \sigma_{sb} \varepsilon W$ and $T_{ref} = T_b$.

The first case could approximately describe cooling at the bottom of the crucible in a silicon furnace, and the second case could describe heat radiation from the free surface. Note that the coefficients p_T at the top and bottom of the melt were equal in the model experiments.

The scaling between the first two cases in Tab. 5.2 is illustrated by 3D simulations in Fig. 5.14. The meshes for the Lorentz force and the flow calculations were up-scaled as in Sec. 4.4.1. In the Lorentz force calculation, the electrical conductivity of the heater and cooler material was also adjusted to keep the S_{em} number constant. To achieve a more realistic transfer to silicon, the temperature interval $T_c \ldots T_h$ was shifted to the range 1700.0…1700.9 K, and a radiation boundary condition using the approximation (5.6) with T_b = 1700.9 K and εW = 1.2 was applied on the top surface. This approximation and the difference in the Prandtl number between GaInSn and silicon make a perfect scaling impossible. Nevertheless, the velocity and temperature distributions in Fig. 5.14 show a good agreement if the scales are transformed according to the dimensionless numbers. Therefore, a realistic transfer of the results between the model experiments and silicon is also generally possible in the non-isothermal regime.

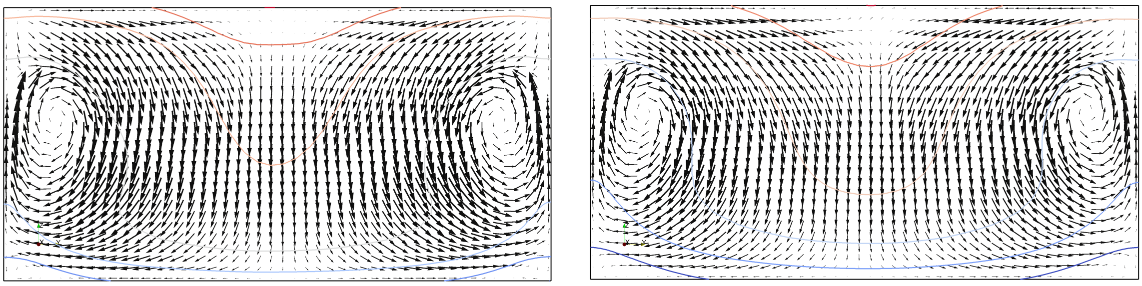

u_{max} = 1.47 cm/s, T = 301.75–305.16 K

(a) GaInSn, L = 10 cm,
f = 50 Hz, I_{0N} = 706 A

u_{max} = 0.62 cm/s, T = 1700.3–1700.68 K

(b) Si, L = 20 cm,
f = 40 Hz, I_{0N} = 395 A

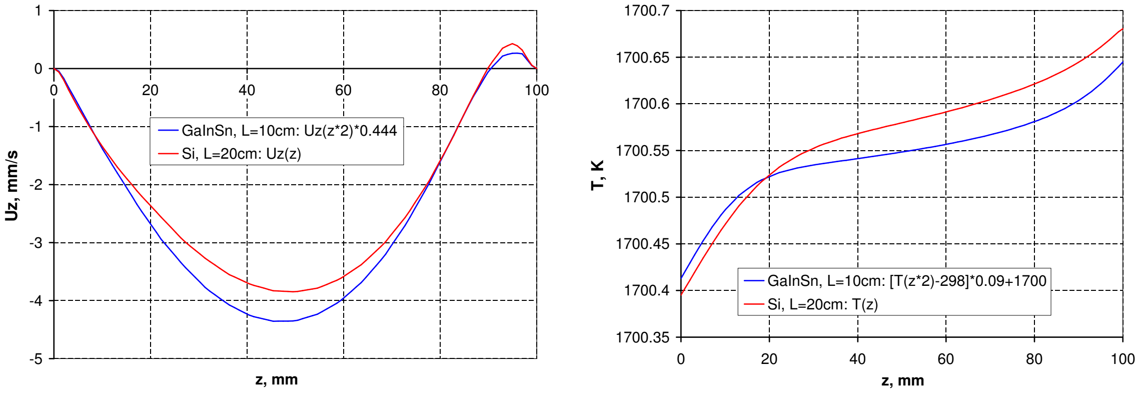

(c)

(d)

Figure 5.14.: Example for scaling the results of model experiments (GaInSn, L = 10 cm) to larger TMF systems with silicon (L = 20 cm) according to Tab. 5.2: (a,b) calculated time-averaged velocity vectors and temperature isolines in a vertical cut through melt center perpendicular to the side wall; calculated time-averaged vertical velocity (c) and temperature (d) profiles through the melt center. For the sake of comparison, the values for the small system are transformed according to the scaling laws as indicated in the diagrams.

The complications with the scaling of the temperature regime disappear if the buoyancy forces play a negligible role in comparison to the Lorentz forces in the melt. The Richardson number $Ri = Gr/Re^2$ was used to compare the role of buoyant and forced convection in the lid-driven cavity case [Iwatsu et al., 1993]. In that case, the forced convection dominates if

$Ri \ll 1$. In our case, there is no explicit velocity scale that allows the Reynolds number to be set, but we can compare the Lorentz forces (F_{em}) and the buoyancy forces (Gr) directly:

- $Gr \ll F_{em}$: the buoyancy forces in the melt are negligible in comparison to the Lorentz forces. The Lorentz forces determine melt convection.
- $Gr \gg F_{em}$: the Lorentz forces are balanced by the buoyancy forces, and the melt convection is very weak. Note that it is not correct to say that the buoyancy forces dominate in the melt; with a stable temperature stratification, there are no buoyancy forces and no melt motion without a second force.
- $Gr \sim F_{em}$: the Lorentz forces and buoyancy forces play a similar role in the melt convection. This case corresponds to Tab. 5.2 because $Gr \sim F_{em} \sim 10^7$.

It must be emphasized that the comparison of the F_{em} and Gr numbers is only a very rough estimate of the role of the corresponding forces. These dimensionless quantities depend on the choice of the characteristic values – the Lorentz force density and the temperature difference in particular. The ultimate criterion is to analyze threshold phenomena in the melt, such as a rapid decrease of melt mixing and an appearance of horizontal vortices at a high temperature gradient. Of course, several related parameters with practical relevance could be defined. Grants and Gerbeth [2008] considered an idealized low-frequency TMF in a cylinder and analyzed the required forcing F_b to exactly balance the buoyant flow at a deflected phase boundary. These researchers obtained $F_b \approx dGr$, where d is the ratio of the deflection to the radius. In a further study [Grants et al., 2009a], the critical forcing F_c causing flow instability was shown to fulfill $F_c \approx Gr$ for $F_c > 4 \cdot 10^5$. The Grashof number was introduced using the temperature difference $R \cdot \partial T / \partial z$.

5.5.2. Application to directional solidification of silicon

3D simulation of TMF flows were validated with velocity and temperature measurements in a GaInSn melt, including the effect of buoyancy forces. These numerical tools can be applied for further analysis of TMF flows during directional solidification of silicon. The noticeable discrepancies between the measured and calculated results in several cases could be explained by the highly unsteady, often transitional character of the flow as well as experimental uncertainties in both the measurements and the parameters of the setup.

It was shown that the typical toroidal flow structure induced by an upward or downward TMF may break down if the temperature gradient in a stable stratification is increased or if the Lorentz forces are decreased. This effect can be described as a thermal damping of the vertical melt motion and a prevention of mixing of the temperature field; the buoyancy forces cause the vertical TMF vortices to tilt and form horizontal vortices, typically two in each corner of a square melt. Such effects occur if the roles of buoyancy forces and Lorentz forces in the melt becomes comparable, which can be roughly estimated from $F_{em} \sim Gr$.

Transition from the flow regime dominated by the Lorentz force (high velocity and melt mixing) to the regime where the Lorentz force is balanced by buoyancy forces (low velocity and melt mixing) exhibits a critical character where the flow velocity drops and the temperature difference increases rapidly. Additionally, this transitional regime may temporarily lead to a significant decrease of the amplitude of flow oscillations.

The critical temperature gradient depends on melt height – 2 K/cm was needed at 5 cm and 1 K/cm at 2.5 cm to observe the appearance of horizontal vortices. Therefore, the natural decrease of the melt height during directional solidification might cause a transition between both flow regimes even with a constant Lorentz force and a constant temperature gradient in the melt. This can be an additional threshold effect in addition to the appearance of the central horizontal vortex at a small melt height in flows dominated by Lorentz forces. Another transition to a new flow regime with an asymmetric 3D torus may appear if the melt's height-to-width ratio exceeds unity.

Such transitions during the crystal growth might induce unwanted effects alone, or the different flow regimes might have different effects on the crystal quality. In both cases, an analysis of crystal growth equipments with respect to such effects in the melt flow is recommended.

Part III.

Numerical studies

Chapter 6

Global temperature distribution in the furnace

At the beginning, a simplified design of a small-scale furnace for directional solidification of silicon is defined on the basis of the available experience. This provides the framework for a global thermal parameter study, which aims to identify main properties of thermal furnace design important for the application of a TMF. As a result, realistic temperature gradients in the melt, phase boundary shape, and crystallization rate for further studies are obtained. A sensitivity analysis allows to estimate the range for the variation of these parameters in reality.

6.1. Reference case

The main control parameters of a directional solidification furnace are the heating and cooling powers. While the heating power can usually be directly set with the electrical power in resistance heaters, the cooling power is controlled indirectly with the conditions for the thermal radiation or for the flow of a cooling medium. A minimal furnace model that allows one to investigate the influence of heating and cooling powers on the thermal conditions in the silicon must include at least a heat sink under the crucible and a thermal insulation behind the heaters. The simplified model geometry used in this chapter is shown in Fig. 6.1. The silicon melt with a full size of 22×22×18 cm^3, which corresponds to a Gen1 crucible size, is contained in a silica crucible with a thickness of 1.5 cm. The crucible is positioned on a graphite heat sink and is supported by graphite plates with a wall thickness of 1.5 cm at the sides. Above the melt, a top heater is located at a distance of 18 cm. Three side heaters are surrounding the crucible with the intention of possibly serving also as TMF inductors. The hot-zone is enclosed by a graphite felt insulation with a thickness of 5 cm.

This model furnace can be constructed with only 5 different materials (also including argon gas). Material properties relevant for thermal calculations are summarized in Tab. 6.1. These values should be considered as approximations for the real temperature-dependent properties. The role of these approximations will be investigated in a dedicated parameter study later in this chapter. Thermal boundary conditions for the reference case are given in Fig. 6.1 (a). Because the hot-zone is usually surrounded by a water-cooled steel vessel, heat radiation to an ambient temperature of 300 K is assumed on the outer surface of insulation. The heating and cooling powers are set to resemble the start of a crystallization process with a temperature of 1686 K at the center of melt bottom. The cooling power at the bottom surface of the heat sink is set to 4 kW, and the heater powers are found using the *Smart heater* method in `Elmer`, which adjusts the heater power to match the prescribed temperature at a control point. All heaters are set to the same power.

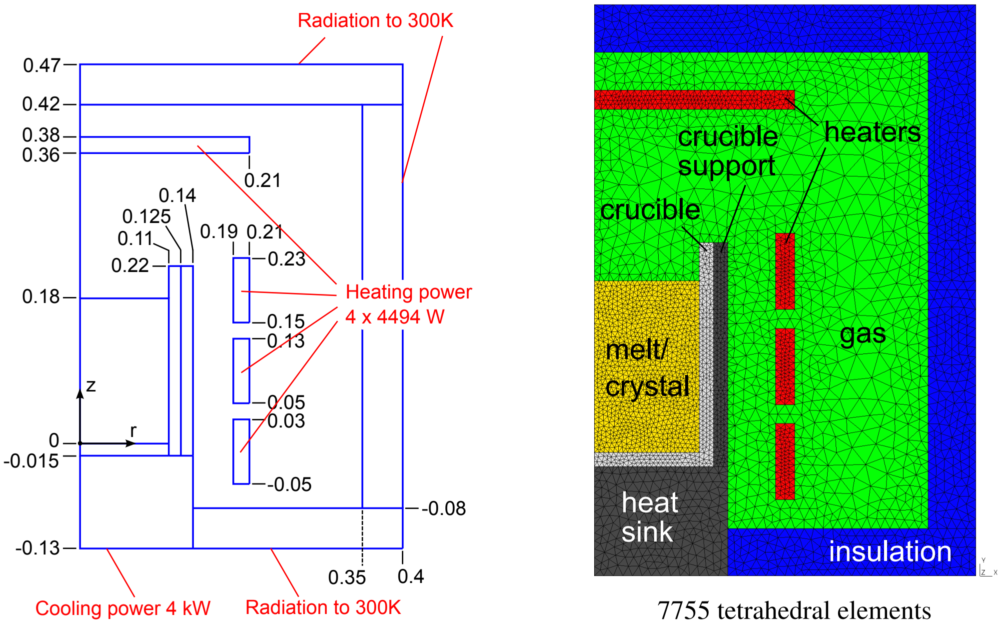

(a)

7755 tetrahedral elements

(b)

Figure 6.1.: Reference case: (a) geometry (coordinates in m) and boundary conditions (steady-state without crystallization); (b) 2D mesh and materials for thermal calculations.

Material	Furnace parts	λ, W/mK	ρ, kg/m^3	c, J/kgK	ε
Graphite	heat sink, heater, crucible support	45	1900	2000	0.9
Graphite felt	insulation	0.3	200	700	0.9
Fused silica	crucible	1.7	2000	1000	0.9
Silicon (liquid)[a]	melt	67	2520	986	0.2
Silicon (solid)	crystal	22	2329	986	0.5
Argon	gas	0.06	0.28	520	–

[a] Phase change at T_m =1685 K releasing a latent heat of Q_l = 1.8·10^6 J/kg.

Table 6.1.: Material properties (typical values from various sources) and furnace parts for global thermal calculations.

The tetrahedral mesh used in 2D calculations with `Elmer` is generated with `Gmsh` using a parametrized input script; see Fig. 6.1 (b). The obtained steady-state temperature distribution is depicted in Fig. 6.2. The maximum temperature in the furnace reaches 1738 K, which is 53 K above the melting point of silicon. Almost the entire temperature decrease down to the lowest temperature of 412 K occurs within the insulation. Large temperature jumps occur also in the crucible walls (100 K in the bottom and 20 K in the side wall), which has a relatively small thermal conductivity. The maximum temperature in silicon reaches about 1700 K, and the distribution shows an increase in radial direction. However, it must be noted that the temperature distribution may change significantly once the crystallization starts and the latent heat is released.

Fig. 6.2 (a) shows also the heat fluxes on various surfaces inside the furnace. The total power of all heaters is 18 kW. It should be noted that this is the effective heater power for an idealized furnace model without many possible heat losses through various gaps or thermal bridges. More than 70% or almost 13 kW of the heating power flows directly into the insulation and is received by the cooling system of the vessel. This percentage is obviously determined primarily by the thickness of the insulation, which is a compromise between the costs of insulation and the costs of energy required for heating and cooling the furnace in the reality. Further 20% or 4 kW of the heating power goes directly to the heat sink so that only a small fraction of the cooling power is available for crystallization. This is a property of the simplified furnace design, which would have to be made more complex to avoid such thermal bridges. Note that the values of the evaluated heat fluxes may be imprecise by about 10% due to the numerical integration involved.

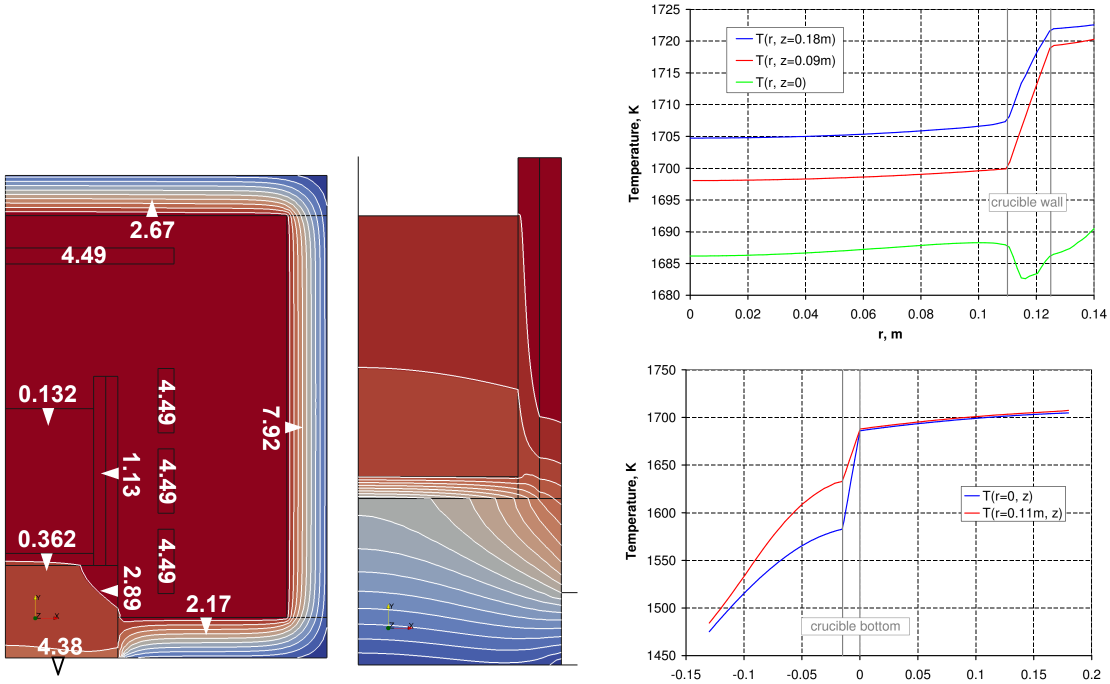

T = 412–1738 K
(a)

T = 1461–1723 K
(b)

(c)

Figure 6.2.: Stationary 2D temperature calculations for the reference case: temperature field and heat fluxes (white numbers, in kW) in the entire system (a) and in silicon (b); (c) axial and radial temperature distribution in the furnace.

6.2. Influence of 3D effects in a quadratic system

Directional solidification of multicrystalline silicon is performed in crucibles with a square cross section; therefore, an exact calculation of the global temperature distribution in the furnace requires a 3D model. Because such calculations are very time-consuming and inefficient for parameter studies, it is important to determine how large is the modeling error introduced by a 2D model with a cylindrical melt and furnace parts.

Two 3D calculations for the reference case in Sec. 6.1 were carried out with `Elmer` – for an axisymmetric geometry and for a square geometry. The axisymmetric geometry corresponds exactly to the 2D reference case. The definition of the square geometry involves several adjustments of the horizontal cross sections:

- Horizontal cross section of the melt is kept constant to preserve the mass of silicon at the same melt height. The melt width L is calculated from $\pi R^2 = L^2$ as 0.195 m.
- Thicknesses of crucible and support crucible are not changed to preserve the same thermal resistance.
- Inner and outer side surfaces of side heaters are kept constant to obtain a similar heater temperature at a similar power. This gives L_{in} = 0.298 m for the inner diameter from $2\pi R_{in} = 4L_{in}$ and L_{out} = 0.330 m for the outer diameter from $2\pi R_{out} = 4L_{out}$. Note that the distance between the support crucible and the heaters decreases from 50 mm to 22 mm, and the heater thickness increases from 20 mm to 32 mm.
- The same condition for the horizontal surfaces of the top heater results in a heater width L of 0.372 m according to $\pi R^2 = L^2$.
- The thickness of insulation is not changed to preserve the same thermal resistance. Inner diameter of the side insulation L_{in} is adjusted to obtain a similar inner surface of the entire insulation. From $2\pi R_{in}^2 + 2\pi R_{in} H = 2L_{in}^2 + 4L_{in} H$, where H is the height of the side insulation, we obtain L_{in} = 0.588 m.

Despite of these adjustments, the temperature levels in the axisymmetric and square cases may be different also at a similar power level. Therefore, heater powers were adjusted as in the 2D calculations in Sec. 6.1 to allow a better comparison of temperature profiles.

The geometry and mesh for both cases are shown in Fig. 6.3 (a, b). Further figures describe the temperature distribution. It can be seen that the temperature profiles on the vertical axis agree very well. The horizontal profiles show a shift due to geometry changes as well as higher temperatures by about 4…8 K in the crucible wall and especially in the corners for the square geometry. The hot corners can be also clearly seen in the temperature distribution in a horizontal cut. This effect can be explained by the fact that a crucible corner receives heat radiation from two heater sides simultaneously. Such corner effects cannot be captured by a 2D model, but otherwise temperature fields in the axisymmetric and square geometries are similar. Of course, an important point is the adjustment of heater power, which slightly increased – from 4.51 kW in the 3D axisymmetric case to 4.58 kW in the square case. With this adjustment, deviations between the 2D (from Fig. 6.2 (c)) and 3D axisymmetric profiles are less than 1 K as can be seen in Fig. 6.3 (d), which demonstrates a good accuracy of the 3D calculation.

6.3. Steady-state sensitivity analysis

To find the parameters of furnace design with the largest influence on the temperature field in the silicon, a sensitivity analysis is performed, where values of input parameters such as material properties or geometrical dimensions are typically decreased or increased by a factor of 2. In each case, the heater power is adjusted to reach a temperature of 1686 K at the melt bottom. The following response parameters are evaluated in all cases:

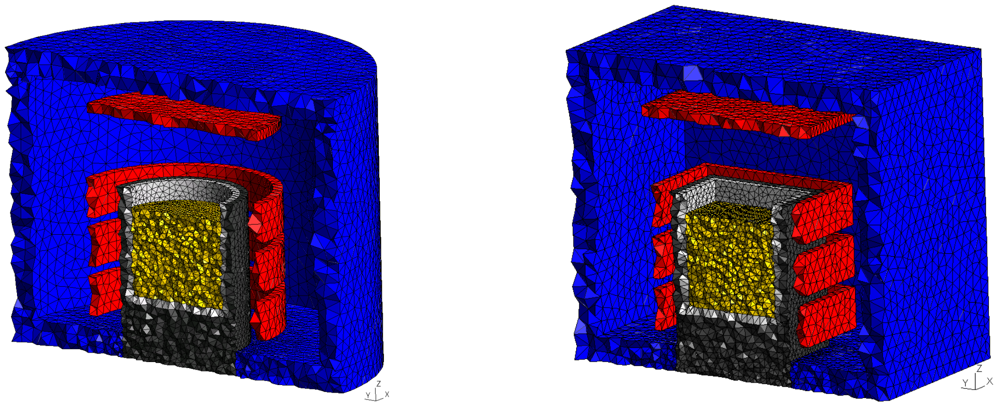

331104 volume and 19422 surface radiation elements 317232 volume and 20380 surface radiation elements

(a) Cylindrical, $R = 0.11$ m (b) Square, $L = 0.19$ m

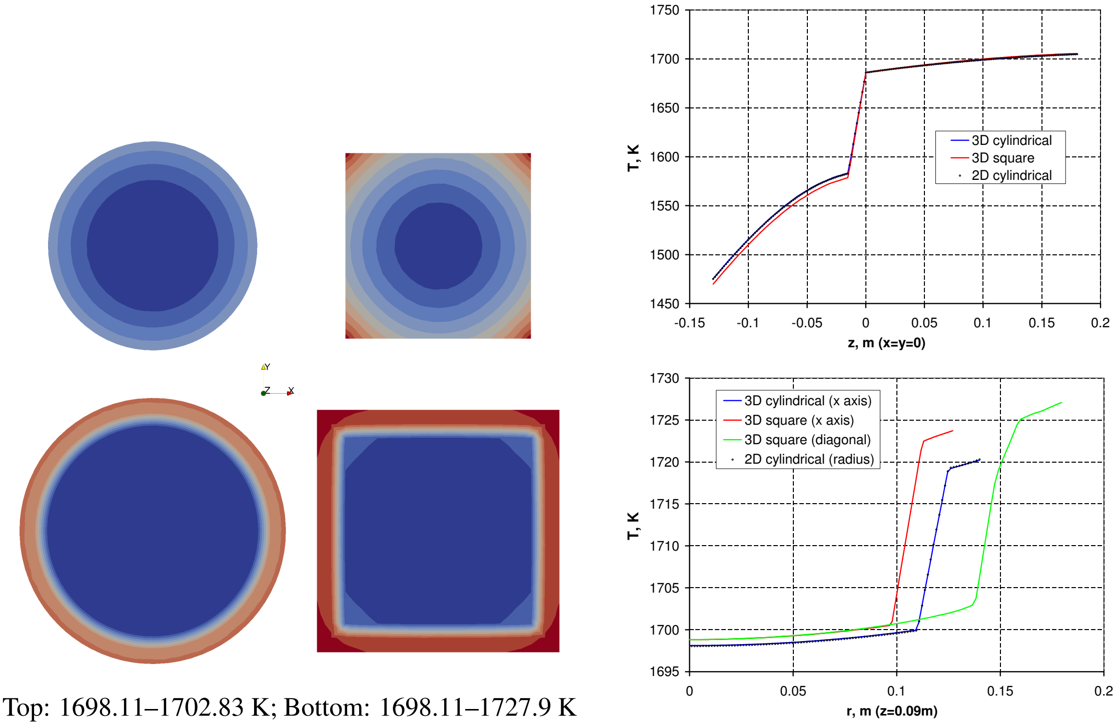

Top: 1698.11–1702.83 K; Bottom: 1698.11–1727.9 K

(c) (d)

Figure 6.3.: Role of 3D effects in global thermal calculations for the reference case in Fig. 6.2 calculated in 3D with a cylindrical and square geometry: (a,b) geometry and mesh used in the calculations; comparison of temperature distributions in a horizontal cut through the melt center in melt (c, top) and in melt + crucible + support crucible (c, bottom); comparison of temperature distributions on the axis (d, top) and on a horizontal line (d, bottom).

- Vertical temperature gradient in the melt approximated with the temperatures at the top and bottom of the melt on the axis
- Horizontal temperature gradient in the melt approximated with the temperature on the axis and on the crucible wall at mid-height
- The adjusted heater power

A comparison of response values for three different input parameters allows one to estimate not only the magnitude of the influence but also the direction.

The results of sensitivity analysis for thermal conductivities and emissivities of various furnace parts are summarized in Fig. 6.4. The thermal conductivity is decreased by a factor of 2 and increased by a factor of 2 from the reference value. The emissivity of the melt (0.2) is increased by factors of 2 and 4; the emissivity of other materials (0.9) is decreased by factors of 2 and 4. Most emissivities have a marginal influence on temperature gradients in the silicon. Only a lower emissivity of graphite is able to increase the vertical temperature gradient in the melt: a smaller amount of heat is received by the support crucible and flows directly to the heat sink. For thermal conductivities, only the values for the silicon and crucible show a larger impact. Consequently, a special attention should be paid to these three input parameters when building models for specific furnaces.

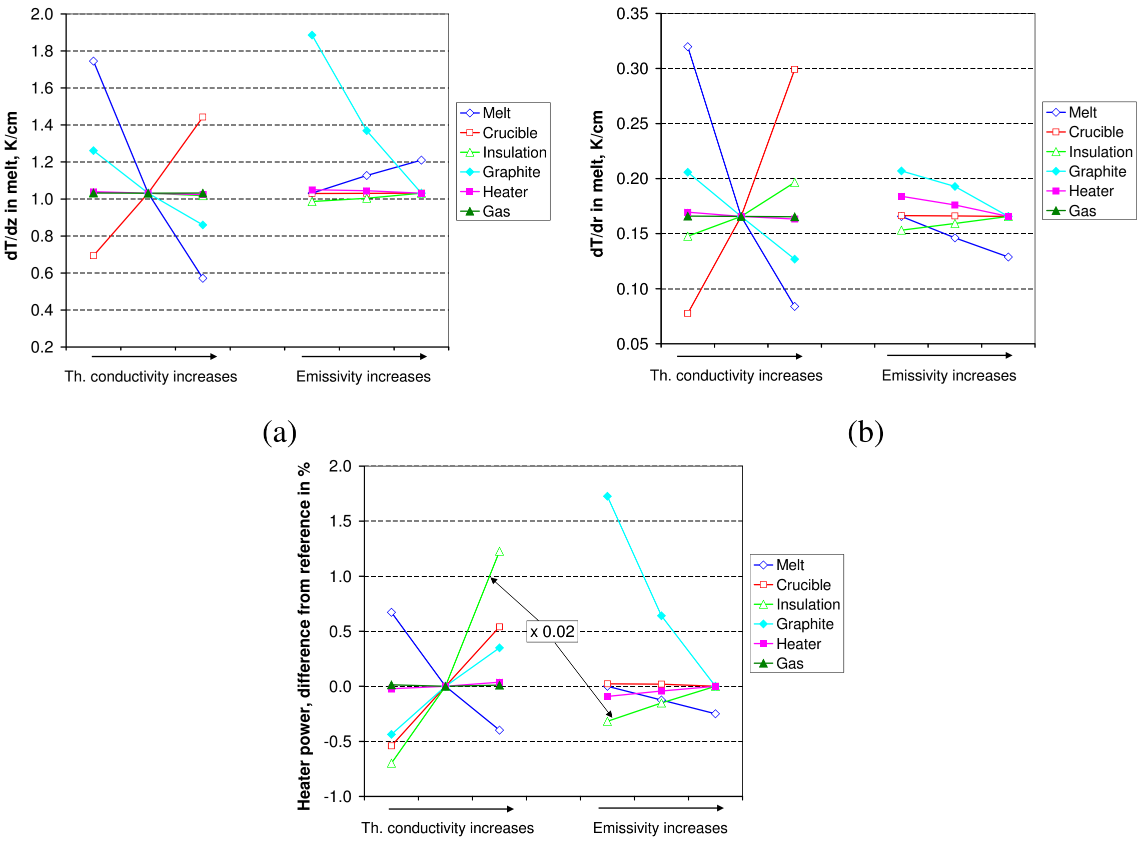

(a) (b)

(c)

Figure 6.4.: Stationary 2D temperature calculations: influence of material properties on the vertical (a) and horizontal (b) temperature gradient in the melt as well as on the heater power (c) adjusted to obtain 1686 K on the melt bottom.

The required changes in heater power to compensate the changes of material properties mostly are not larger than about 1% or 45 W from the reference power in one heater. Two exceptions are the thermal conductivity and emissivity of the insulation. The thermal conductivity of insulation basically sets the required level of heating power. As a simple physical model, let us consider a cube with an inner distance between walls $l_i = 0.6$ m, wall thickness $l_w = 5$ cm, and thermal conductivity of walls $\lambda_w = 0.3$ W/mK. The total heat flux through the

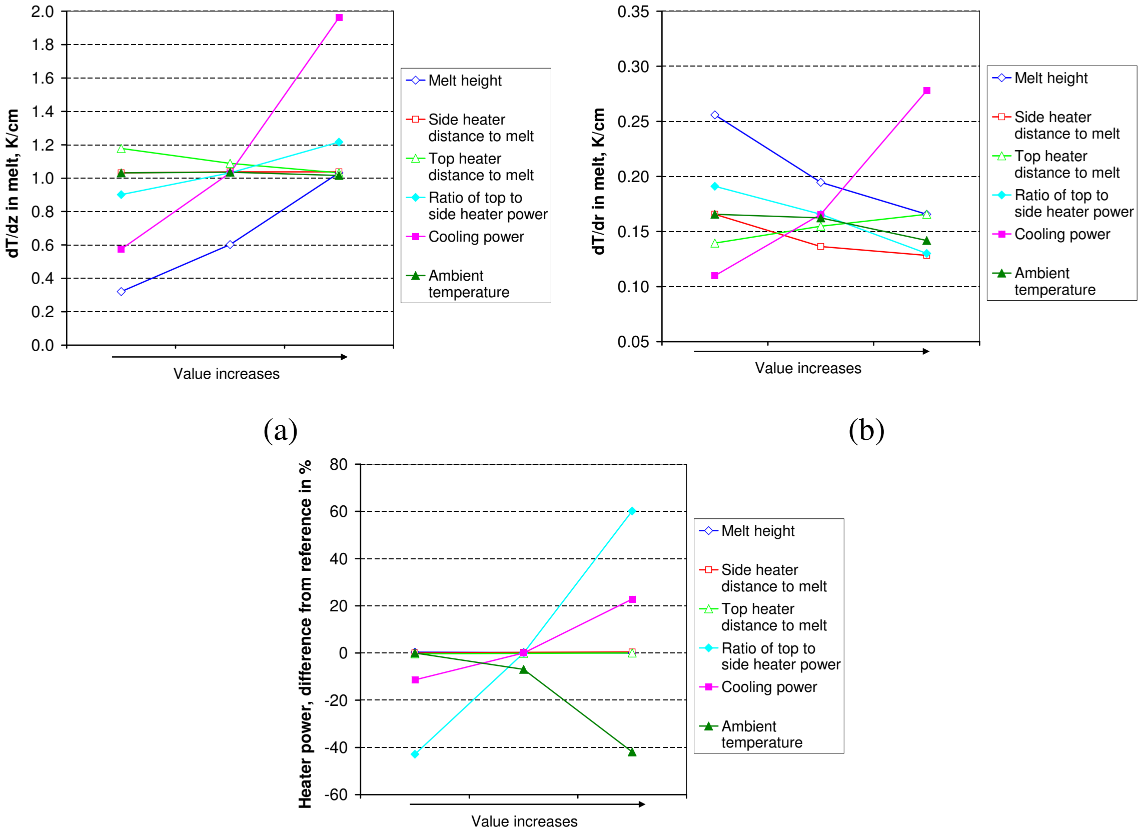

(a) (b)

(c)

Figure 6.5.: Stationary 2D temperature calculations: influence of geometric parameters and thermal boundary conditions on the vertical (a) and horizontal (b) temperature gradient in the melt as well as on the heater power (c) adjusted to obtain 1686 K on the melt bottom.

walls in [W] can be estimated as

$$Q_w = \lambda_w \frac{\Delta T}{l_w} \cdot 6 l_i^2, \tag{6.1}$$

where ΔT is the temperature difference between the outer and inner surface of the cube. With $\Delta T = 1700 - 300 = 1400$ K, we obtain Q_w = 18.1 kW, which qualitatively agrees with the difference of 14 kW between the total heating power and cooling power in the reference case.

In a further series of calculations, geometric parameters and thermal boundary conditions were varied. The results are summarized in Fig. 6.5. The melt height was decreased from the reference value to 9 cm and 4 cm. It can be seen that a lower value decreases the vertical temperature gradient in the melt and increases the radial temperature gradient. The distance between the side heaters and the crucible was increases by 5 cm and 10 cm, the distance between the top heater and the melt was decreased by 5 cm and 10 cm. Both these distances have a remarkably small influence on the temperature field in silicon and practically no influence on the required heating power. A somewhat larger influence is caused by the ratio of top heater power to side heater power, which was decreased to 1:2 and increased to 2:1 from the reference value of 1:1. A higher side heater power (a smaller ratio) causes a smaller vertical temperature gradient and a larger radial temperature gradient, as expected. Note that the heating power changes in Fig. 6.5 are given for the top heater alone – the total required heating power changed by less than 0.1%. Finally, the cooling power was decreased by a factor of 2 (to 2 kW) and increased by a factor of 2 (to 8 kW). It can be seen that a higher cooling power significantly increases both temperature gradients in the melt because all heat fluxes increase (and the required heating power rises).

To check whether the assumed cooling powers at the bottom of the heat sink are realistic, we can estimate the required ambient temperature for a cooling by heat radiation from the bottom surface of the heat sink. The expression for the radiative heat flux Q_c allows one to find the ambient temperature T_a in the following way:

$$Q_c = \pi R_c^2 \sigma_{sb} \varepsilon_c (T_c^4 - T_a^4) \quad \Rightarrow \quad T_a = \left(T_c^4 - \frac{Q_c}{\pi R_c^2 \sigma_{sb} \varepsilon_c} \right)^{1/4}, \tag{6.2}$$

where ε_c, T_c, and R_c are the emissivity, temperature, and radius of the bottom surface of the heat sink, respectively. Assuming $\varepsilon_c = 0.9$, $T_c = 1500$ K (see Fig. 6.2 (c)), and $R_c = 0.14$ m, we obtain for $Q_c = 2 \ldots 10$ kW a temperature interval $T_a = 1450 \ldots 1171$ K. Obviously, the considered cooling powers theoretically could be achieved also with a radiative cooling from the heat sink.

In summary, temperature conditions in the melt can be controlled most efficiently using the cooling power and the ratio between the top and side heater powers (in addition to the total heating power). These parameters will be further varied in unsteady calculations with crystallization in the following section. It is important to note that temperature gradients in the melt may significantly change with melt height.

6.4. Unsteady calculations

6.4.1. Available crystallization rates and temperature gradients in melt

Stationary calculations allow one to estimate the role of various parameters on the temperature conditions in the furnace, but directional solidification is a distinctly unsteady process. Both the released latent heat and the moving crystallization interface (the changing fraction of solid and liquid silicon) may significantly influence thermal conditions in the furnace. Therefore, the analysis of the velocity and shape of crystallization interface requires unsteady calculations.

The temperature distribution from the reference case is applied as the initial condition for the unsteady crystallization process. Obviously, to decrease the temperature level in the melt and initiate crystallization, the cooling has to be increased. Simultaneously, the heating power may have to be adjusted to obtain optimal temperature gradients in the melt. A parameter study for the first 3 hours of crystallization was performed with different cooling powers and controlled temperatures of the top heater (the powers of side heaters were not changed). The temperature at the melt top (describing the vertical temperature gradient in the melt) and the position of crystallization interface on the axis after 3 hours (describing the crystallization velocity) for all cases are given in Fig. 6.6 (a,b).

We can distinguish three parameter ranges:

1. With a low cooling power and high heater temperature, no solidification occurs (interface position remains at zero) because temperature in the melt remains above the

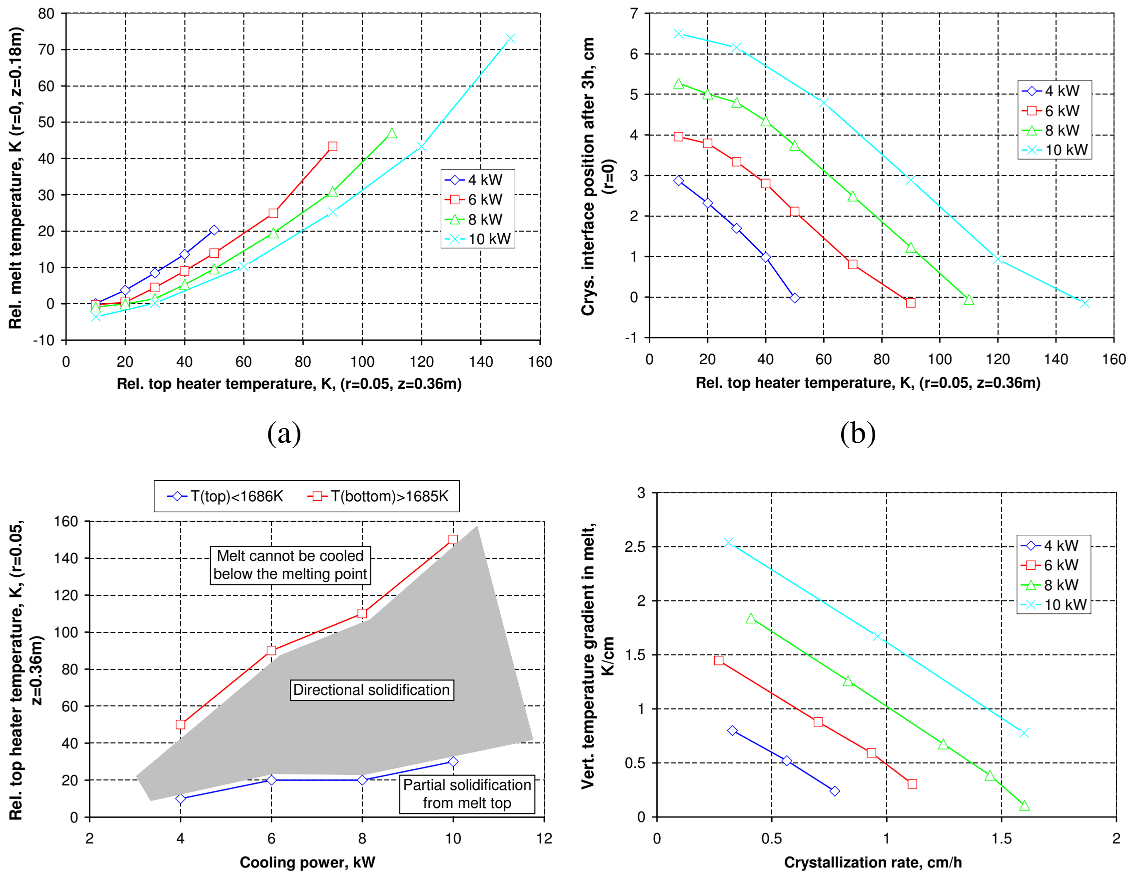

(a) (b)

(c) (d)

Figure 6.6.: Unsteady 2D temperature calculations: temperature (given relative to 1685 K) at the melt top (a) and interface position on the axis (b) after 3 h for different cooling powers and top heater temperatures (given relative to 1685 K). Possible combinations of values: heater temperature – cooling power (c); temperature gradient in the melt – crystallization velocity (d).

melting point.

2. With a high cooling power and low heater temperature, temperature gradients in the melt tend to zero, crystallization rates are high, but crystallization may simultaneously occur from the melt bottom and top (temperature at the melt top drops below 1685 K).

3. With an optimal cooling power and heater temperature, a directional solidification from the bottom to the top is observed. The crystallization velocity and temperature gradient in the melt simultaneously depend on the cooling power and heater temperature. This parameter window is illustrated in Fig. 6.6 (c).

With a careful adjustment of cooling power and top heater temperature, any combination of crystallization rate and temperature gradient in the melt can be achieved as shown in Fig. 6.6 (d). Of course, only within the available range of cooling powers and heater temperatures in the reality. For example, if the maximum available cooling power is 6 kW, a crystallization velocity higher than 1 cm/h is related to a nearly zero temperature gradient in the melt.

Fig. 6.6 (d) shows a linear dependence between the crystallization rate v and vertical temperature gradient in the melt dT/dz. It can be approximated for all cooling powers P_c as

$$\frac{dT}{dz}[K/cm] = 0.3 \cdot P_c[kW] - 1.35 \cdot v[cm/h]. \tag{6.3}$$

A similar expression can be obtained from the Stefan conditions describing the heat balance at the crystallization interface (2.71). If we express the temperature gradient in the crystal as $P_S/\pi R_S^2 \lambda_S$, where P_S is the effective cooling power at the melt bottom with a radius R_S, we obtain for the gradient in the melt:

$$\begin{aligned}\frac{dT}{dz}[K/m] &= \frac{1}{\pi R_S^2 \lambda_L} \cdot P_S[W] - \frac{Q_l \rho_S}{\lambda_L} \cdot v[m/s] \quad \Rightarrow \\ \frac{dT}{dz}[K/cm] &= 3.9 \cdot P_S[kW] - 1.74 \cdot v[cm/h]. \end{aligned} \tag{6.4}$$

A comparison of the first terms on the right-hand side in the numerical and analytical expressions allows one to estimate the ratio of the effective cooling power to the actual cooling power: P_S/P_c = 0.08, i.e., only 8% of cooling power contributes to the crystallization. As already mentioned, this effect occurs due to a direct connection between the heating and cooling systems in the considered model furnace. This effect is the main deviation from an idealized system where the heater power would set the temperature gradient in the melt and the cooling power would determine the crystallization rate. In the current system, both input parameters influence both response parameters.

6.4.2. Reference calculations

For the reference calculation of a complete crystallization process, the case with a cooling power of 8 kW and a top heater temperature of 1685+50 K is selected. A linear decrease of the top heater temperature to 1685+30 K during 20 h is defined to allow the entire melt to be solidified. The interface position and temperature at the melt top in dependence of time are shown in Fig. 6.7 (a,b). It can be seen that the crystallization is finished after about 19 h, which gives an average crystallization velocity of 1 cm/h. The interface shape is slightly concave (3 mm) at the beginning and slightly convex (3 mm) at the end of crystallization. The vertical temperature gradient in the melt drops from an initial value of about 1 K/cm to 0.5 K/cm at the half melt height. The radial temperature gradient in the melt changes its sign: temperature isolines in Fig. 6.7 (c) are convex in the top part and concave in the bottom part.

Steady-state calculations indicated that the radial temperature gradient can be influenced by the power ratio between the top and side heaters. To investigate the influence on the shape of crystallization interface, the power of side heaters is reduced by a factor of 2 – to 2.25 kW. Because the temperature of the top heater is prescribed, its power increases. It turned out that the top heater temperature has to be increased to avoid crystallization from the melt top. Obviously, the optimal range of parameters in Fig. 6.6 (c) is influenced also by the power ratio between the top and side heaters. With the reduced power of side heaters, a similar crystallization velocity (without a crystallization from the top) as in the previous case was achieved when the top heater temperature was set to +90 K, with a linear decrease to +50 K during 20 h.

The time-evolution in Fig. 6.7 (a,b) shows that the crystallization is finished after 15 h, which gives an average crystallization velocity of 1.2 cm/h. The interface shape is concave during the entire crystallization, and the deflection decreases from 1 cm at the beginning to 7 mm at the end. This is an expected effect of the smaller side heater power because the heating at the melt side decreases. The vertical temperature gradient at half melt height is 0.8 K/cm – the value is larger than in the previous case with a higher side heater power. The top heater power after 3 h was 11.29 kW (4.52 kW previously). The temperature difference in the melt between the axis and the side is 1.2 K, which corresponds to an approximate radial gradient of 0.1 K/cm. To keep constant temperature gradients in the melt or a constant interface deflection, an adjustment of both the power of all heaters and the cooling would be required for the considered furnace geometry.

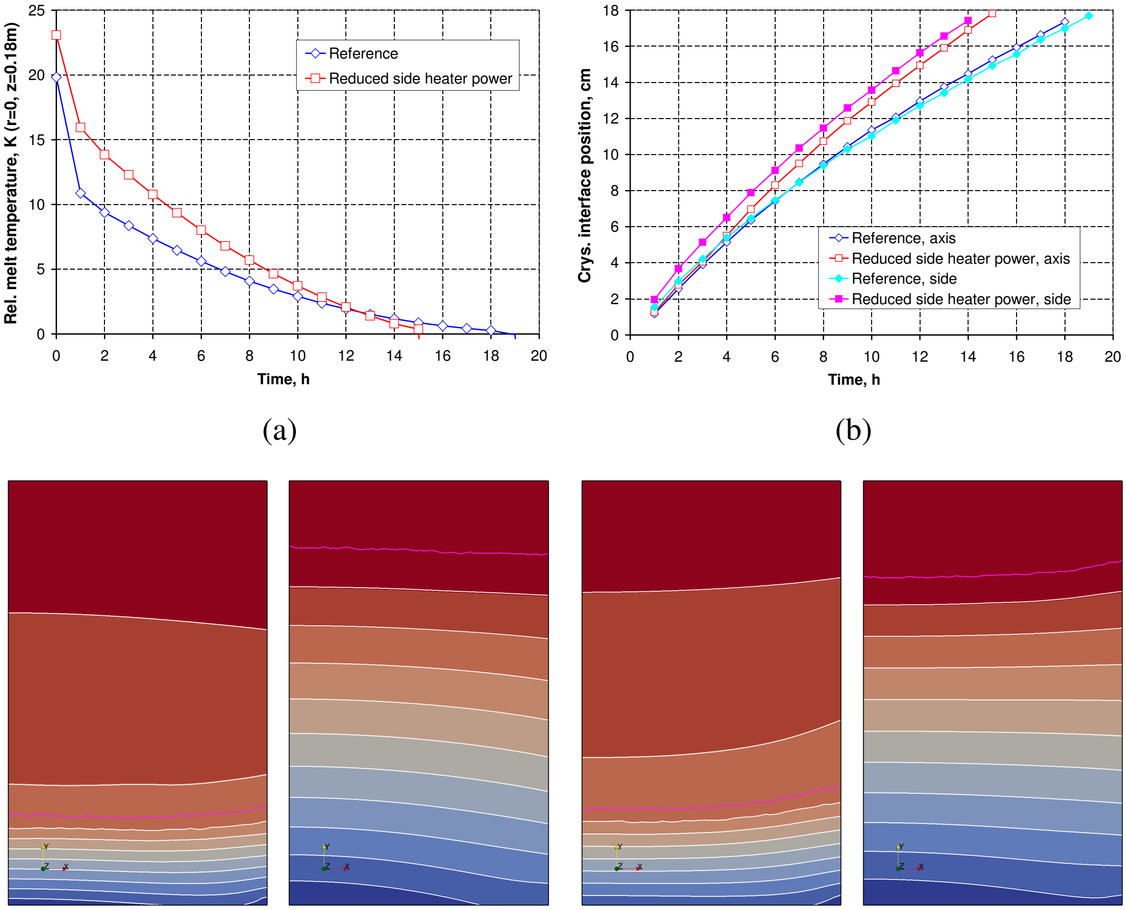

(a) (b)

T = 1646.5–1695.1 K, *T* = 1585.5–1686.5 K *T* = 1633.8–1698.9 K, *T* = 1570.4–1688.2 K

(c) (d)

Figure 6.7.: Unsteady 2D temperature calculations: temperature at the melt top (a) and interface position (b) in dependence of time; temperature distribution 3 h after the start and 5 h before the end of crystallization (the pink line denotes the crystallization interface) for the cases with the standard (c) and reduced (d) power of side heaters.

6.4.3. Relation between lateral temperature gradients and interface deflection

The deflection of crystallization interface is primarily determined by the lateral heat flux at the melt side, but both the relative vertical heat flux at the melt top and the relative cooling power at the bottom may have an influence. These dependencies can be investigated more exactly in a local model. We consider a steady-state model in `OpenFOAM`, which consists of the melt and crystal domains alone as described in Sec. 3.3.2.1. The cooling heat flux at the crystal bottom Q_b is adjusted according to the heat balance with the heat flux at the melt top Q_t, heat flux at the melt side Q_s, and the prescribed steady-state growth velocity v_{n0}: $Q_b = Q_t + Q_s + \rho_s Q_l v_{n0}$. This condition ensures that a steady-state crystallization interface at a growth velocity near the prescribed value v_{n0} exists. Some deviations between the prescribed and adjusted (to keep the point at the interface center at its initial position) values of v_{n0} may occur if the interface is very deflected and its surface area, i.e., the corresponding integral latent heat change.

The calculated interface deflections for various values of Q_t (the equivalent temperature gradient in the melt is given), Q_s, and initial v_{n0} are summarized in Fig. 6.8. For the reference case with v_{n0} = 1 cm/h, a convex deflection of 1 cm is reached at a lateral heat flux toward the melt of about 4000 W/m^2, which corresponds to a temperature gradient at the melt side of 0.6 K/cm. The increase of the concave interface deflection is much steeper for a lateral heat flux out of the melt, where a deflection of 1 cm is reached already at 1675 W/m^2, corresponding to 0.25 K/m at the melt side. For a growth velocity of 1 cm/h and temperature gradient at melt top of 1 K/cm, the theoretical maximum heat flux out of the melt side is 4587 W/m^2. Then the required cooling Q_b at the melt bottom is zero, and the solidification would actually start at the melt side.

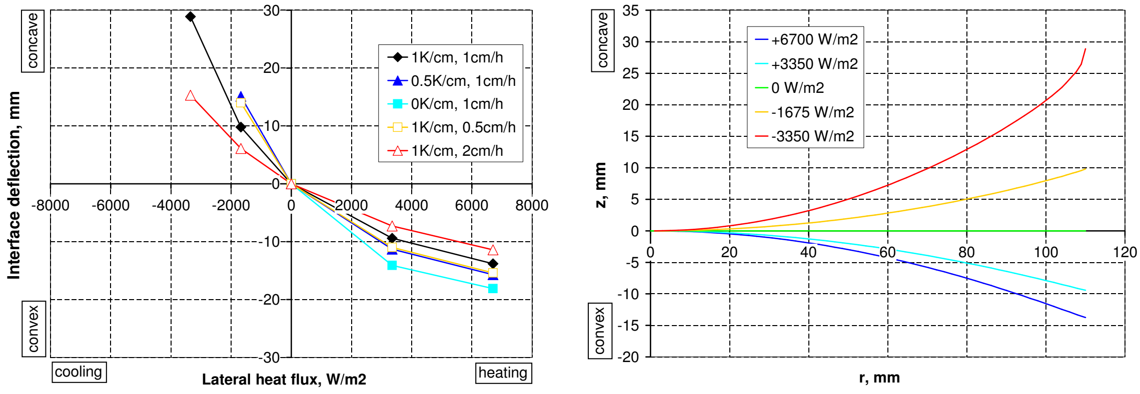

(a) (b)

Figure 6.8.: Steady-state 2D calculations of crystallization interface shape in a local model: (a) dependence of interface deflection of the lateral heat flux, steady-state crystallization velocity, and vertical temperature gradient at the melt top; (b) comparison of steady-state interface shapes for different lateral heat fluxes (with a crystallization velocity of 1 cm/h and a vertical gradient of 1 K/cm).

6.5. Discussion

6.5.1. Role of various furnace parameters

From all properties of materials in the considered model furnace, mainly thermal conductivities of crucible and silicon as well as the emissivity of graphite have a significant influence on temperature gradients in the melt in a steady-state. The influence of most other material properties can be compensated by an adjustment of the absolute level of heater powers. Such adjustments are crucial for the thermal conductivity of insulation, which basically sets the required level of heating power in the furnace. The density and heat capacity of materials are irrelevant in steady-state calculations and were not investigated.

From the geometric and thermal parameters, mainly the cooling power and the power ratio of the top and side heaters influence the temperature gradients in the melt in a steady-state. Most other parameters, such as the distance between the heaters and the melt, have a rather small influence. The influence of the size of various furnace parts, which was not investigated explicitly, can be estimated from the influence of thermal conductivity: for a constant heat flux through a wall, an increase of the wall thickness is equivalent to a decrease of its thermal conductivity, with respect to the temperature field.

The cooling power and the top heater temperature (power) allow one to achieve any combination of crystallization rates and vertical temperature gradients in the melt. However, due to a direct connection between the heating and cooling systems in the considered model furnace, both input parameters significantly influence both response parameters.

6.5.2. Derivation of boundary conditions for local models

As reference values of **crystallization velocity** and **vertical temperature gradient in the melt** during the crystallization, 1 cm/h and 1 K/cm, respectively, are chosen. These values can be achieved with a cooling power of 8 kW and a total heating power of about 18 kW, distributed among 3 side heaters and 1 top heater. Both the crystallization velocity and the vertical temperature gradient tend to decrease during the crystallization.

As a reference value for the **deflection of crystallization interface**, 1 cm is chosen. This is a typical value that can be achieved by changing the side heater power. The corresponding **radial temperature gradient in the melt** during the crystallization is 0.1 K/cm. A local increase up to 0.3 K/cm at the melt side is possible.

6.5.3. Scaling

The theoretical analysis in Sec. 2.4 shows that there are various possibilities for the up-scaling of the temperature field in a furnace as summarized in Tab. 2.3. For the scaling between a smaller and larger system with silicon, the temperature level in both cases should be the same, which restricts the scaling to the case B1 in Tab. 2.3. This requires that the ratio of thermal conductivities in target and source cases is equal to the ratio of the length scales. The prescribed heat fluxes in [W] have to be increased quadratically. No other changes of reference parameters from Sec. 6.1 are required. The finite element mesh for the target case was not re-generated but up-scaled.

Fig. 6.9 illustrates an up-scaling by a factor of 4. It can be seen that temperature distributions in both cases agree exactly. The heat fluxes increase quadratically by a factor of 16. Of course, this scaling example is purely theoretical, and such adjustments of thermal conductivities may not be realistic. However, the sensitivity analysis in 6.3 indicated that only a few material properties play a significant role for the temperature field in silicon; consequently, a large number of material properties could be neglected for the scaling.

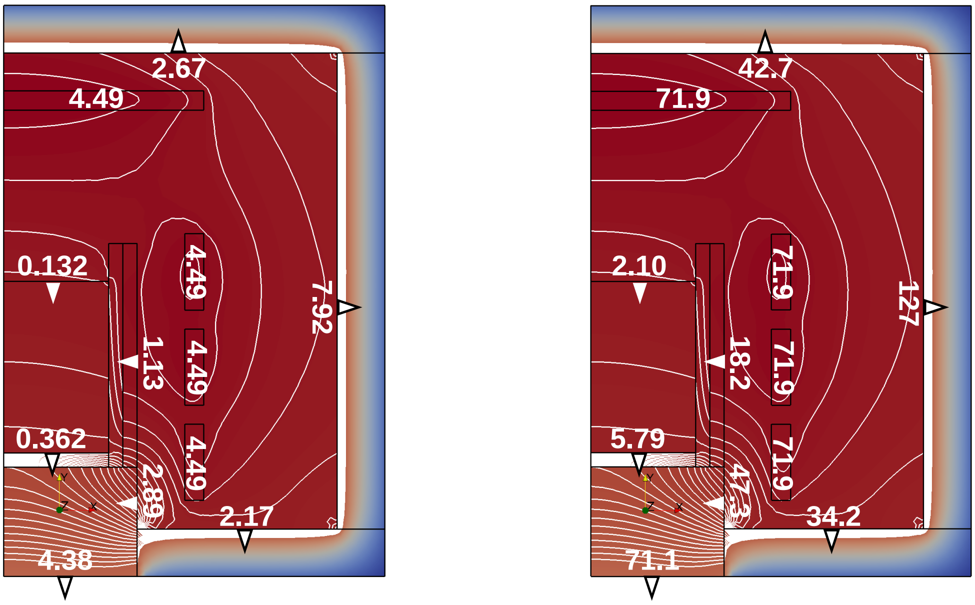

T = 412–1738 K (isolines 1500–1740 K)
(a) Si, $L = 22$ cm, λ

T = 412–1738 K (isolines 1500–1740 K)
(b) Si, $L = 88$ cm, $4 \cdot \lambda$

Figure 6.9.: Example for scaling the temperature field between a research-scale (a; L = 22 cm) and industrial-scale (b; L = 88 cm) silicon crystallization furnace according to the reference case described in Sec. 6.1 and the case B1 in Tab. 2.3: temperature field and selected heat fluxes (white numbers, in kW) in the entire system.

Chapter 7

Lorentz force in the melt

A simple system that consists of three TMF inductors surrounding a square melt still has over ten degrees of freedom, which determine the Lorentz force distribution in the melt. These parameters are consecutively varied to identify the most important ones and to obtain a recipe for the generation of a Lorentz force distribution with an arbitrary force density, force direction, and skin depth. Finally, a realistic parameter range for a crystallization furnace is defined for further studies.

7.1. Reference case

We consider a system of TMF inductors which surround a silicon melt in a crystallization furnace. If the heaters were coupled with the TMF inductors, then the furnace geometry discussed in Chapter 6 could be used also for electromagnetic calculations. However, only the electrically conducting parts are relevant for these calculations. In addition to the melt, solid silicon and graphite are electrical conductors, with typical electrical conductivities of $5 \cdot 10^4$ S/m and $8 \cdot 10^4$ S/m, respectively. The skin depth of the magnetic field for a frequency of 50 Hz can be estimated according to $\delta_{em} = 1/\sqrt{\pi \mu_0 \sigma f}$ as 32 cm and 25 cm, respectively. An increase of the frequency by a factor of 10 would decrease the skin depth to 10 cm and 8 cm, respectively. The most critical part with respect to magnetic field shielding is the crucible support made of graphite, which is located directly between the melt and the inductors. However, its thickness is about 1.5 cm, which is much smaller than the skin depth; therefore, the crucible support would have practically no influence on the magnetic field in the melt. The graphite heat sink and the solid silicon with dimensions on the order of 10 cm could have some influence at higher frequencies, but their positions below the melt are less critical. Therefore, a system that consists of the melt, the TMF inductors, and the surrounding gas is defined as the reference case geometry for electromagnetic calculations.

The inductor geometry from Chapter 6 is used, with the melt height decreased from 18 cm to 11 cm (with a constant top position); see Fig. 7.1. The outer boundary of the calculation domain, which is assumed impermeable to the magnetic field, is set at a distance where it has a negligible influence on the magnetic field in the melt. Crystallization furnaces are usually enclosed by an electrically conducting steel vessel. Such a vessel is excluded from the reference geometry and its influence is investigated separately. The 2D system geometry shown in Fig. 7.1 (a) is also used in 3D with the following deviations:

- Radial dimensions of circles in 2D correspond to the half width of squares in 3D; vertical dimensions are transferred directly. Exceptions are noted in Fig. 7.1 (a).
- In 3D, current supplies are added to the inductors – symmetrically at the center of the side with $x > 0$. The thickness and the height of the current supplies are identical to the heater, and the horizontal gap between the supplies is 2 cm.

The mesh for 2D and 3D calculations is generated with `Gmsh` with a parametrized input script. The geometries and meshes are shown in Fig. 7.1 (b,c). The size of the tetrahedral elements in the melt was set to 5 mm in 2D and 1 cm in 3D. Boundary conditions for 2D and 3D calculations differ only in the way how the inductor current is set. In 2D, the current density for each inductor is calculated as $j_S = I_0/S_{ind}$ in [A/m^2] using the current amplitude I_0 and inductor surface S_{ind}. In 3D, a potential difference is prescribed to the current supplies (one potential is set to zero) and inductor's resistance is calculated in a stationary calculation of the electric field and current in the inductor. The potential difference is adjusted to obtain the required inductor current I_0 for Lorentz force calculations. In time-harmonic calculations, the real and imaginary parts are specified; in unsteady calculations, the full time-dependence is given. Both in 2D and 3D calculations, eddy currents in inductor's volume (the skin effect) are neglected by treating this volume as non-conducting or by using a small electrical conductivity (e.g., that of graphite). Inductor current parameters for the reference case are defined as follows (see also Fig. 7.1 (a)):

- Current amplitude (sinusoidal current): I_0 = 300 A[1]
- Current frequency: f = 50 Hz
- Phase shift between inductors: ϕ = 60° for TMF up

The calculated distributions and time-dependencies of the Lorentz force, magnetic field, and induced current density for the 2D reference case are summarized in Fig. 7.2. The various diagrams will help to develop an understanding of the formation of a resulting Lorentz force density, which will be important for the following analysis of the influence of various inductor parameters. The starting point is the time-dependent current in all three inductors, which varies with time as shown in Fig. 7.3 (a). In the case of TMF up, current maxima on the time axis are ordered from the bottom inductor to the top inductor. Each inductor produces its own magnetic field, but the melt is influenced by a superposition of all fields.

The resulting **magnetic field** at a monitor point on the melt surface shown in Fig. 7.2 (b) still oscillates with the current frequency, but there is a phase shift between the radial and axial components; the amplitude of the axial component is almost 4 times larger and reaches 1.873 mT. As a result, the magnetic field vector at the monitor point actually rotates on an ellipse as illustrated in Fig. 7.3 (b). The time-average value of the magnetic field vector is zero. The height and width of the ellipse are determined by the amplitudes of both magnetic field components; the inclination of the ellipse is determined by the phase shift between both components. It can be seen in Fig. 7.2 (b) that both these parameters vary in both the axial and the radial direction.

The amplitude of the dominating axial magnetic field component varies on the melt side surface by approximately 0.2 mT or 10%, which is a deviation from an idealized TMF wave. In contrast, the phase angle of the axial magnetic field component shows a linear distribution on the melt side surface, which would correspond to a constant wave number of the TMF

---

[1] The calculation of current amplitude from the local current density may have a relatively high numerical error in 3D cases. A more precise evaluation later showed that the actual current amplitude in the reference case is higher by 5%.

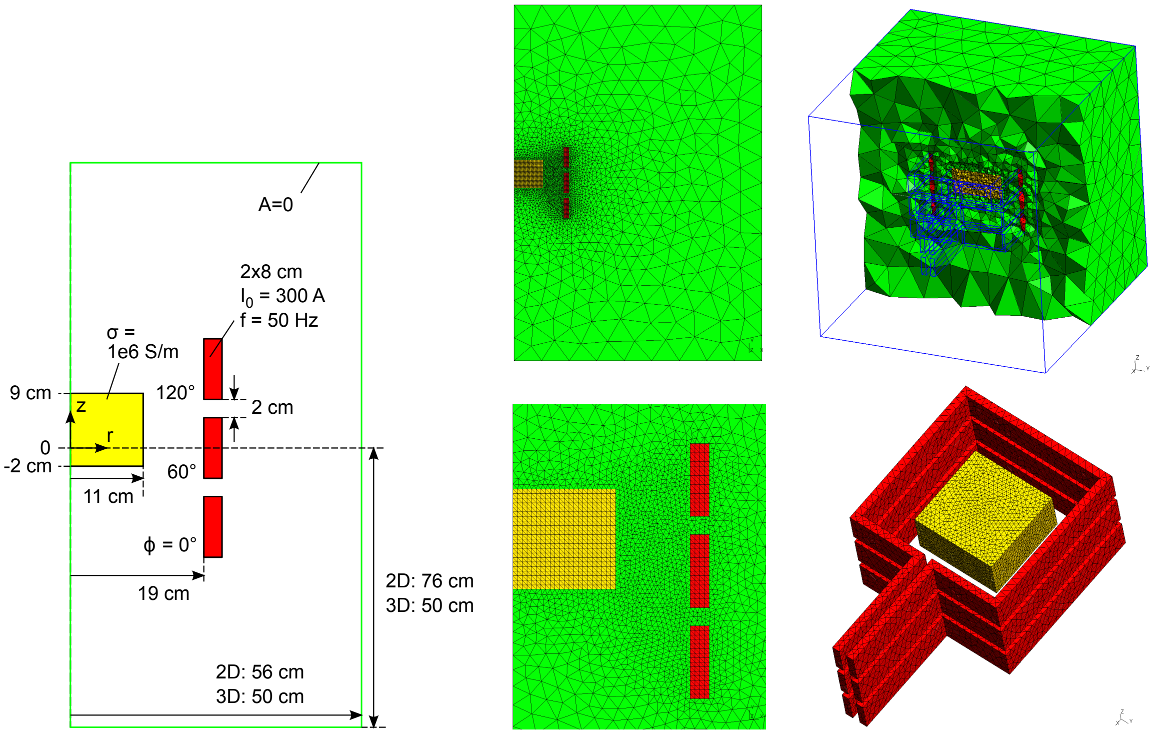

(a) (b) 2D (c) 3D

Figure 7.1.: Reference case: geometry, materials, and boundary conditions (a); finite element mesh for 2D (b; 5493 triangles) and 3D (c; 124875 tetrahedrons) electromagnetic calculations.

wave. Using the approximation (2.27), the TMF wave number at the monitor point can be calculated as $\alpha = 5.63$ 1/m.

The **induced current density** in Fig. 7.2 (c) has only an azimuthal component; its amplitude decreases almost linearly to zero on the axis. The integral induced current as well as the induced heat power can be obtained by integrating the complex 2D current density distribution over a half cross section S (see Sec. 2.1.2):

$$I_{ind} = \int_S j(r,z)drdz, \quad Q_{ind} = 2\pi \int_S \frac{|j(r,z)|^2}{2\sigma} r\,drdz. \tag{7.1}$$

We obtain for the reference case: $I_{ind} = -149 + i \cdot 12$ A and $Q_{ind} = 0.69$ W. The amplitude of the integral current is 149.5 A, which is on the same order as the inductor current. The induced heat power is negligible in comparison with typical heater powers in a furnace.

The oscillations of **Lorentz force** components at a monitor point shown in Fig. 7.2 (a) result from the vector product $\vec{F}_L(t) = \vec{j}(t) \times \vec{B}(t) = -jB_z\vec{e}_r + jB_r\vec{e}_z$, which indicates that the axial magnetic field component is responsible for the radial Lorentz force component and vice versa[2]. The numerical result shows that the Lorentz force oscillates with the double frequency of the inductor current; the radial and axial components have different non-zero time-average values. These oscillations again can be described as a vector rotation on an

---

[2] An idealized TMF wave is usually defined only with the axial magnetic field component, which would generate only a radial force at first sight. However, the radial magnetic field component is always used implicitly because it is required due to the magnetic field continuity $\operatorname{div}\vec{B} = 0$.

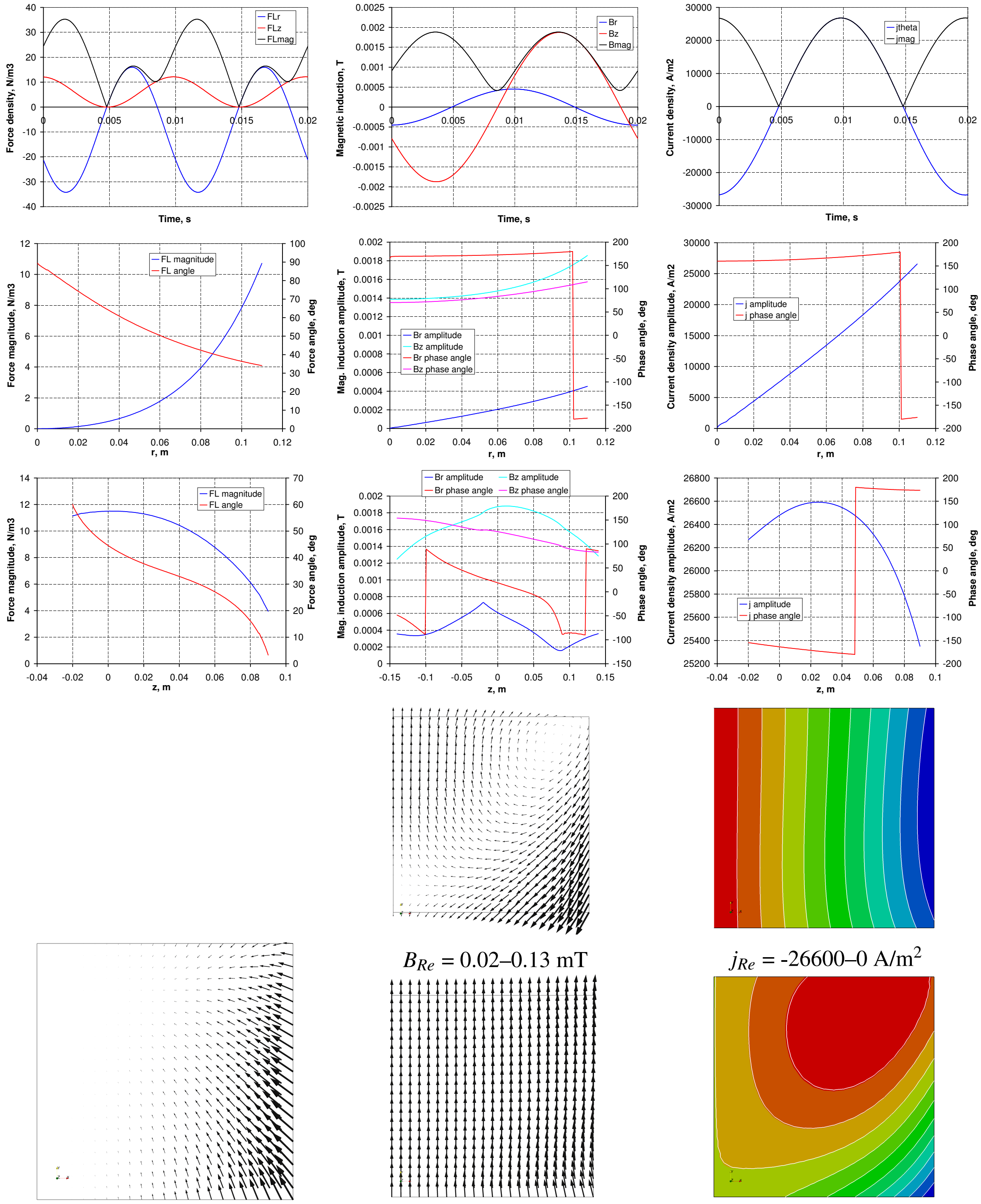

B_{Re} = 0.02–0.13 mT

j_{Re} = -26600–0 A/m^2

F_{Lmax} = 11.5 N/m^3

(a)

B_{Im} = 1.27–1.72 mT

(b)

j_{Im} = -11300–4300 A/m^2

(c)

Figure 7.2.: 2D electromagnetic calculations for the reference case: Lorentz force (a), magnetic field (b), and induced current density (c) in the melt. From top to bottom: time dependence of vector components at the point $r = 0.11$, $z = 0.035$ m; radial distribution at $z = 0.035$ m of the vector magnitude and direction (for Lorentz force), of the amplitude and phase angle of vector components (for other); the same on a vertical line at $r = 0.11$ m; time-averaged field (for Lorentz force), real and imaginary fields (for other) in 2D.

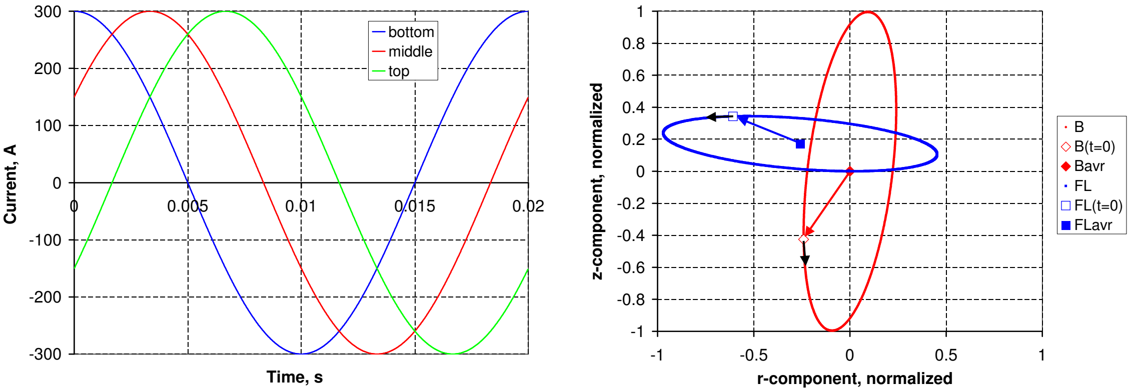

(a) (b)

Figure 7.3.: 2D electromagnetic calculations: time-dependence of inductor current (a) and of magnetic field and Lorentz force vectors at the point $r = 0.11$, $z = 0.035$ m (b). The magnetic field and Lorentz force are normalized using the maximum axial components.

ellipse, but in this case vector's origin is shifted and the ellipse is extended in radial direction; see Fig. 7.3 (b). The time-average values of both the induced current and the magnetic field are zero, but the time-average Lorentz force is not zero. This can be explained by the phase shift between the oscillations of induced current and magnetic field: the time-average of a product of two sinusoidal signals with the same frequencies is zero only if the phase shift is 90°.

The spatial Lorentz force distribution is obtained by calculating the vector product at each point in the melt. The time-averaging can be significantly simplified in the time-harmonic case as described in Sec. 2.1.2. Both the magnetic field and the induced current have a real and an imaginary part, which can be simply interpreted as the instantaneous fields at the time instants $t = 0$ and $t = 0.75/f$ according to (2.16). The time-average Lorentz force field then equals the average value of the vector products of both real parts and both imaginary parts; see eq. (2.18). Several characteristic features of the time-average Lorentz force can be seen in Fig. 7.2 (a):

- The force density increases in radial direction. At an axial coordinate $z = 0.035$ m, it decreases from $F_{L1} = 10.9$ N/m^3 on the surface to $F_{L2} = 4.0$ N/m^3 at a distance $d = 3$ cm to the surface. The corresponding skin depth for an assumed exponential decrease can be approximated as $\delta_{\mathrm{TMF}} = d/ln(F_{L1}/F_{L2})$ = 3 cm. The real part of both the induced current density and the magnetic field show a similar behavior.

- The radial and axial components of the Lorentz force are comparable; the force direction on the surface at $z = 0.035$ m forms an angle $\varphi = 33.9°$ with the horizontal plane. The imaginary part of the magnetic field is almost axial and would lead to a horizontal force. Therefore, both parts of the magnetic field contribute to the resulting Lorentz force.

- The radial force component mostly points into the melt and not out of the melt. This effect is related to the phase shift between the oscillations of current density and axial magnetic field component, which is smaller than 90°.

- The force density distribution is nonuniform in vertical direction with a higher force density at the melt bottom where the upward TMF "enters" the melt. This effect occurs because vertical mid-points of the melt and the inductors do not coincide. The same trend can be also observed for the magnetic field amplitude on the melt side surface.

7.2. Influence of 3D effects in a quadratic system

The 3D reference case geometry differs from the 2D case with a square shape and with current supplies at one side. These geometrical differences may lead to both qualitative (e.g., in the corners) and quantitative differences in the Lorentz force distribution. The results of 3D calculation for the reference case are summarized in Fig. 7.4; magnetic field, induced current density, and time-average Lorentz force distributions in a horizontal cut through the melt center are shown.

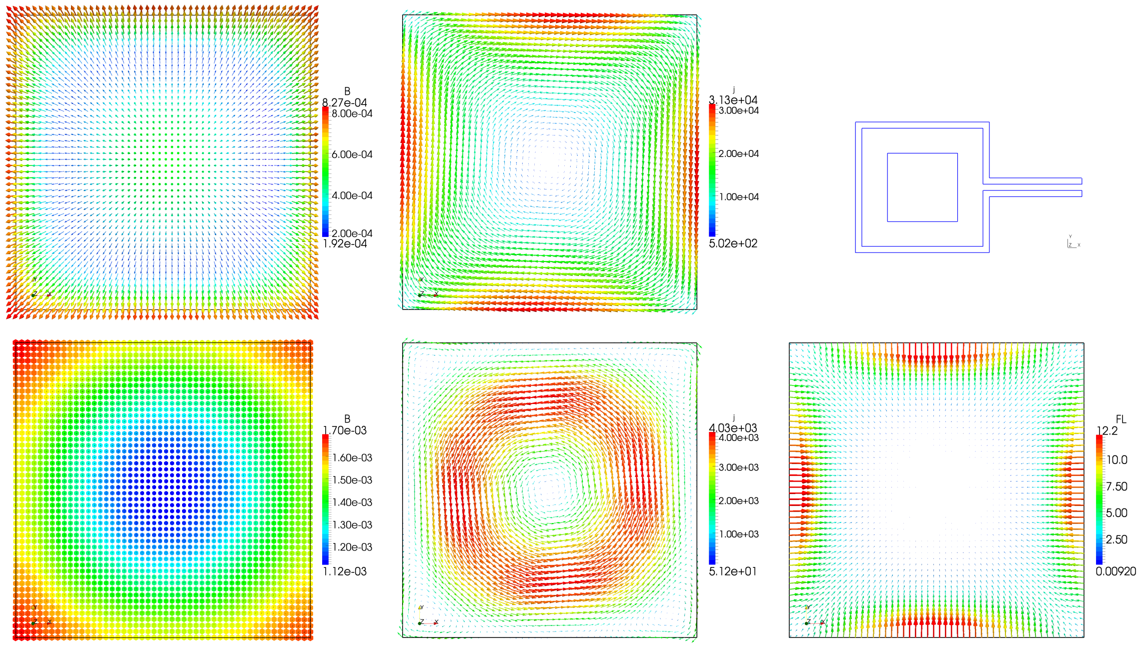

(a) (b) (c)

Figure 7.4.: Role of 3D effects in electromagnetic calculations: magnetic field (a) in [T], eddy current (b) in [A/m^2], and Lorentz force (c) in [N/m^3] in a horizontal cut through the melt center. The time-average distribution is shown for the Lorentz force; real (top) and imaginary (bottom) parts are shown for other fields. Vectors are colored according to their magnitude. The position of current supplies in depicted in the top right corner.

Main features of magnetic field and current density distributions are very similar in 2D (see Fig. 7.2) and 3D cases (directions of both vector fields are reversed due to the chosen inductor current directions in 3D). The imaginary part of magnetic field dominates; it reaches approximately 1.7 mT and the vectors are almost vertical. The real part of induced current still flows “azimuthally”, with a decreasing magnitude toward the melt center. In good agreement with 2D results, maximum magnitude of the imaginary part is located between the melt center and the side surface (in a horizontal cut at mid-height).

The magnitude of the imaginary part of magnetic field is significantly higher in the corners of the 3D geometry. In contrast, the real part of current density is higher at the sides; the imaginary part of the “azimuthal” current almost seems to “ignore” the corners, producing only weak secondary eddy current vortices there. Consequently, Lorentz force as a product of the induced current density and the magnetic field is characterized by a high force density at the sides and distinct minima in the corners as shown in Fig. 7.4 (c). The force density, angle, and skin depth in the 3D case at the point ($x = 0$, $y = 0.11$, $z = 0.035$) m are 12.1 N/m^3, 31.1°, and 2.6 cm, respectively. These values deviate from 2D results only by about 10%.

The influence of current supplies at one side of the melt leads to a slight decrease of Lorentz force density at the corresponding side in Fig. 7.4 (c). The role of gap width between the current supplies was investigated in a further study where the gap was varied between 2 cm (reference) and 16 cm. Inductor current was adjusted to obtain a maximum Lorentz force density of 15 N/m^3 in the melt. A gap of 16 cm required inductor currents that are by 12% higher than for a gap width of 2 cm. Lorentz force distributions on two perpendicular horizontal lines are compared in Fig. 7.5. The Lorentz force distribution on a line parallel to the current supplies shows a small difference of 6% between both endpoints for a gap width of 2 cm. The difference increases to 31% for a gap width of 16 cm. Except this asymmetry, the Lorentz fore distribution in the melt volume remains qualitatively the same. It should be noted that because of present inductor geometry with effectively "one winding", the asymmetry at the current supplies cannot be avoided. For example, a local variation of inductor's cross section would not change the total current flowing through this section.

In summary, the 3D inductor geometry leads to rather small deviations (about 10%) from previous 2D results if the gap between current supplies is kept small. It is important to note that the radius in 2D geometry was assumed equal to half width of the square in 3D geometry. This approach leads to a better agreement of the calculated Lorentz forces, which can be explained by the fact that the induced eddy-currents partly "ignore" melt corners. Therefore, further parameter studies in this chapter will be performed in 2D.

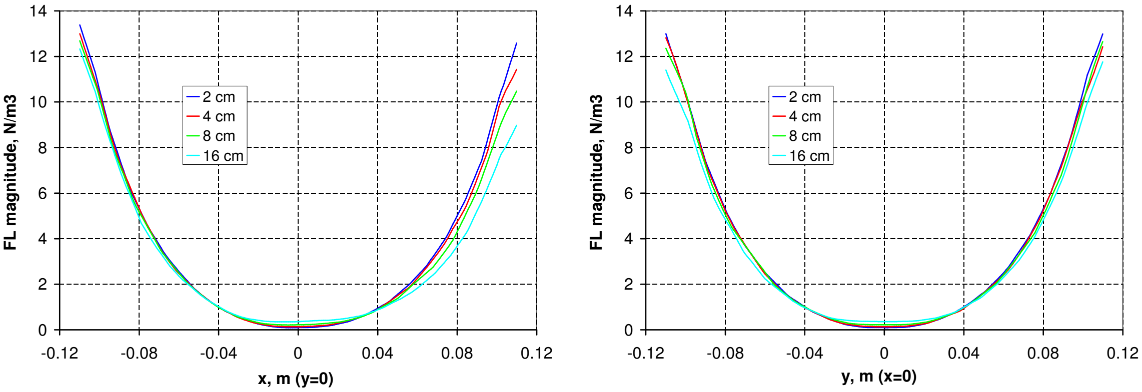

(a) (b)

Figure 7.5.: Role of 3D effects in electromagnetic calculations: Lorentz force distribution on two horizontal lines (a,b) through the melt center for different gaps between the current supplies. Current supplies are located at the side $x > 0$. Inductor current is adjusted to obtain a maximum Lorentz force density of 15 N/m^3 in the melt.

7.3. Influence of analytical TMF parameters

The representation of a TMF in the form of an idealized magnetic wave described in Sec. 2.1.5 has an advantage of a relatively small number of degrees of freedom, which all can

Idealized TMF wave	**Realistic TMF inductors**
Magnetic field frequency	Inductor current frequency
Magnetic field amplitude	Inductor current amplitude
Melt radius	Melt radius
TMF wave number	Melt height
	Inductor radius
	Inductor height
	Inductor width
	Distance between inductors
	Number of inductors
	Vertical position of inductors
	Phase shift between inductors
	Current distribution among inductors
	Phase cut of inductor current
	Inductor distance to conducting walls

Table 7.1.: Degrees of freedom for a cylindrical melt in an idealized TMF wave and in a realistic system of TMF inductors.

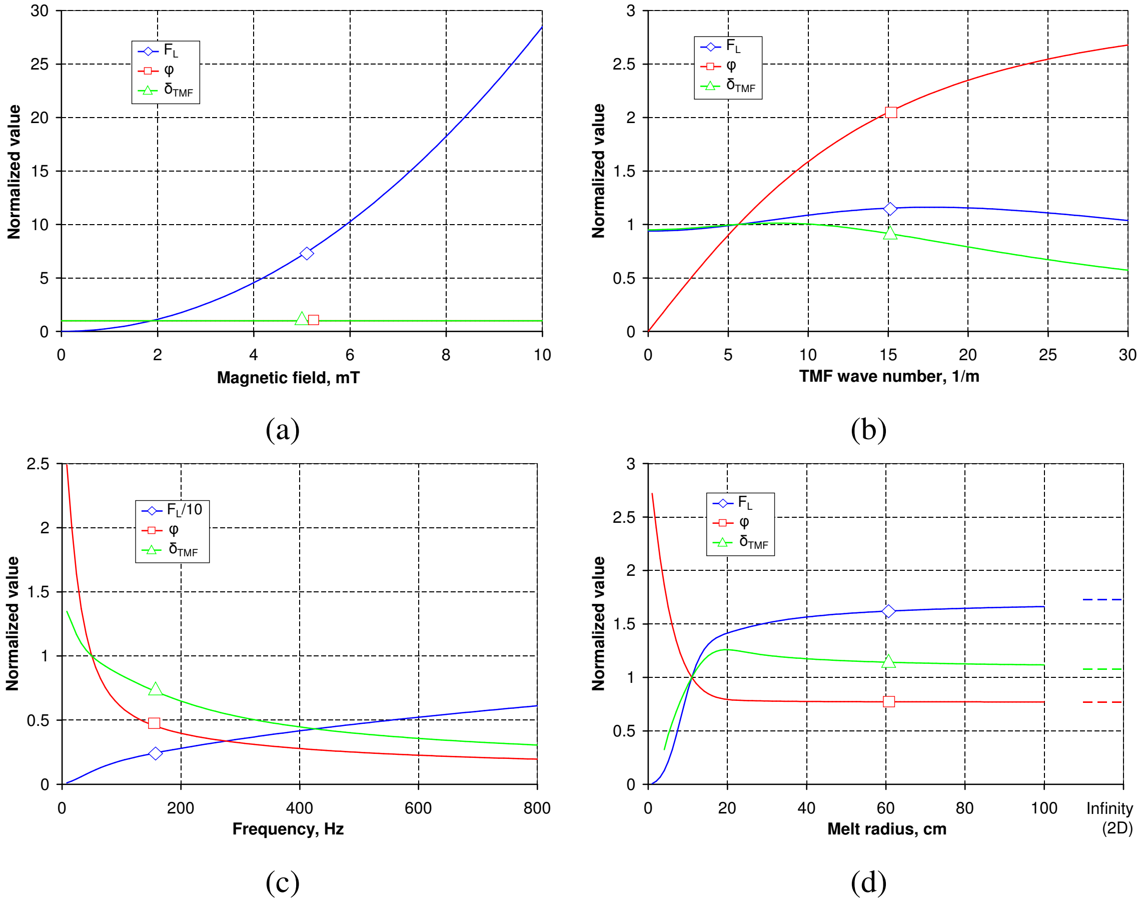

Figure 7.6.: Analytical solution for a long cylinder (silicon) in a TMF: influence of the magnetic induction (a), TMF wave number (b), frequency (c), and melt radius (d) on the force density F_L (11.8 N/m^3), force angle with the horizontal plane φ (29.4°), and skin depth of the force δ_{TMF} (3.2 cm). The values are normalized to the reference case given above in brackets.

be analyzed using analytical methods. A TMF generated by a realistic system of TMF inductors has at least 3 times more degrees of freedom, as summarized in Tab. 7.1, and requires numerical methods to analyze their influence on the generated Lorentz force. Therefore, the analytical solutions from Sec. 2.1.5 are used here to analyze the role of TMF wave parameters on the Lorentz force distribution. In the following sections, degrees of freedom of realistic TMF inductors are investigated by numerical means to analyze the resulting magnetic field and Lorentz force distributions. In this way, the following questions can be answered:

- What is the influence of analytical TMF parameters describing an idealized TMF wave on the generated Lorentz force distribution?
- How close can an idealized TMF wave be generated by realistic TMF inductors and what are the relations between their degrees of freedom?
- What is the influence of the parameters of realistic TMF inductors on the generated Lorentz force distribution and can this influence be physically understood in terms of the idealized TMF parameters?

The influence of 4 degrees of freedom of an idealized TMF wave from Tab. 7.1 on Lorentz force distribution is summarized in Fig. 7.6. The approximate TMF parameters from the reference case are used in the analytical solution: melt radius $R = 0.11$ m, TMF wave number α = 5.63 1/m, and TMF amplitude B_{0z} = 1.873 mT. Lorentz force distribution is evaluated in a similar way: the force magnitude and direction on the surface are determined; the skin depth is approximated using the force magnitude at $r = R$ and $r = R - 0.03$ m. It can be seen that Lorentz force parameters given in the legend of Fig. 7.6 agree very well with the 2D reference case in Sec. 7.1 – deviations are only about 10%. Consequently, the reference system of TMF inductors approximates an idealized TMF wave well.

It can be easily seen in the analytical expression (2.29) that force density depends quadratically on **TMF amplitude (magnetic induction)**, which, on the other hand, has no influence on the force angle and skin depth. This conclusion is formally confirmed in Fig. 7.6 (a). In contrast, the **frequency** of magnetic field significantly influences all characteristics of the Lorentz force distribution as shown in Fig. 7.6 (c). If the frequency is increased from 50 Hz to 400 Hz, force density increases 4 times, force angle decreases 3.7 times, and skin depth decreases 2.3 times. If the skin depth decreases, magnetic field penetrates less into the melt. Consequently, the radial magnetic field component decreases, which results in a decrease of the axial Lorentz force component. Hence, the force angle decreases, too.

The **TMF wave number** α primarily determines the force angle, which increases from 0° (radial force) at $\alpha = 0$ to 90° (axial force) at high values of α. High wave numbers also tend to decrease the skin depth. This obviously happens when both terms under the square root in argument $r \cdot \sqrt{\alpha^2 + i\sigma\mu_0\omega}$ in the analytical solution become comparable: $\alpha^2 \sim \sigma\mu_0\omega$. A similar condition also determines the threshold when the **radius** of the system does not have an influence any more (the system effectively becomes planar and expressions (2.30) can be applied) as shown in Fig. 7.6 (d). In the present case this happens approximately at $R = 0.4$ m. Hence, we can estimate:

$$R \cdot \sqrt{\alpha^2 + i\sigma\mu_0\omega} \approx 0.4 \cdot \sqrt{5.63^2 + i \cdot 395} \approx 8\sqrt{i} \quad \Rightarrow \quad R \gtrsim \frac{8}{\sqrt{\sigma\mu_0\omega}} = 6\delta_{em}. \qquad (7.2)$$

Consequently, the radius must be 6 times larger than the approximate skin depth δ_{em} to consider the system effectively planar. At a smaller radius, the force magnitude and skin depth decrease, while the force angle increases.

7.4. Influence of inductor current parameters

The influence of inductor current parameters of realistic TMF inductors is summarized in Fig. 7.7. Inductor current amplitude in Fig. 7.7 (a) directly corresponds to the TMF amplitude of an idealized system. The same is true for the frequency, which shows in Fig. 7.7 (c) the same effects as in an idealized system. However, note also a small influence on the TMF wave number and TMF amplitude. Other inductor current parameters leave the skin depth practically unchanged, while the force angle is influenced in the same way as the TMF wave number and the force magnitude is influenced in the same way as the TMF amplitude. Therefore, for a better understanding, we can look for a connection between the inductor current parameters and the idealized TMF parameters. The analytical solution provides then the explanation of the influence on the Lorentz force.

The resulting **magnetic field** at each point in the system is determined by a superposition of magnetic fields of all inductors. These fields depend on the distance to the monitor point and are phase-shifted. The influence of phase shift on the resulting field amplitude can be explained by a simple model that neglects amplitude differences between the individual magnetic fields. The sum of N signals with identical amplitudes (assumed equal to 1) and with a phase shift ϕ can be written as:

$$\begin{aligned}\sin(\omega t)+\sin(\omega t+1\phi)+\sin(\omega t+2\phi)+\ldots+\sin(\omega t+N\phi) &= \\ &= \frac{\sin\frac{N+1}{2}\phi}{\sin\frac{1}{2}\phi}\cdot\sin\left(\omega t+\frac{N\phi}{2}\right). \qquad (7.3)\end{aligned}$$

Obviously, the resulting amplitude is zero if $0.5(N+1)\phi=\pi k$ or $\phi=2\pi k/(N+1)$, where k = 1, 2,.... For N = 2, which corresponds to 3 inductors, the first zero occurs at ϕ = 120°. This agrees with the very low magnetic induction B_{0z} at 120° in 7.7 (d). In the case of 6 inductors and N = 5, the first zero would occur already at 60°, the second at 120°, etc. However, it should be noted that this analytical approximations is valid only if the distances of all inductors to the melt are similar. For the case with different distances, an analytical expression can be written for 3 inductors and 2 different amplitudes (e.g., 3 inductors are vertically arranged symmetrically to the melt) B_1 and B_2:

$$B_1\sin(\omega t-\phi)+B_2\sin(\omega t)+B_1\sin(\omega t+\phi)=(2B_1\cos\phi+B_2)\cdot\sin\omega t. \qquad (7.4)$$

This expression gives a zero resulting amplitude if $\cos\phi=-0.5B_2/B_1$. With $B_1=B_2$, we obtain ϕ = 120°, again. With $B_1=0.5B_2$, the critical phase shift increases to a maximum at 180°. Consequently, with a larger distance between the inductors, a higher phase shift is required to eliminate the amplitude of the resulting field.

The **TMF wave number** shows a linear dependence of the phase shift (up to approximately 90°) and of the number of inductors (up to approximately 4). The wave number has been approximated previously in Sec. 2.1.5 as $\partial\phi/\partial z$. This relation can be written in a discrete form as

$$\alpha=\frac{\Delta\phi}{\Delta z}, \qquad (7.5)$$

where $\Delta\phi$ and Δz are the phase shift and the distance between two neighboring inductors,

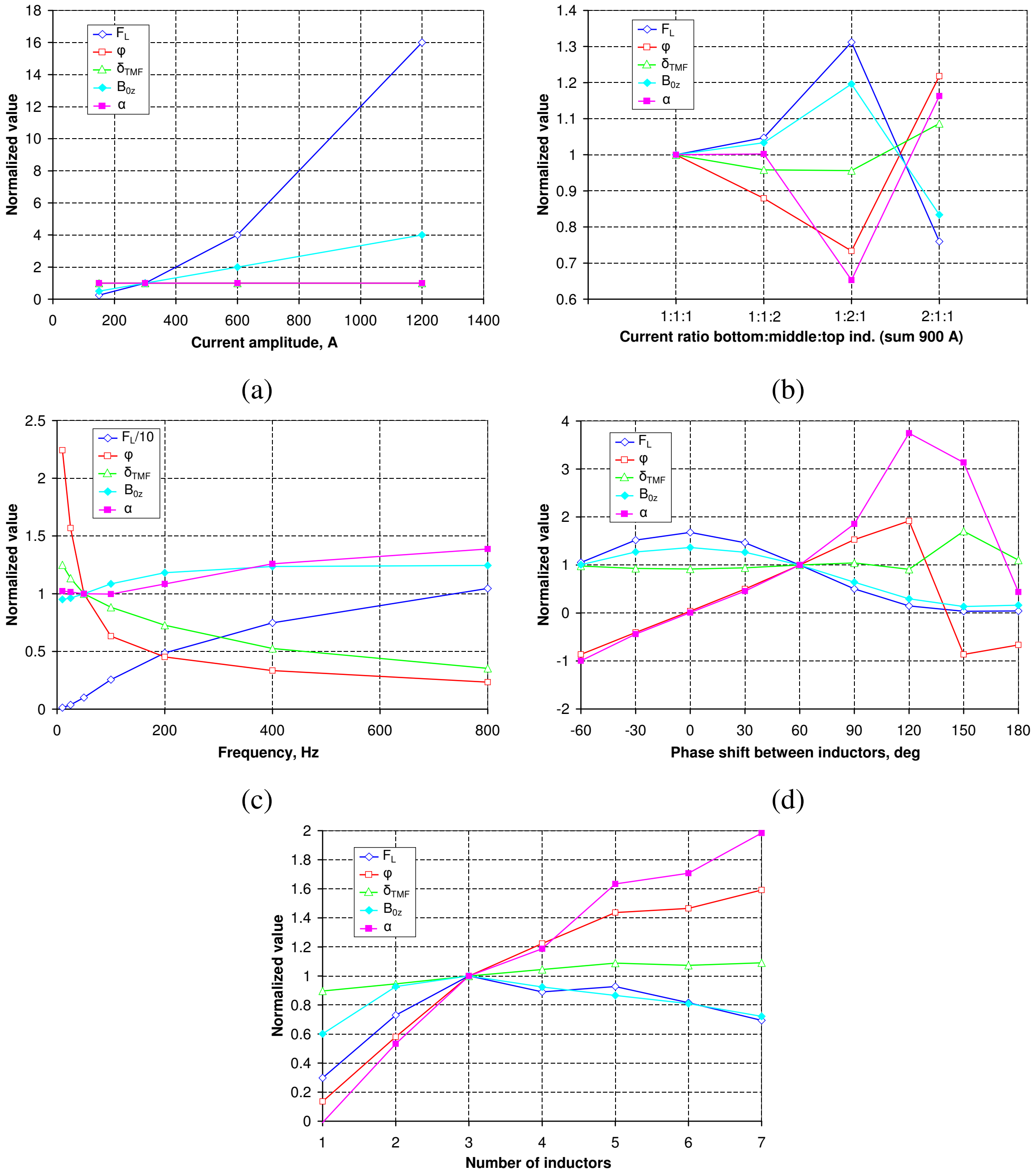

(a) (b)

(c) (d)

(e)

Figure 7.7.: 2D electromagnetic calculations for a silicon melt in a TMF: influence of various current parameters (a–e) on the force density F_L (10.9 N/m^3), force angle with the horizontal plane φ (33.9°), skin depth of the force δ_{TMF} (3.0 cm), approximate TMF wave number α (5.63 1/m), and approximate TMF amplitude B_{0z} (1.873 mT). The values are normalized to the reference case given above in brackets.

respectively. This approximation can be physically understood in the following way: the phase shift of the resulting magnetic field is determined by the phase shift of the inductor closest to the monitor point – contributions from other inductors are smaller due to a larger distance. This model explains the linear dependence between α and ϕ. A higher number of inductors increases the maximum phase difference in the system and the phase shift of the resulting signal as can be seen from the term $0.5N\phi$ in eq. (7.3). This effect can be included in the approximation (7.5) if all inductors are symmetrically divided into two groups and the average values of phase shifts and vertical positions of the inductor groups are used.

In practical applications, the power of a current is often controlled not by changing its amplitude but by introducing the so-called **phase cut**: the current is cut-off (set to zero) in each period at a given phase of the sinusoidal time-dependence; see Fig. 7.8 (b). To calculate the induced Lorentz force, the time-harmonic assumption can not be used in this case. Therefore, the influence of a phase cut was investigated in a series of time-dependent calculations. The Lorentz force is calculated for two current periods (0.04 s) and averaged over the time interval 0.02... 0.04 s. Fig. 7.8 (a) summarizes the influence of phase cut on the Lorentz force distribution. The Lorentz force density is shown for two cases: the maximum current amplitude (300 A) is not changed (as shown in Fig. 7.8 (b)); the current amplitude is adjusted to obtain the same integral power, i.e., $\int I(t)^2 dt = const$. The latter case leads to an increase of the current amplitude to 434 A with a phase cut at 90°; and to 1932 A with a phase cut at 150°.

The results in Fig. 7.8 (a) show that the phase cut has a small influence on the time-average Lorentz force density for cuts up to 90° if the integral power is preserved. If the power is decreased, the Lorentz force also decreases and shows an approximately linear dependence up to a phase cut of 90°: the force density at 90° (corresponding to the half power) is approximately 2 times smaller than at 0° (corresponding to the full power); at higher phase cuts than 90°, the Lorentz force density decreases rapidly. If the integral power is preserved, the Lorentz force density increases, while the force angle and the skin depth both decrease. This effect can be explained by the appearance of higher frequencies in the spectrum of inductor current due to the phase cut. Although the trends are qualitatively the same as for the variation of the harmonic frequency in Fig. 7.7 (c), there are quantitative differences. For instance, the force angle at high phase cuts practically reaches zero, while the skin depth decreases only by a factor of 2.

7.5. Influence of geometric parameters

7.5.1. Basic melt and inductor dimensions

The influence of geometric parameters of realistic TMF inductors is summarized in Fig. 7.9. Only the melt radius has a direct counterpart in the idealized system; and the numerical results in Fig. 7.9 (b) agree very well with the analytical results in Fig. 7.6 (d). All geometric parameters can be divided in two groups: dimensions in the horizontal and the vertical direction.

The next relevant **horizontal dimension** after the melt radius is the distance between the melt and the inductors. Fig. 7.9 (a) shows that a 2 times higher distance leads to about 2 times lower Lorentz force density and force angle. These changes are accompanied by a corresponding decrease of TMF amplitude and wave number. A decrease of the magnetic induction can be explained by the fact that the magnetic field in the center of a circular current

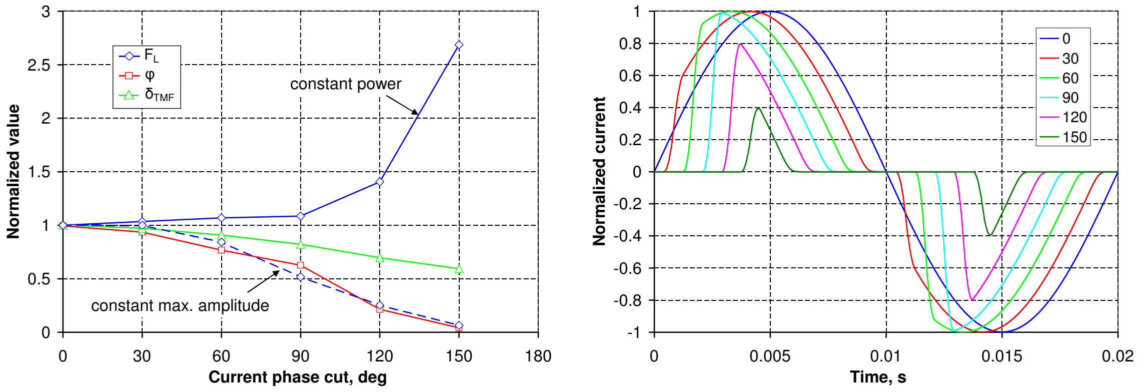

(a) (b)

Figure 7.8.: 2D electromagnetic calculations for a silicon melt in a TMF: (a) influence of current phase cut on the force density F_L (10.9 N/m^3), force angle with the horizontal plane φ (33.9°), and skin depth of the force δ_{TMF} (3.0 cm) – normalized to the reference case given in brackets; (b) time-dependence of the current (normalized to unity and shifted on time axis) for various phase cuts (in degrees) used in calculations.

loop is inversely proportional to the radius of the circle. A decrease of the wave number intuitively follows from the following consideration: if the distance between inductors becomes much smaller than the distance to the melt, the distances between the separate inductors and any point in the melt become very similar. Consequently, the phase difference between any two points in the melt tends to zero and the TMF wave number also approaches zero.

It was assumed for the reference configuration that the boundary of the calculation domain is at a large distance from the inductors and that there are no additional conducting bodies in between. In reality, the **walls** of a furnace vessel can be located relatively close to the inductors. Because the walls usually are made of stainless steel, they could also influence the magnetic field in the melt. In a series of calculations, a wall with a height of 1 m (symmetrically to the inductors) and thickness of 2 cm was horizontally shifted between the inductors and the domain boundary. Electrical conductivity of stainless steel was assumed $1.4 \cdot 10^6$ S/m, which allows to estimate the skin depth at 50 Hz as $\delta_{em} = 6$ cm. Consequently, a significant part of the magnetic field still is able to cross the 2 cm thick wall, but some deformation of the magnetic field can be expected. Results of calculations summarized in Fig. 7.9 (c) show a moderate influence of the wall on the Lorentz force distribution. If the distance between the inductors and the wall is not smaller than the inductor radius, the changes of force parameters are below 10%. Smaller distances tend to decrease the force density and to increase the force angle. Note that the use of magnetic steel could lead to a much larger influence because the high magnetic permeability $\mu \sim 1000$ would decrease the skin depth in the wall by a factor of $\sqrt{\mu} \sim 30$.

The inductors possess at least three different **dimensions in the vertical direction** – height, distance, and positions of midpoints – but they are not independent of each other. In a first series of calculations, the distance between the inductors is increased, but the inductor height is kept constant. In a second series of calculations, the inductor height is increased, but the distance between inductors is kept constant; the values of inductor height are chosen so that the midpoints match the first series. The very similar influence on the Lorentz force in both series in Figs. 7.9 (d,e) indicates that the distance between the midpoints of the inductors is the most important vertical dimension. Its role can be explained as follows: a

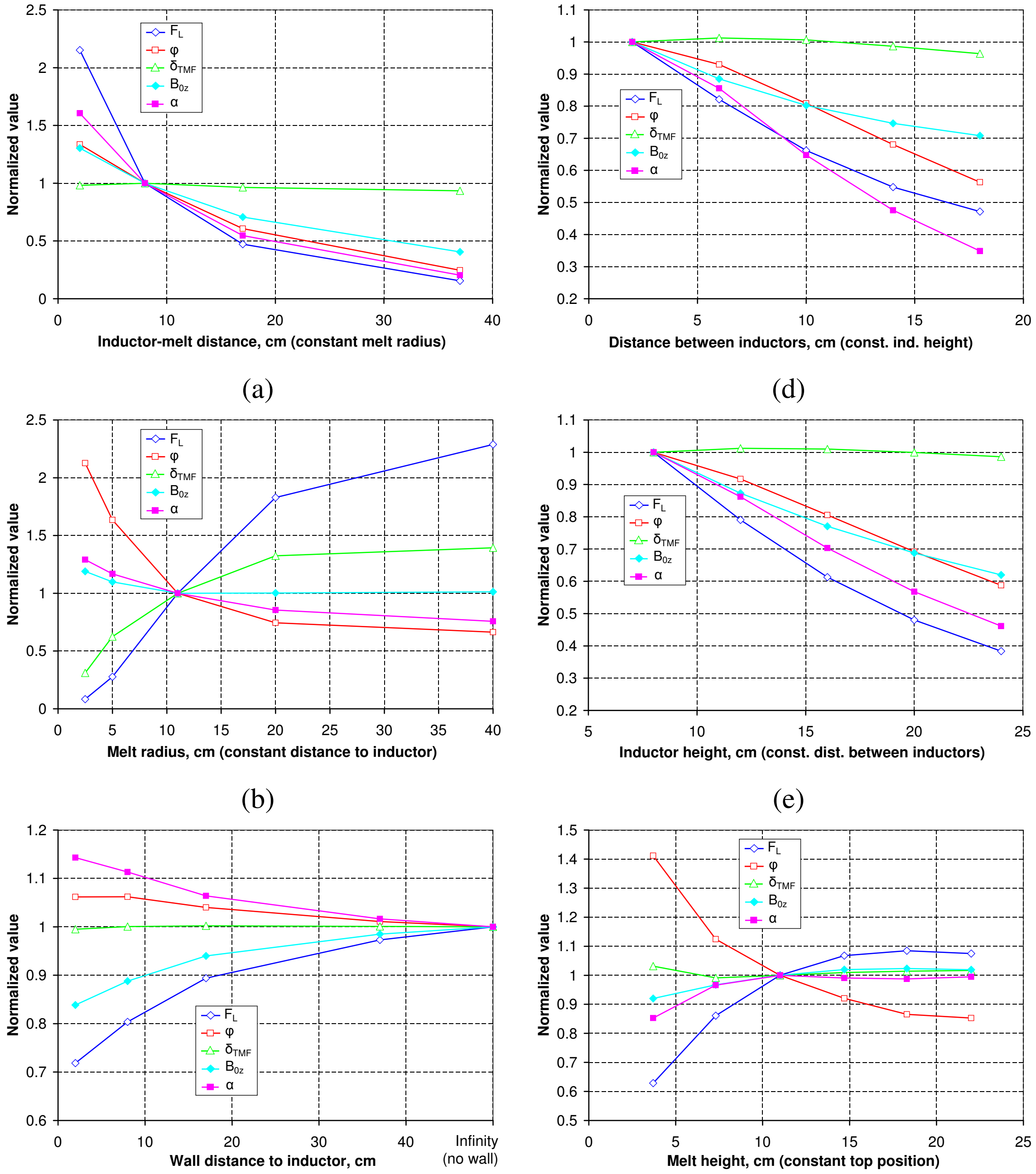

(a) (d)

(b) (e)

(c) (f)

Figure 7.9.: 2D electromagnetic calculations for a silicon melt in a TMF: influence of geometric dimensions in horizontal direction (a–c) and in vertical direction (d–f) on the force density F_L (10.9 N/m^3), force angle with the horizontal plane φ (33.9°), skin depth of the force δ_{TMF} (3.0 cm), approximate TMF wave number α (5.63 1/m), and approximate TMF amplitude B_{0z} (1.873 mT). The values are normalized to the reference case given above in brackets.

higher vertical distance between the midpoints leads to a higher distance of the inductors to the melt and decreases the TMF amplitude; similarly, a higher distance decreases the TMF wave number according to the approximation (7.5) because Δz increases. The same effect can be expected for the width of the inductors: if the midpoint of an inductor remains at the same position, the influence of the width should be marginal.

The analytical solutions for the Lorentz force induced by a TMF wave are valid only for a long cylinder; however, the melt height in a crystallization process decreases from the initial value to zero. The calculations for various melt heights in Fig. 7.9 (f) show that the effect of a finite melt height disappears only for heights larger than 18 cm or height-to-diameter ratios larger than 0.8. The critical melt height can be also expressed in terms of the skin depth of the magnetic field as $H \gtrsim 2.5\delta_{em}$. At a smaller melt height, the Lorentz force density decreases and the force angle increases.

7.5.2. Topology of inductors

So far it has been assumed that inductors surround the melt and follow a circular or rectangular path. In some practical applications, inductors may also have a meander shape or form horizontal or vertical current loops that do not surround the melt. In this case, magnetic fields generated by neighboring parts of an inductor may partially cancel. To obtain a general understanding of such effects, we consider three analytical models shown in Fig. 7.10 (a). The magnetic field of each wire is approximated using the expression for an infinitely long wire (see Sec. D.2.1). A current of 1000 A is assumed in the wires.

The resulting magnetic field is analyzed in dependence of the distance from the inductor to a control point (e.g., at the melt side) in Fig. 7.10 (b,c). It can be seen that only a large vertical loop can generate at a close distance a higher magnetic field than a single wire. However, the magnetic field falls off with the distance faster than in the case of a single wire. The same effect can be observed also for all other considered geometries. Consequently, wire loops at the melt side generally lead to weaker magnetic fields than a single wire at the melt side.

7.6. Discussion

7.6.1. Analytical understanding of realistic TMF inductors

Although all geometric and current parameters of TMF inductors can be investigated numerically, an approximate analytical understanding of the resulting Lorentz force distribution might be helpful. The axisymmetric analytical model for an idealized TMF wave analyzed in Sec. 7.3 showed relatively simple relationships between the TMF wave characteristics and the Lorentz force. The correlations between these characteristics in numerical calculations with non-idealized TMF inductors are summarized in Fig. 7.11. It can be seen that the analytical laws are reproduced well: the force density is proportional to the squared TMF amplitude, and the force angle is proportional to the TMF wave number (for $\alpha \lesssim 10$ 1/m). Deviations appear mainly for extremal values of the inductor frequency or melt radius in accordance with the analytical model. Consequently, the idealized analytical model is able to explain the main effects in realistic inductor geometries.

The parameters of an idealized TMF wave – the TMF amplitude B_{0z} and wave number α – are accessible for an analytical understanding in the following way:

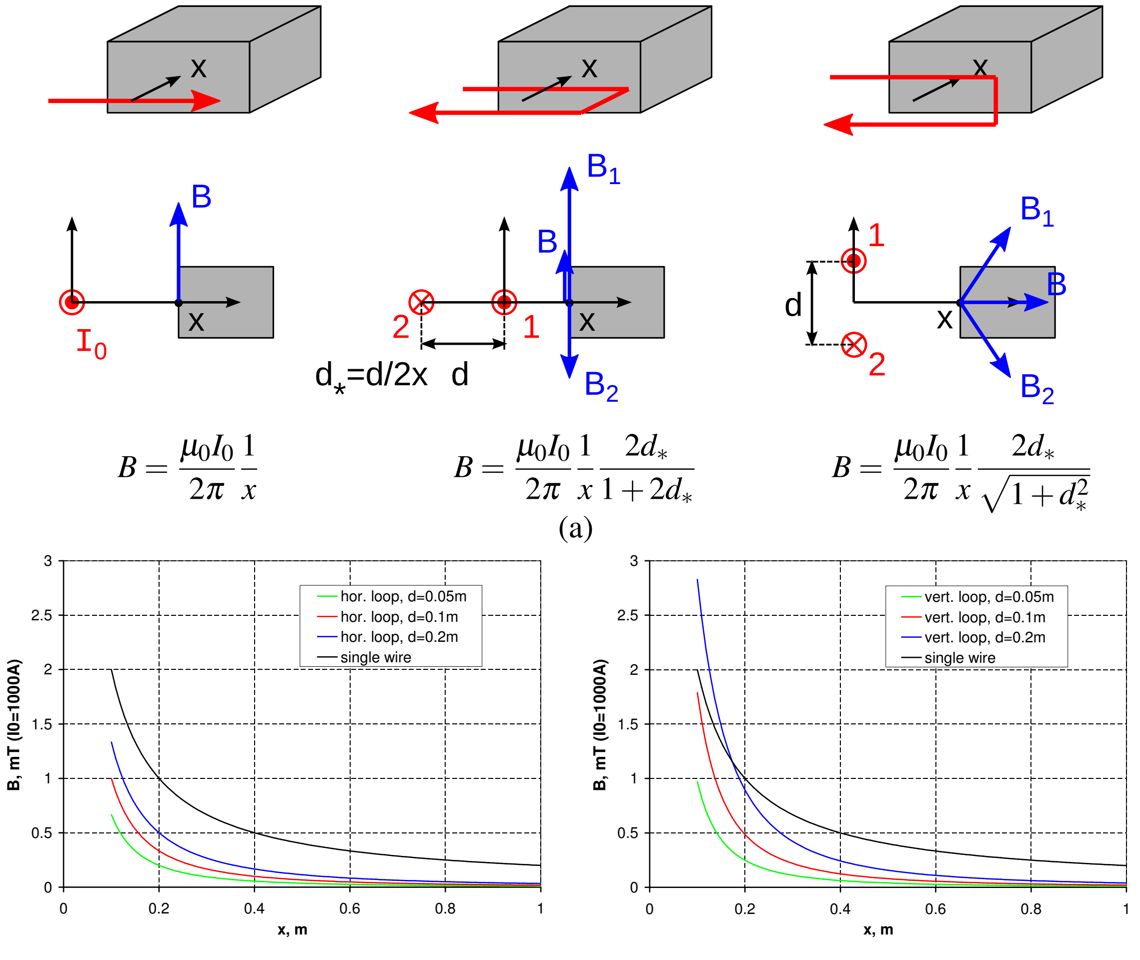

$$B = \frac{\mu_0 I_0}{2\pi}\frac{1}{x} \qquad B = \frac{\mu_0 I_0}{2\pi}\frac{1}{x}\frac{2d_*}{1+2d_*} \qquad B = \frac{\mu_0 I_0}{2\pi}\frac{1}{x}\frac{2d_*}{\sqrt{1+d_*^2}}$$

(a)

(b) (c)

Figure 7.10.: Influence of inductor topology on the resulting magnetic field: (a) geometry and analytical expressions for a single wire, horizontal loop, and vertical loop (from left to right); (b,c) dependence of the resulting magnetic field B on the melt–inductor distance x.

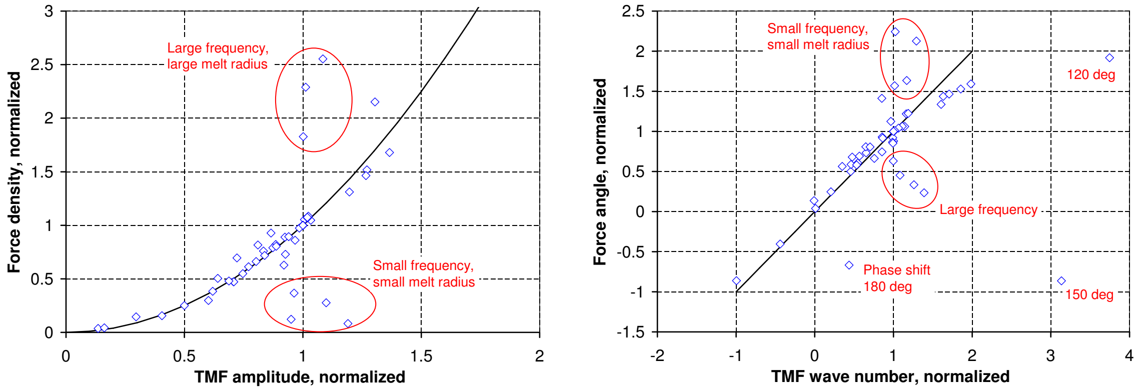

(a) (b)

Figure 7.11.: 2D electromagnetic calculations for a silicon melt in a TMF: (a) correlation between force density F_L (10.9 N/m^3) and approximate TMF amplitude B_{0z} (1.873 mT); (b) correlation between force angle with the horizontal plane φ (33.9°) and approximate TMF wave number α (5.63 1/m). The values are normalized to the reference case given in brackets. Approximations with a quadratic law $F_L \sim B_{0z}^2$ and a linear law $\varphi \sim \alpha$ are added.

- The amplitude of the resulting magnetic field is basically determined by the phase shifts between inductors and the inductor–melt distances
- The TMF wave number is proportional to the ratio of the phase shift to the vertical separation between the phase-shifted currents

7.6.2. Design and scaling of TMF inductors

The parameters of realistic TMF inductors can be divided into three groups:

- Parameters for TMF control during the process: current amplitude; frequency; phase shift
- Parameters for TMF design: height, width, distance, and number of inductors; melt–inductor distance
- Parameters determined by the furnace design: current distribution and phase cut; inductor–wall distance; melt radius and height

Consequently, the choice of TMF inductor parameters could be made in the following way:

1. Inductor geometry is chosen to obtain the required range of Lorentz force densities and angles:
    - Higher force densities can be achieved with a smaller melt–inductor distance, a larger inductor–wall distance, or a smaller distance between inductor midpoints
    - Higher vertical force components can be achieved with a larger number of inductors
2. Skin depth is tuned using the current frequency
3. Force angle is tuned using the phase shift
4. Force density is tuned using the (square of) current amplitude

Steps 3–4 could be carried out also during the crystallization, e.g., to compensate the effect of a decreasing melt height. This could be achieved by decreasing the phase shift to keep the force angle constant and by increasing the current amplitude to keep the force density constant. However, a melt flow analysis should be performed first to determine whether such adjustments are necessary.

It has been discussed previously in Sec. 2.4 that the requirement for a perfect geometrical similarity might be a significant restriction for the transfer of the results between systems of different size. For example, the up-scaling of model experiments demonstrated in Chapter 4 would require the use of an inductor radius of 2.4 m in a system with the melt width increased from 0.1 m to 0.8 m. However, the scaling of melt flow requires only a proportionally scaled Lorentz force distribution. It could be obtained also for a constant inductor–melt distance in the following way (see Fig. 7.9 (b)):

- Frequency is decreased to obtain the same relative skin depth
- Phase shift is increased to compensate the decrease of the force angle
- Current amplitude is adjusted to obtain the required force density

The relative importance of all previously discussed inductor parameters for the characteristics of the Lorentz force distribution is illustrated in Tab. 7.2.

7.6.3. Inductor parameters for a crystallization furnace

The reference geometry proposed at the beginning of this chapter, which is compatible with the global thermal furnace model discussed in Chapter 6, allows to obtain (in 3D) a Lorentz force density of 12 N/m^3, force angle of 31°, and skin depth of 2.6 cm at the melt side with the following reference parameters:

- **Current frequency of 50 Hz**
- **Current amplitude of 300 A**
- **Phase shift between the inductors of 60°**

These parameters will be used as the starting point of flow calculations in the following chapter.

Parameter	Force density	Force angle	Skin depth
TMF control			
Inductor current frequency	↑↑↑	↓↓↓	↓↓
Inductor current amplitude	↑↑↑	—	—
Phase shift between inductors	↓↓↓	↑↑↑	∗∗
TMF design			
Inductor radius	↓↓↓	↓↓	—
Inductor height	↓↓	↓	—
Distance between inductors	↓↓	↓	—
Number of inductors	∗∗	↑↑↑	—
Furnace design			
Current distribution among inductors	∗	∗	—
Phase cut of inductor current	↓↓↓	↓↓↓	∗
Inductor distance to conducting walls	↑	—	—
Melt radius	↑↑↑	↓↓↓	↑↑
Melt height	↑↑	↓↓	—

Table 7.2.: The relative importance of all previously discussed inductor parameters for the characteristics of Lorentz force distribution. The importance is estimated from the observed change of the normalized reference values, which is shown by the number of symbols: —(<20%), ∗ (<50%), ∗∗ (<100%), ∗ ∗ ∗ (>100%). The characteristic direction of influence is indicated by arrows where possible.

Chapter 8

Melt flow, crystallization interface, and species transport

A local model for a square melt in a TMF is used here for investigations of the flow, temperature, and species concentration in the melt as well as of the motion of the crystallization interface. Local temperature boundary conditions and parameters for TMF inductors from the studies in the previous chapters are applied. Coupled and decoupled, steady and unsteady, analytical and local 3D models of the melt flow and crystallization interface are compared. This allows us to discuss both the optimal TMF parameter range for crystallization furnaces and the optimal simulation strategy for further investigations.

8.1. Reference case

The 3D reference case geometry is chosen identical to Chapter 7. The time-average 3D Lorentz force distribution described previously in Sec. 7.2 is imported in `OpenFOAM` for 3D unsteady flow calculations. We consider a melt with dimensions of 22×22×11 cm^3, usually located at the coordinates $x = -0.11 \ldots 0.11$ m, $y = -0.11 \ldots 0.11$ m, $z = -0.055 \ldots 0.055$ m (the Lorentz force distribution is shifted vertically). The melt is surrounded by 3 side inductors with a frequency of 50 Hz, current amplitude of 300 A, and phase shift of 60° (see Sec. 7.6.3) generating an upward TMF. The 3D inductor geometry is not fully symmetric because it contains current supplies on one side ($x > 0$).

Temperature boundary conditions on melt surfaces follow from the results in Chapter 6. For the reference case, a vertical temperature gradient of 1 K/cm (without a flow) and a zero lateral temperature gradient are assumed. During a crystal growth process, the temperature on the melt free surface at the top is determined by the received heat radiation; the temperature on side surfaces is not fixed and is determined by heat conduction in the crucible walls. Therefore, temperature boundary conditions in the reference case are set as follows:

- Bottom: melting point temperature of 1685 K
- Top: a radiation heat flux to an ambient temperature of 1725.4 K. In the case without a melt flow, this ensures a temperature gradient of 1 K/cm (a temperature of 1696 K at the top surface)
- Sides: zero heat flux

The melt flow analysis is started with unsteady 3D calculations with a fixed flat shape and fixed position of the crystallization interface. In addition to the assumed flat shape, this implies two other approximations. First, it is assumed that the upward motion of the interface does not significantly change the melt flow. This assumption seems plausible as long as the crystallization velocity of about 1 cm/h = $2.8 \cdot 10^{-6}$ m/s is much smaller than the melt flow velocity. Secondly, it is assumed that the back-reaction of the flow-induced changes of the interface shape on the flow itself can be neglected. The validity of this assumption can be analyzed only in fully coupled calculations, which will be presented later in this chapter.

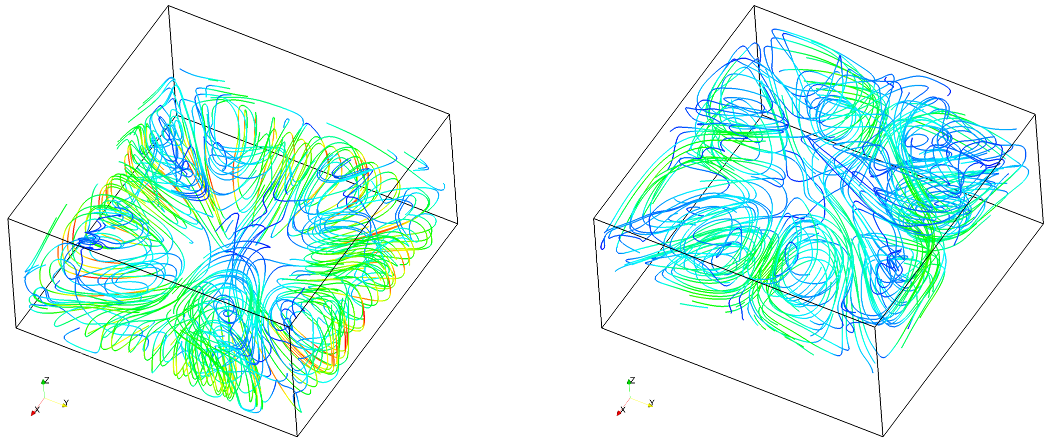

Figure 8.1.: 3D melt flow calculations for the reference case with L = 22 cm, H = 11 cm, I_0 = 300 A, ϕ = 60°, TMF up: streamlines for the time-average (300...1500s) velocity field (u_{max} = 0.62 cm/s). The melt is vertically divided into two parts that are shown separately.

The calculated time-average flow pattern is depicted in Fig. 8.1 using 3D streamlines. The characteristic TMF torus extends approximately only to the mid-height of the melt. Above the torus, horizontal vortices prevail in the top half of the melt. As already known from model experiments in Chapter 5, this flow structure indicates a strong effect of buoyancy forces in the melt flow. Further details of the velocity field can be seen in the cuts given in Fig. 8.2. In the top part of the melt, four jets appear at the centers of all sides and then turn to the corners, forming 8 horizontal vortices. In the vicinity of the crystallization interface, the flow is uniformly directed from the center to the rim, with a small low-velocity zone in the center. This velocity distribution would be decisive for the mixing of impurities.

The time-average temperature field in Fig. 8.2 shows rather small deformations of isolines by the melt flow in a vertical cut. The maximum melt temperature is decreased by 0.5 K, and the temperature distribution in a horizontal cut 3 cm from the top shows flow-induced temperature differences of 0.7 K. The asymmetry due to the current supplies, which is less distinct in the velocity distribution, now becomes clearly visible. However, the temperature distribution 3 mm above the crystallization interface still remains symmetric; the temperature is higher in the central part. It can be estimated from the temperature distribution that the flow changes the vertical temperature gradient from 1 K/cm to 1.6 K/cm in the central part and to 0.3 K/cm at the rim. These changes in the temperature gradient would determine the flow influence on the crystallization interface.

The unsteady character of the flow is demonstrated in Fig. 8.3. The calculation is started from a zero velocity field and a uniform temperature distribution of 1700 K. The flow velocity at a selected monitor point shows an oscillation period of about 200 s; the oscillation

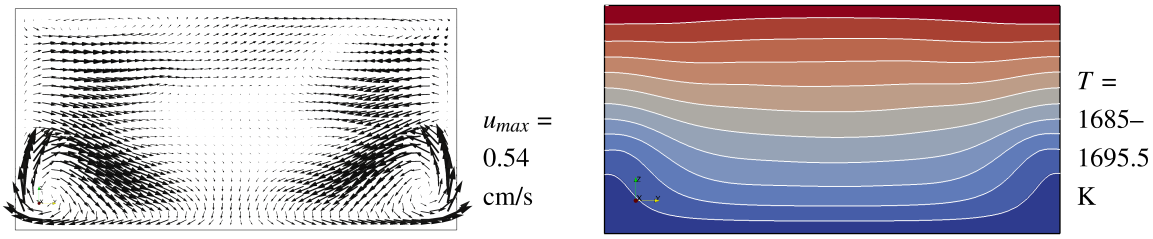

(a) Vertical cut through the melt center

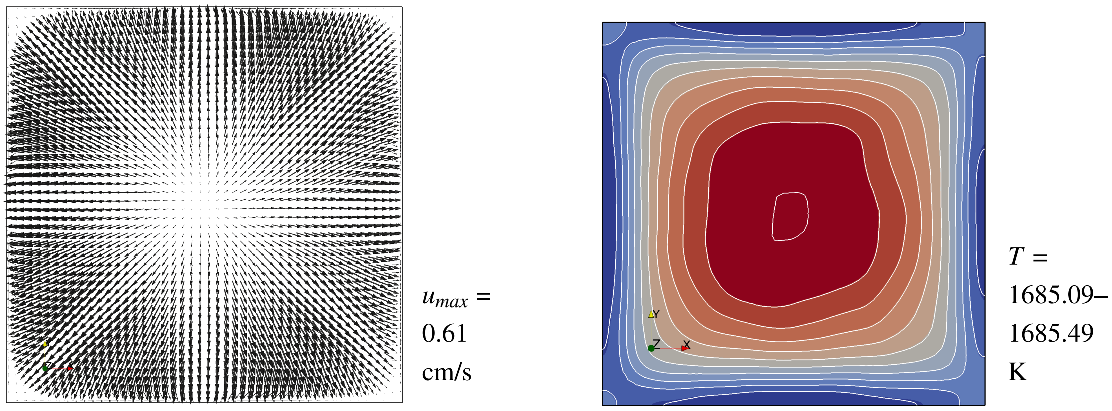

(b) Horizontal cut 3 mm from the bottom

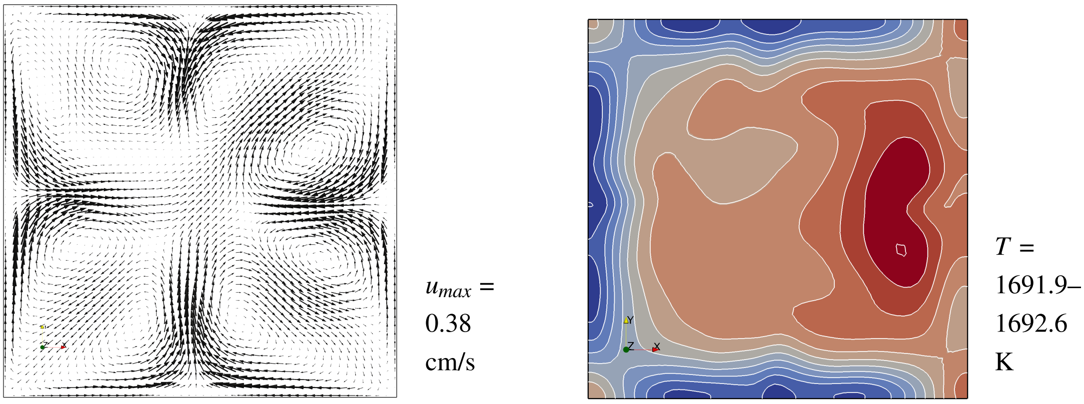

(c) Horizontal cut 3 cm from the top

Figure 8.2.: 3D melt flow calculations for the reference case with L = 22 cm, H = 11 cm, I_0 = 300 A, ϕ = 60°, TMF up: time-average (300. . . 1500s) velocity and temperature fields in a vertical cut through the melt center (a), in horizontal cuts 3 mm from the bottom (b) and 3 cm from the top (c).

amplitude is significantly higher than the average value. In contrast, the temperature reaches a stable average value only after about 500 s and continues to oscillate with a small amplitude of about 0.2 K.

8.2. Influence of numerical parameters

The independence of relevant calculation results of grid resolution has been defined in Chapter 4 as a requirement to justify unsteady 3D calculations without turbulence models. Rel-

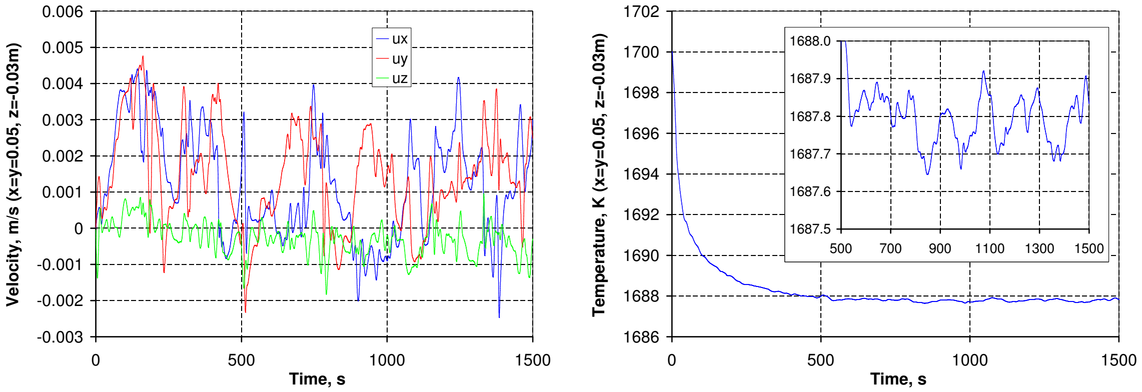

(a) (b)

Figure 8.3.: 3D melt flow calculations for the reference case with $L = 22$ cm, $H = 11$ cm, $I_0 = 300$ A, $\phi = 60°$, TMF up: oscillations of velocity components (a) and temperature at a fixed point.

evant calculation results are in this case the time-averaged velocity and temperature fields. Fig. 8.4 shows temperature and velocity distributions on a vertical line. In the reference case, the mesh for flow calculations contains 160550 hexahedrons with a bulk element size of 4 mm (reduced to 0.4 mm at the walls). To check the grid sensitivity, element size in the entire volume was decreased by a factor of 2 (936000 elements, 2 mm bulk size) and increased by a factor of 2 (34656 elements, 8 mm bulk size). Although the numbers of elements on the finest and roughest grids differ by a factor of 27, differences in the profiles for an inductor current of 300 A are small and occur mainly in the velocity profile at the top of the torus. The deviations are not significantly larger also for an inductor current of 675 A, which corresponds to flow velocities higher by a factor of 5. Consequently, the mesh in the reference case can be used for further 3D calculations. Larger differences between the distributions can be observed for the smaller inductor current if the averaging time interval is reduced. This is obviously caused by the relatively large oscillation period and temperature changes during the first 500 s as shown in Fig. 8.3.

While the no-slip condition ($\vec{u} = 0$) is a reasonable assumption for the velocity on the side walls of the crucible and on the crystallization interface, conditions at the free melt surface are somewhat unclear. If the surface is completely free, Marangoni forces act along the surface according to (2.54) where the tangential stress is proportional to the tangnetial temperature gradient and the Marangoni coefficient. The exact value of the Marangoni coefficient strongly depends on the contents of gas atmosphere – it can vary by a factor of 4 in dependence of oxygen concentration [Mukai et al., 2000]. If the surface is heavily oxidized or covered by islands of solid silicon or some impurities, it could be appropriate to assume a partial slip/no-slip boundary, without additional forces. This assumption could be simplified either to a slip (stress-free) boundary or to a no-slip boundary. Velocity profiles on a vertical line for the cases with a no-slip, slip, and Marangoni boundary condition are compared in Fig. 8.4. A Marangoni coefficient of –0.00035 N/mK was assumed, which corresponds to an oxygen-saturated atmosphere at 1693 K [Mukai et al., 2000]. It can be seen that the boundary condition leads only to small changes in the top part of the melt. Marangoni forces pull the melt in the opposite direction than the melt flows with a slip condition; consequently the Marangoni condition effectively agrees with the no-slip case. Due to the uncertainty in the reality and the localized influence of this boundary condition, the no-slip condition was

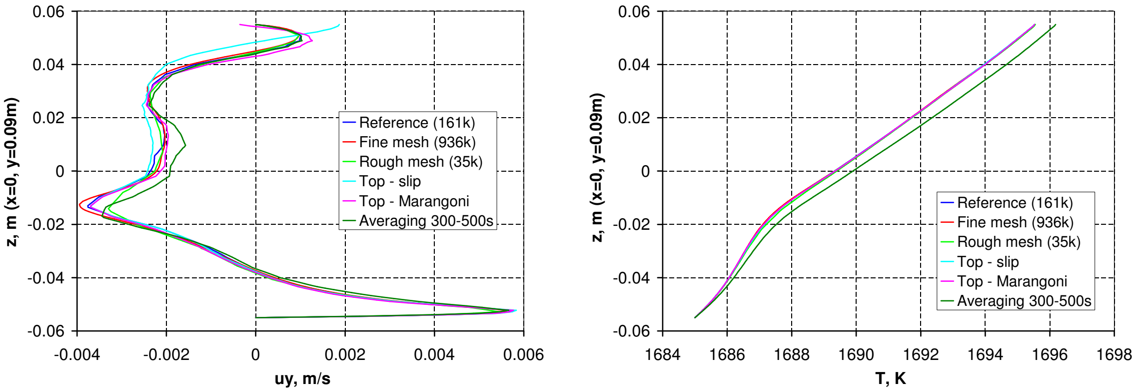

(a) I_0 = 300 A (b) I_0 = 300 A

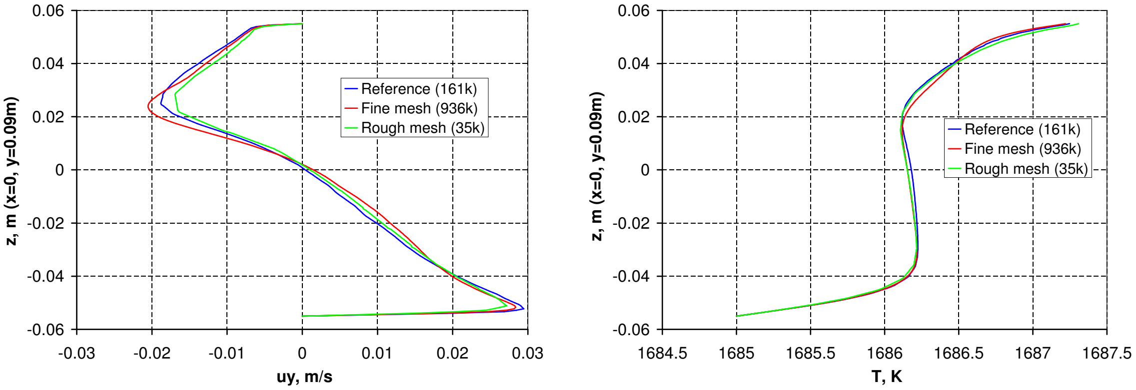

(c) I_0 = 675 A (d) I_0 = 675 A

Figure 8.4.: 3D melt flow calculations for the case with L = 22 cm, H = 11 cm, ϕ = 60°, TMF up: vertical profiles of time-averaged velocity and temperature for an inductor current I_0 of 300 A (a,b) and 675 A (c,d). The influence of various numerical parameters is shown: mesh with 160550 hexahedrons (reference) and with 2 times smaller and larger elements in the entire volume; no-slip (reference), stress-free (slip), and Marangoni-stress boundary condition on the top surface; averaging over a time interval of 300…1500s (reference) or 300…500s.

selected for all further studies in the current work as the simplest alternative.

8.3. Influence of inductor current parameters

Non-isothermal model experiments in Chapter 5 showed that the interaction between buoyancy and Lorentz forces depends on the ratio of these forces. A transition between different flow regimes occurs if the temperature gradient in the melt or the inductor current are changed. An approximate criterion for the dominance of Lorentz forces was derived: $Gr \ll F_{em}$. For a specific system, it is important to determine the transition point between the flow regimes exactly. Therefore, the calculation from the reference case is repeated with different inductor currents for both isothermal (without buoyancy forces) and non-isothermal flows. When the difference between both cases becomes very small, the role of buoyancy forces in the melt is small in comparison to Lorentz forces.

Fig. 8.5 shows changes of maximum melt velocity and temperature as inductor current is increased from zero. A sudden onset of the mixing of temperature field occurs at inductor currents above 300 A; it leads to a decrease of the maximum melt temperature as well as a steeper increase of the maximum melt velocity . Consequently, the reference case with an inductor current of 300 A is located at the upper boundary of the flow regime with a strong influence of buoyancy. This was already presumed in Sec. 8.1. The maximum flow velocity indicates that the role of buoyancy becomes almost negligible only at inductor currents exceeding 675 A. Then, the maximum Lorentz force density in the melt reaches 70 N/m^3, which is 5 times higher than in the reference case with 14 N/m^3.

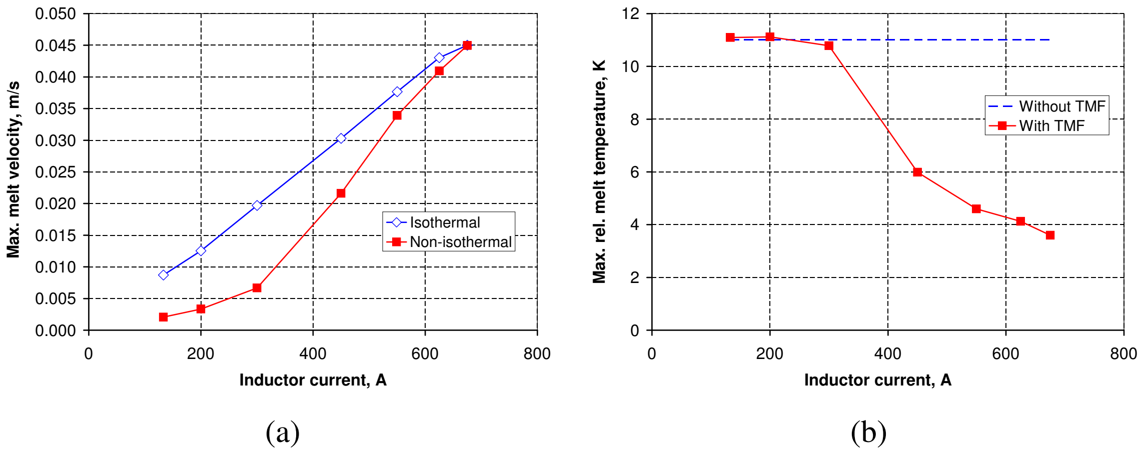

(a) (b)

Figure 8.5.: 3D melt flow calculations for the case with $L = 22$ cm, $H = 11$ cm, $\phi = 60°$, TMF up, and various inductor currents: maximum melt velocity (a) and temperature (b) in dependence of inductor current for isothermal (without buoyancy) and non-isothermal cases. Temperature is given relative to the 1685 K melting point.

While inductor current changes only the force density, the phase shift between the inductors has a significant influence on both the force density and the force direction. Therefore, it could be an important parameter for the TMF control in a real crystallization furnace. The influence of the phase shift was not investigated in model experiments in Chapters 4 and 5, where the phase shift was fixed to 60°. Here, the calculation from the reference case is repeated with different phase shifts in the range 0...180°. In each case, inductor current is adjusted to keep the maximum Lorentz force in the melt equal to the reference case. In this way, the role of the force direction alone on both the flow pattern and the velocity magnitude can be investigated.

Fig. 8.6 summarizes velocity distributions in horizontal and vertical cuts. Both isothermal and non-isothermal cases are considered. A comparison of isothermal cases with 60° and 120° shows a very similar flow pattern, but the velocity is higher by a factor of 1.5 in the case of 120°. This is an effect of a significantly increased vertical Lorentz force component. However, note that the required inductor current to achieve the same level of force density is almost 3 times higher. If inductor current were increased at 60°, the same velocity could be achieved already at about 450 A according to Fig. 8.5. Consequently, the smaller phase shift of 60° is more efficient with respect to the melt mixing in the Lorentz-force-dominated regime. The same conclusion holds for the buoyancy-influenced flow regime: the flow velocity is not higher with 120°; the flow pattern shows a vertically extended torus while the velocity distribution at the crystallization interface remains the same.

The case with a phase shift of 180° in Fig. 8.6 (c) shows a completely different flow pattern in comparison to the reference case: it contains several toroidal flow structures. However, the

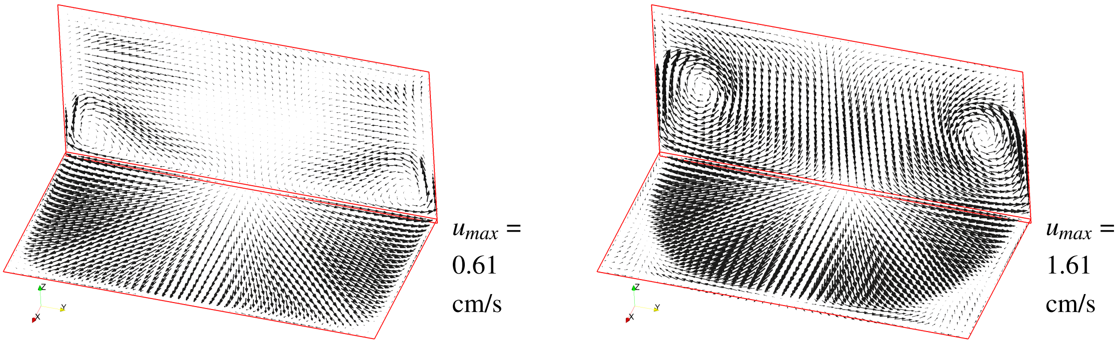

(a) ϕ = 60°, TMF up, I_0 = 300 A

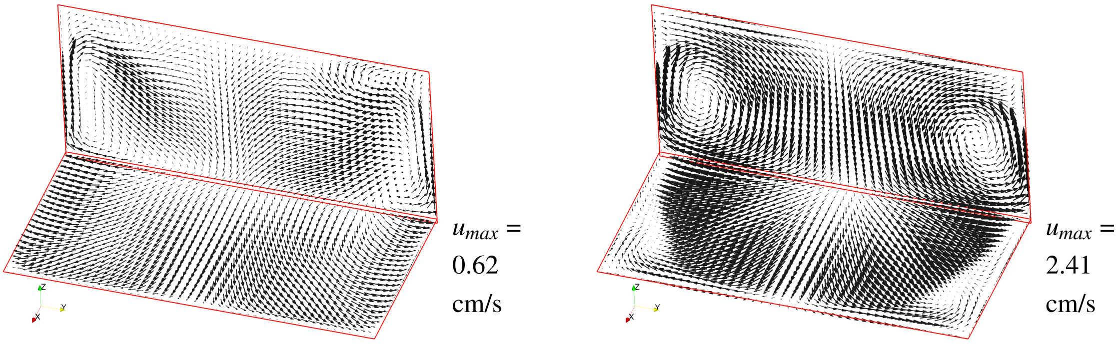

(b) ϕ = 120°, TMF up, I_0 = 896 A

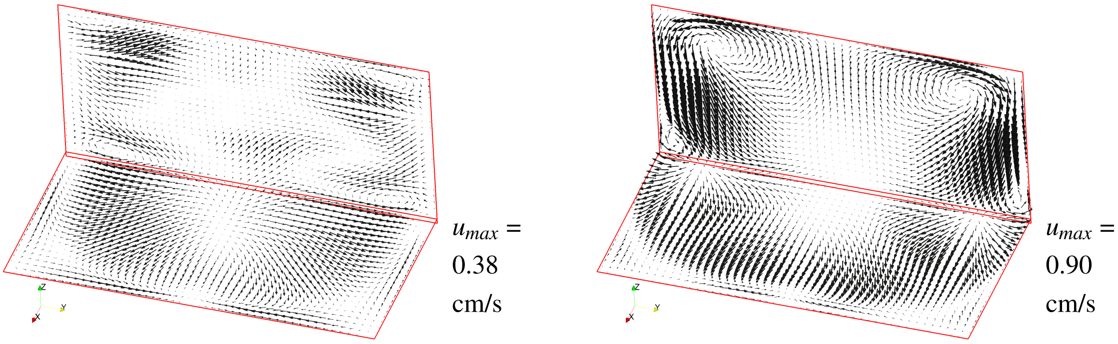

(c) ϕ = 180°, TMF up, I_0 = 970 A

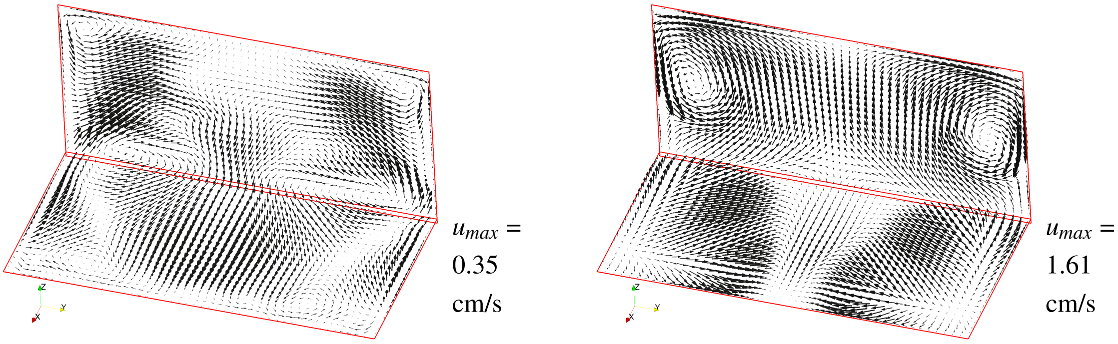

(d) ϕ = 60°, TMF down, I_0 = 300 A

Figure 8.6.: 3D flow velocity distribution for cases with $L = 22$ cm, $H = 11$ cm, and various phase shifts and TMF directions (a–d). Inductor current is adjusted to obtain the same maximum Lorentz force density as in the reference case (a). Both isothermal (right) and non-isothermal (left) cases are considered.

flow velocity is very low: although inductor current is increased more than 3 times, the flow velocity is almost 2 times lower. The other extreme case with a phase shift of 0° is shown separately in Fig. 8.7; strictly speaking, it is not a TMF but an alternating magnetic field. The flow structure remains very similar to the reference case, but with a distinct second torus at the top in the isothermal case. An interesting flow structure is observed: a horizontal vortex appears in the central part similarly to the model experiments at small melt heights ($H/L = 0.25$). Obviously, the double-torus structure effectively divides the melt into two parts each occupying a half of the full height. The flow velocity with 0° is almost 2 times smaller than in the reference case in the Lorentz-force-dominated regime and approximately the same in the buoyancy-influenced regime.

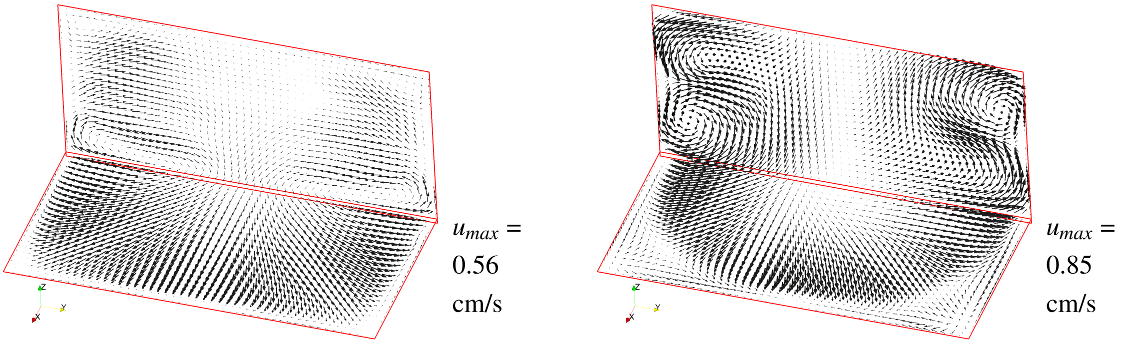

(a) Non-isothermal

(b) Isothermal

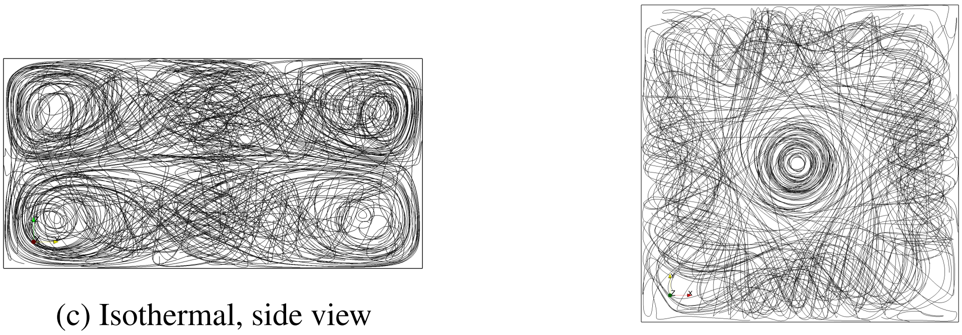

(c) Isothermal, side view

(d) Isothermal, top view

Figure 8.7.: 3D melt flow calculations for the case with $L = 22$ cm, $H = 11$ cm, $I_0 = 239$ A, $\phi = 0°$ (alternating field): 3D velocity distribution for the isothermal (b) and non-isothermal (a) case; 3D streamlines for the isothermal case in side (c) and top (d) views.

In summary, a TMF with a phase shift of 60° seems to be near the optimum with respect to a strong melt mixing. In contrast to 0°, it allows also a reversal of the flow direction in the isothermal case as shown in Fig. 8.6 (d) with a downward TMF. In the non-isothermal case, the reversal is only partial because the flow at the crystallization interface is still directed to the rim in the central part. The flow velocity is then about 2 times smaller than with an upward TMF. Note also that the velocity distribution at the bottom is significantly less uniform in case of a downward TMF.

8.4. Influence of melt dimensions

We could use the reference case geometry and adjust parameters such as current frequency, current amplitude, and temperature gradient to investigate flow regimes that correspond to realistic conditions in melts of different size. This approach would leave the question open how to achieve these conditions in the reality. Therefore, a more direct approach is chosen where for different melt dimensions, realistic inductor geometries and temperature gradients are considered. In this way, all considered cases are realistic and practically relevant.

In the first series of calculations, melt width L is varied between 10 cm and 80 cm keeping a constant height to width ratio of 1/3. In the second series, melt height is varied in the range $H/L = 1/6 \dots 2/3$ at $L = 40$ cm. The entire inductor geometry is scaled proportionally with the melt width except inductor thickness (2 cm) and inductor-melt distance (8 cm). The basic geometry is very similar to the reference case from Sec. 7.1, but the total height of inductors is set to $0.3 \cdot L$, the distance between inductors to $0.05 \cdot L$, and the distance between current supplies to $0.1 \cdot L$. The TMF inductors as well as the melt with a full height of $2/3 \cdot L$ are located symmetrically to $z = 0$. The bottom of the melt with a half height of $H = 1/3 \cdot L$ is located at $z = 0$. The width and the height of the calculation domain are set to the double inner inductor width and $3 \cdot L$, respectively. Fig. 8.8 shows the geometry and the mesh for the smallest and the largest melt. The element size in the melt is scaled proportionally to the melt width between 5 mm and 2 cm.

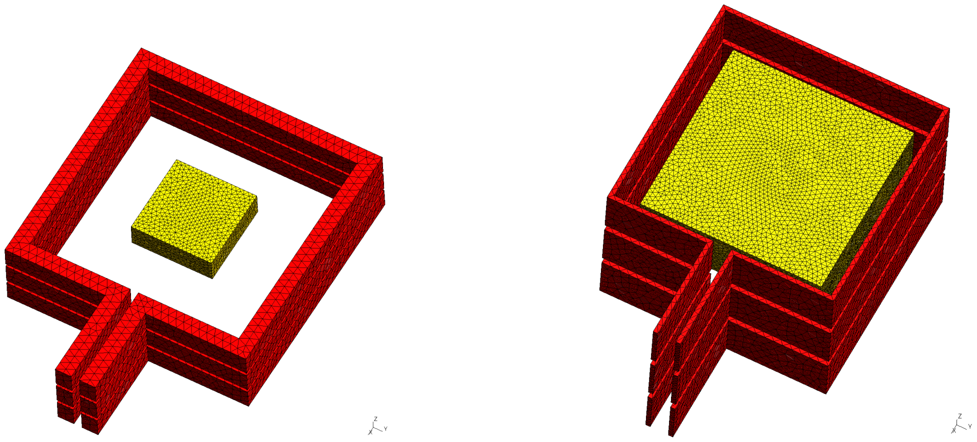
(a) $L = 10$ cm

(b) $L = 80$ cm

Figure 8.8.: Geometry and mesh for electromagnetic calculations with `GetDP` for the parameter study with different melt dimensions. Cases with melt widths of 10 cm (a) and 80 cm (b).

Due to changes in inductor geometry, the Lorentz force distribution differs for various melt dimensions. The changes of Lorentz force density, force angle, and skin depth are summarized in Fig. 8.9. With an increasing melt width, the force angle decreases, the force density has a maximum at $L = 40$ cm, and the skin depth increases. In contrast to the results described in Chapter 7, the force density does not increase monotonically and the skin depth increase does not reach a saturation at $L = 40$ cm. A significant difference in present calculations is the 3D geometry and the variation of the vertical dimensions of inductors.

In absolute values, the skin depth increases from 1.3 cm at $L = 10$ cm to 5.6 cm at $L = 80$ cm. However, relatively to the melt width, it decreases from 13% to 7% – by a factor of 2. Consequently, this parameter study allows us to investigate the influence of the relative skin depth on the flow pattern. Two other main properties of the Lorentz force distribution – the force angle and the force density – were already analyzed in the previous section. It must be noted that the force angle also changes with the melt width. Similar angles are obtained only for the two largest melts with L of 40 and 80 cm.

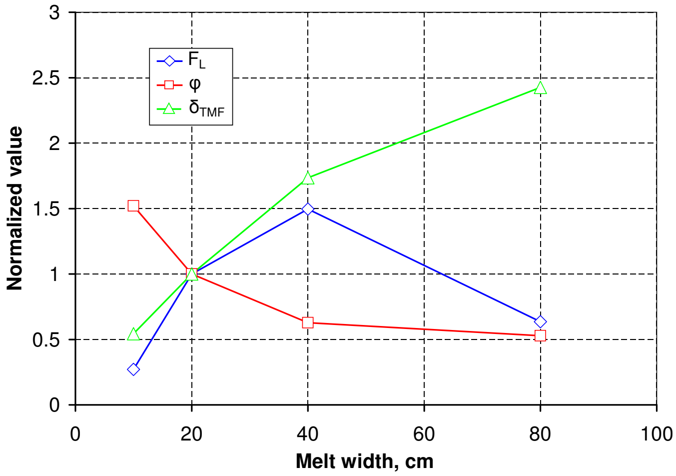

Figure 8.9.: 3D Lorentz force calculations with $H/L = 1/3$, $I_0 = 300$ A, $\phi = 60°$, TMF up: influence of the melt width L on the force density F_L (8.7 N/m^3), force angle with the horizontal plane φ (37.4°), skin depth of the force δ_{TMF} (2.3 cm). The values are calculated as described in Chapter 7 and are normalized to the case with L = 20 cm given above in ().

The mesh size in flow calculations was varied between 93600 elements for $L = 10$ cm and 370025 elements for $L = 80$ cm. For each melt geometry, a series of calculations with different inductor currents was performed for the isothermal and non-isothermal case. In the non-isothermal case, a vertical temperature gradient of 1 K/cm was applied to the melt by adjusting the ambient temperature at the top surface. A comparison of the cases with and without buoyancy forces allows one to determine the transition to the Lorentz-force-dominated flow regime. Fig. 8.10 shows the behavior of maximum flow velocity for various inductor currents. The absolute velocity level at a constant force density increases with the melt width reaching 9 cm/s at $L = 80$ cm and $F_L = 150$ N/m^3. For all melt sizes, an additional temperature gradient decreases the melt velocity at low Lorentz force densities, and the difference disappears at high force densities. The ratio of flow velocities in both cases shows a better agreement between various melt sizes if the vertical Lorentz force component is plotted on the horizontal axis instead of the force magnitude. It can be estimated that the ratio reaches 0.4 at $F_{Lz} = 10$ N/m^3 and 0.9 at $F_{Lz} = 60$ N/m^3. These two ratios correspond to the extremal cases with a suppressed TMF flow and a negligible buoyancy effect, respectively.

The time-averaged temperature and velocity fields in a vertical cut for the extremal cases marked in Fig. 8.10 (b) are given in Fig. 8.11. The calculations were usually carried out for a time interval of 500…1800 s to obtain reliable time-average values. In the cases without buoyancy forces, the TMF torus reaches the top of the melt for all melt widths. However, the horizontal extension of the torus decreases so that the velocity at the interface in the central melt part becomes smaller. This is an effect of a smaller relative skin depth at larger melt sizes. Consequently, the current frequency at larger melt sizes should be reduced to increase the skin depth and to obtain a more uniform velocity distribution at the crystallization interface.

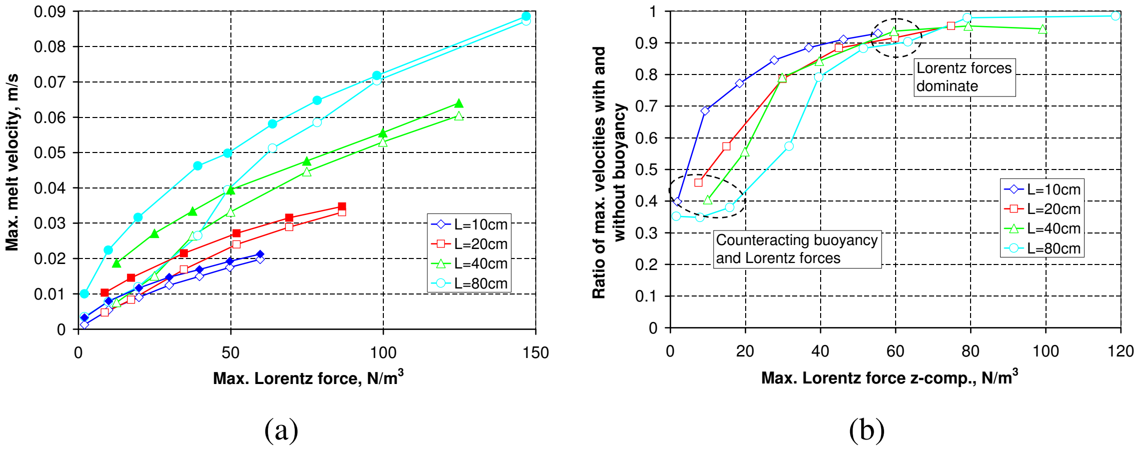

Figure 8.10.: 3D melt flow calculations with $H/L = 1/3$, $\phi = 60°$, TMF up: melt velocity in the isothermal (filled symbols) and non-isothermal (white symbols) case in dependence of the Lorentz force in the melt (inductor current) for various melt sizes.

In the cases with buoyancy forces in Fig. 8.11, the TMF torus clearly is more suppressed at a larger melt width. While at $L = 10$ cm the torus extends almost to the top of the melt, at $L = 80$ cm it is located at the crystallization interface, in the lower quarter of melt height. Obviously, the ratio of the isothermal and non-isothermal flow velocities (approximately 0.4 here) is not a sufficient criterion for the flow structure in the buoyancy-influenced flow regime.

Strictly speaking, each melt and inductor geometry in the present study is a different case with its own force distribution (force angle and skin depth) and with its own scaling laws. Nevertheless, we can try to find a characteristic of the force distribution that correlates well with flow conditions in all cases. As shown in Fig. 8.12, the Reynolds number and the TMF forcing parameter lead to a good correlation in the case without the buoyancy forces independently of the melt width. The dimensionless numbers are defined as:

$$Re = \frac{u_0(L/2)\rho}{\eta}, \quad F_{em} = F_{Lzmax}\frac{\rho(L/2)^3}{\eta^2}, \tag{8.1}$$

where the F_{em} number is based on the vertical Lorentz force component. If the isothermal cases with various H/L ratios in the range 1/6 … 2/3 are considered as well, the following approximate correlation holds:

$$Re = 1.8\frac{H}{L}\sqrt{F_{em}}. \tag{8.2}$$

The square-root dependence between the velocity and force density follows also from simple physical considerations. Let us consider the acceleration of a fluid particle during its upward motion along the side wall starting with a zero velocity at the bottom. The length of the path L_p is related to the final velocity at the top u_p with $L_p = u_p^2/2a_p$, where a_p is the acceleration of the particle. According to Newton's second law, the acceleration is determined by the force density on the particle as $a_p = F_p/\rho$. Hence, we obtain:

$$u_p = \sqrt{\frac{2L_pF_p}{\rho}}. \tag{8.3}$$

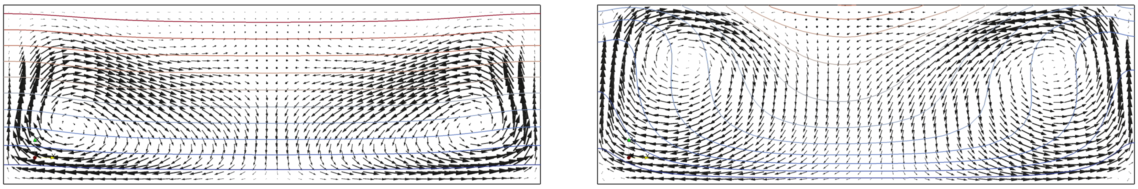

u_{max} = 0.12 cm/s, T_{max} = 1688.4 K u_{max} = 1.77 cm/s, T_{max} = 1687.5 K

(a) L = 10 cm

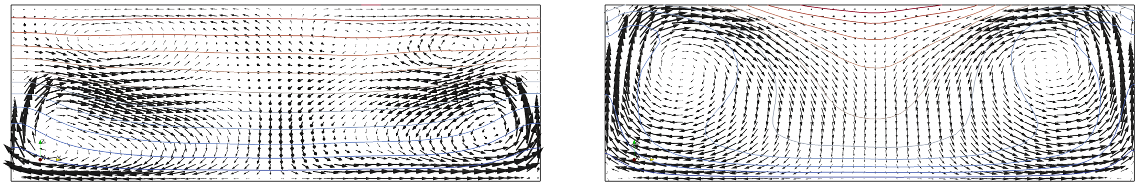

u_{max} = 0.37 cm/s, T_{max} = 1691.5 K u_{max} = 2.44 cm/s, T_{max} = 1688.3 K

(b) L = 20 cm

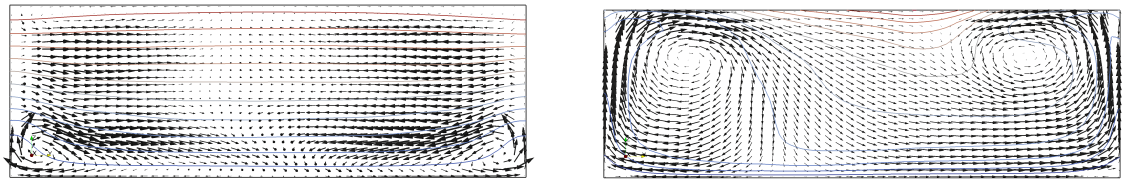

u_{max} = 0.44 cm/s, T_{max} = 1698.3 K u_{max} = 3.4 cm/s, T_{max} = 1690.4 K

(c) L = 40 cm

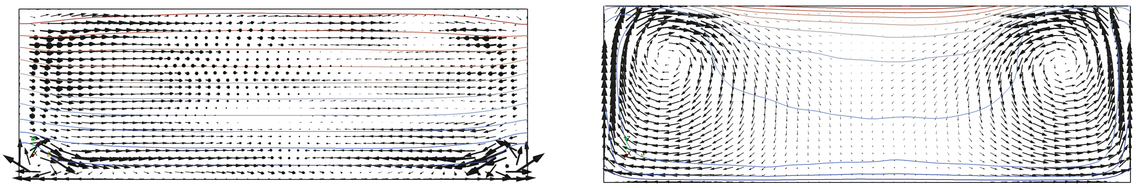

u_{max} = 0.75 cm/s, T_{max} = 1712.5 K u_{max} = 4.5 cm/s, T_{max} = 1692.9 K

(d) L = 80 cm

Figure 8.11.: 3D melt flow calculations with H/L = 1/3, ϕ = 60°, TMF up: time-average velocity and temperature in a vertical cut through the melt center perpendicular to the side wall for different melt widths (a–d), for a flow regime with a strong (left) and small (right) buoyancy effect. The chosen cases are marked in Fig. 8.10 (b).

The correlation (8.2) can be rewritten as

$$u_0 = 0.9\sqrt{\frac{H}{L}}\sqrt{\frac{2HF_{Lzmax}}{\rho}}, \tag{8.4}$$

which basically differs only with the coefficient in front of the square root.

The same correlation between the flow velocity and Lorentz force density holds in the non-isothermal case in the range with dominating Lorentz forces. The transition to this regime can be approximately determined using a comparison of the forcing parameter and the Grashof number: $F_{em} > Gr$. For the cases with dominating Lorentz forces in Fig. 8.11, the Gr number defined using the maximum temperature difference (without a melt flow) was

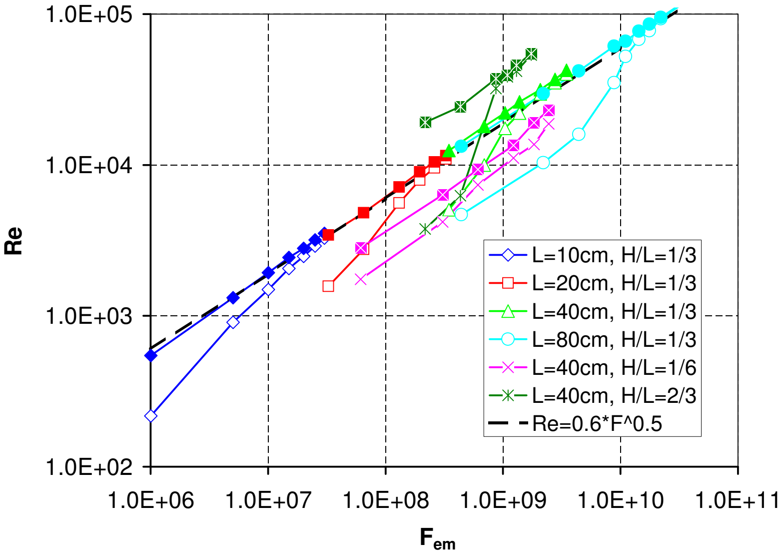

Figure 8.12.: 3D melt flow calculations with $H/L = 1/3$, $\phi = 60°$, TMF up: correlation between the Reynolds number and the TMF forcing parameter for different melt sizes for the isothermal (filled symbols) and non-isothermal (white symbols) cases.

roughly similar to the F_{em} number deviating less than by a factor of 2. However, because the temperature difference is always decreased due to the melt mixing, the actual Gr values are effectively smaller.

8.5. Unsteady coupled calculations of melt flow and crystallization interface

A full analysis of melt flow influence on the crystallization interface and the species transport including the segregation requires a coupled calculation of all three phenomena. Additionally, a changing melt height and melt temperature may require a recalculation of the global temperature field and the Lorentz force distribution. Because the crystallization process may last several tens of hours, such an analysis in 3D can be very time consuming. The complexity of coupled calculations could be significantly reduced by introducing several physical approximations as summarized in Tab. 8.1. The validity of the various simplifications is discussed in this section on the basis of several coupled 3D calculations.

The reference case from Sec. 8.1 is extended with a solid crystal of 11 cm height at the bottom (the interface is located at $z = 0$). The mesh contains 202800 elements in the melt and 139425 elements in the crystal with a bulk size of 4 mm. Element size is decreased to 0.4 mm at the sides, the free surface, and the crystal side of the interface; and to 0.1 mm at the melt side of the interface. Zero heat flux is set on the crystal sides and a constant temperature gradient of 10 K/cm is set on the bottom surface. The initial vertical temperature gradients in the melt (1 K/cm) and crystal (10 K/cm) correspond to heat fluxes of Q_L = 6700 W/m^2 and Q_S = 22000 W/m^2, respectively. The difference of 15300 W/m^2 is the effective cooling power available for crystallization. From the expression (2.71) for the latent heat $\rho_s Q_l v_n$, we can estimate the crystallization velocity as 1.3 cm/h. Other boundary conditions for the temperature and velocity fields are used as described in Sec. 8.1. It is important to preserve

No.	Approximation	Possible justification
1	Fixed thermal conditions at melt boundaries	No significant influence of the local phenomena on the assumed local boundary conditions
2	Constant/interpolated Lorentz force distribution for a varying melt height	No significant differences between a deformed/interpolated and recalculated Lorentz force distribution
3	Analysis of time-average flow patterns for several discrete melt heights	No significant hysteresis and transition effects in the flow
4	Quasi steady-state of crystallization interface with a pinned interface position for the analysis of melt flow influence on interface shape	Reaction time of interface (development of deflection) is smaller than the total growth time. Oscillations of the interface shape are small.
5	Fixed (prescribed) crystallization interface shape and velocity for the analysis of melt flow influence on species concentration	Reaction time of interface is smaller than the time interval considered in species calculation or the transitional effects are insignificant for species concentration
6	2D calculations of melt flow influence on crystallization interface and species concentration	Relevant results are similar in 2D and 3D, i.e., the 3D results show an axial symmetry

Table 8.1.: Approximations for coupled local calculations of melt flow, crystallization interface, and species transport.

heat flux boundary conditions on the sides to enable a free movement of the triple-point line. Coupled unsteady calculations with `OpenFOAM` were carried out for cases with TMF up and down; for time intervals of 10000 s and 1000 s, using an inductor current of 300 A and 450 A, respectively. Additionally, the case without a TMF (without any melt flow) was calculated for 10000 s. The movement of each point of the crystallization interface is calculated in each time step according to the balance of heat fluxes (2.71) on both sides of the interface. The calculations are started from a flat interface shape, zero velocity field, and a steady-state temperature field determined by the boundary conditions. It is important to notice that due to the assumed temperature boundary conditions and a stable stratification, there is no melt flow without a TMF. Buoyancy forces start influencing the melt flow once the TMF-induced flow has deformed temperature isolines.

If heat radiation with a constant ambient temperature is used as a boundary condition on the top surface of the melt and the melt height decreases, the equilibrium temperature on the surface remains constant and the temperature gradient in the melt increases. During 10000 s of crystallization with estimated 1.3 cm/h, the melt height would decrease by 3.6 cm – to 7.4 cm from the initial value of 11 cm. Consequently, the temperature gradient would increase from 1 K/cm to 1.5 K/cm. According to global temperature calculations in Chapter 6 (Fig. 6.7 (a)), the tendency in a growth process is rather the opposite – the temperature gradient decreases at small melt heights. Such changes could be easily implemented in the present model by using a time-dependent ambient temperature. In present calculations, it is assumed that the ambient temperature remains constant. This assumption may still be compatible with **Approximation 1** in Tab. 8.1 because radiation boundary conditions generally allow changes of the surface temperature and of the corresponding heat flux, caused by the melt mixing. This would not be the case, e.g., with a fixed surface temperature.

If the melt height decreases from 11 cm to 7.4 cm, it follows from the previous Lorentz force analysis summarized in Fig. 7.9 (f) that the Lorentz force density may decrease by 20% and the force angle may increase by 20%. Because these differences are relatively small and both changes have an opposite influence on the flow velocity, it is assumed that a constant Lorentz force density distribution can be used by deforming it together with the mesh, according to **Approximation 2**. Of course, for larger melt height changes, this assumption might lead to incorrect results. For small height-to-width ratios near 0.25 in particular, where transitions in the flow structure are possible, small changes in the Lorentz force distribution might have a significant role.

8.5.1. Analysis of crystallization interface

The velocity and temperature fields as well as the shape of the crystallization interface after 10000 s for the cases with an inductor current of 300 A are shown in Fig. 8.13. Temperature and velocity fields are not averaged over time because the melt height changes considerably and stable average values probably do not exist. This makes an exact comparison with the previous results at a fixed melt height of 11 cm in Fig. 8.6 (a,d) impossible. Qualitatively, typical velocities, flow structure, and deformation of the temperature field seem to be preserved. It can be concluded that no indications have been found that **Approximation 3** is invalid for slow changes of melt height.

The crystallization interface has moved in 10000 s upward by approximately 3 cm in both cases shown in Fig. 8.13. However, the final shape of the crystallization interface is different with TMF up and down (for an inductor current of 300 A). The TMF up significantly decreases the temperature gradient at the rim and increases the temperature gradient in the central part. Consequently, the crystallization rate increases at the rim and decreases in the center, leading to a concave interface shape. The maximum deflection after 10000 s reaches 8 mm. In the case of TMF down with 300 A in Fig. 8.13, the deformation of the temperature field by the melt flow is stronger at the top surface than at the crystallization interface. Consequently, the deformation of the interface shape is smaller, reaching a maximum deflection of only 3 mm. However, the shape becomes very asymmetric, with the largest deflection concentrated at the side of inductor's current supplies. The almost symmetric interface in case of TMF up could be explained by the TMF-induced toroidal flow structure directly at the melt bottom; see the time-averaged flows in Fig. 8.6 (a,d). With TMF down, the vortices are more distinct at the melt top, and the secondary flow structure at the bottom is more complex, i.e., less regular and with a point of converging flow at the center. Note that the asymmetry in the Lorentz force distribution caused by the current supplies is of similar magnitude for both the TMF up and TMF down. Obviously, the difference in the resulting interface shape is caused by a strong bi-directional coupling between the interface shape and the flow.

With an inductor current of 450 A, it was possible to calculate only 1000 s because the time step significantly decreased and calculation time increased due to higher melt flow velocities. Therefore, only the tendencies of the interface shape can be analyzed in these calculations. A comparison of interface shapes with TMF up and TMF down in Fig. 8.14 shows the same trends as with 300 A – a concave shape with TMF up and a convex but very asymmetric shape with TMF down. The maximum deflection in the case of TMF down reaches 4 mm

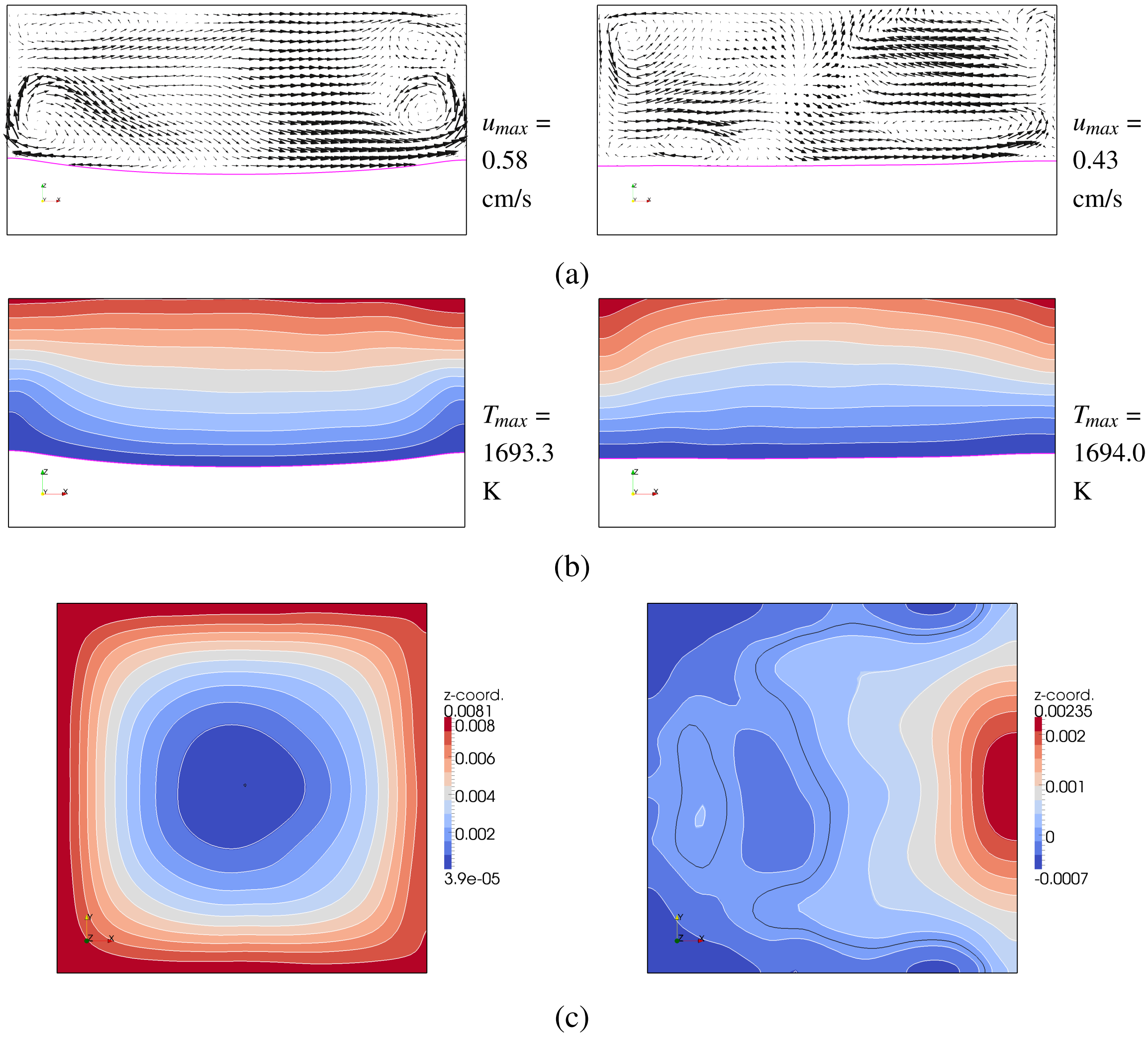

Figure 8.13.: Coupled 3D calculations of melt flow and crystallization interface with $L = 22$ cm, $H = 11$ cm (initial), $I_0 = 300$ A, $\phi = 60°$. Instantaneous velocity (a) and temperature (b) fields in a vertical cut and the vertical interface position relative to the center (c) after 10000 s. Cases with TMF up (left) and TMF down (right) are shown.

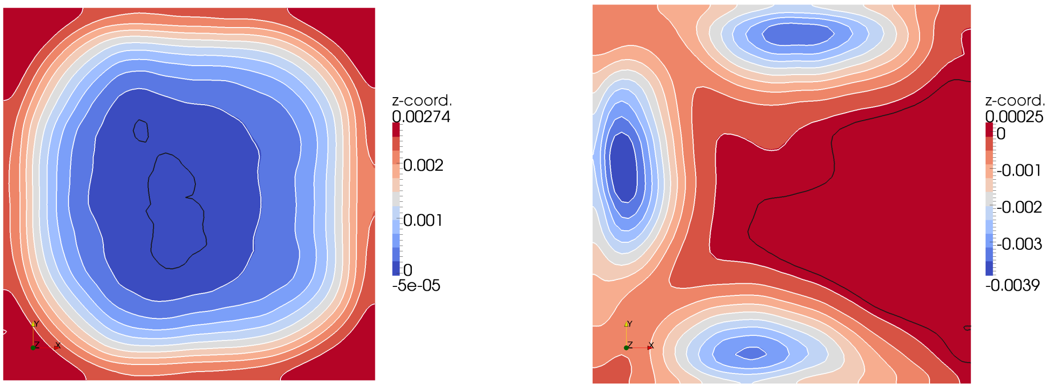

Figure 8.14.: Coupled 3D calculations of melt flow and crystallization interface with $L = 22$ cm, $H = 11$ cm (initial), $I_0 = 450$ A, $\phi = 60°$. Vertical interface position relative to the center after 1000 s. Cases with TMF up (left) and TMF down (right) are shown.

already after 1000 s, indicating a significant increase in comparison to an inductor current of 300 A.

To determine whether the interface shape has reached a quasi steady-state, it is necessary to analyze its evolution over time. Fig. 8.15 (a,b) shows the time-dependencies of the vertical interface position at the melt center and of the maximum interface deflection. A continuous upward movement with a relatively constant growth velocity is observed. The central point moves by 29 mm in the case of TMF up and by 34 mm in the cases without a TMF and with TMF down during 10000 s of crystallization. These distances correspond to an average growth rate of 1.04 cm/h and 1.22 cm/h, respectively. Both values agree well with the previous estimation of 1.3 cm/h. The interface shape in a vertical cut is shown for several time instants in Fig. 8.15 (c) for TMF up and in Fig. 8.15 (d) for TMF down. It can be seen that in both cases the interface deflection converges toward a saturation, i.e., a final quasi steady-state. However, with both TMF up and down, the saturation is still not fully reached after 10000 s. While the characteristic flow-induced shape changes can be observed also after 2000 s, their magnitude continues to grow longer than 10000 s. Because the crystallization process is significantly longer than 10000 s, a quasi steady-state may still be reached. However, it would be more efficient to accelerate the convergence of the interface shape using steady-state calculations according to **Approximation 4**. Such calculations will be described later in this chapter.

Further details of the crystallization dynamics are summarized in Fig. 8.16 showing the time-dependencies of the instantaneous crystallization velocity and heat fluxes at the interface center. The long-period changes of these parameters are the key to the new quasi steady-state of the interface. The development of the concave interface deflection in the case with TMF up in comparison to the case without a TMF can be summarized as follows:

1. The downward flow in the melt center generated by the upward TMF increases the temperature gradient at the interface (Fig. 8.16 (b) – ‘No TMF’ vs. ‘TMF up, 300 A’).

2. Growth velocity in the center is reduced in comparison to the case without a TMF, and the interface starts to bend forming a concave shape because its center moves slower (Fig. 8.15 (c); 8.16 (a)–‘No TMF’ vs. ‘TMF up, 300 A’).

3. The deflected interface causes an increase of the temperature gradient in the crystal in the central part (Fig. 8.16 (b)–‘No TMF, solid’ vs. ‘TMF up, 300 A, solid’).

4. Growth velocity starts increasing again, and the entire interface continues moving upward with the new quasi steady-state shape (Fig. 8.15 (c); 8.16 (a)–‘TMF up, 300 A’).

The fact that the heat flux in the melt remains approximately constant in Fig. 8.16 (b) (‘TMF up, 300 A’) would allow one to estimate the influence of the melt flow on the interface deflection using constant time-average heat fluxes in the melt, without calculating melt flow for time intervals of 10000 s.

While the global motion of the crystallization interface in Fig. 8.15 (a) looks very smooth, Fig. 8.16 reveals that the crystallization velocity exhibits oscillations with an amplitude of about 0.1 cm/h already for an inductor current of 300 A. They correlate well with the oscillations of the heat flux density in the melt reaching an amplitude of about 0.1 W/cm^2 (see Fig. 8.16 (b)). The influence of inductor current on crystallization velocity oscillations is summarized in Fig. 8.17 (a) for a time interval from 0 to 1000 s. It can be seen that in case of an inductor current of 450 A the amplitude of oscillations is up to a factor of 5 higher than

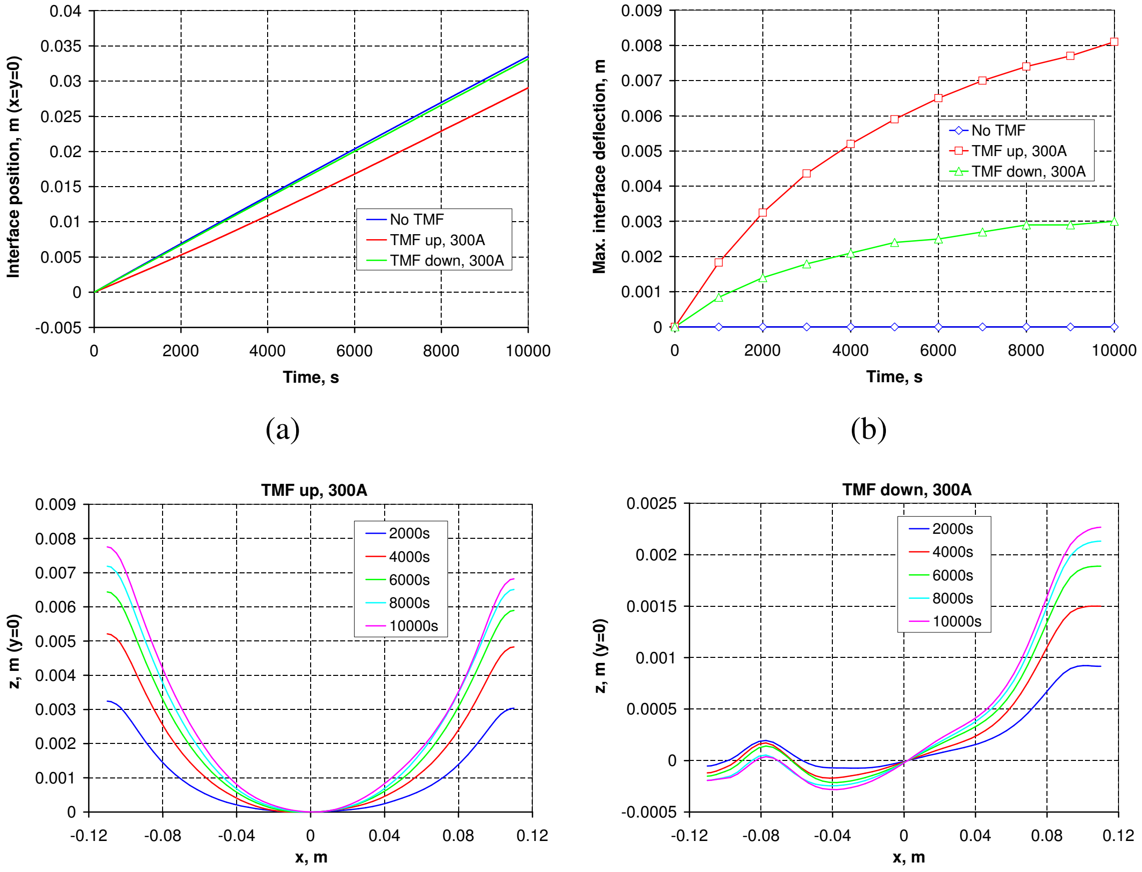

(a) (b)

(c) (d)

Figure 8.15.: Coupled 3D calculations of melt flow and crystallization interface with L = 22 cm, H = 11 cm (initial), I_0 = 300 A, ϕ = 60°: time-dependence of crystallization interface position (a) and maximum deflection (b); shape of crystallization interface on the x axis for various time instants for TMF up (c) and TMF down (d) with the central point shifted to $z = 0$.

for 300 A in the case of TMF up. Also for the case with TMF down, the amplitude of crystallization velocity oscillations increases at higher inductor currents. The resulting oscillations of the interface position can be visualized graphically if the average motion is subtracted. This was done for all cases for a time interval 500...1000 s. The resulting time-dependencies in Fig. 8.17 (b) show a typical amplitude of 10 µm for interface position, with somewhat higher values only for the case with 450 A and TMF up.

The relation between the oscillation amplitudes of temperature in the melt, crystallization velocity, and interface position can be also estimated theoretically. If we consider sinusoidal oscillations of the temperature in the melt $T(t) = T_{avr} + \Delta T_{osc} \sin \omega_T t$ at a point with the distance l_0 to the crystallization interface, the heat flux density can be estimated as:

$$Q_L(t) \approx \lambda_L \frac{T(t) - T_0}{l_0} = \underbrace{\lambda_L \frac{T_{avr} - T_0}{l_0}}_{Q_{Lavr}} + \underbrace{\lambda_L \frac{\Delta T_{osc}}{l_0}}_{Q_{Losc}} \sin \omega_T t. \tag{8.5}$$

The crystallization velocity follows directly from the heat balance (2.71) including also the

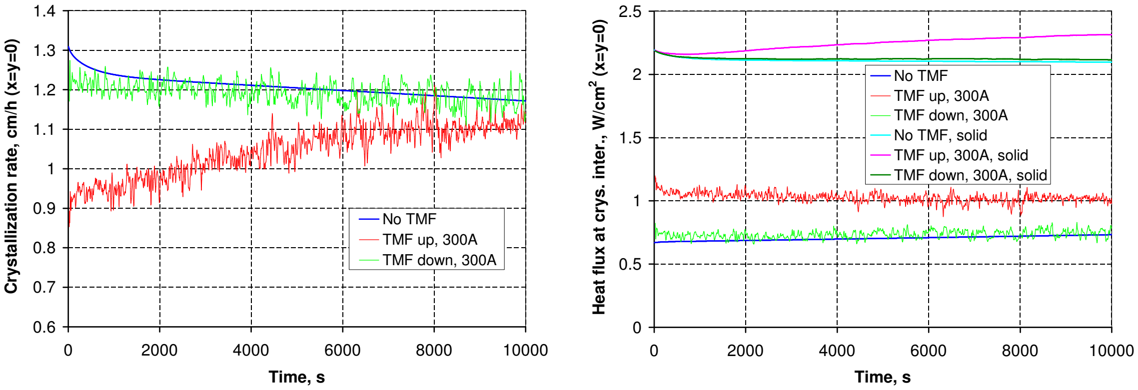

(a) (b)

Figure 8.16.: Coupled 3D calculations of melt flow and crystallization interface with L = 22 cm, H = 11 cm (initial), I_0 = 300 A, ϕ = 60°: time-dependence of crystallization velocity (a) and heat fluxes on both sides of the interface (b) at the point in the center.

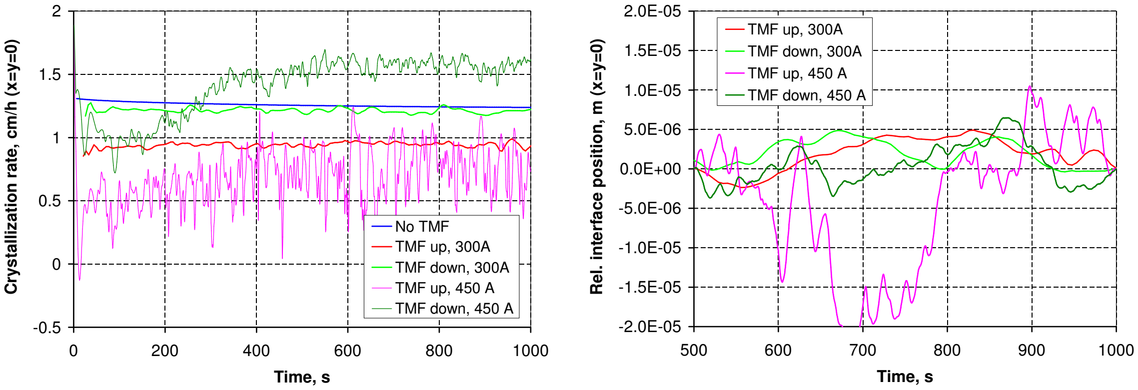

(a) (b)

Figure 8.17.: Coupled 3D calculations of melt flow and crystallization interface with L = 22 cm, H = 11 cm (initial), ϕ = 60°: time-dependence of crystallization velocity (a) and relative interface position (b) at the point in the center. Cases with various inductor currents and TMF directions are considered.

heat flux in the crystal Q_S:

$$v(t) = \frac{1}{\rho_S Q_l}(Q_S - Q_{Lavr} - Q_{Losc} \sin \omega_T t). \tag{8.6}$$

The calculation of the crystallization interface position $Z(t)$ requires integration:

$$Z(t) = \int_0^t v(t)dt = \underbrace{\frac{1}{\rho_S Q_l}(Q_S - Q_{Lavr})t}_{Z_{avr}} + \underbrace{\frac{1}{\rho_S Q_l}\frac{Q_{Losc}}{\omega_T}}_{Z_{osc}} \cos \omega_T t|_0^t. \tag{8.7}$$

Consequently, the interface position oscillates with the amplitude

$$Z_{osc} = \frac{1}{\rho_S Q_l}\frac{Q_{Losc}}{\omega_T} = \frac{\lambda_L}{2\pi\rho_S Q_l}\frac{\Delta t_{osc}\Delta T_{osc}}{l_0}, \tag{8.8}$$

where the frequency ω_T was replaced by the oscillation period Δt_{osc}. For the case with an inductor current of 300 A and TMF up, we can evaluate at the interface center from the flow calculation: Δt_{osc} = 30...200 s, ΔT_{osc} = 0.05...0.1 K (l_0 = 1 cm) and obtain Z_{osc} = 0.4...5 µm, which qualitatively agrees with the results of calculations in Fig. 8.17 (b). We observe both small short-period and larger long-period oscillations.

8.5.2. Analysis of species transport

An unsteady calculation of the crystallization interface also enables the calculation of species transport including species segregation at the interface, which depends on the crystallization velocity. For the cases with TMF up and down with 300 A, the concentrations of carbon and oxygen were considered in coupled calculations for 10000 s of solidification. These two types of impurities are both relevant for directional solidification of silicon and also possess different behaviors during the growth process. Carbon has a small segregation coefficient k_0 = 0.07 and thus a strong segregation effect, which is much less distinct and even in the opposite direction for oxygen with k_0 = 1.25. Note that segregation coefficients in the range k_0 = 0.25...1.4 are reported in the literature for oxygen. The values of the segregation coefficients of oxygen k_0 = 1.25 and carbon k_0 = 0.07 from [Reimann, 2010] were adopted in this work. While carbon can be assumed to remain in the silicon melt as in a closed system, oxygen has a very distinct tendency of evaporation at the melt free surface; see, e.g., [Reimann, 2010]. Consequently, the consideration of carbon and oxygen allows one to investigate the two main aspects of the melt flow influence: mixing of a distinct segregation boundary layer and mixing of the entire melt volume, enhancing the transport between the crystallization interface and the melt free surface.

The segregation condition is set as a boundary condition on the crystallization interface for both carbon and oxygen; the actual instantaneous local velocity of the crystallization interface is used. All other boundaries are considered as closed, without any mass exchange, except for oxygen at the free melt surface. There, the evaporation process is approximated using a Poincare-type boundary condition:

$$D\frac{dC}{dn} = p_C(C - C_{ref}), \tag{8.9}$$

where the normal vector points out of the melt. The coefficient $p_C = -150 \cdot D$ m/s and the reference value in the gas phase C_{ref} = 0 were taken as typical values from the work by Reimann [2010]. Note that the evaporation rate at the free surface can be also considered as an “effective” rate describing both oxygen sources and oxygen sinks at the melt boundaries. Material properties such as diffusion coefficients are given in Appendix B. Calculations are started from a uniform field $C = 1$ in the entire melt volume. Consequently, the concentration values are always given in arbitrary units. Because the equations are linear, any units can be assigned to the obtained concentration values, e.g., atoms/cm^3.

The time-dependencies of the maximum concentration in the melt and of the concentration at the center of the crystallization interface are shown in Fig. 8.18 for both carbon and oxygen. Without any melt flow and a with flat interface, the maximum of the carbon concentration is located on the interface and increases more than by a factor of 5 during 10000 s. For the same case, oxygen concentration on the interface decreases by 20%, but the maximum concentration in the bulk remains higher. Both time-dependencies for the values on the interface agree very well with Smith's analytical solution for the pure diffusive case from Tab. 2.2, using a constant crystallization rate of 1.2 cm/h. In this case, oxygen concentration on the crystallization interface is obviously not influenced by the evaporation at the free surface.

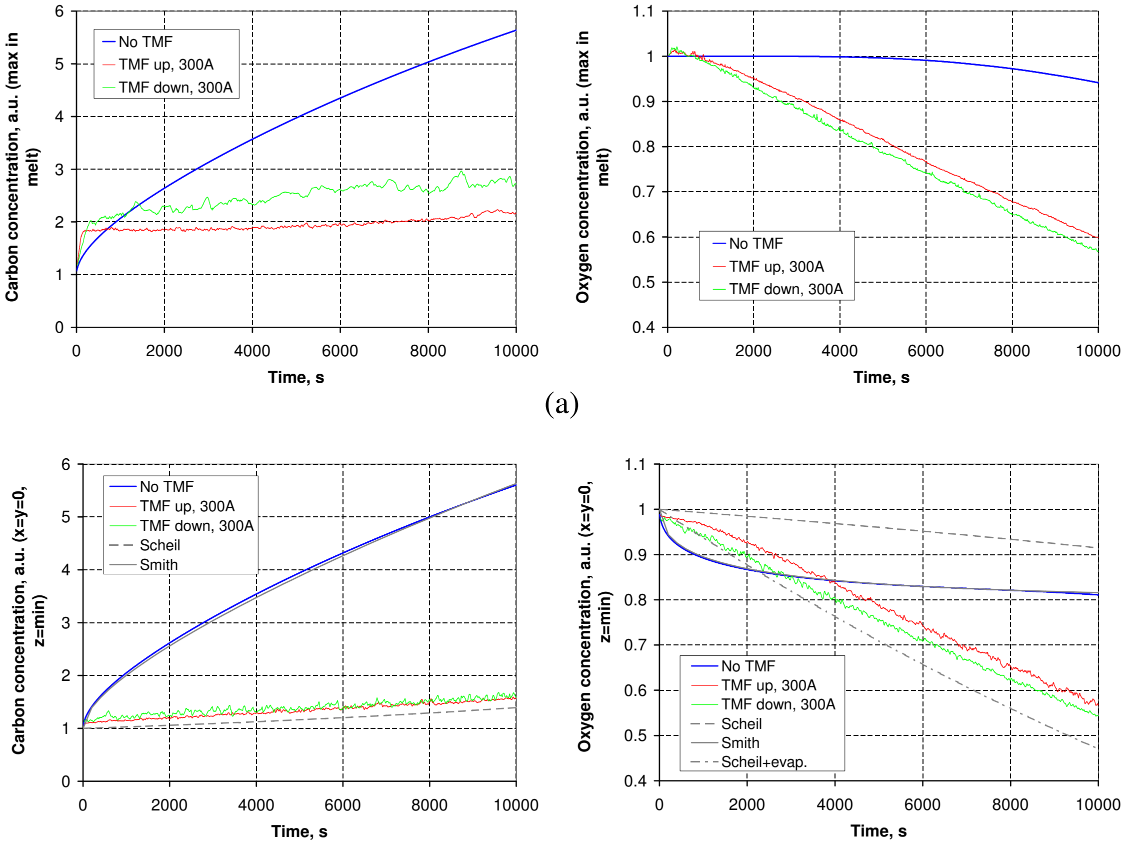

(a)

(b)

Figure 8.18.: Coupled 3D calculations of melt flow and crystallization interface with $L = 22$ cm, $H = 11$ cm (initial), $I_0 = 300$ A, $\phi = 60°$: maximum species concentration in the melt (a) and concentration at the center of crystallization interface (b) in dependence of time for various inductor currents and TMF directions. Concentrations of carbon (left) and oxygen (right) are considered.

The addition of a TMF has a similar effect for both TMF directions for the carbon concentration on the crystallization interface; see Fig. 8.18. The temporal evolution of carbon concentration at the interface is very close to the analytical Scheil's solution from Tab. 2.2 for a complete species mixing. However, note that this is true only for the chosen monitor point at the interface center. The maximum carbon concentration shows up to 1.5 times higher values with TMF down. For oxygen, Scheil's solution gives a decreasing concentration due to $k_0 > 1$, but it does not match the calculation result. If an evaporation term is added to Scheil's solution as derived in Sec. C.2, the calculated oxygen concentration at the monitor point is close to the analytical solution. The behavior of the maximum oxygen concentration is identical. Obviously, the level of oxygen concentration in the melt is practically determined by the evaporation at the free surface. It should be noted that in the first 2000 s,

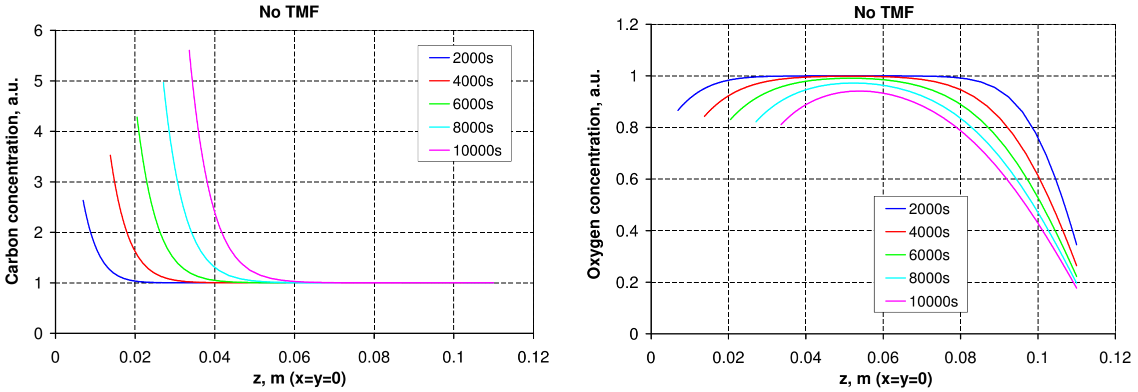

(a) No TMF

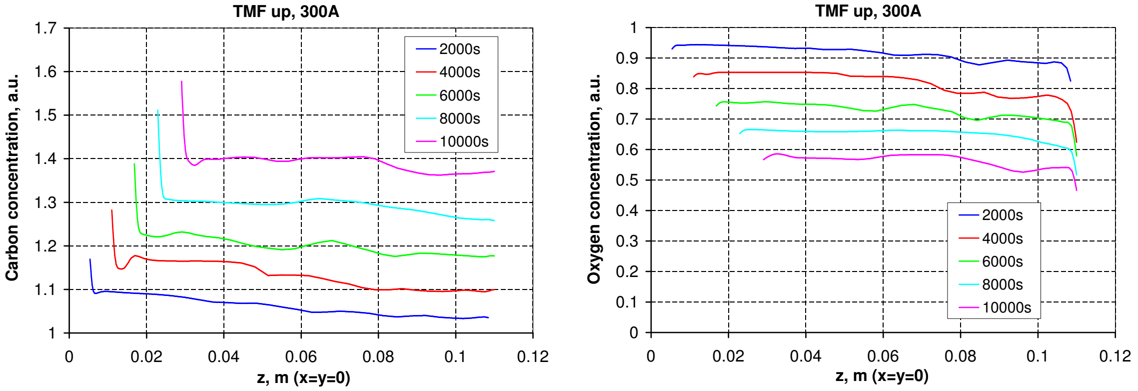

(b) TMF up

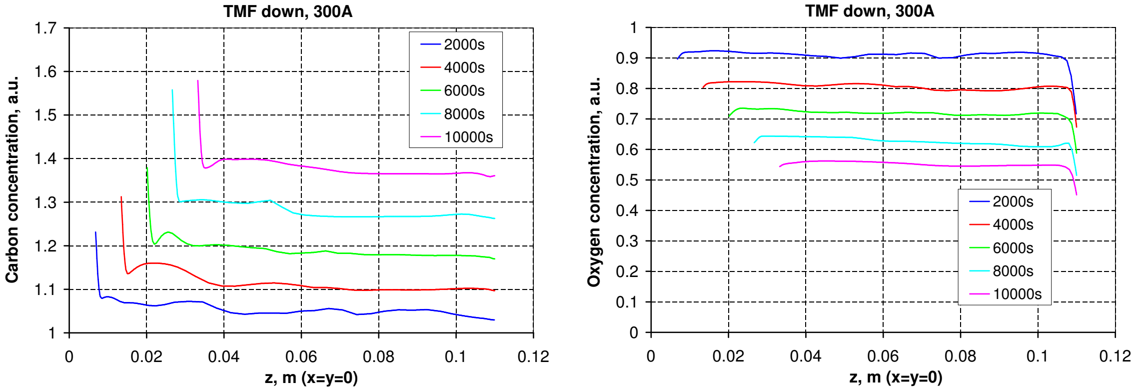

(c) TMF down

Figure 8.19.: Coupled 3D calculations of melt flow and crystallization interface with L = 22 cm, H = 11 cm (initial), I_0 = 300 A, ϕ = 60°: distribution of carbon (left) and oxygen (right) concentration on a vertical line for various time instants without TMF (a), with TMF up (b) and TMF down (c).

oxygen concentration still decreases faster in the case without a melt flow. Therefore, short time intervals in the calculations are not suitable for an analysis of stirring and evaporation of oxygen.

Concentration profiles on a vertical line in the melt center are summarized for all cases in Fig. 8.19. In the case without any melt flow, it can be observed that a segregation boundary layer builds up, with a higher concentration for carbon and a lower concentration for oxygen. The thickness of this diffusion boundary layer in a steady-state is independent of the segregation coefficient and is determined only by the ratio of diffusion coefficient and crystallization velocity D/v_g. A similar diffusion process determines the evaporation of oxygen from the top part of the melt. Note that the resulting boundary layer at the free surface is still far from the crystallization interface after 10000 s. The concentration profiles in Fig. 8.19 become very different with an additional TMF, whereby the differences between both TMF directions are rather small. Carbon concentration becomes almost uniform over the entire melt height, with a steep increase by approximately 15% in a thin boundary layer of a few millimeters at the crystallization interface. Oxygen behaves identically, but the boundary layer is more distinct at the free melt surface.

In practice, the impurity concentration on the crystallization interface is the most essential because it determines the final concentration built into the crystal. Fig. 8.20 shows the distribution of species in a vertical cut and directly on the crystallization interface after 10000 s for an inductor current of 300 A and both TMF directions. Carbon concentration is characterized by a low level in the bulk and high values at the rim of the interface. The high-concentration region clearly extends more into the central part with TMF down than with TMF up. This effect qualitatively agrees with the velocity distributions in Fig. 8.6 (a,d) where in both cases the velocity is mainly directed to the rim, but the distribution is more uniform for TMF up. It must be emphasized that the velocity distribution changes significantly with TMF down for higher Lorentz force densities, where the buoyancy becomes negligible. The distribution of oxygen shows a reversed picture: the concentration is high in the bulk and low at the free surface; at the interface, regions with high and low oxygen concentrations correspond to regions with low and high carbon concentrations, respectively. However, while the concentration differences for carbon reach 26%, oxygen varies on the interface by less than 4%.

The correlation of the species distribution with the velocity distribution at the interface gives an indication that the characteristic regions of high and low concentrations could be also investigated using **Approximation 5** with a fixed shape and velocity of the crystallization interface for relatively short time intervals. Such calculations will be carried out later in this chapter. However, to investigate mass exchange phenomena such as evaporation, the considered time interval should not be smaller than a few thousands of seconds to exclude transitional effects in species distribution. Reliable results could be obtained also from analytical models, such as an extended Scheil's model, because species concentration seems to be close to the limit of complete mixing, also with relatively small melt flow velocities (below 1 cm/s). Then, boundary condition parameters such as the evaporation rate dominate the concentration in the melt.

While the time-average velocity distributions in Fig. 8.6 (a,d) can be approximately considered axi-symmetric, their oscillations have a distinct three-dimensional character; see, e.g., Fig. 8.13. Moreover, seemingly small asymmetries and 3D features of the time-average flow may have a large influence on the shape of the crystallization interface. Therefore, 2D calculations according to **Approximation 6** can be expected to give only qualitatively correct results and only for axi-symmetric flow regimes. 2D calculation would probably allow one to estimate basic effects such as the typical melt flow influence on the interface deflection or on the radial species distribution. But 2D calculations would not show the influence of flow asymmetry, the processes in melt corners, quantitatively precise field values that are determined by 3D mixing of temperature and species in the unsteady flow regime in particular.

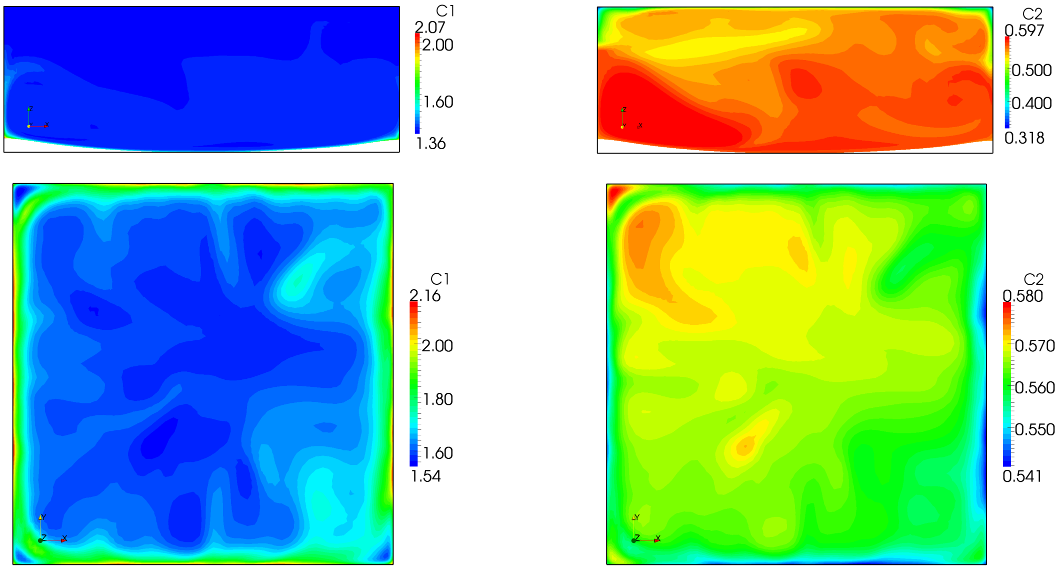

(a) TMF up

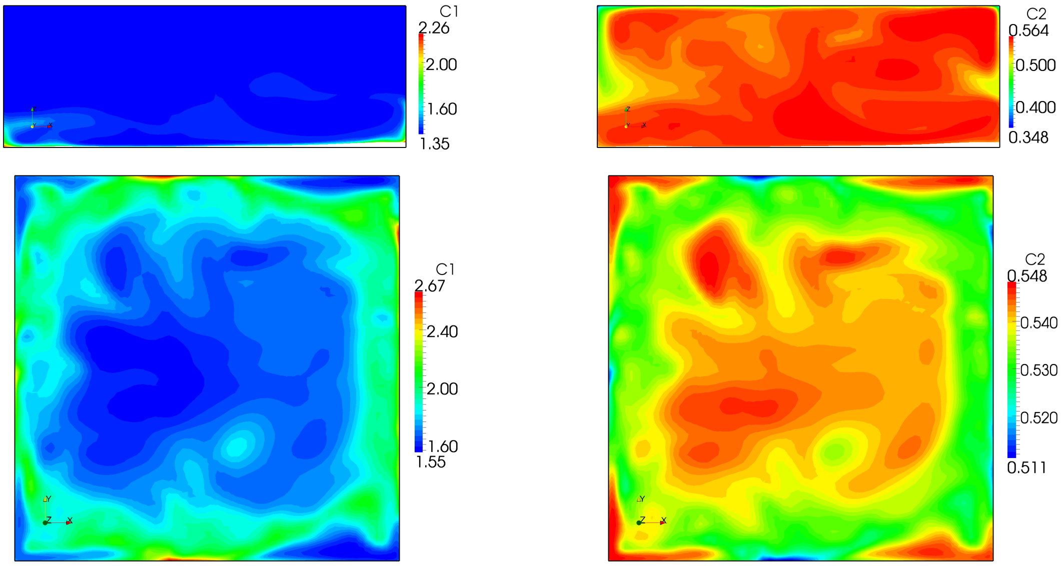

(b) TMF down

Figure 8.20.: Coupled 3D calculations of melt flow and crystallization interface with L = 22 cm, H = 11 cm (initial), I_0 = 300 A, ϕ = 60°: distribution of carbon (left) and oxygen (right) concentration (in a.u.) in a vertical cut through the melt center and on the crystallization interface after 10000 s for TMF up (a) and TMF down (b).

8.5.3. Possibility of constitutional supercooling

An unsteady melt flow can lead to intense oscillations of temperature gradients at the crystallization interface and of the crystallization velocity as shown in Figs. 8.16, 8.17. On the other hand, Fig. 8.18 reveals distinct flow-induced oscillations of the species concentration at the crystallization interface. All these oscillations may have an impact on the morphology of the crystallization interface due to the carbon-related supercooling effect as discussed in Sec. 2.3.2.2.

To evaluate the possibility of constitutional supercooling, temperature and concentration gradients in the melt directly at the crystallization interface must be determined according to the criterion (2.67). This was done for the cases with various TMF directions and inductor currents, considering a monitor point in the interface center for a time interval 100…1000 s. The temperature gradient was calculated from the local heat flux in the control volume at the crystallization interface. The concentration gradient was evaluated from the local concentration on the interface and the local crystallization velocity using the segregation boundary condition (2.62). Note that concentration calculations were carried out using arbitrary units, i.e., in a normalized form C'. The evaluation of the true concentration C requires a definition of a reference concentration: $C = C'C_r$. The stability criterion (for absence of constitutional supercooling) (2.67) can then be rewritten as

$$\frac{dC}{dn}\frac{dT_L}{dC} \le \frac{dT}{dn} \quad \Rightarrow \quad C_r\frac{dT_L}{dC}\cdot\frac{dC'}{dn} \le \frac{dT}{dn}. \tag{8.10}$$

It can be assumed that carbon concentration in the melt reaches the solubility limit of $5\cdot10^{18}$ cm^{-3} [Reimann, 2010], i.e., $C_r = 5\cdot10^{18}$ cm^{-3}. This would also maximize the probability of constitutional supercooling. The slope of the liquidus line dT_L/dC can be estimated from the Si-C phase diagram as $7\cdot10^{-21}$ cm^{3}K [Reimann, 2010].

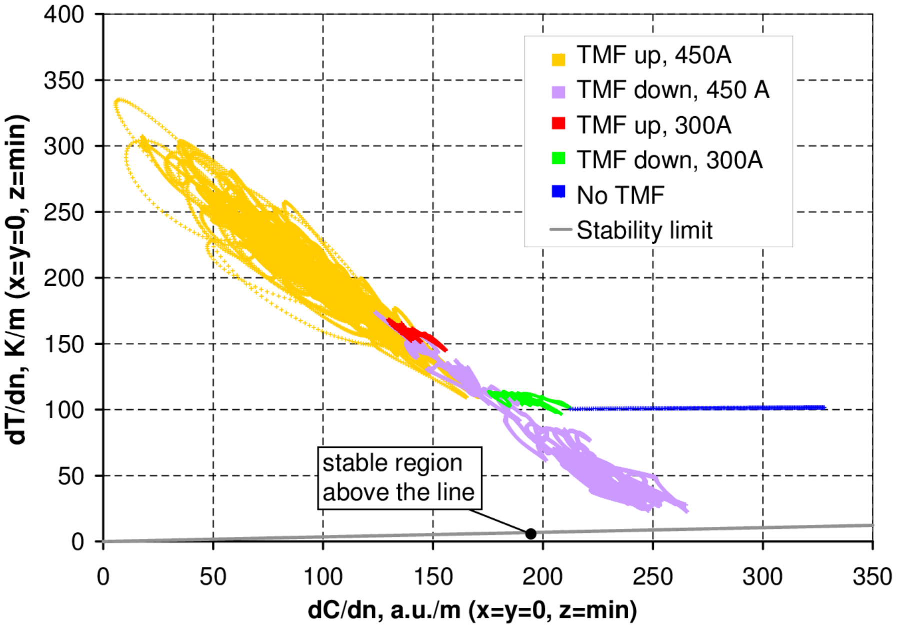

Figure 8.21.: Coupled 3D calculations of melt flow and crystallization interface with L = 22 cm, H = 11 cm (initial), ϕ = 60°: evaluation of interface stability with respect to constitutional supercooling for various inductor currents. Temperature and concentration gradients for a time interval 100…1000 s at a monitor point in the interface center are considered. For the stability limit, a slope of the liquidus line of $7\cdot10^{-21}$ cm^{3}K and an initial carbon concentration at the solubility limit of $5\cdot10^{18}$ cm^{-3} is assumed.

The results of the analysis are summarized in Fig. 8.21. It can be seen that the stability criterion is fulfilled in all cases and constitutional supercooling would not occur. In the case without a TMF, the stability is guaranteed by the relatively high temperature gradient of 1 K/cm in the melt. The cases with a TMF show a tremendous increase of the variation of temperature and concentration gradients at higher inductor currents. For the case with TMF down, the range of oscillations comes very close to the stability limit. Consequently, the possibility of constitutional supercooling for limited time intervals or regions of the crystallization interface cannot be completely excluded also in well-mixed melts.

8.6. Melt flow influence on steady-state crystallization interface

In this section, steady-state calculations of crystallization interface are performed. Before that, it must be discussed what is the physical meaning of a steady-state in directional solidification. In several other growth processes from the melt, a steady-state position and shape of the crystallization interface is natural. In Czochralski and float-zone techniques, the growing crystal is continuously pulled away from the melt so that the crystallization interface stays approximately at a constant position with respect to the melt. In VGF technique or directional solidification, the crystallization interface moves continuously from the melt bottom to the top and the melt height changes from the initial value to zero (melt height decreases also in Czochralski growth, but it is possible to hold the melt free surface at a constant level by adjusting the vertical crucible position). Therefore, the term *steady-state interface position* is meaningless for directional solidification.

A less strict term is *steady-state interface shape*, which indeed allows for a physical interpretation. From the viewpoint of the interface, if the temperature gradients on both sides of the interface remain constant over a part of the growth process, the interface moves with a constant velocity and can preserve its shape. The gradient in the crystal is determined by the cooling and is not fully independent of the crystal height, i.e., the temperature at the crystal bottom. The gradient in the melt is determined by the heating and is influenced by the melt motion – it is also not fully independent of the melt height. Therefore, a quasi steady-state of the crystallization interface is only an approximation. It is more likely to work for longer crystallization times, for larger heights of melts and crystals.

To calculate the steady-state shape of the crystallization interface during directional solidification, the following method has been used in the literature; e.g., [Vizman et al., 2007] and [Frank-Rotsch et al., 2008] using the codes `STHAMAS3D` and `CrysMAS`, respectively. The triple-point line between the solid silicon, liquid silicon, and crucible is fixed at a given position on the crucible wall. Additional heat sources are defined on the crystallization interface according to a prescribed crystallization velocity. It must be emphasized that the crystallization velocity is required as input data and cannot be calculated as a result (but it can be determined by fitting, e.g., the interface shape to experimental results). The shape of the interface is iteratively fitted to the melting point isosurface during a coupled calculation of the temperature field.

The model with a fixed triple-point line may limit some 3D effects of the melt flow influence on the crystallization interface as pointed out by Miyazawa et al. [2008a]. Several alternative approaches have been developed [Liu et al., 2007; Miyazawa et al., 2008a,b; Kuliev et al., 2007]. Although the algorithms have not been described in detail in the literature, the ideas include: fixing the central point of the crystallization interface; imposing a steady-state position with thermal boundary conditions. A new steady-state model with a free triple-point line has been implemented also in `OpenFOAM`. The global steady-state crystallization velocity is adjusted to keep a specified interface point fixed as described in Sec. 3.3.2.1. In this way, both the correct steady-state crystallization velocity and the interface shape are obtained as

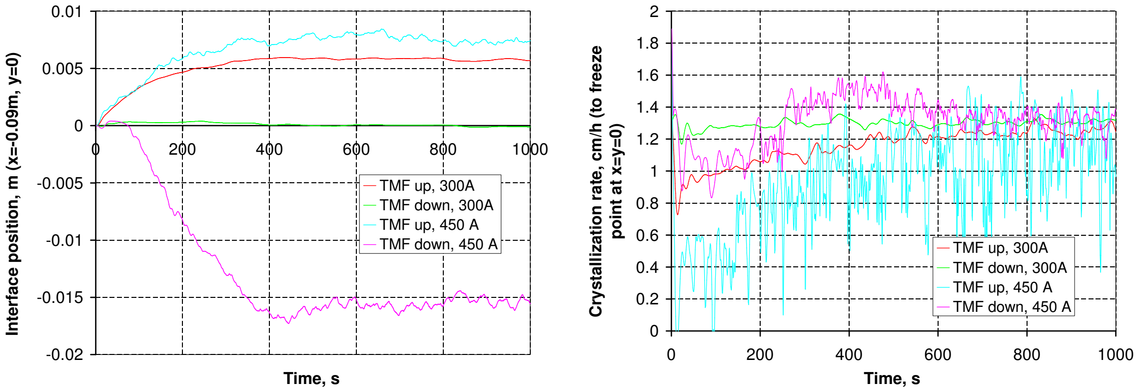

(a) (b)

Figure 8.22.: Coupled 3D calculations of melt flow and steady-state crystallization interface with $L = 22$ cm, $H = 11$ cm (initial), $\phi = 60°$: time-dependence of the interface position at a point near the melt side (a) and of the fitted crystallization velocity in the center (b). Cases with various inductor currents and TMF directions are considered.

a result. Both results are determined only by thermal boundary conditions.

The steady-state interface shape with the new algorithm was calculated for the cases considered in Sec. 8.5 in unsteady calculations. The time-dependencies of the interface position near the melt side are summarized in Fig. 8.22 (a). The monitor point in the center cannot be used because it serves the adjustment of the crystallization velocity and stays at its initial position. It can be seen that the interface reaches a quasi steady-state after about 500 s. Such calculation times are possible only due to the artificial acceleration of the interface movement. This approach significantly reduces the required computing time because the melt flow needs to be calculated only for about 1000 s instead of more than 10000 s. The global crystallization rate required to freeze the point at the center in Fig. 8.22 (b) shows strong oscillations during the convergence to an average value of approximately 1.3 cm/h. It must be noted that both the oscillations of the interface position and the oscillations of the adjusted crystallization rate are not physical – to a large extent they are produced by the iterative and accelerated algorithm of the interface movement.

The final 3D quasi steady-state shapes of the crystallization interface for all cases as well as the time-averaged temperature and velocity fields are given in Fig. 8.23. Because the melt height does not change continuously, time-averaging is meaningful in contrast to the unsteady coupled calculations. The interface shape with an inductor current of 300 A agrees very well with the previous unsteady results after 10000 s. With TMF up, the maximum interface deflection has slightly increased from 8 mm to 9 mm; with TMF down, it has increased from 3 mm to 3.7 mm. These small deviations are reasonable because the unsteady solutions were not fully converged after 10000 s. The velocity distribution and magnitude agrees well with the results with a fixed interface in Fig. 8.6; however, note that the flow near the interface shows a distinct asymmetry. The initially rather small asymmetry in the flow field over a flat interface has been increased due to the interaction of the melt flow and interface shape.

The increase of inductor current from 300 A to 450 A leads to a qualitatively similar interface shape, but the maximum deflection increases several times. It reaches 1.9 cm in case of TMF up and 2 cm in case of TMF down. An increase of more than 6 times with TMF down is related to the TMF torus, which extends over the entire melt height at higher

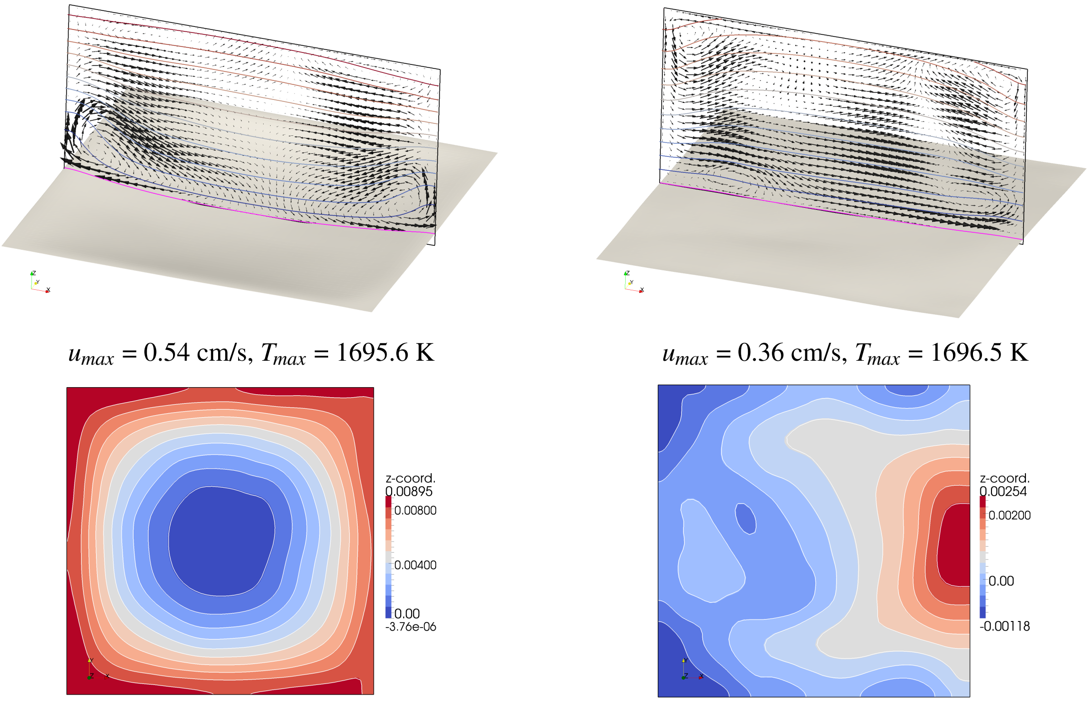
u_{max} = 0.54 cm/s, T_{max} = 1695.6 K

u_{max} = 0.36 cm/s, T_{max} = 1696.5 K

(a) I_0 = 300 A

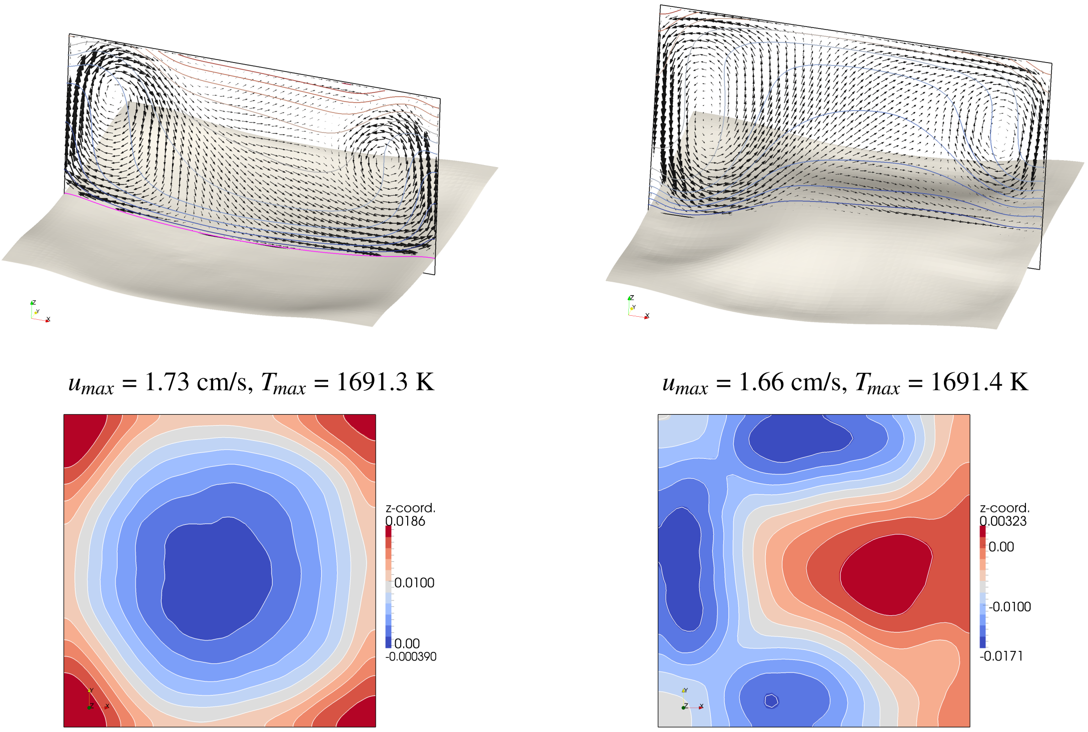
u_{max} = 1.73 cm/s, T_{max} = 1691.3 K

u_{max} = 1.66 cm/s, T_{max} = 1691.4 K

(b) I_0 = 450 A

Figure 8.23.: Coupled 3D calculations of melt flow and steady-state crystallization interface with L = 22 cm, H = 11 cm (initial), ϕ = 60°: time-average (0…1000 s) velocity and temperature fields in a vertical cut, steady-state 3D shape of the crystallization interface, and the vertical interface position relative to the center. Cases with an inductor current of 300 A (a) and 450 A (b) with TMF up (left) and TMF down (right) are considered. The current supplies are on the right side of the figures ($x > 0$).

inductor currents. Such large interface deflections are rather unwanted because they may, e.g., increase thermal stresses in the crystal. A question arises whether a strong mixing of impurities in the melt is not always related to large interface deflections. From basic physical considerations, several other parameters can be identified that could be used to reduce the influence on the interface shape[1]:

- Flow structures with the largest velocities at the top of the melt or with partly horizontal vortices. An example is the case with TMF down and 300 A, where species mixing is similar to TMF up, but interface deflection is more than 2 times smaller (although distinctly asymmetric).
- A decrease of the temperature gradient in the melt proportionally decreases the impact on the crystallization interface. A TMF flow in a nearly isothermal melt would have almost no influence on the interface.
- An increase of the crystallization velocity is related to an increase of temperature gradients in the crystal. Consequently, the changes of temperature gradients in the melt become smaller relatively to the gradients in the crystal. Therefore, changes of the interface shape also become smaller.

8.7. Melt flow influence on species transport

8.7.1. 3D calculations for small time intervals with flat interface shape

Results in Sec. 8.5.2 indicate that already for an inductor current of 300 A in the reference case, convection dominates over diffusion for both oxygen and carbon. The flow velocity determines both the local species distribution at the interface and the vertical mixing in the melt. A further increase of the melt mixing level decreases the concentration faster but is unlikely to lead to qualitatively different results as long as the flow pattern does not change. Therefore, it is important to determine the critical melt flow velocity to reach this regime of species mixing.

The inductor current from the reference case is decreased from 300 A to very small values. In each case, segregation of carbon in a closed system is calculated for 3500 s, starting from a uniform distribution. The phase interface is moved vertically with a constant velocity of 1 cm/h. The interface shape is assumed flat, neglecting possible flow-induced concave deflections of up to 8 mm observed in Sec. 8.5. This allows us to separate the role of interface shape (it is addressed in the following section) and that of flow velocity.

The maximum flow velocity shows a linear dependence of the Lorentz force density in the range above 2 N/m^3 as can be seen in Fig. 8.24 (b). This deviation from the previously derived dependence with a power of 1/2 can be explained with the buoyancy-influenced flow regime. Carbon concentration on the interface decreases rapidly already at small force densities below 2 N/m^3 in Fig. 8.24 (a). A comparison of species distributions in Fig. 8.25 shows practically the same effect, with impurities accumulated at the rim for flow velocities

---

[1] These effects were investigated in detail by 3D numerical calculations in cooperation with Prof. Daniel Vizman from the West University of Timisoara (Romania). References to the corresponding publications are given in Appendix E.

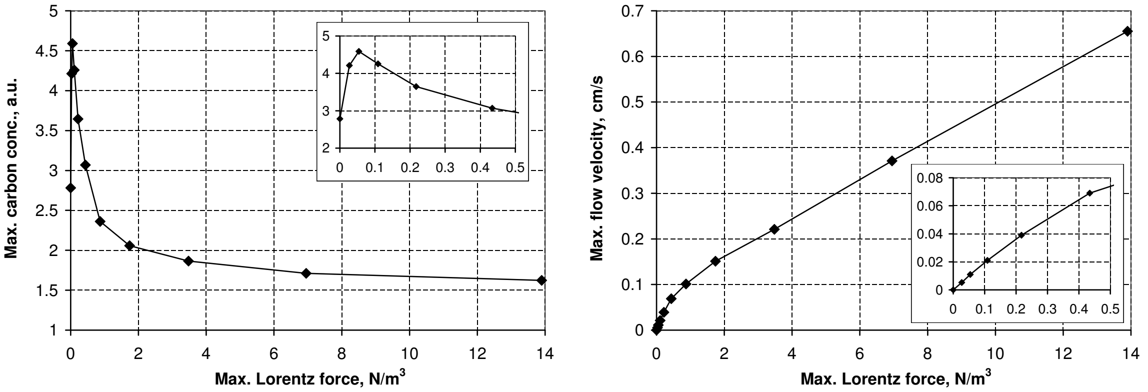

(a) (b)

Figure 8.24.: 3D melt flow calculations with a prescribed crystallization interface motion, $L = 22$ cm, $H = 11$ cm (initial), $\phi = 60°$, TMF up: carbon concentration on the interface (a) and maximum melt velocity (b) in dependence of Lorentz force density (inductor current).

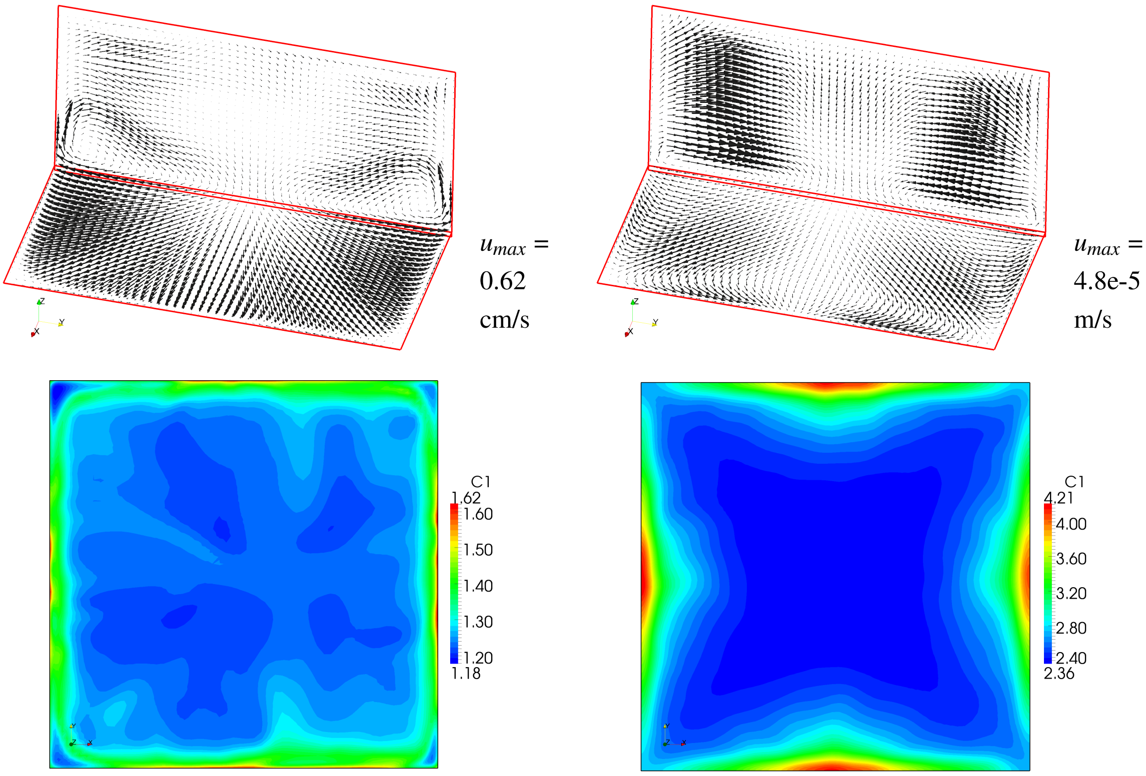

(a) $I_0 = 300$ A (b) $I_0 = 13$ A

Figure 8.25.: 3D melt flow calculations with a prescribed crystallization interface motion, $L = 22$ cm, $H = 11$ cm (initial), $\phi = 60°$, TMF up: time-average (300…3500 s) velocity in a vertical and horizontal cut (3 mm above the interface) and carbon concentration on the interface for inductor currents of 300 A (a) and 13 A (b) – corresponding to Lorentz force densities of 13.9 and 0.03 N/m^3, respectively.

differing more than by a factor of 10^4. A formal estimation of the solutal Peclet number for the smallest flow velocity ($4.8 \cdot 10^{-5}$ m/s)

$$Pe_S = \frac{u_0 L_0}{D} \tag{8.11}$$

gives $Pe_S = 260$ with $D = 2 \cdot 10^{-8}$ m^2/s and $L_0 = 0.11$ m. Consequently, carbon diffusion is formally negligible in comparison to carbon convection already at small melt velocities. However, the maximum impurity concentration at the rim is higher with a very small flow velocity than in the case without any melt flow. This effect is further elucidated in Fig. 8.26 with horizontal and vertical species distributions after 3500 s. Obviously, below force densities of 0.2 N/m^3, impurities are transported along the interface, but the boundary layer in the vertical direction is preserved. Only above this critical force density, the melt is mixed vertically as well.

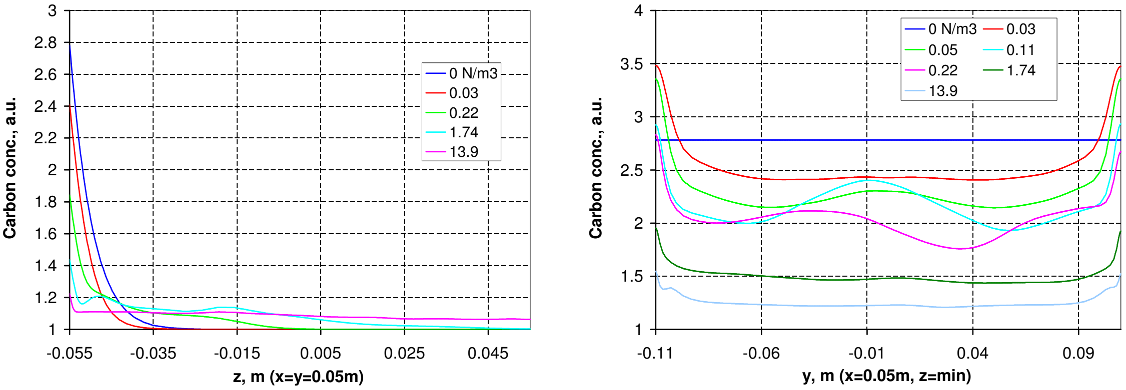

(a) (b)

Figure 8.26.: 3D melt flow calculations with a prescribed crystallization interface motion, L = 22 cm, H = 11 cm (initial), ϕ = 60°, TMF up: carbon concentration on a vertical (a) and horizontal line (b) after 3500 s for different Lorentz force densities (inductor currents).

8.7.2. 3D calculations for small time intervals with deflected interface shape

In Sec. 8.5.2, the influence of an upward or downward TMF on the species distribution on the interface was compared with the case without a TMF. However, in the case without a TMF, there was no flow at all because no lateral temperature gradients were considered. The global temperature calculations in Chapter 6 showed that small lateral temperature gradients in the melt are realistic. Nevertheless, it would be important to analyze the added value of a TMF in comparison to purely buoyant flows generated by lateral temperature gradients.

A lateral temperature gradient leads to a deflected phase interface: cold melt sides cause a concave interface shape, and hot melt sides cause a convex interface shape. In this section, the interface shape is assumed fixed: either flat, or convex/ concave with a deflection of 2 cm. The shape is assumed parabolic. The deflection is set to zero in the corners and is defined elsewhere as

$$d(x,y) = d_x(x) + d_y(y), \tag{8.12}$$

where $d_x(x)$ and $d_y(y)$ are parabolic functions of x and y coordinate, respectively. Both functions are zero on the two corresponding melt sides and equal to the maximum deflection at the melt center. In this case, both maximum values are 1 cm, leading to a total deflection of 2 cm between the melt corner and the center. This algorithm was implemented in both a `Gmsh` script for mesh generation for Lorentz force calculation and in `GridGen3D` for mesh generation for flow calculations; i.e., the influence of interface deflection on the Lorentz force was taken into account. As expected, this influence was relatively small with no significant effects on the force distribution; the maximum value changed by less than 5%.

The value of the lateral temperature gradient dT/dx corresponding to an interface deflection of 2 cm (convex or concave) can be roughly estimated as 0.2 K/cm according to Sec. 6.4.3. This value is set as a flux boundary condition on all side surfaces and generates buoyancy forces in the entire melt volume. With the previously used zero flux condition, buoyancy forces would be present only in the vicinity of the deflected crystallization interface.

In the previous section, it was shown that also a very small flow velocity significantly alters species distribution along the interface. Of course, the velocity distribution resulting from the interaction of buoyancy and TMF forces plays a decisive role. Here, we consider again the segregation of carbon in a closed system, starting from a uniform distribution. Nevertheless, the results would be qualitatively similar for any other segregating species. A vertical movement of the interface with 1 cm/h for 3500 s is calculated as in the previous section.

For the segregation calculation, the crystallization velocity normal to the interface is used, which deviates from the prescribed uniform vertical velocity. On interface parts with a higher deflection, the resulting normal velocity is smaller. Additionally, the curved interface shape causes horizontal concentration gradients. Both these factors cause a non-uniform species distribution on the interface also without any melt flow. Carbon distributions after 3500 s are compared in Fig. 8.27.

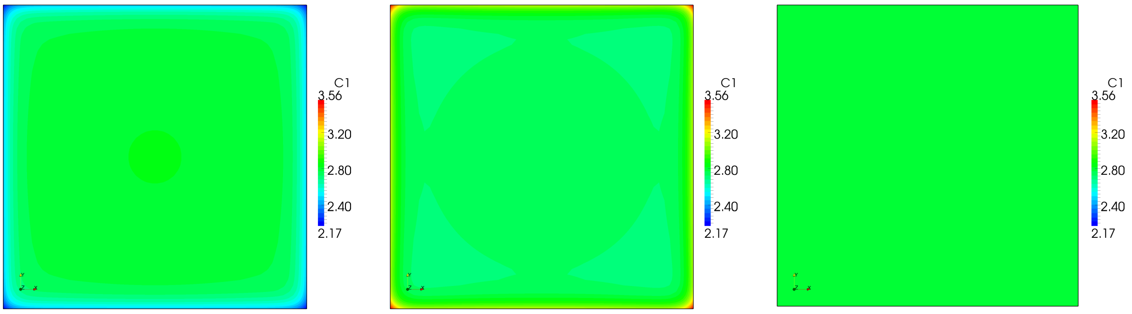

(a) 2 cm concave (b) 2 cm convex (c) flat

Figure 8.27.: 3D melt flow calculations with a prescribed crystallization interface motion without melt flow, L = 22 cm, H = 11 cm (initial): carbon concentration (in a.u.) on the interface after 3500 s for a 2 cm concave (a), 2 cm convex (b), and a flat (c) crystallization interface.

All results with a melt flow are summarized in Fig. 8.28 showing both the calculated time-average velocity distributions and the species distribution on the interface. In the case with pure buoyancy forces, the flow is directed from the center to the rim for a convex interface and in the opposite direction for a concave interface. Both flows continue at the side wall in an upward and downward direction, respectively. These observations agree with the typical

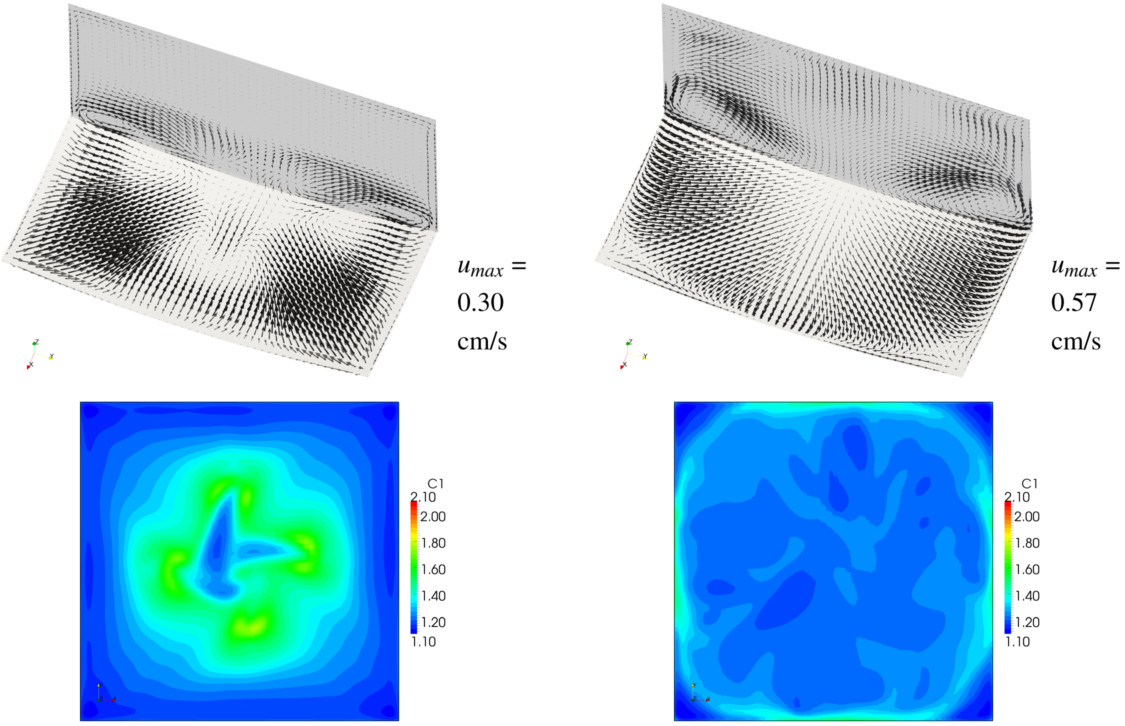

(a) Concave (b) Concave + TMF up

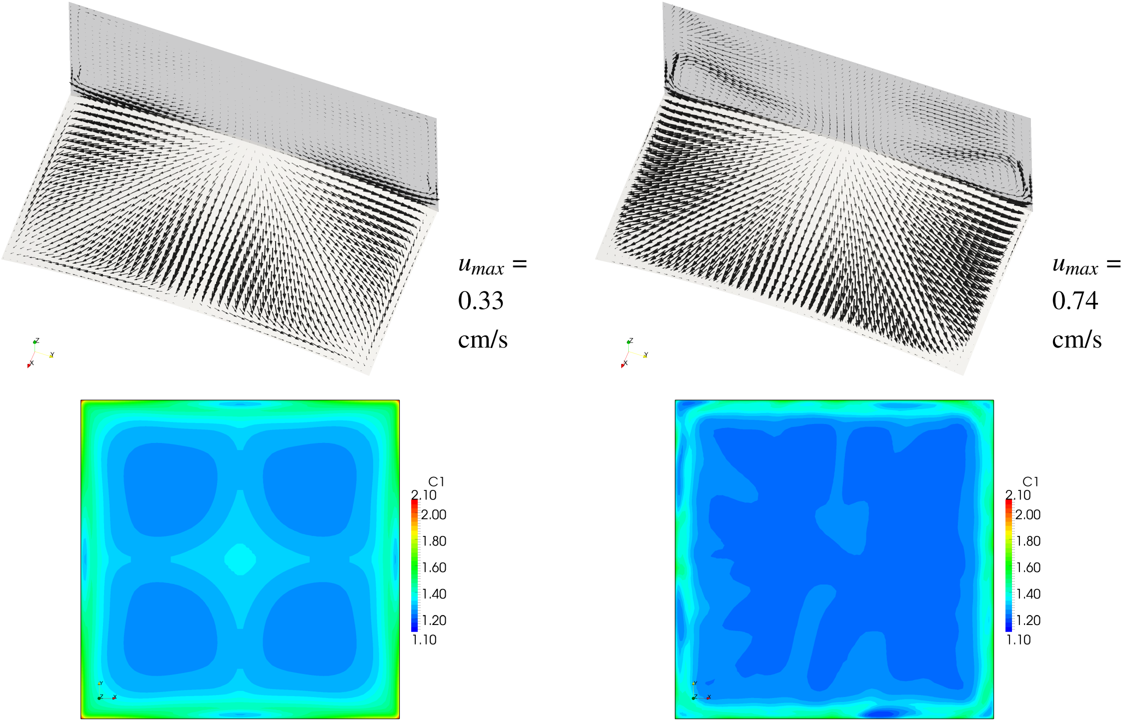

(c) Convex (d) Convex + TMF up

Figure 8.28.: 3D melt flow calculations with a prescribed crystallization interface motion, $L = 22$ cm, $H = 11$ cm (initial), $I_0 = 300$ A, $\phi = 60°$, TMF up: time-average (300. . . 3500 s) velocity in a vertical and horizontal cut (3 mm above the interface) and carbon concentration on the interface after 3500 s for a 2 cm concave (a,b) and 2 cm convex (c,d) interface; without a TMF (a,c) and with TMF up (b,d).

behavior of buoyant flows "moving upward along a hot wall and downward along a cold wall". Species distributions show an accumulation of impurities in the melt center for a concave interface and at the rim for a convex interface, as expected.

The case with impurities accumulated at the rim of the melt is obviously more preferable for directional solidification because the side parts of the ingot are cut off during wafering. Because an upward TMF causes a flow to the rim, it could avoid the central accumulation in the concave case and also improve the convex case. As shown in Fig. 8.28, the maximum concentration is indeed reduced in the convex case, and the flow direction is reversed in the concave case. The exact point of such a reversal has been investigated in [Grants and Gerbeth, 2008; Grants et al., 2009a] in 2D calculations with an idealized TMF. The balance between buoyancy and TMF forces was found to fulfill an approximate criterion $F_{em} \approx Gr \cdot d/R$, where d/R is the relative interface deflection and the Grashof number is defined using the temperature difference $dT/dz \cdot R$.

8.8. Discussion

8.8.1. Optimal TMF parameters

The optimal TMF parameters depend on the purpose of the use of a TMF in a crystallization furnace. In the context of directional solidification, this can be both the mixing of impurities and the control of the crystallization interface deflection. The main effects of TMF parameters such as inductor current, phase shift, or frequency are briefly summarized below.

In a (nearly) isothermal melt without buoyancy forces, the inductor **current amplitude** determines the level of melt flow velocity. For various melt sizes it was found that the flow velocity is proportional to the square root of the Lorentz force density or to the inductor current. Below a critical TMF strength, which can be estimated from the comparison of the TMF forcing parameter and Grashof number, the buoyancy starts to damp the TMF-induced flow. In this regime (e.g., the reference case with 300 A), the influence of the melt flow on the crystallization interface is moderate, while the species mixing may still be near to the complete mixing limit.

An inductor **current frequency** of 50 Hz is sufficient to generate a uniform velocity distribution along the entire crystallization interface for a Gen1 melt with $L = 22$ cm. With larger melt sizes, the absolute skin depth may still increase due to electromagnetic effects, but the relative skin depth decreases. Consequently, a reduction of current frequency below 50 Hz would be necessary for larger melts to increase the flow velocity in the central part of the crystallization interface.

A **phase shift** of 60° between the inductors seems to be near the optimum with respect to a high flow velocity at a given Lorentz force density (inductor current) for the considered Gen1 system. Higher phase shifts (e.g., 120°) require significantly higher inductor currents to achieve the same Lorentz force density. Lower phase shifts (e.g., 0°) lead to an almost horizontal force and disable the option of the switching of flow direction.

An upward or downward **direction of the TMF** leads to similar but reversed flow structures in the isothermal limit. However, with a strong buoyancy effect, a complex flow structure and a nonuniform velocity distribution forms at the crystallization interface in case of TMF down. Consequently, the phase interface obtains a very asymmetric convex shape, and the impurities are transported from the rim to the melt center. In contrast, a TMF up leads to a concave interface shape and transports the impurities to the more advantageous location at the rim.

The **current supplies** of the TMF inductors with a gap between them cause a weaker Lorentz force at the corresponding melt side and a slight asymmetry of the velocity field. However, in some cases, with TMF down in particular, this small asymmetry may have a large impact on the shape of the crystallization interface. Therefore, it seems to be preferable to reduce the influence of current supplies on the Lorentz force distribution.

8.8.2. Modeling strategy

3D calculations are necessary to obtain both qualitative and quantitative results with square melt geometries and small inductor asymmetries like current supplies. However, fully coupled calculations of melt flow, crystallization interface, and species transport are very time-consuming also for local models due to the large time intervals of several tens of hours involved. Several approximations that showed a good agreement with fully coupled calculations are briefly summarized below.

The influence of melt flow on the crystallization interface can be analyzed in a **quasi steady-state approximation of the interface shape** because these states can be reached within typical solidification times. A prescribed global crystallization rate can be adjusted to keep, e.g., the point at the center of the interface at a constant position; and the movement of the interface can be accelerated using a multiplier 50…100 for its velocity. In this manner, a converged quasi steady-state shape of the interface can be obtained in 500…1000 s also with a free triple-point line. The tendencies of interface shape changes can be analyzed also in unsteady calculations for small time intervals (e.g., 1000 s).

Although the species mixing may reach the complete mixing limit already at relatively small flow velocities (still in the buoyancy-influenced regime), the concentration distribution on the crystallization interface may be still very nonuniform. These distributions can be analyzed also after relatively short time intervals (e.g., 3500 s) in calculations with a **prescribed shape and velocity of the crystallization interface**.

8.8.3. Scaling

The scaling of the melt flow determined by buoyancy and Lorentz forces was already discussed in Chapter 5. Two aspects are new in the current chapter: the influence of melt flow on the crystallization interface and on the species transport. The crystallization process requires the consideration of two dimensionless numbers related to the Stefan condition as discussed in Sec. 2.4:

$$J_L = \lambda_L \frac{T_a - T_m}{Q_l \rho_S} \frac{1}{L_0 v_0}, \quad J_S = \lambda_S \frac{T_m - T_b}{Q_l \rho_S} \frac{1}{L_0 v_0}, \tag{8.13}$$

where the temperature scales for the melt and the crystal are defined using the ambient temperature at the free melt surface T_a and the temperature at the crystal bottom T_b, respectively (T_m is the temperature on the crystallization interface, i.e., the melting point). If the temperature differences $T_a - T_m$ and $T_m - T_b$ are kept constant, the crystallization velocity v_0 is proportional to the inverse system size $1/L_0$. This would keep also the dimensionless number Pe_v constant, which describes the time-dependent temperature field in the crystal.

In the calculations in Sec. 8.5, a fixed temperature gradient was used on the crystal bottom. This gradient can be adjusted to keep the temperature difference in the crystal $T_m - T_b$ constant. The radiation condition on the free melt surface can be linearized according to

(5.6) and written in a dimensionless form using a temperature scale $T = T_m + (T_a - T_m)T'$:

$$\frac{dT'}{dn} = R_{1lin}(T' - 1), \quad R_{1lin} = \frac{4\sigma_{sb}\varepsilon W T_a^3 L_0}{\lambda}. \tag{8.14}$$

The product of the emissivity and the view factor εW can be adjusted to keep the dimensionless number R_{1lin} constant for changing T_a and L_0.

The scaling of the Lorentz force due to a TMF requires a change of the current frequency to keep the S_{em} number constant as discussed in Chapter 5. The scaling of the melt flow requires an adjustment of the inductor current for the forcing parameter F_{em} and of the temperature difference in the melt for the Grashof number Gr. Note that the numbers Gr and J_L contain the products $(T_a - T_m)L_0^3$ and $(T_a - T_m)/L_0$, respectively. Consequently, it is not possible to up-scale the crystallization process and the buoyancy-influenced flow simultaneously. In the following example, we will disregard the Gr number and focus on the crystallization.

The species concentration in the melt is described by the solutal Peclet number $Pe_S = u_0 L_0 / D$, which remains constant if the Reynolds number does not change. The segregation boundary condition on the crystallization interface (2.62) can be written in a dimensionless form using a concentration scale $C = (C_1 - C_0)C'$ and velocity scale $v = v_0 v'$:

$$\frac{dC'}{dn} = -Pe_k v'_n C', \quad Pe_k = \frac{(1 - k_0)v_0 L_0}{D}. \tag{8.15}$$

The dimensionless number Pe_k remains constant if the product containing the crystallization velocity $v_0 L_0$ does not change.

We consider the reference case with melt and crystal domains from Sec. 8.1. The up-scaling of the Lorentz force, melt flow, crystallization process, and species transport with segregation from a melt size of L = 22 cm to a 4 times larger system with L = 88 cm is performed. According to the discussion above, the current frequency is reduced from 50 Hz to 3.125 Hz, the inductor current of 300 A is preserved, the temperature gradient at the crystal bottom is reduced from 10 K/cm to 2.5 K/cm, the ambient temperature at melt surface of 1725.4 K is preserved, and the product εW is reduced 4 times. The calculations were carried out in 2D using `GetDP` for Lorentz force calculations and `OpenFOAM` with an upwind scheme for flow calculations.

The results for the small and large silicon melt are summarized in Fig. 8.29 for three cases: crystallization and segregation without a melt flow, additional melt flow with Lorentz forces only (i.e., under theoretical zero-gravity conditions), and additional melt flow with Lorentz and buoyancy forces (with different Gr numbers for both systems). It can be seen that a perfect scaling between both systems can be achieved in first two cases – with identical flow patterns, interface shapes, temperature fields, and concentration fields. In the third case, the Gr number of the large system is 64 times higher, which results in a strong suppression of the TMF flow by the buoyancy forces. Note that the resulting flow pattern is not realistic due to the two-dimensional restriction.

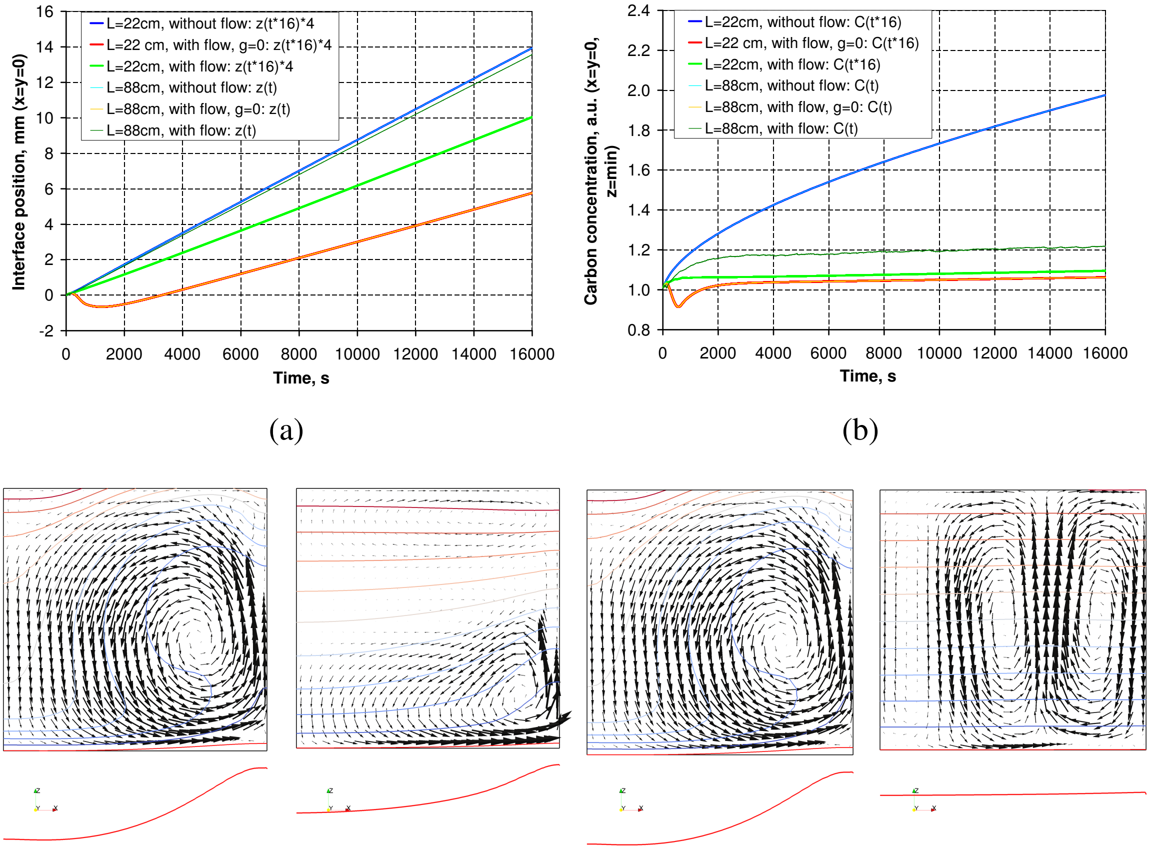

u_{max} = 1.87 cm/s
T_{max} = 1690.1 K

(c) L = 22 cm, TMF (g=0)

u_{max} = 0.53 cm/s
T_{max} = 1694.8 K

(d) L = 22 cm, TMF + buoyancy

u_{max} = 0.47 cm/s
T_{max} = 1690.1 K

(e) L = 88 cm, TMF (g=0)

u_{max} = 0.05 cm/s
T_{max} = 1695.2 K

(f) L = 88 cm, TMF + buoyancy

Figure 8.29.: Example for scaling the coupled melt flow, crystallization interface, and species transport between a research-scale (L = 22 cm) and industrial-scale (L = 88 cm) silicon melt: time-dependencies of interface position (a) and carbon concentration (b) in the center; melt flow and temperature for the small (c,d) and large (e,f) system after 1000 s (16000 s) including also the shape of the crystallization interface (extended vertically 10×). Results of 2D calculations corresponding to the reference case in Sec. 8.1 without a melt flow, with a TMF flow in zero gravity (g=0), and with a buoyant TMF flow are shown. The values for the small system are transformed according to scaling laws for comparison as indicated in the diagrams.

Chapter 9

Inductor optimization and practical realization

The classical configuration with three TMF inductors surrounding a square melt at the sides has been investigated in previous chapters with respect to Lorentz force, melt flow, species transport, and crystallization interface. After a brief summary of main limitations of this classical configuration, several novel concepts of inductor geometry are proposed in this chapter. The practical aspects of the use of TMF inductors inside a furnace are discussed, and the implementation in a new Gen1 furnace is presented. First experimental results of directionally solidified Gen1 ingots conclude this work.

9.1. Limitations of the classical TMF configuration

The classical way of generating a TMF in crystal growth is to use several circular coils that surround the melt at the sides. Such inductor systems have been used with axisymmetric geometries by Lantzsch et al. [2008] outside the furnace and by Rudolph et al. [2009a] inside the furnace (coupled with the heating system). First results for a square melt surrounded by coupled inductors–heaters have been recently presented by Kiessling et al. [2011, 2012]. This classical geometry was the starting point also for the current work. However, the results in previous chapters have shown that this inductor geometry has several disadvantages. Main limitations are briefly summarized below:

- The melt flow at the crystallization interface is uniform in the case of an upward TMF and a melt height-to-width ratio of about 0.5. At smaller aspect ratios, the flow structure may change to a horizontal vortex and a “dead water zone” in the central part. This could lead to regions with a poor melt mixing and with species accumulation at the crystallization interface.

- The toroidal flow structure strongly deforms the temperature field and hence also the crystallization interface. Although this can be a convenient method to influence the interface shape, a large interface deflection can be also an unwanted effect.

- Numerical studies for large melt sizes indicated that a smaller relative skin depth of the Lorentz force leads to a TMF torus more concentrated at the rim. Consequently, the mixing in the central part of the melt is lower.

These effects are related primarily to the toroidal flow structure that a TMF typically generates. This flow structure is determined by the resulting Lorentz force distribution with a vertical force component at the melt side. However, we have already seen that, for example, a gap between the current supplies can have an influence on the velocity field. The question is whether a TMF-similar inductor geometry can be used to generate other flow patterns than the classical torus. This would offer more flexibility in the choice and optimization of melt flow pattern.

Several modifications of the classical TMF configuration have been already discussed in the literature. Dropka et al. [2011] propose a superposition of two TMFs with different frequencies, which is able to reduce the Lorentz force maximum and the flow velocity at the crucible wall. This could reduce the melt–crucible interaction in directional solidification. Rudolph et al. [2011] have developed additional circular inductors at the bottom of the melt, generating a TMF that travels radially inward or outward. The resulting flow pattern in a Czochralski furnace was able to reduce the radial temperature gradients in the melt, which initiated the growth of square-shaped crystals instead of cylindrical ones.

Several new modifications of the classical TMF inductor geometry will be discussed in the following section:

- Parallel bars at the top (or bottom) of the melt
- Segmented side inductors with separate parts for each side of the melt

The obtained Lorentz force distributions and eventually new flow patterns will be analyzed.

9.2. 3D calculations of Lorentz force and melt flow for various inductor geometries

9.2.1. Top TMF inductors

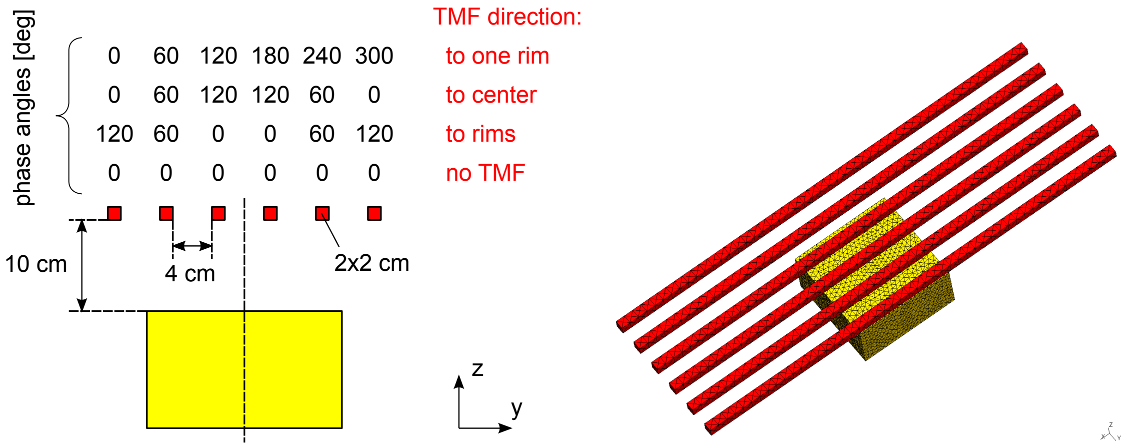

(a) (b)

Figure 9.1.: TMF inductor geometry with 6 bars at the melt top: (a) geometry with examples for possible phase shifts; (b) mesh for 3D electromagnetic calculations.

The Lorentz force generated by more than 3 (e.g., 6) inductors at the melt side was already described in Chapter 7. If we increased the melt radius until the system becomes effectively planar, the main characteristics of the Lorentz force distribution would not change much, which was investigated in Chapter 7 as well. If such a system is rotated by 90°, we basically

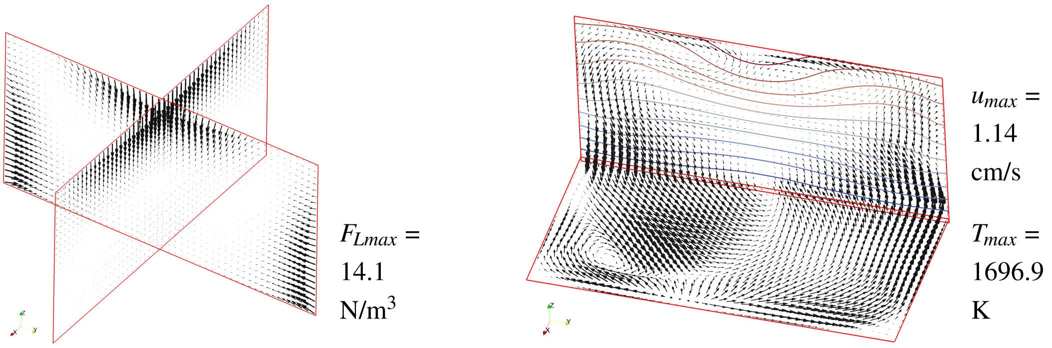

(a) ϕ = 0°, I_0 = 842 A

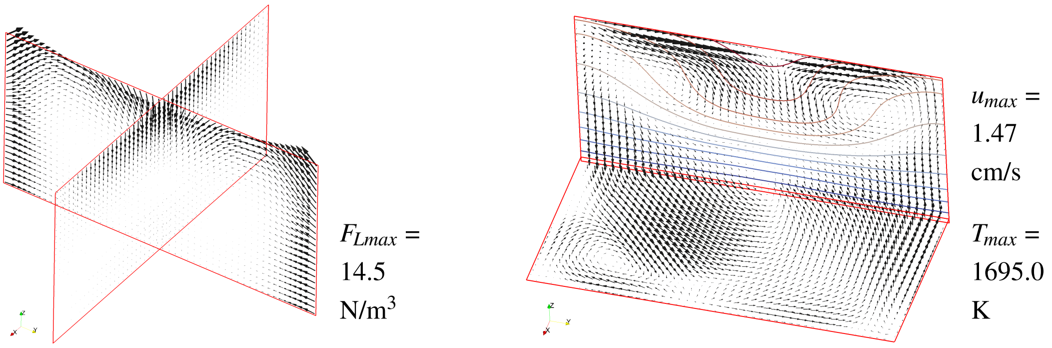

(b) ϕ = 60° (to center), I_0 = 933 A

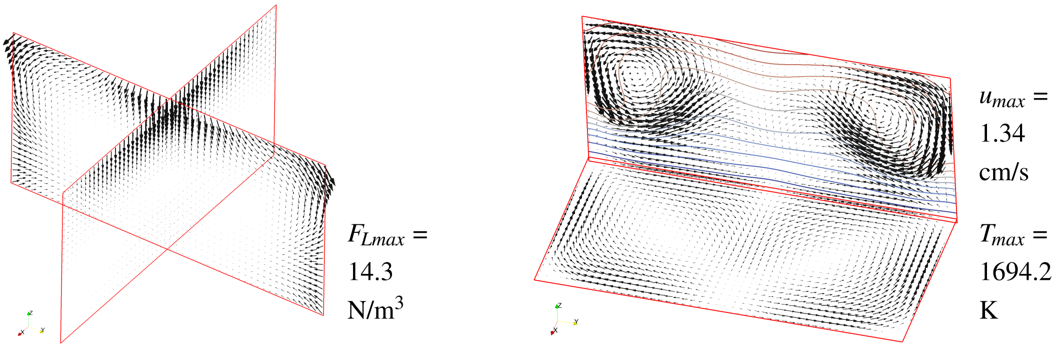

(c) ϕ = 60° (to both rims), I_0 = 958 A

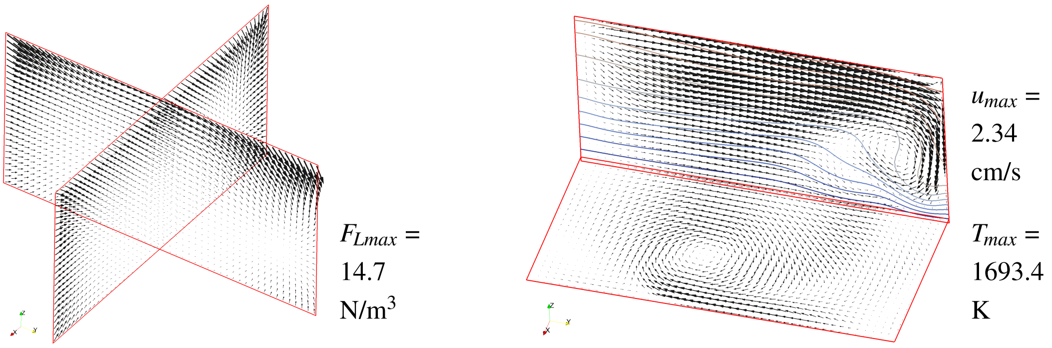

(d) ϕ = 60° (to one rim), I_0 = 545 A

Figure 9.2.: TMF inductor geometry with 6 bars at the melt top: Lorentz force in two vertical cuts; time-average (300…1500 s) velocity vectors and temperature isolines in a horizontal (3 mm above the melt bottom) and vertical cut for various phase shifts between the inductors (a–d). Inductor current I_0 is adjusted to obtain a maximum Lorentz force density of 15 N/m^3.

obtain a TMF inductor at the flat melt top as shown in Fig. 9.1. Only inductor geometry is specified because melt geometry from Sec. 7.1 is preserved. Note that the current supplies are simplified by extending the bars in x direction to the outer boundary of the calculation domain. It is advantageous to use a higher number of inductors at the melt top to allow also phase shifts with more than one direction, e.g., from both sides to the center and from one side to the opposite side. The corresponding phase angles are given in Fig. 9.1.

Four different phase shifts were considered in the calculations: 0°, 60° to one rim, 60° to the center, and 60° to both rims; see Fig. 9.1 (a). The inductor current was adjusted in each case to obtain a maximum Lorentz force density in the melt of 15 N/m^3, which is very similar to the value in the reference case in Sec. 8.1. The resulting Lorentz force distributions and velocity fields are summarized in Fig. 9.2. Lorentz force is acting mainly at the top of the melt, where the force direction resembles the phase shift and the traveling direction of the magnetic field (the force is vertical with 0°, i.e., the field is not traveling). But in most cases, there is also a relatively high Lorentz force at the two sides of the melt, parallel to the bars. The distribution is very similar to the distribution observed previously with side inductors (only bars are considered in the present calculations). Obviously, the outer bars, which extend over the melt width, act similarly on the melt sides as side inductors. Note that the required inductor current to achieve the same force density is approximately 2 to 3 times higher than with side inductors. A lower current would be required for a closer inductor distance to the melt, but there might be practical limitations for very small distances, e.g., the height of the crucible (usually significantly higher than the melt to accommodate the less dense feedstock material).

The melt flow velocities in Fig. 9.2 are more than 2 times higher than the value in the reference case with 3 side inductors. The highest velocity is achieved in the case with a phase shift of 60° to one rim and reaches 2.3 cm/s. In all cases, the flow pattern differs from the previous results. In the case with a phase shift of 0°, the Lorentz force is normal to the top surface and generates two weak vortices at the top. However, the flow structure is dominated by a large central vortex rotating in the horizontal direction with two secondary vortices in the corners; see also Fig. 9.3 (a). The same flow structure is preserved also with a phase shift of 60° to the center, but with more distinct vortices in the top part of the melt. An opposite

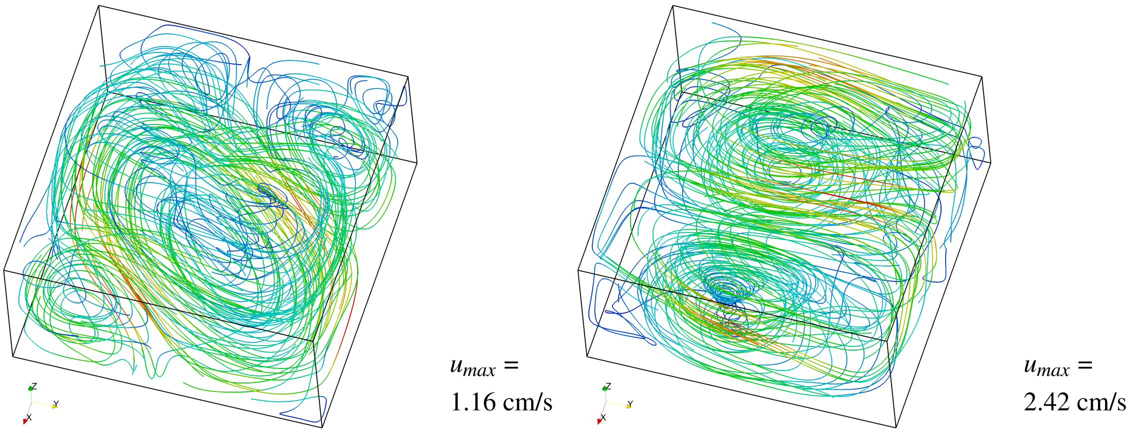

(a) $\phi = 0°$, $I_0 = 842$ A (b) $\phi = 60°$ (to one rim), $I_0 = 545$ A

Figure 9.3.: TMF inductor geometry with 6 bars at the melt top: 3D streamlines for the time-average (300. . . 1500 s) velocity for a phase shift of 0° (a) and 60° to one rim (b).

phase shift – from the center to both rims – leads to a complex flow structure with two large vortices extending over the entire melt depth at the top and with four horizontal vortices in the bottom part. In all three cases, temperature isolines at the crystallization interface are only slightly deformed by the dominating horizontal vortices. This is not the case for a phase shift of 60° to one rim: two large horizontal vortices appear in the melt as shown in Fig. 9.3 (b), but the downward flow at the melt side facing the Lorentz force causes a strong local increase of the temperature gradient.

Only TMF inductors at the melt top were considered in the calculations; however bottom inductors would act on the melt in the same way. Nevertheless, inductors at the melt bottom may have the disadvantage that the distance to the melt increases during the crystallization as the crystallization interface moves upward. Shielding effects from various furnace parts may become relevant as well if the bottom inductors are located below the graphite parts under the crucible.

9.2.2. Segmented side TMF inductors

The square shape of the melt encourages to consider the possibility of using separate inductors for each of the four melt sides. This would allow one to generate different Lorentz force distributions at different sides of the melt and to obtain new melt flow structures. The reference geometry from Sec. 7.1 is modified by dividing each side inductor into 4 separate inductors (segments) as shown in Fig. 9.4. The width of each inductor (segment) is set to 34 cm so that a small gap of 2 cm appears in the corner.

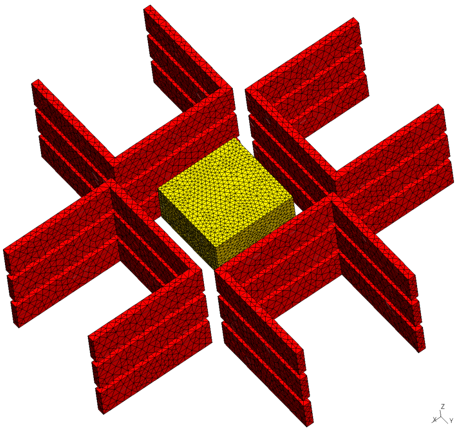

Figure 9.4.: TMF inductor geometry with segmented side inductors: mesh for 3D electromagnetic calculations.

If a phase shift of 60° between the inductors as in the reference case in Sec. 7.1 is used at all melt sides, we obtain the same TMF configuration, but without current supplies at the center of one side. However, now it is possible to switch off the TMF at separate melt sides. In a series of calculations, the number of magnetically active sides was varied from 1 to 4. Possible implications for the heating system will be discussed later in this chapter. The calculated Lorentz force distributions and velocity fields are summarized in Fig. 9.5. The Lorentz force distribution resembles well the switching-off at the chosen melt sides. The inductor current was adjusted in each case to obtain a maximum Lorentz force density in the melt of 15 N/m^3 in all cases. A smaller number of active melt sides leads to a higher inductor current, as expected. However, also with all 4 sides active, the required inductor

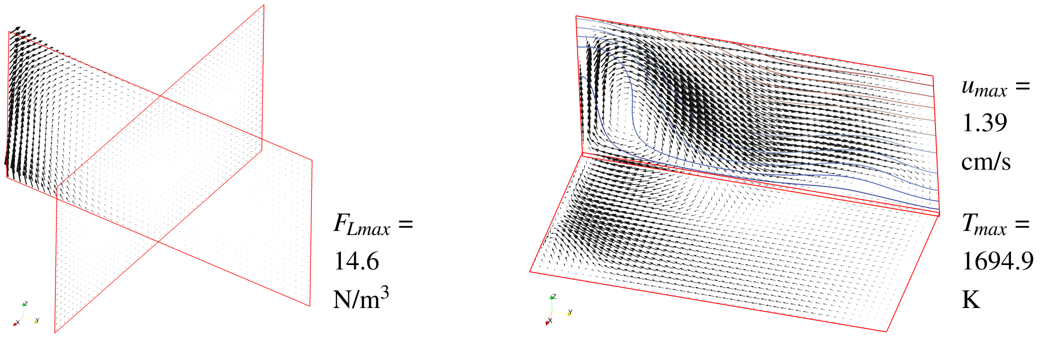

(a) 1 active side, I_0 = 897 A

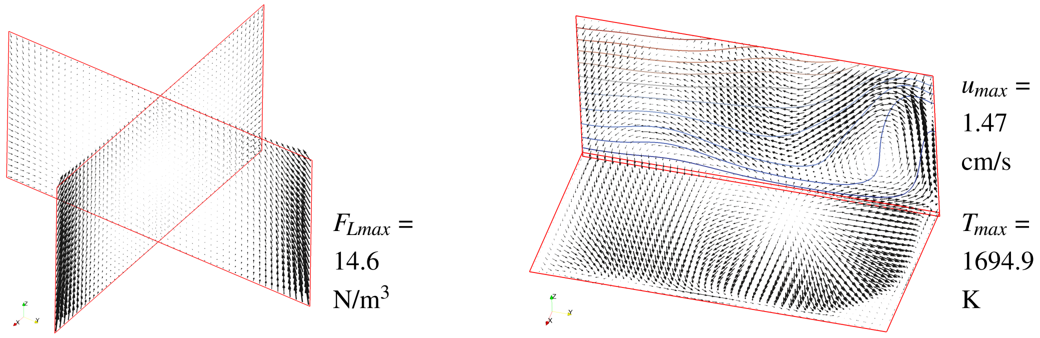

(b) 2 active sides, I_0 = 719 A

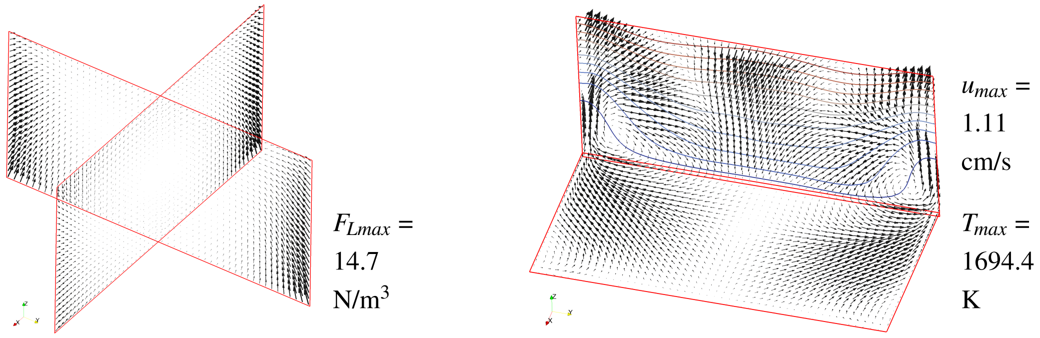

(c) 3 active sides, I_0 = 596 A

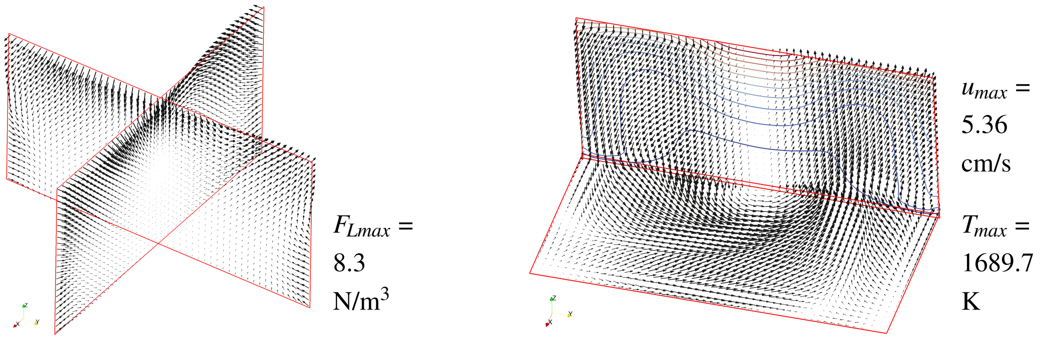

(d) rotating magnetic field, I_0 = 1497 A

Figure 9.5.: TMF inductor geometry with segmented side inductors: Lorentz force in two vertical cuts; time-average (300…1500 s) velocity vectors and temperature isolines in a horizontal (3 mm above the melt bottom) and vertical cut for various numbers of active sides (a–c); for a phase shift between the inductors generating a rotating magnetic field (d). Inductor current is adjusted to obtain a maximum Lorentz force density of 15 N/m^3.

current of 526 A was almost 2 times higher than in the reference case with continuous side inductors. This can be explained by the gaps between the segmented inductors in the corners. An increase of inductor width at two opposite sides of the melt to form an overlap allowed to decrease the required current by about 30%. The current distribution in inductor's corners was still not as uniform as in the case with continuous inductors because it has a turning point in the corner.

Velocity fields in Fig. 9.5 show that melt flow is always directed upward at the magnetically active sides. The flow at the melt bottom is always directed from the inactive to the active sides, but a single large vertical vortex over the entire volume does not occur. Velocity fields in a vertical cut for the cases with 1 and 2 active sides clearly show that the melt flows downward before reaching the melt center. On the top of this structure, two horizontal vortices form in the top part of the melt, which is visualized by using 3D streamlines in Fig. 9.6 (a). If some sides are inactive, the melt flow velocity at the same Lorentz force density becomes about 2 times higher than with continuous side inductors in Sec. 8.1, which may achieve better melt mixing. This effect could be enhanced by using an opposite direction of TMF at opposite sides of the melt.

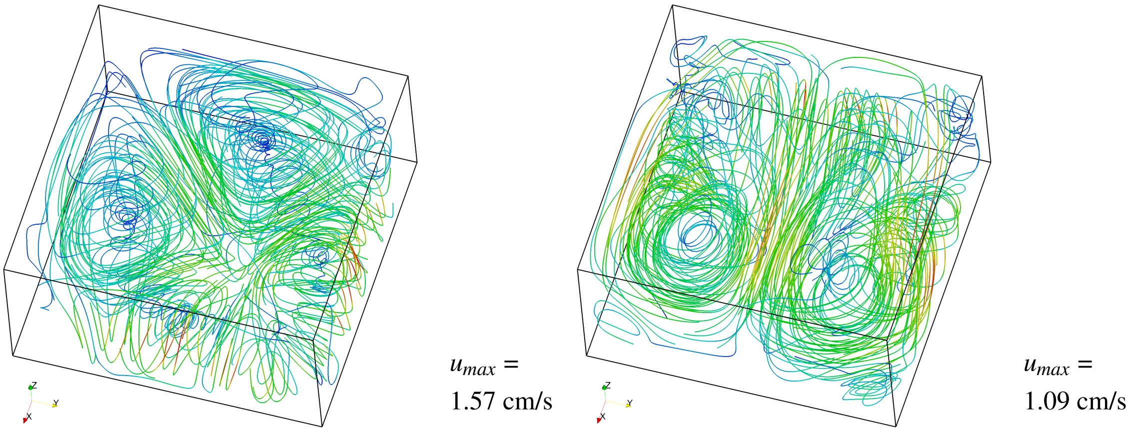

(a) 2 active sides, I_0 = 719 A

(b) 3 active sides, I_0 = 596 A

Figure 9.6.: TMF inductor geometry with segmented side inductors: 3D streamlines for the time-average (300. . . 1500 s) velocity for two (a) and three (b) active sides.

The segmentation of side inductors allows also an interesting new scheme of phase shifts: if all 3 inductors at the first melt side are set to a phase shift to 0°, at the second side to 90°, etc., then the configuration resembles a rotating magnetic field with two pairs of coils. Indeed, the calculated Lorentz force in Fig. 9.5 (d) shows a distinct azimuthal force component. The required inductor current to achieve the same Lorentz force density as in the reference case is Sec. 8.1 is nearly 5 times higher, but the resulting flow velocity is nearly 10 times higher. The velocity distribution indicates a global rotation in the entire melt volume. A secondary flow appears in the “meridional plane” manifesting itself in a large deformation of the temperature field.

The asymmetric temperature field deformation by the melt flow in the case of at least one magnetically inactive side would also lead to an unfavorable asymmetric shape of the crystallization interface. However, because the reaction time of the interface shape is on the order of 1000 s and that of the flow is on the order of 100 s (see Chapter 8), it might be possible to change the active sides periodically during the crystallization process. With a high frequency of switching, the flow would effectively “see” a Lorentz force at all melt sides simultaneously, leading to the reference configuration with all sides active. With a low frequency of switching, an asymmetric melt flow influence on the interface shape might appear. With an optimal frequency, the crystallization interface “sees” a symmetric time-average temperature field, while the impurity concentration is well mixed by the instantaneous high flow velocity.

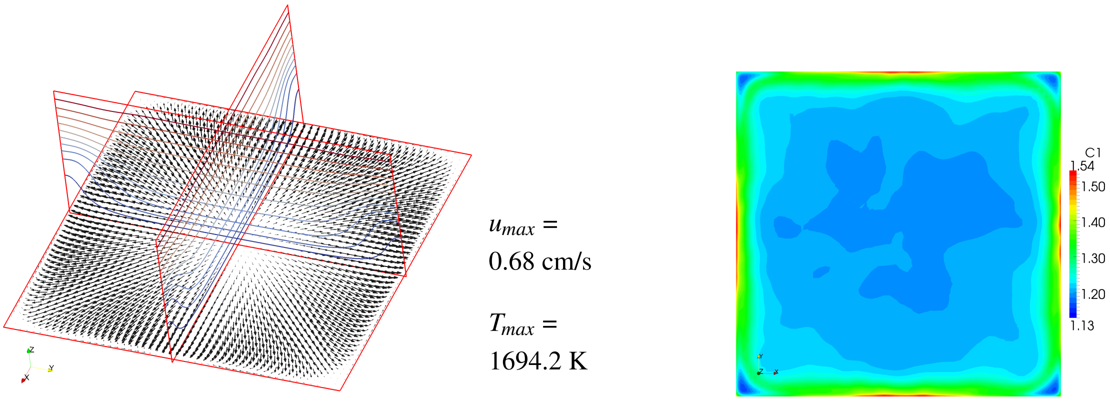

u_{max} = 0.68 cm/s

T_{max} = 1694.2 K

(a) 4 active sides

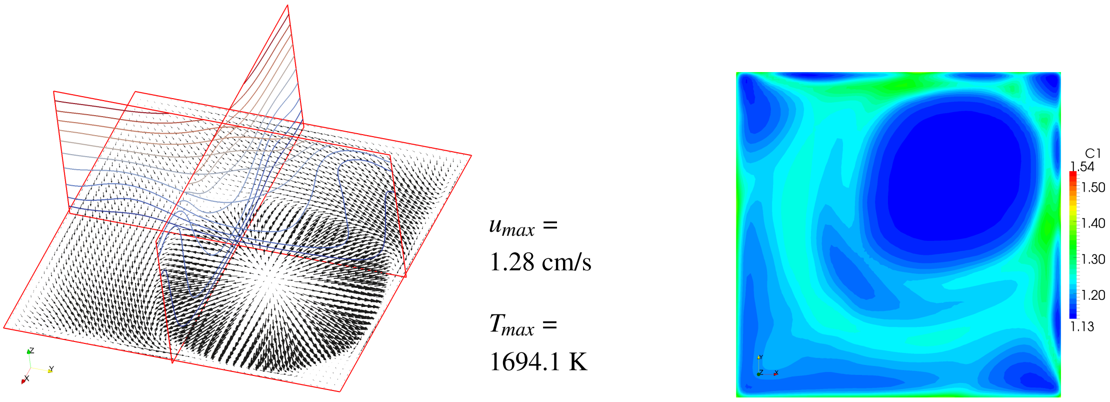

u_{max} = 1.28 cm/s

T_{max} = 1694.1 K

(b) 2 active sides

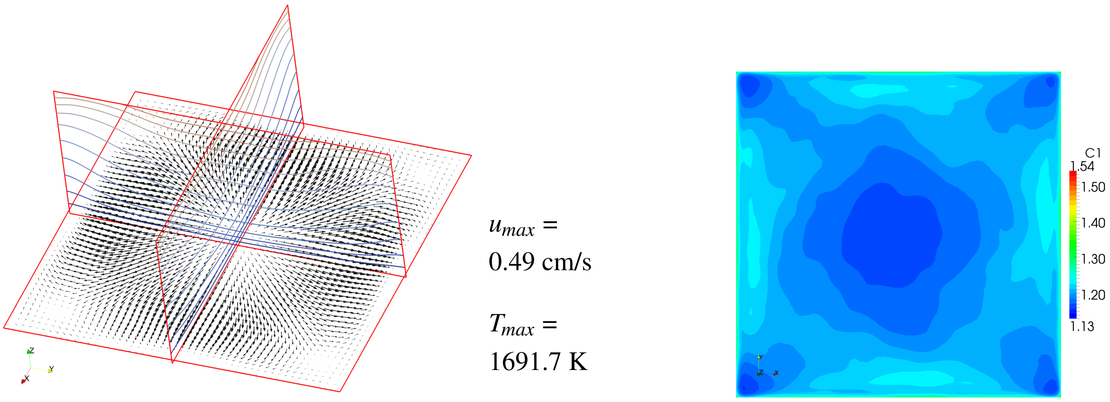

u_{max} = 0.49 cm/s

T_{max} = 1691.7 K

(c) 2 active sides switched each 100 s

Figure 9.7.: TMF inductor geometry with segmented side inductors: time-average (2400…3600 s) velocity (3 mm above the melt bottom), temperature (isolines in two vertical cuts), and carbon concentration field (in a.u., on the crystallization interface) for various numbers of active sides, including switching.

In a series of calculations, three cases were compared: 4 active sides, 2 active sides, and 2 active sides switched around the melt periodically. The switching was carried out by first calculating 4 different Lorentz force distributions (active melt sides: 1+2, 2+3, 3+4, 4+1) and then using different distributions for different time intervals. The switching to the next side is performed each 100 s and a total time interval of 3600 s is considered. Segregation of carbon in a closed system is considered to investigate the influence on the species transport; see the analysis in Sec. 8.7.

Fig. 9.7 compares the time-average distributions of velocity, temperature, and carbon concentration for the time interval 2400…3600 s that contains 2 full switching cycles. While the melt flow and temperature fields are symmetric with 4 active sides, the case with 2 active sides exhibits a very strong asymmetric deformation of the temperature field. Carbon concentration shows a less distinct increase at the melt rim in the case with 2 active sides. The additional switching of the 2 active sides is able to eliminate the time-average temperature asymmetry and also to decrease the magnitude of deformation. At the same time, carbon concentration is more uniform along the entire crystallization interface. A comparison of the time-dependencies of velocity and carbon concentration in Fig. 9.8 shows a significant increase of the oscillation amplitude in the case with switching. Note that the absolute value should not be compared because the monitor point is fixed but the flow structure changes.

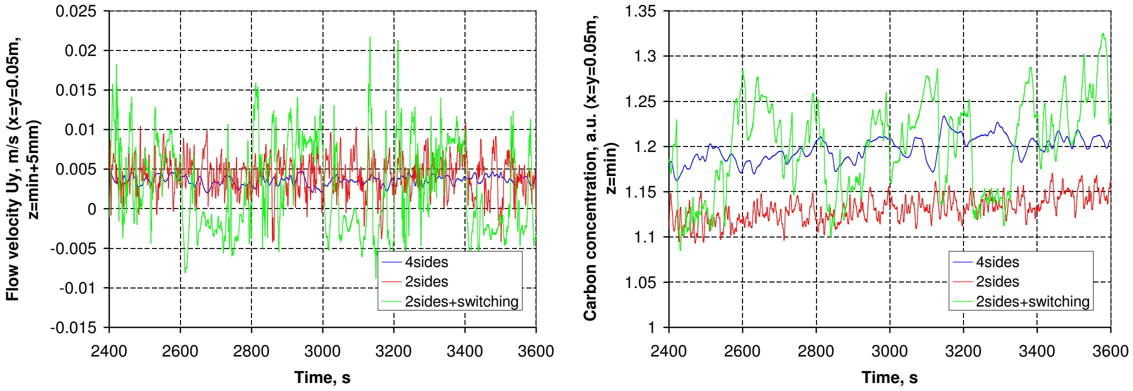

(a) (b)

Figure 9.8.: TMF inductor geometry with segmented side inductors: oscillations of velocity (a) and carbon concentration (b) at a monitor point for various numbers of active sides, including switching.

9.3. Possibilities to generate a TMF in crystallization furnaces

9.3.1. Coupling of TMF inductors and heaters

Placing the TMF inductors outside the crystallization furnace offers a full control of the magnetic field. However, the technical realization of this configuration is not suitable for very large furnaces not only due to high costs of such inductors but also due to increasing shielding effects. The possibilities to install TMF inductors inside the furnace can be generally summarized as follows (see also Fig. 9.9):

1. Resistance heaters are supplied with an AC current, which generates both Joulean heat sources in the heater and a magnetic field, e.g., [Dietrich et al., 2007]. Both effects are controlled by a single parameter – the amplitude of the AC current – and cannot be changed independently.[1]

2. Resistance heaters are supplied with a modulated DC current that contains both DC and AC components. This can be imagined as a vertical shift of a sinusoidal current. The DC component generates heat sources and a weak steady magnetic field, while the AC component generates a magnetic field and, hopefully, weak heat sources. Consequently, the DC and AC amplitudes allow a partly independent control of the heating and the magnetic field. This is known as the heater–magnet or KristMAG concept [Rudolph, 2008].

3. Independently of the heating system, additional inductors (possibly containing a cooling system) are installed inside the furnace, e.g., [Julsrud and Rudshaug, 2007]. Cooling of the inductors would usually be necessary to protect their material from the high temperatures inside the furnace. This requirement significantly increases the complexity of this configuration.

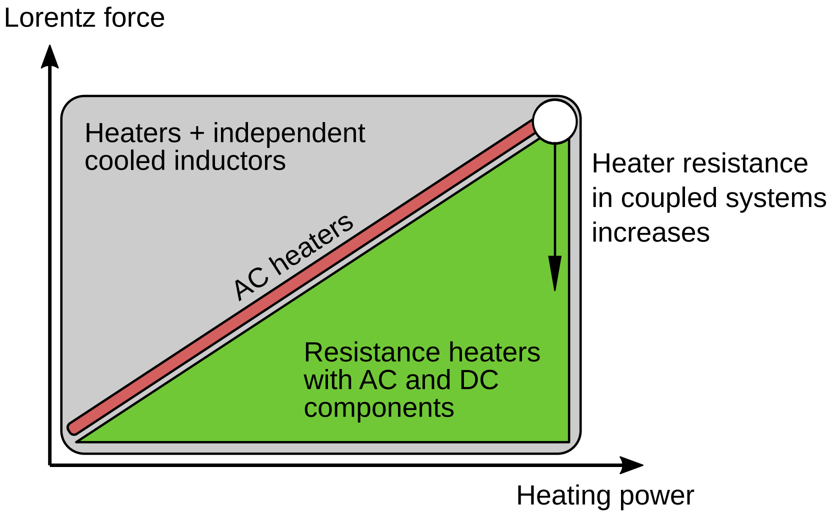

Figure 9.9.: Available parameter regions of Lorentz force and heater power in a schematic diagram for various concepts of coupling between TMF inductors and heaters.

The above listing names the solutions in the order of increasing decoupling between the magnetic and heating systems, but also in the order of increasing complexity. The second option can be analyzed more quantitatively. Let us consider a voltage signal that consists of both a constant DC component U_{DC} and a time-dependent AC component with an amplitude U_{AC}. Using Ohm's law, the voltage $U(t)$ and the current $I(t)$ can be written as

$$U(t) = U_{DC} + U_{AC} \sin \omega t, \quad I(t) = \underbrace{\frac{U_{DC}}{R_{el}}}_{I_{DC}} + \underbrace{\frac{U_{AC}}{R_{el}}}_{I_{AC}} \sin \omega t, \tag{9.1}$$

---

[1] In practical applications, the heating power is usually controlled by the phase cut technique. But the phase cut also influences the Lorentz force as discussed in Sec. 7.4.

where R_{el} is the electrical resistance of the heater. The instantaneous power

$$P_{mom}(t) = I(t)^2 R_{el} = (I_{DC} + I_{AC}\sin\omega t)^2 R_{el} \tag{9.2}$$

allows one to obtain the average power in one current period $t_p = 1/f$ by integration:

$$P_{avr} = \frac{1}{t_p}\int_0^{t_p} P_{mom}(t)\,dt = \frac{R_{el}}{t_p}\int_0^{t_p} (I_{DC} + I_{AC}\sin\omega t)^2\,dt = \underbrace{I_{DC}^2 R_{el}}_{P_{DC}} + \underbrace{0.5 I_{AC}^2 R_{el}}_{P_{AC}}, \tag{9.3}$$

where P_{DC} and P_{AC} are the heating powers due to DC and AC components of the current, respectively. In practical applications, one usually has a target value for the (maximum) AC current amplitude I_{AC} to achieve the desired magnetic field and a target value for the (maximum) DC heating power P_{DC}. Other heater parameters can be expressed in terms of these parameters in the following way:

$$I_{AC}(max) \quad \Rightarrow \quad P_{AC} = \frac{I_{AC}^2 R_{el}}{2}, \quad U_{AC} = I_{AC} R_{el} \tag{9.4}$$

$$P_{DC}(max) \quad \Rightarrow \quad I_{DC} = \sqrt{\frac{P_{DC}}{R_{el}}}, \quad U_{DC} = I_{DC} R_{el} \tag{9.5}$$

Inductor geometries considered in the current work can be simplified as shown in Fig. 9.10 so that the resistance of the inductor can be estimated according to $R_{el} = L_h/\sigma_h S_h$, where $\sigma_h = 9.1 \cdot 10^4$ S/m is the electrical conductivity of the inductor (heater) material; L_h and S_h are the length and the cross section of the current path in the heater, respectively. We assume 1000 A for the AC current amplitude and 15 kW for the entire heater in all cases. The resulting heater parameters are summarized in Tab. 9.1. It can be seen that the resulting AC power reaches 37…55 % from the DC power. Consequently, it would be impossible to reduce the total heating power below this level without reducing the magnetic field. In the case of a segmented side heater or a top heater, the required heater voltage becomes very small, which could lead to low efficiencies of the required power supplies. Both the power and the voltage depend on heater resistance, which can be set by the cross section of the heater.

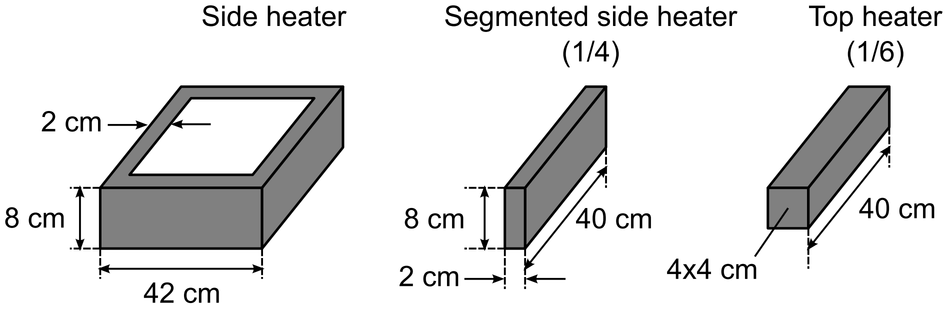

Figure 9.10.: Various heater geometries for resistance calculations. The same heater cross section is used in all cases.

The influence of the heater cross section is further evaluated in Fig. 9.11 for a side heater without segmentation. A larger cross section (smaller heater resistance) would decrease the AC power at a given AC current amplitude, but it would also decrease the heater voltage.

Configuration	R_{el}, mΩ	I_{AC}, A	F_{Lmax}, N/m^3	P_{AC}, kW	U_{AC}, V	I_{DC}, A	P_{DC}, kW	U_{DC}, V
Side heater	11.0	**1000**	140	5.5	11.0	1168	**15**	12.8
Segmented side heater (1/4)	2.75	**1000**	54	5.5/4	2.75	1168	**15/4**	3.21
Top heater (1/6)	2.75	**1000**	17	8.25/6	2.75	953	**15/6**	2.62

Table 9.1.: The current, voltage, and power of AC and DC components for various heater geometries according to Fig. 9.10. Values in bold face are prescribed, other are calculated. The maximum Lorentz force due to the AC component is given from previous calculations for a full TMF (in upward direction) configuration with a phase shift of 60°: 3 continuous side inductors; 3 segmented side inductors with all 4 sides active; 6 bars at the top with a phase shift to the center.

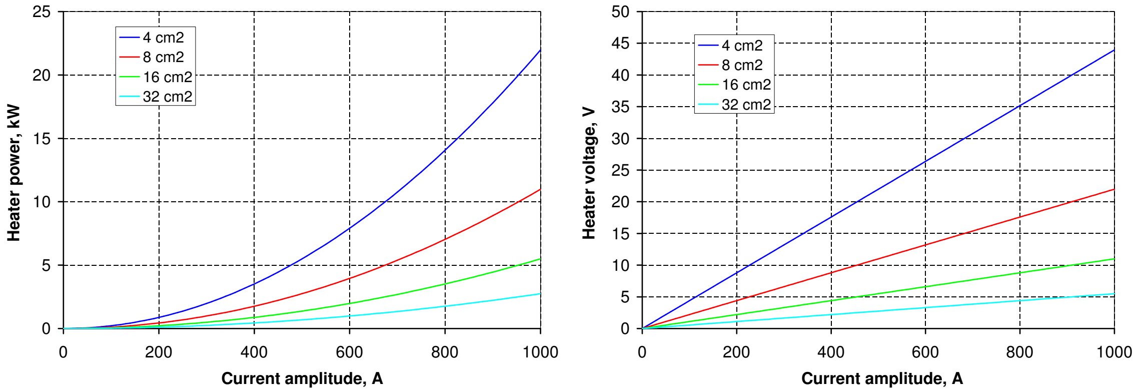

(a) (b)

Figure 9.11.: Dependence of heater power (a) and voltage (b) of the current amplitude for various cross sections. The case with a side heater is considered.

Consequently, a decoupling of the magnetic field control and the heating control within the AC+DC concept is possible only to a limited extent, depending on the level of heater power and the available range of heater voltages. Of course, the same conclusions apply to the case with an AC current alone.

9.3.2. Sources of phase-shifted currents

To generate a TMF, a phase shift between the currents in several inductors is needed. The use of modulated DC currents usually requires inverters, which also enable the adjustment of current frequencies and phase shifts in definite ranges, e.g., $f = 10\ldots600$ Hz, $\phi = 5\ldots120°$ [Rudolph, 2008]. The options are more limited in the case of a simple 50 Hz AC power supply. The three-phase current produced by power stations consists of three separate alternating currents with a phase shift of 120° – the current phases L1, L2, L3. The voltage in the line with respect to the ground varies as:

$$\text{L1}: \quad U_1(t) = U_0 \sin(\omega t - 0 \cdot \pi/180) \tag{9.6}$$

$$\text{L2}: \quad U_2(t) = U_0 \sin(\omega t - 120 \cdot \pi/180) \tag{9.7}$$

$$\text{L3}: \quad U_3(t) = U_0 \sin(\omega t - 240 \cdot \pi/180) \tag{9.8}$$

where $U_0 = 220$ V. On the time axis, these signals are in the order L1, L2, L3, with a phase shift of 120°. A combination of different current phases allows one to obtain various phase shifts in the range 0…300° with a step of 60° as shown in Fig. 9.12 (a). The resulting time-dependencies are calculated from the differences of both signals: $U_1(t) - U_2(t)$ for L1−L2, etc. Care must be taken in case of several inductors to avoid accidental shifts by 180° – the left part of a phase pair should be always connected to, e.g., the current supply on the left side.

In cases with a large number of inductors (e.g., 6 bars of a top inductor), the current supply can be significantly simplified using direct connections between the inductors. As illustrated in Fig. 9.12 (b), only 3 current supplies are needed instead of 12 for a top inductor to obtain a phase shift of 60° to one rim. A similar reduction is possible also for the segmented side inductors, but it must be noted that a connection disables the possibility to control the connected inductor parts independently. A switching of inductors with some inactive sides would require separate current supplies for each of the 12 inductors. However, the switching effect could be achieved also with simple AC power supplies if the inactive sides are approximated by a large phase shift (e.g., 180°) that effectively reduces the Lorentz force to zero.

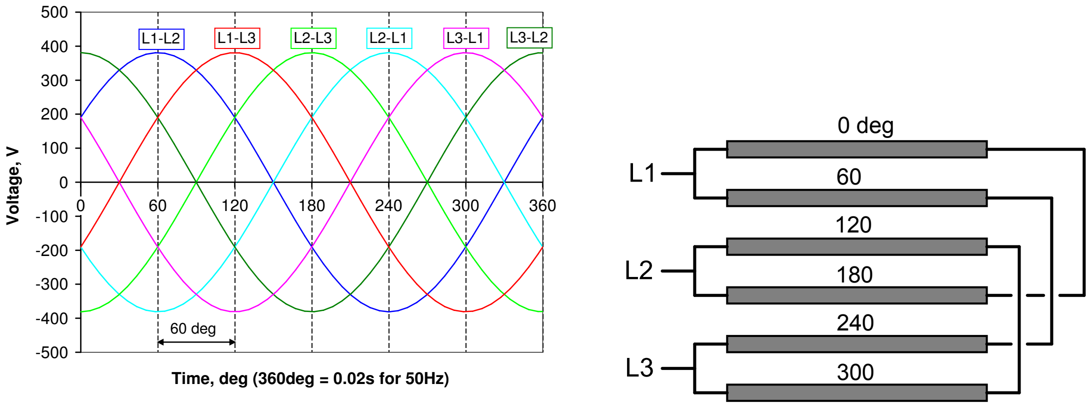

(a) (b)

Figure 9.12.: (a) Phase shifts between various combinations of 3 current phases; (b) Example of connection for a top inductor with a phase shift of 60° to one rim.

9.4. Realization of the TMF concept in a research-scale furnace

9.4.1. Description of the furnace

A research-scale furnace was put into operation at Fraunhofer THM during the last stage of this work in the summer of 2010.[2] This section briefly illustrates how the academic models developed and investigated in the frame of this were implemented in the reality. The furnace geometry is depicted in Fig. 9.13, including a sketch of the hot zone in a vertical cut. The heating system consists of five resistance heaters: top heater, bottom heater, and three side

---

[2] The conceptual development of the furnace was conducted by a team at Fraunhofer THM under the supervision by Dr. Ulrike Wunderwald and with participation of the author in many discussions.

heaters surrounding the crucible. The top and bottom heaters are made as meanders with two parts in a parallel connection; both heaters are located at a relatively large distance of about 40 cm to the melt bottom. Each side heater forms a single loop around the melt with the current supplies in the corner as shown in Fig. 9.13 (c,d). The side heaters were implemented in the initial stage without the segmentation, but preserving this option for the future.

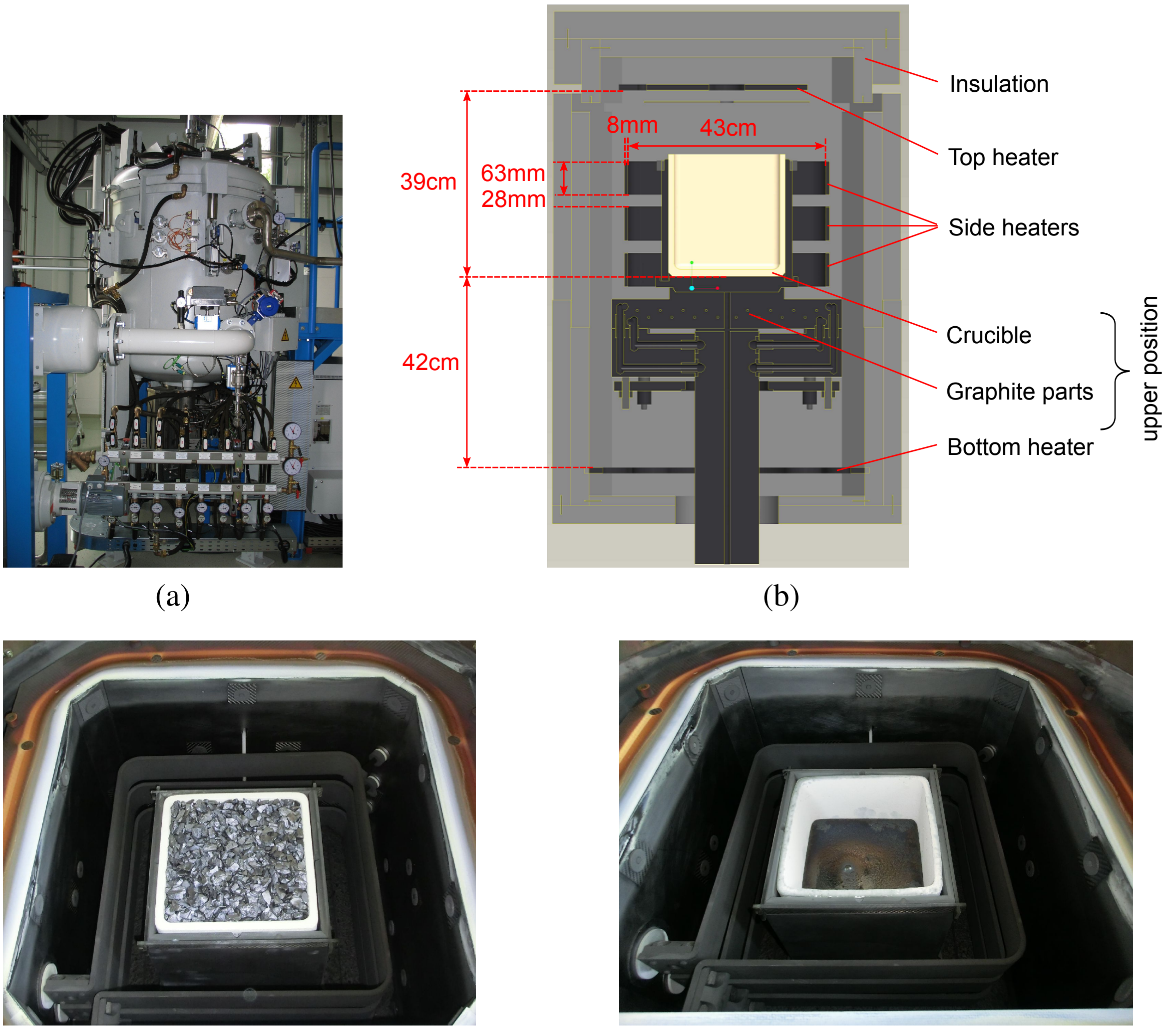

(a) (b)

(c) (d)

Figure 9.13.: Research-scale furnace at Fraunhofer THM: photo with the furnace from outside (a), with open hot-zone containing the ingot before (c) and after (d) the crystallization process; (b) furnace geometry in a vertical cut. [ExpTHMfurnace, 2011]

The cooling at the bottom of the crucible is possible in two ways. First, using active cooling with a coolant flow in the central support. Second, changing the vertical crucible position: it can be moved from the upper position where the bottom wall of the crucible is approximately on the same level as the bottom surface of the bottom side heater downwards by 10 cm.

All heaters are supplied with an alternating current with a frequency of 50 Hz and act simultaneously as magnetic field inductors. The phase angle of the lower side heater is set to 0°, while the phase angles of the middle and upper side heaters can be varied (also during the process) in the range 0…270° with a step of 60°. Therefore, an upward or downward TMF with various phase shifts can be produced using the side heaters. The initial current amplitude in the side heaters is fixed, and the heater power is controlled using the phase cut method so that the sinusoidal current is transformed as shown previously in Fig. 7.8. Consequently, the change of the phase shift with discrete steps is the only way of controlling the magnetic field and the heater power independently. The manetic field control basically follows the diagram Fig. 7.7 (d). This method is not as flexible as the KristMAG concept [Rudolph, 2008], but it allows one to significantly simplify the current supply.

As it can be seen in Fig. 9.13 (b), dimensions of side heaters were adjusted during the construction of the furnace and do not match the reference geometry in Sec. 7.1. However, the deviations are not large and would not cause essentially different Lorentz force distributions and densities. The distance and the shape of the top and bottom heaters would rather lead to a small magnetic influence on the melt flow. Powers and current amplitudes of all heaters are summarized in Tab. 9.2, which allows to estimate the generated magnetic induction and the Lorentz force density. A single side heater can be approximated as a circular current loop with a radius R. A top/bottom heater can be approximated as a short straight wire at a distance d from the melt. The magnetic induction for both cases (using the expression for a long wire) reads (see Sec. D.2.1):

$$B_{\text{loop}} = \frac{\mu_0 I_0}{2R}, \quad B_{\text{wire}} = \frac{\mu_0 I_0}{2\pi d}, \tag{9.9}$$

where I_0 denotes the current amplitude. Geometric parameters are given in Fig. 9.13 (b). The Lorentz force density can be roughly estimated using the 2D approximation (2.34). The estimated magnetic induction and Lorentz force is summarized in Tab. 9.2 and should only give a rough approximation of the magnetic effect from the various heaters. The Lorentz force from top and bottom heaters is two orders of magnitude smaller than that from side heaters and can be neglected in melt flow analysis. However, if the small force density on the order of 1 N/m^3 were the only source of external forces for the melt flow, it would have an impact on the species transport – results in Sec. 8.7.1 showed some influence already at 0.03 N/m^3.

Heater	Maximum power, kW	Current amplitude, A	Magnetic field, mT	Lorentz force, N/m^3
Top	16	730	0.37	0.78
Side×3	14.5×3	760×3	2.2×3	26×9
Bottom	16	730	0.35	0.7

Table 9.2.: Heater parameters: maximum power and current amplitude, approximate magnetic field amplitude and induced Lorentz force in the melt.

9.4.2. First experimental results

This section presents the first experimental results, with a focus on the role of melt flow. Two ingots with a weight of about 15 kg and dimensions of 22×22×14 cm^3 have been grown for the two extreme phase shift between the side heaters[3]:

- Phase sift of 0°, corresponding to a high Lorentz force density and strong melt flow

---

[3] These crystallization experiments as well as the characterization of the ingots were carried out by Iven Kupka from Fraunhofer THM under the supervision by Dr. Ulrike Wunderwald.

- Phase shift of 180°, corresponding to a low Lorentz force density and very weak melt flow

The results shown previously in Fig. 7.7 (d) allow to estimate the ratio of Lorentz force densities in both cases as about 40. Flow calculations presented in Sec. 8.3 also indicated very different flow structures. However, the real growth process differs from the previous "academic" models in several aspects:

- Phase cut of the heater current
- Heater power (and current amplitude) is not constant over the process
- Very non-uniform power (and current) distribution among side heaters

To compare the experimental conditions with the previous simulations, the inductor current for magnetic field generation can be estimated in the following way: a typical effective current (including the phase cut) for each side heater is chosen; an average value for all three side heaters is calculated; the corresponding current amplitude is calculated. This approximation leads for both experimental processes to a current amplitude of 400 A. In Fig. 8.5, this current at a phase shift of 60° correspond to a typical melt flow velocity of 2 cm/s. It can not be determined what is the exact role of buoyancy in the experiments because currently there are no reliable data about the temperature gradients in the melt. Although a basic understanding of the effects in the experiments could be obtained on the basis of this approximate assignment to the academic models analyzed in the current work, a precise understanding would certainly require further numerical studies in 2D and 3D.

An additional problem in the interpretation of experimental results is related to the control of heater power. It is possible to prescribe either power profiles or temperature profiles to the heaters. In the latter case, the power is adjusted automatically to reduce the difference between the actual and the prescribed heater temperature. If temperature profiles are prescribed, it seems to be more likely that some effects of the melt flow are compensated by the automatic adjustment of heater power. Therefore, heater powers from the first process with a phase shift of 0° were directly prescribed in the second process with a phase shift of 180°. A comparison of the time-dependencies of heater powers and temperatures for both processes in Fig. 9.14 (a,b) shows a very good agreement. Some deviations occur only at the end of crystallization because the process with a phase shift of 0° lasts slightly longer. This may have been caused by a higher ingot weight by about 0.5 kg in tis case.

The advance of crystallization was controlled during the process by periodically immersing a quartz glass rod into the melt and determining the position of the crystallization interface in the center. The time derivative gives the crystallization velocity. The comparison in Fig. 9.14 (c,d) shows that the crystallization velocity is about 1.5 cm/h during the middle part of the crystallization in both cases. This velocity corresponds for the solidification of a Gen1 melt to a latent heat release of 0.84 kW.

A first characterization of the obtained silicon ingots was performed using infrared transmission microscopy (IR) to investigate the occurrence of inclusions and lateral photovoltage scanning (LPS) technique (see Sec. 1.2.3) to analyze the shape of crystallization interface as it was during the process (see Sec. 1.2.3). In both cases, a vertical cut from the central part of the ingot was used. The IR images in Fig. 9.15 (b) clearly indicate that there are inclusions at the top part of the ingot in both cases. These are most likely the typical inclusions of SiC clusters and Si_3N_4 rods [Reimann, 2010], but the exact composition has not yet been determined. The appearance of a crystalline structure with very fine grains at exactly the same region could indicate carbon (SiC) inclusions, which have been shown in the literature to cause such effects [Beaudhuin et al., 2011] (the fine grains are known as *grits*). Currently,

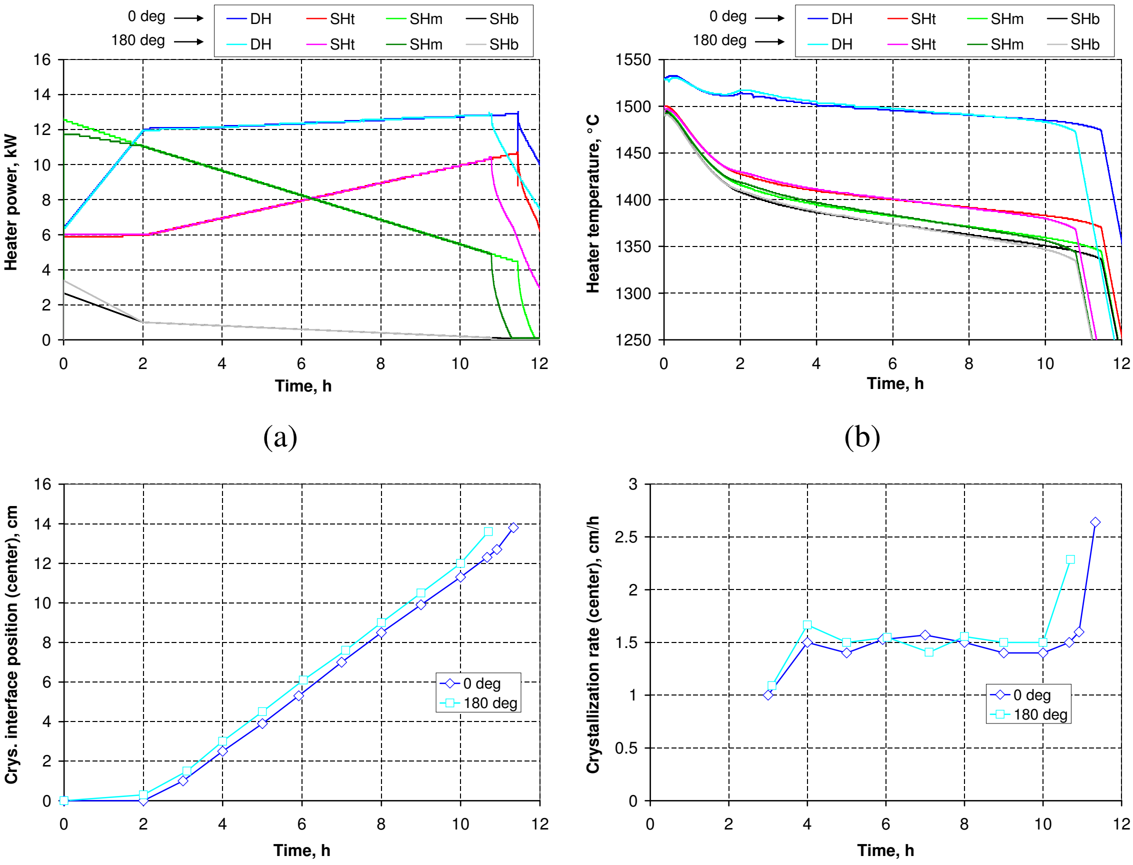

(a) (b)

(c) (d)

Figure 9.14.: Experimental results with phase shifts of 0° and 180°: heater power (a); heater temperature (b), measured position of crystallization interface (c), and calculated crystallization rate (d) during the solidification. The abbreviations DH, SHt, SHm, and SHb denote the top, side-top, side-middle, and side-bottom heater, respectively. [ExpTHMfurnace, 2011]

we may only speculate that the inclusions are related to exceeding the solubility limit as the concentration rapidly increases with a decreasing melt volume (as described by Scheil's equation (2.63)). The melt flow seems to play a significant but not decisive role in this case: there are inclusions in both case, but the area with a high number of inclusions in the vertical cut is significantly smaller for the case with a phase shift of 0° and strong melt mixing. Further analysis of the concentration profiles would be necessary for a better understanding.

The LPS images in Fig. 9.15 (c) show a distinct asymmetry with a higher interface deflection at the side of current supplies in the case with a phase shift of 0°. This effect is not present in the case with 180°, therefore, it can not be caused by the asymmetry of thermal conditions in the furnace (e.g., at the current supplies). It is very likely that the asymmetry in the interface shape is caused by the strong melt flow in the case with a phase shift of 0°. Such effects have been observed in Sec. 8.5 for a downward TMF with a phase shift of 60°. It is possible that due to the higher current concentration in the upper side heaters (see Fig. 9.14 (a)), the phase shift of 0° resembles a downward TMF to some extent. A precise analysis is not possible without a precise magnetic and flow model of the furnace.

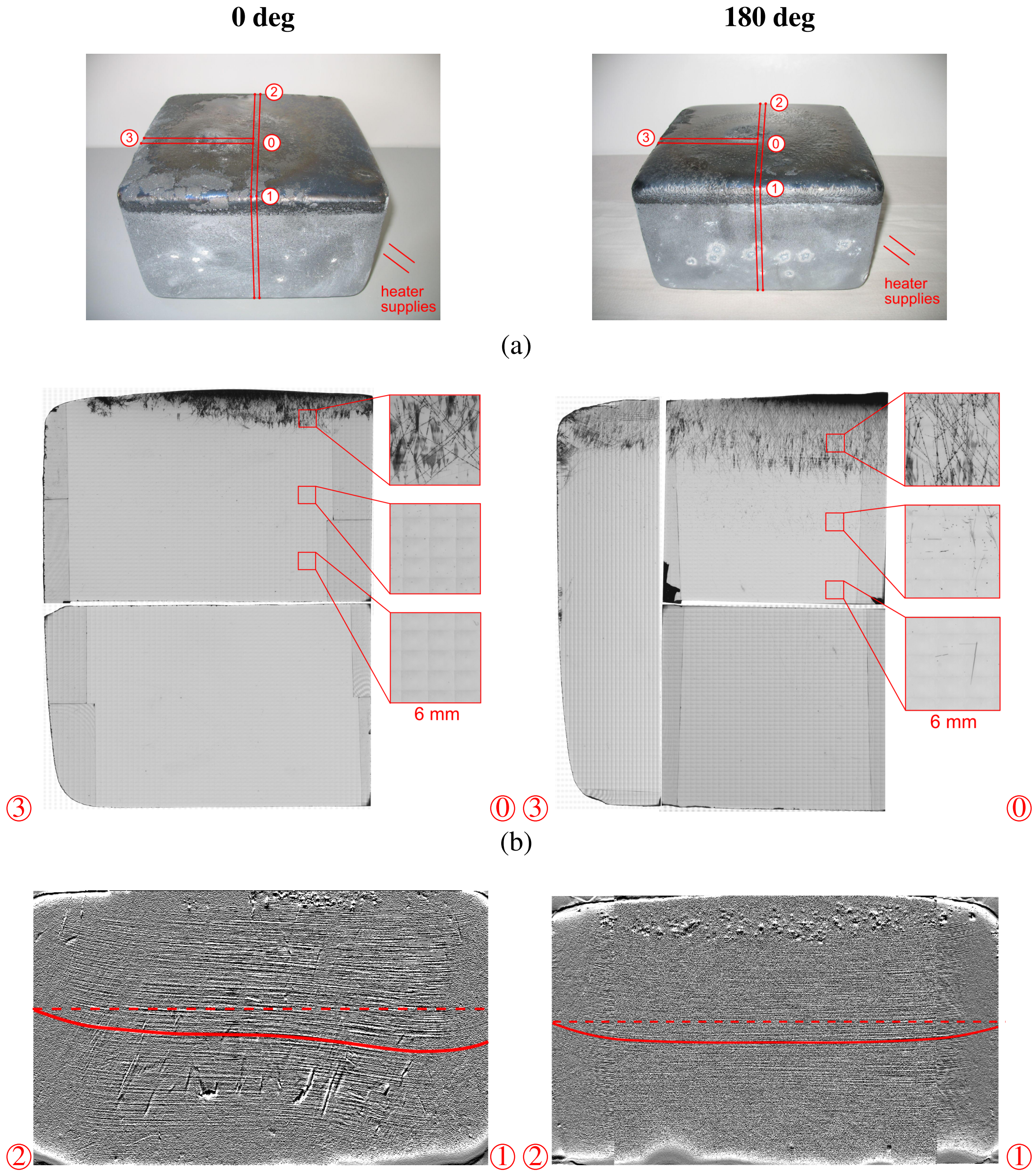

(a)

(b)

(c)

Figure 9.15.: Experimental results with phase shifts of 0° (left) and 180° (right): (a) photo of the ingots showing the cuts for the sample (approx. 3 mm thick) and the position of the current supplies; (b) infrared transmission microscopy image of the sample; (c) lateral photovoltage scanning image of the sample. [ExpTHMfurnace, 2011]

9.5. Discussion

A modified TMF generated by inductors at the melt top or by segmented inductors at the side allows one to obtain other melt flow patterns than the classical TMF torus. Inductors at the melt top tend to generate vertical vortices at the melt top, while secondary horizontal flow structures appear in the bottom part. Theoretically, this flow pattern addresses at least two limitations of the classical TMF discussed at the beginning of this chapter. First, the horizontal vortices at the melt bottom reduce the influence on the crystallization interface and do not limit melt mixing to the skin layer at the melt sides. Second, the vertical vortices at the melt top allow for a mass exchange between the top and bottom parts of the melt, which is important for the evaporation of impurities.

Segmented side inductors allow one to switch off the TMF at several of the four melt sides. This configuration requires higher values of the inductor current to achieve a given Lorentz force density, but large flow vortices extending over the entire melt volume can be generated, reducing the role of the skin effect. Moreover, the flow velocity becomes about 2 times higher. The global vortices tend to cause strong local deformations of the temperature field. However, if the asymmetric configuration is consecutively switched from one melt side to the next one, the temperature field becomes symmetric again, while the mixing of impurities in the segregation boundary layer is enhanced.

The academic models of TMF inductors developed and analyzed in the frame of this work were successfully implemented in a Gen1 furnace for directional solidification of multi crystalline silicon. In particular, the concept with segmented side heaters (the segmentation was not realized in the first stage of construction), a strong Lorentz force, and TMF control using phase shifts between the heaters was selected. First experimental results indicated that the melt flow can significantly influence the interface shape an the amount of impurity inclusions in the crystal. This remains a topic for further experimental research.

Chapter 10

Conclusion

10.1. Summary

A set of **numerical codes** based mainly on the non-commercial open-source libraries `GetDP`, `OpenFOAM`, and `Elmer` has been developed and adapted for three-dimensional simulations of coupled thermal, electromagnetic, and convective phenomena during directional solidification of silicon in time-dependent magnetic fields. All numerical models were verified for numerical correctness by using analytical solutions or well-known benchmark cases.

To validate the physical models, such as a local melt flow influenced by buoyancy and Lorentz forces, a **new experimental setup with a low-melting-point metallic alloy** (GaInSn) in a traveling magnetic field was developed. Direct velocity measurements using ultrasonic techniques were carried out for both isothermal and stably stratified melts up to a size of 10×10×10 cm^3. Despite the relatively large number of experimental uncertainties, such as the exact inductor current or the conditions on melt boundaries, the simulated velocity and temperature fields generally showed a good agreement with the measurements. Consequently, unsteady three-dimensional flow calculations on relatively rough grids are able to model turbulent flows in traveling magnetic fields also without explicit turbulence models, provided that grid sensitivity of the relevant results is routinely checked. Grid-independent time-average flow quantities could be obtained on grids with the number of elements of about 10^5 for Reynolds numbers up to at least 16000.

The complementary use of model experiments and numerical simulations allowed detailed insights into the **flow structures induced by a traveling magnetic field in a square melt**. The melt height, which crosses a wide range during the directional solidification, plays a decisive role: at a height-to-width ratio of 0.25, the typical torus is constrained to the rim and arbitrary rotation appears in the central part; at a ratio of 1.0, a distinct three-dimensional asymmetry appears also in a geometrically symmetric system. These effects are present in both isothermal and non-isothermal melt, but an additional vertical temperature gradient introduces new threshold phenomena. At low Lorentz force densities, the buoyancy forces damp all vertical melt motion and tend to form horizontal vortex structures. At high Lorentz force densities, the temperature field is mixed and the role of buoyancy forces becomes negligible.

Using the verified and validated numerical tools, several comprehensive parameter studies were carried out for the application of a traveling magnetic field to directional solidification of silicon. A simplified **global thermal model of a crystallization furnace** showed that mainly the thermal conductivities of the silicon and the crucible as well as the heating and cooling powers determine the temperature gradients in the melt and the crystallization interface. A vertical temperature gradient of 1 K/cm, a radial temperature gradient of 0.1 K/cm, and a crystallization velocity of 1 cm/h can be selected as typical values for a Generation 1 furnace.

A simplified **electromagnetic model** that consists of a melt surrounded by 3 phase-shifted inductors at the side can be approximated well by an idealized traveling magnetic field wave, which enables a fundamental analytical understanding. The analysis clearly shows that an increase of the melt width or of the current frequency reduces the vertical Lorentz force component and thus the efficiency of the traveling magnetic field. With realistic inductor parameters, a Lorentz force angle with the horizontal plane of about 30° and a maximum force density of about 15 N/m^3 can be reached in a Generation 1 melt. A similar Lorentz force distribution in a larger melt would require a complex adjustment of the current frequency, amplitude, and phase shift as a minimum. The square geometry of the melt leads to smaller Lorentz force densities in the corners, so that axisymmetric models generally work well if such three-dimensional features as the current supplies have a small influence.

The **combination of a Lorentz force** density of 15 N/m^3 **and a vertical temperature gradient** of 1 K/cm **in a Generation 1 melt** leads to an unsteady flow with a typical velocity of 0.6 cm/s and still a strong effect of the buoyancy. The temperature isolines are visibly deformed by the flow, and the influence on the deflection of the crystallization interface is up to about 8 mm. Nevertheless, this relatively weak flow is able to stir the distribution of such impurities as carbon and nitrogen, so that the bulk conditions correspond nearly to the analytical limit of a complete melt mixing. Mainly the impurity distribution along the crystallization interface still shows some sensitivity to the exact details of the velocity field. An increase of the force density by about a factor of 2 puts the flow into a regime dominated by the Lorentz forces, which is followed by a distinct increase of the interface deflection to 2 cm. The relatively small asymmetry caused by the current supplies in the Lorentz force distribution leads to a very asymmetric interface shape in case of a downward traveling magnetic field. An upward traveling field does not show such effects and also is able to transport the impurities to the more favorable location at the melt rim over both a concave and a convex crystallization interface. The melt flow at high Lorentz force densities exhibits large oscillations of the temperature and concentration gradients at the interface, which may cause constitutional supercooling despite of the strong melt mixing effect.

A further numerical study indicated that the **modification of the classical inductor geometry** by splitting each side inductor into 4 separate segments gives significantly more freedom in the choice of the melt flow pattern beyond the classical toroidal structure. An asymmetric magnetic field configuration is able to enhance the mixing of impurities, while a periodic rotation of the asymmetry along the melt sides symmetrizes the impact on the crystallization interface. This novel inductor geometry together with the results from various numerical studies was applied in the **concept of a research-scale furnace**. Another novel approach has been developed for the coupling of the magnetic field inductors with heaters inside the furnace. The control of the magnetic field is achieved by changing the phase shift between the heaters, which allows for a relatively simple 50 Hz power source. A much more complex power supply with superimposed direct and alternating current components would still have a limited decoupling of the heating and the magnetic field due to the Joulean heating by the alternating component. First solidified multicrystalline silicon ingots still require further characterization, but they seem to confirm several conclusions from the numerical studies: a strong melt mixing can reduce the amount of inclusions in the crystal, but it may also have a large and asymmetric influence on the interface shape.

10.2. Outlook

The **numerical models** developed in the present work can be adjusted to match the exact geometry and process conditions of the new crystallization furnace. A global thermal model in 2D or 3D requires exact dimensions of the relevant furnace parts as well as the corresponding thermal properties of the materials for both heat conduction and radiation. In practice, these values are known only to a limited extend or to a limited precision, and a comprehensive calibration of the model must be carried out by comparing calculations and experimental measurements. Furthermore, various approximations for boundary conditions are required to represent, e.g., convective cooling in the furnace. A better agreement with reality can be expected in Lorentz force calculations, where only a few furnace parts and material properties need to be considered. However, the importance of precise data for the inductor current and eventually of an optimal harmonic approximation for time-dependent signals should not be underestimated. Finally, a local coupled model of melt flow and crystallization has the main challenge in setting the local boundary conditions. Heat fluxes or ambient temperatures for heat radiation on the surfaces of melt and crystal can be extracted from global thermal calculations.

The present work indicates two main problems to be addressed in further **model development**. First, fully coupled three-dimensional calculations over large time intervals are very time-consuming due to the high temporal resolution required in the flow calculation in particular. Various approximations were discussed in this work; these results could contribute to more efficient algorithms with regard to computing power. An efficient parallelization of the algorithms needs a special attention. An open question remains the possibility of a partial decoupling between the unsteady melt flow and the unsteady movement of the crystallization interface in numerical calculations. For example, the convective heat fluxes at the interface could be averaged over short time intervals and then applied in the interface calculation over much larger time intervals. The applicability of such approaches is related to the second question requiring further attention. In the numerical modeling of turbulence, a working approach could be found in this work. However, a physical analysis of the role of turbulence and of the turbulent flow structures as well as a reliable and efficient turbulence model for the present system are still open.

Model experiments with liquid metals with a low melting point could be developed in at least two directions in the future. First, velocity measurements in model melts should be extended to allow simultaneous measurements of several profiles in 2D or 3D, which would allow a better analysis of complex flow structures. Simultaneously, the precision of unsteady measurements and signal distortions near the walls should be investigated and improved. These aspects are especially important to analyze the flow properties in the turbulent regime. The second future direction could address a better agreement between the conditions in model experiments and real crystallization processes. In addition to a more precise transfer of melt and inductor geometries, non-isothermal model experiments could be extended to include a solidification process (e.g., with pure gallium). This could open a new perspective in the software validation and in the development of physical understanding through the use of model experiments. Finally, a careful determination of all setup parameters, such as current amplitude, thermal boundary conditions, etc., remains an important topic for a successful application of model experiments.

The silicon ingots already produced in the new crystallization furnace need to be analyzed further by using various methods of **characterization**. The concentration of such impurities as carbon, oxygen, or nitrogen can be measured by using the Fourier transformation infrared spectroscopy methods and could reveal effects of the melt flow for different melt heights during the crystallization. The analysis of concentration distributions in the horizontal plane (combined with measurements of the crystallization interface shape) could hint at the melt flow pattern near the interface. More information about the **conditions during the crystallization** is of equal importance to investigate the role of melt flow. Temperature measurements on the melt surface and in the melt would provide more information about the actual temperature gradients in the melt. Direct velocity measurements in liquid silicon might become possible in the future.

Another aspect to be addressed in further **crystallization experiments** is the design of the process to allow a better comparison and determination of the exact role of the melt flow. An indispensable tool in such studies is numerical simulation which allows one to virtually switch on and off various phenomena. It must be emphasized that experiments and simulations do not substitute but rather support each other. Flow phenomena at small or large aspect ratios in the model experiments first manifested themselves simply as unexpected deviations from the numerical results; only a closer analysis in both simulations and experiments enabled the discovery of previously unknown flow structures. A practical example in the design of experiments is the choice between temperature-controlled and power-controlled heaters. It is not obvious which case allows different flow conditions to cause, for example, larger differences in the interface shape.

A significant theoretical effort in the present work has been put into the formulation of **scaling laws** to transfer various phenomena related to the melt flow between different parameter ranges, especially different geometric dimensions. Although a precise up-scaling is often limited by the high exponents in the scaling laws and by the same parameters in different dimensionless numbers, the Lorentz-force-dominated flow regime could be transferred to 2…8 times larger systems in a realistic way. The up-scaling of the coupled phenomena of melt flow, crystallization interface, and species transport in the melt is also theoretically possible in this flow regime. Approximate scaling of the Lorentz force distribution could be applied to avoid the requirement for a perfect geometric similarity of the inductors. This approach would allow the transfer of the optimized flow conditions from the new research-scale furnace to the industry.

Appendix A

Abbreviations and notation

Abbreviation	Meaning
AC	Alternating current
AMF	Alternating magnetic field
a.u.	arbitrary units
CAD	Computer aided design
CDS	Central differencing scheme
CV	Control volume
CZ	Czochralski
DC	Direct current
DNS	Direct numerical simulation
DS	Directional solidification
EM	Electromagnetic
FEM	Finite element method
FTIR	Fourier transformation infrared spectroscopy
FVM	Finite volume method
GUI	Graphical user interface
Gen1,2...	Generation of mc-silicon ingot size (width)
IR-TM	Infrared transmission microscopy
LES	Large eddy simulation
LPS	Lateral photovoltage scanning
MHD	Magnetohydrodynamic
mc-Si	Multicrystalline silicon
nD	n-dimensional
PV	Photovoltaic
QUICK	Quadratic upwind interpolation for convective kinetics
PISO	Pressure-implicit split-operator
RANS	Reynolds averaged Navier Stokes
RMF	Rotating magnetic field
SIMPLE	Semi-implicit method for pressure-linked equations
TMF	Traveling magnetic field
UDS	Upwind differencing scheme
UDV	Ultrasonic Doppler velocimetry
VGF	Vertical gradient freeze

Table A.1.: Abbreviations.

Table A.2.: Symbols used globally in the current work. Denotations introduced and used in the text only locally are not listed.

Symbol	Meaning	Units
Δ	Laplace operator	
div	Divergence operator	
grad	Gradient operator	
$i = \sqrt{-1}$	Imaginary unit	
$\mathfrak{Im}$	Imaginary part	
$\mathfrak{Re}$	Real part	
rot	Curl operator	
$\times$	Vector product	
$g = 9.81$	Gravitational acceleration	[m/s^2]
$\mu_0 = 4\pi \cdot 10^{-7}$	Magnetic constant	[T/mA]
$\sigma_{sb} = 5.67 \cdot 10^{-8}$	Stefan-Boltzmann constant	[W/m^{2}K^4]
$\vec{A}$	Magnetic vector potential	[Tm]
$\vec{B}$	Magnetic induction	[T]
C	Species concentration	e.g. [atoms/cm^3]
$\vec{E}$	Electric field intensity	[V/m]
$\vec{F}_L$	Lorentz force density	[N/m^3]
H_e	Enthalpy	[J/m^3]
h_e	Specific enthalpy	[J/kg]
$\vec{j}$	Current density	[A/m^2]
p	Pressure	[Pa]
Q	Heat flux	[W]
q	Heat flux density	[W/m^2]
T	Temperature	[K], [°C]
t	Time	[s]
$\vec{u}$	Flow velocity	[m/s]
$v_{\sqcup}$	Crystallization velocity	[m/s]
V	Electric scalar potential	[V]
x, y, z, r	Coordinates	[m]
H	Melt height	[m]
I_0	Inductor current amplitude	[A]
f	Frequency	[Hz]
L	Melt width	[m]
R	(Melt) radius	[m]
α	TMF wave number	[rad/m]
δ_{TMF}	Skin depth of TMF-induced Lorentz force	[m]
δ_{em}	Skin depth of magnetic field	[m]
$\omega = 2\pi f$	Angular frequency	[rad/s]
φ	Force angle	[deg]
ϕ	Phase shift or angle	[deg]
c	Specific heat capacity	[J/kgK]
D	Diffusion coeff.	[m^2/s]
k_0	Segregation coeff.	[–]

Continued on next page

Continued from previous page

Ma	Marangoni coeff.	[N/mK]
Q_l	Latent heat	[J/kg]
T_m	Melting point	[K]
β	Thermal expansion coeff.	[1/K]
ε	Emissivity	[–]
η	Dynamic viscosity	[Pas]
ν	Kinematic viscosity	[m^2/s]
λ	Thermal conductivity	[W/mK]
μ	Magnetic permeability	[–]
ρ	Density	[kg/m^3]
σ	Electrical conductivity	[S/m]
Co	Courant parameter	[–]
F_{em}	Forcing parameter for Lorentz force	[–]
Gr	Grashof number	[–]
Pe	Peclet number	[–]
Pe_S	Solutal Peclet number	[–]
Pr	Prandtl number	[–]
Re	Reynolds number	[–]
Rm	Magnetic Reynolds number	[–]
S_{em}	Shielding parameter for electromagnetic field	[–]

Appendix B

Material data used in numerical simulations

Material properties used in this work are compared to updated literature data in Tab. B.1 for GaInSn and in Tab. B.2 for solid and liquid silicon. Significant deviations exceeding 50% occur for electrical conductivity of solid silicon. However, this value was used only to justify the approximation of neglecting eddy currents in solid silicon in electromagnetic problems. This assumption still holds for the updated material data. Tab. B.3 contains material data for impurity diffusion in liquid silicon.

Property	Symb.	This work	Literature update	Dev., % (20°C)	Dev., % (50°C)
Melting point, °C	T_m		10.5		
Density, kg/m^3	ρ	6360	$6372 - 0.44T$ (25…200 °C)	–0.05	+0.16
Viscosity, Pa·s	η	$2.16\cdot 10^{-3}$	$10^{-6}\rho(0.3853-\frac{1.926}{10^3}T+\frac{3.2686}{10^6}T^2)$ (25…200 °C)	–2	+14
El. conductivity, S/m	σ	$3.2\cdot 10^6$	$10^6(3.4882-\frac{9.32}{10^3}T+\frac{13.933}{10^6}T^2)$ (20…200 °C)	–3	+4.7
Therm. conductivity, W/mK	λ	39	39 (100°C)	0	0
Heat capacity, J/kgK	c	361	$368.01-\frac{110}{10^3}T+\frac{6.67}{10^6}T^2$ (25…200 °C)	–1.3	–0.4
Therm. expansion coeff., 1/K	β	$1.32\cdot 10^{-4}$			

Table B.1.: Physical properties of liquid GaInSn ($Ga^{68}In^{20}Sn^{12}$). Last two columns show the deviation of values used in the current work from updated literature data [Müller and Bühler, 2001] at two different temperatures.

Property	Symb.	This work	Literature update	Dev., % (T_{min})	Dev., % (T_{max})
Solid					
Density, kg/m^3	ρ_S	2329	2330	0	0
El. conductivity, S/m	σ_S	$5 \cdot 10^4$	$10^2 \cdot 10^{4.247-2924/T}$ (T>500 K)	+674	+54
Therm. conductivity, W/mK	λ_S	22	$22.2 + 422 \cdot 10^{-T/588}$ (300…1685 K)	–16	–3
Heat capacity, J/kgK	c_S	986	$23.698 + \frac{3.305}{10^3}T - \frac{4.354}{10^5}T^{-2}$ (300…1685 K)	+1.2	–5
Therm. expansion coeff., 1/K	β_S		$10^{-6}(-15.2459 + 3.43026 \ln T - \frac{5.394}{10^3}T + \frac{1.286}{10^6}T^2 - 88.6853T^{-1})$ (100…1400 K)		
Emissivity	ε_S	0.5	0.46	+9	+9
Melting point, K	T_m	1685			
Latent heat, J/kg	Q_l	$1.8 \cdot 10^6$	$1.8 \cdot 10^6$	0	0
Liquid					
Density, kg/m^3	ρ_L	2520	2560	–1.6	–1.6
Viscosity, Pa·s	η	$7.6 \cdot 10^{-4}$	$10^{-3} \cdot 10^{-0.727+819/T}$	+32	+35
El. conductivity, S/m	σ_L	$1 \cdot 10^6$	$1.39 \cdot 10^6$	–28	–28
Therm. conductivity, W/mK	λ_L	67	62	+8	+8
Heat capacity, J/kgK	c_L	986	1004	–1.8	–1.8
Therm. expansion coeff., 1/K	β_L	$1.44 \cdot 10^{-4}$	$1.03 \cdot 10^{-4}$	+40	+40
Emissivity	ε_L	0.2	0.25	–20	–20

Table B.2.: Physical properties of solid and liquid silicon. Last two columns show the deviations of values used in the current work from updated literature data: mainly recommended vales from [Hibiya et al., 2008] with estimations of temperature-dependencies after [Kimura and Terashima, 1997]; σ_S (intrinsic) from [Fulkerson et al., 1968]; λ_S (fit) from [Glassbrenner and Slack, 1964]; c_S and β_S from [Glazov and Pashinkin, 2001]. Temperature interval $T_{min} \ldots T_{max}$ is assumed 1200…1685 K for solid and 1685…1720 K for liquid silicon.

Impurity	D, m^2/s	k_0
Carbon	$2 \cdot 10^{-8}$	0.07
Nitrogen	$3.6 \cdot 10^{-8}$	0.0007
Oxygen	$4.1 \cdot 10^{-8}$	1.25

Table B.3.: Diffusion coefficient D and segregation coefficient k_0 for various impurities in liquid silicon [Reimann, 2010].

Appendix C

Derivations

C.1. Analytical 2D approximation for a TMF[1]

An idealized TMF with a magnetic induction amplitude B_0, wave number α, and cyclic frequency ω induces in a semi-infinite conducting body (at $x > 0$) with an electrical conductivity σ the following Lorentz force distribution [Krumin, 1983]:

$$F_{Lx} = -\frac{\omega\sigma B_0^2}{2}\mathfrak{Im}\left[\frac{\exp[-(\gamma+\gamma^*)x]}{\gamma}\right], \quad F_{Lz} = \frac{\alpha\omega\sigma B_0^2}{2|\gamma|^2}\exp[-(\gamma+\gamma^*)x], \tag{C.1}$$

where $\gamma = \sqrt{\alpha^2 + i\sigma\mu_0\omega}$ and γ^* denotes the complex conjugate. The complex square root γ can be written in an algebraic from as

$$\gamma = \frac{1}{\sqrt{2}}\sqrt{\sqrt{\alpha^4+(\sigma\mu_0\omega)^2}+\alpha^2} + i\frac{1}{\sqrt{2}}\sqrt{\sqrt{\alpha^4+(\sigma\mu_0\omega)^2}-\alpha^2}. \tag{C.2}$$

Let us consider two limiting cases for the wave number α and the value $\delta_{em}^2 = 2/\sigma\mu_0\omega$:

$$\alpha \ll \frac{\sqrt{2}}{\delta_{em}} \quad\Rightarrow\quad \gamma = \frac{1}{\delta_{em}}(1+i), \quad \gamma+\gamma^* = \frac{2}{\delta_{em}}, \quad \mathfrak{Im}\frac{1}{\gamma} = -\frac{\delta_{em}}{2}, \quad |\gamma|^2 = \frac{2}{\delta_{em}^2} \tag{C.3}$$

$$\alpha \gg \frac{\sqrt{2}}{\delta_{em}} \quad\Rightarrow\quad \gamma = \alpha, \quad \gamma+\gamma^* = 2\alpha, \quad Im\frac{1}{\gamma} = 0, \quad |\gamma|^2 = \alpha^2 \tag{C.4}$$

We obtain for the force components:

$$\alpha \ll \frac{\sqrt{2}}{\delta_{em}} \quad\Rightarrow\quad F_{Lx} = \frac{B_0^2}{2\mu_0}\frac{1}{\delta_{em}}\cdot\exp(-2x/\delta_{em}), \quad F_{Lz} = \frac{B_0^2}{2\mu_0}\alpha\cdot\exp(-2x/\delta_{em}); \tag{C.5}$$

$$\alpha \gg \frac{\sqrt{2}}{\delta_{em}} \quad\Rightarrow\quad F_{Lx} = 0, \quad F_{Lz} = \frac{B_0^2}{2\mu_0}\frac{2}{\alpha}\frac{1}{\delta_{em}}\cdot\exp(-2\alpha x). \tag{C.6}$$

From the exponential dependence, we obtain the skin depth of the Lorentz force for both cases:

$$\alpha \ll \frac{\sqrt{2}}{\delta_{em}} \quad\Rightarrow\quad \delta_{\mathrm{TMF}} = 0.5\delta_{em}, \quad \alpha \gg \frac{\sqrt{2}}{\delta_{em}} \quad\Rightarrow\quad \delta_{\mathrm{TMF}} = 0.5/\alpha. \tag{C.7}$$

---

[1] See Sec. 2.1.5 for a physical background and further details.

In the first case, the quantity δ_{em} obtains a physical interpretation as the double skin depth of the Lorentz force induced by a TMF.

C.2. Scheil's law extended by an additional evaporation term[2]

We consider the mass balance of impurities in a finite melt volume with a height H and cross section S. The concentration is assumed constant in the entire melt, e.g., due to an intensive melt stirring. At the bottom, solidification with a velocity v_g is considered. During a time interval Δt, a melt layer of thickness $\Delta x = v_g \Delta t$ is solidified. If the net mass of impurities in this layer is $C\Delta x S$, then an amount $k_0 C \Delta x S$ leaves the melt according to the segregation law.

On the top boundary of the melt, we assume a mass exchange according to a Poincare-type boundary condition

$$D\frac{dC}{dx} = p_C(C - C_{ref}), \tag{C.8}$$

where the expression on the right-hand side can be interpreted as the amount of impurities removed from the melt (if $p_C < 0$ and $C > C_{ref}$) per time interval Δt and area S according to Fick's law. Now we can calculate the mass of impurities in the melt for two consecutive time instants t and $t + \Delta t$ as

$$C|_t \cdot S \cdot H|_t = M_0, \quad C|_{t+\Delta t} \cdot S \cdot H|_{t+\Delta t} = M_0 + p_C(C|_t - C_{ref})\Delta t \cdot S - k_0 C|_t v_g \Delta t \cdot S \tag{C.9}$$

and obtain a differential equation

$$\begin{aligned} &\frac{C|_{t+\Delta t} \cdot H|_{t+\Delta t} - C|_t \cdot H|_t}{\Delta t} = p_C(C|_t - C_{ref}) - k_0 C|_t v_g \quad \Rightarrow \\ &\frac{d(C \cdot H)}{dt} = p_C(C - C_{ref}) - k_0 C v_g. \end{aligned} \tag{C.10}$$

Using the chain rule and the definition $H = H_0 - v_g t$ we arrive at

$$(H_0 - v_g t)\frac{dC}{dt} = p_C(C - C_{ref}) - k_0 C v_g + v_g C \equiv Ca + b, \tag{C.11}$$

where temporary designations a and b vere introduced. This differential equation can be solved by separation of variables and integration:

$$\ln|Ca + b| = \frac{a}{-v_g}\ln|H_0 - v_g t| + \ln K, \quad a \neq 0 \tag{C.12}$$

where $\ln K$ is an integration constant. With $H_0 - v_g t > 0$, we can rewrite the expression as

$$|Ca + b| = K(H_0 - v_g t)^{-a/v_g}. \tag{C.13}$$

The constant K follows from the condition $C|_{t=0} = C_0$. Finally, after expanding a and b, we

---

[2] See Sec. 2.3.2.1 for a physical background and Sec. 8.5.2 for an application example.

obtain:

$$\frac{C[p_C + v_g(1-k_0)] - p_C C_{ref}}{C_0[p_C + v_g(1-k_0)] - p_C C_{ref}} = \left(1 - \frac{v_g t}{H_0}\right)^{-p_C/v_g - 1 + k_0}, \tag{C.14}$$

where the modulus can be dropped because $Ca + b$ cannot change its sign with time. With $p_C = 0$, this corresponds to Scheil's law. We excluded in eq. (C.12) the case $a = 0$ or $p_C = -v_g(1-k_0)$. This case is described by a degenerate form of (C.11) that can be solved in an identical manner and leads to

$$C = C_0 + \frac{p_C C_{ref}}{v_g} \ln\left(1 - \frac{v_g t}{H_0}\right). \tag{C.15}$$

The mass of impurities built into the crystal in the case of Scheil's equation is simply $C_0 H_0$; this value is equal to the initial mass in the melt because the system is closed. For the case with evaporation described by eq. (C.14), the mass can be calculated by integration:

$$M_{crys} = k_0 \int_0^{H_0} C(x)\,dx = -k_0 \frac{b}{a} + k_0 \left(C_0 + \frac{b}{a}\right) \frac{H_0}{1 - a/v_g}, \tag{C.16}$$

where $x = v_g t$, $a = p_C + v_g(1-k_0)$, and $b = -p_C C_{ref}$. For the case with $C_{ref} = 0$, a simple expression can be obtained for the mass evaporated from the melt:

$$M_{evap} = C_0 H_0 - M_{crys} = -C_0 H_0 \frac{p_C}{k_0 v_g - p_C}. \tag{C.17}$$

C.3. Analytical solution for heat radiation between two spherical shells[3]

We consider two spherical shells with a common origin. The inner shell is located between $r_{hi} \ldots r_{ho}$ and acts as a heater; it has a uniformly distributed volume heat source P [W], thermal conductivity λ_h, and surface emissivity ε_h. The outer shell acts is located between $r_{ii} \ldots r_{io}$ and acts as an insulation; it has a thermal conductivity λ_i and surface emissivity ε_i. The boundary condition on the outer surface is

$$\frac{\partial T}{\partial r} = \sigma_{sb} \varepsilon_i (T^4 - T_a^4), \tag{C.18}$$

where T_a is the ambient temperature. In the cavity enclosed by the inner shell and in the cavity between both shells, heat exchange occurs only by radiation. The steady-state radial temperature distribution can be calculated consecutively as summarized below.

(1) The temperature on the outer surface of insulation follows from the heat balance with the radiation to the ambient:

$$P = \sigma_{sb} \varepsilon_i (T_{io}^4 - T_a^4) \cdot 4\pi r_{io}^2 \quad \Rightarrow \quad T_{io} = \left[\frac{P}{\sigma_{sb} \varepsilon_i 4\pi r_{io}^2} + T_a^4\right]^{1/4}. \tag{C.19}$$

---

[3] See Sec. 3.4.2.1 for an application example.

(2) Heat conduction in the insulation is described by the heat equation in spherical coordinates, which can be solved in a general form as [Baehr and Stephan, 2010, Ch. 2]:

$$\frac{1}{r^2}\frac{\partial}{\partial r}\left(r^2\lambda\frac{\partial T}{\partial r}\right)+Q=0 \quad \Rightarrow \quad \frac{\partial T}{\partial r}=-\frac{Q}{\lambda}\frac{r}{3}-\frac{a}{r^2}, \quad T(r)=-\frac{Q}{\lambda}\frac{1}{3}\frac{r^2}{2}+\frac{a}{r}+b, \tag{C.20}$$

where a, b are arbitrary constants and $Q=P/V$ is the power density per volume. In the insulation, $Q=0$ and the temperature distribution can be calculated by using the known temperature T_{io} and the temperature gradient on the outer surface:

$$\lambda_i 4\pi r_{io}^2\left.\frac{\partial T}{\partial r}\right|_{r=r_{io}}=-P \quad \Rightarrow \quad T_i(r)=T_{io}+\frac{P}{4\pi\lambda_i}\left[\frac{1}{r}-\frac{1}{r_{io}}\right], \tag{C.21}$$

where an equilibrium condition is assumed: the heat generated in the heater is radiated at the outer surface of the insulation. The temperature on the inner surface of insulation T_{ii} follows with $r=r_{ii}$.

(3) The temperature on the outer surface of heater follows from the radiation heat exchange between the heater and the insulation. In a cavity between two spherical surfaces [Baehr and Stephan, 2010, Sec. 5.5.3]:

$$\begin{aligned} &P=\sigma_{sb}\varepsilon_{hi}(T_{ho}^4-T_{ii}^4)\cdot 4\pi r_{ho}^2, \quad \frac{1}{\varepsilon_{hi}}=\frac{1}{\varepsilon_h}+\frac{r_{ho}^2}{r_{ii}^2}\left[\frac{1}{\varepsilon_i}-1\right] \\ &\Rightarrow T_{ho}=\left[\frac{P}{\sigma_{sb}\varepsilon_{hi}4\pi r_{ho}^2}+T_{ii}^4\right]^{1/4}. \end{aligned} \tag{C.22}$$

(4) Temperature distribution in the heater is calculated from the general equation (C.20) with a zero flux boundary condition on the inner surface (in a steady-state, the heat can flow only outward) and with the known temperature on the outer surface:

$$\left.\frac{\partial T}{\partial r}\right|_{r=r_{hi}}=0, \quad T(r_{ho})=T_{ho} \quad \Rightarrow \quad T_h(r)=T_{ho}+\frac{P}{V_h}\frac{1}{3\lambda_h}\left[\frac{r_{ho}^2}{2}-\frac{r^2}{2}+\frac{r_{hi}^3}{r_{ho}}-\frac{r_{hi}^3}{r}\right], \tag{C.23}$$

where the heater volume V_h can be calculated as $4\pi(r_{ho}^3-r_{hi}^3)/3$. The temperature on the inner heater surface follows with $r=r_{hi}$.

Due to the heat flow direction, T_{io} is the minimum temperature and T_{hi} is the maximum temperature in the system.

Appendix D

Software utilities

D.1. Grid generation and interpolation

D.1.1. `Gmsh`

An open source pre- and post-processing tool `Gmsh` [Geuzaine and Remacle, 2009, 2011] was adopted for the generation of 2D and 3D meshes. `Gmsh` comes with a cross-platform graphical user interface (GUI), but all commands can be executed also using scripts in a GEO file. GEO scripts allow one to define loops and user variables and have clear advantages for geometric parameter studies. In this case, one can use the GUI only for commands such as grid generation, optimization, export, etc.

Geometry definition in `Gmsh` follows a bottom–up strategy where points are defined with coordinates and connected into lines, lines are connected into surfaces, and surfaces are connected into volumes. Geometric entities can be grouped together in physical groups according to which the mesh elements are labeled. For 3D geometries with several volumes, this approach of geometry definition becomes relatively complex because no Boolean operations can be automatically performed with solid 3D objects, such as cylinders or cubes. For example, if the geometry contains a small cube within a large cube, the 6 surfaces from the inner cube must be defined as a hole in the outer cube. `Gmsh` can also import solid geometries in exchange formats such as STEP or IGES; however, then an additional CAD tool for the geometry construction is needed. There are several active open source tools, for example, `FreeCAD` [FreeCAD, 2011], but first tests showed that an import into `Gmsh` often leads to geometry errors. Some fragments of GEO files for the geometry in Fig. 3.5 (b):

```
// ---------- sh6.geo: main GEO file (fragments) ----------
// Define all parameters:
hzd = 0.118;

// Include another GEO script (several times)
hz0 = hzm+2.5*hzd-0.5*hh;    n = 300;
Include "sh_circ_closed.geo";

// Define other volumes and, finally, subtract them from the gas volume
Volume(n+27) = {(n+19):(n+24), (300+85):(200+100*hn+85):100, n+26};

// ---------- sh_circ_closed.geo: define the volume of a circular coil (fragments) ----------
// Define points, lines, surfaces, and volumes
Point(n+3) = {hx0+0.5*hlx, hy0-0.5*hly, hz0, hcl};
//...
Circle(n+3) = {n+3,n+33,n+4};
//...
Line Loop(n+53) = {n+3,n+36,-(n+19),-(n+35)};    Ruled Surface(n+69) = {n+53};
//...
Surface Loop(n+85) = { (n+67):(n+76) };    Volume(n+86) = {n+85};
```

The grid element size is given at the node points an then linearly interpolated on further geometric entities. Alternatively, various sizing functions can be defined for each volume (activated by the `Gmsh` option *Mesh.CharacteristicLengthExtendFromBoundary = 0*), but a mix of both strategies currently is not possible. `Gmsh` supports automatic meshing with triangles on surfaces and with tetrahedrons in volumes. Structured meshes can be defined on lines (with additional controls for element size growth; see below), on surfaces, or in volumes using the *Transfinite* algorithm, which is often useful for boundary layers. In this case, meshes of quadrangles and hexahedrons are possible, but the capability to generate a prism layer between tetrahedrons and hexahedrons is currently missing. The generated mesh can be exported to the native MSH format or to several other exchange formats.

The nodes on a line in the *Transfinite* algorithm can be distributed according to a geometric progression, where the element size increases with a growth factor k from the smallest value d_{min} as $d_i = d_{i-1} \cdot k$. The following expressions relate the thickness of the boundary layer d, the number of elements n, and the maximum element size d_{max}:

$$n \approx \frac{\ln\left[1 - \frac{d(1-k)}{d_{min}}\right]}{\ln k}, \quad d = d_{min}\frac{1-k^n}{1-k}, \quad d_{max} = d_{min} \cdot k^{n-1}. \tag{D.1}$$

Usually, the thickness d, the number of elements n, and the growth factor k are specified. For example, the following commands are used to refine the elements at the melt side in Fig. 3.5 (b):

```
BLrn = 6;  BLrmin = 0.001;  BLrg = 1.3;
BLr = BLrmin*(1-BLrg^BLrn)/(1-BLrg);
Transfinite Line{9:12} = BLrn  Using Progression BLrg;
```

D.1.2. `blockMesh`

`blockMesh` [OpenFOAM, 2011] is a simple grid generator included in the open source `OpenFOAM` library. This grid generator is capable of producing structured hexahedral meshes of several 3D blocks. The geometry must be defined with the bottom–up method as in `Gmsh`, but without the possibilities of scripting using user variables, loops, etc. The main advantage lies in the fact that the mesh is saved directly in the `OpenFOAM` mesh format. Therefore, this grid generator is used in this work for simple 3D meshes with a single domain (possibly containing several blocks to allow bi-directional element size grading). To facilitate the preparation of `blockmesh` input files, e.g., for a 3D cylindrical sector (the way in which `OpenFOAM` treats axisymmetric geometries), a small script was developed in Python programming language. In this manner, user variables, mathematical expressions, and loops can be included in the definition of the geometry and the mesh.

Node distribution in x, y, or z directions of a block in the *simpleGrading* algorithm can be described by a geometric progression, where the thickness d, number of elements n, and the ratio between the largest and the smallest element are specified (see (D.1)). The following fragment of a Python script illustrates how the element expansion factors can be calculated and written to a `blockmesh` input file:

```
def BLn(L,m,g):
    if g < float(1.0):
        gg=1.0/g
    else:
        gg=g
    if g == float(1.0):
```

```
        return int(math.ceil(L/m))
    else:
        return int(math.ceil( math.log(1-L*(1-gg)/m)/math.log(gg) ))

BLy1    = float(0.01)
BLy1m   = float(0.0004)
BLy1g   = float(1.2);
BLy1n   = BLn(BLy1,BLy1m,BLy1g)
BLy1gi  = math.pow(BLy1g,BLy1n-1)
# ...

bfile.write( '    hex (28 16 17 29 0 4 5 1) (' + # (0 16 17 1 0 4 5 1)
             str(BLx1n)  + ' ' + str(BLy1n)  + ' ' + str(1) + ') simpleGrading (' +
             str(BLx1gi) + ' ' + str(BLy1gi) + ' ' + str(1) + ')\n' )
```

It should be noted that another grid generator has been recently included into `OpenFOAM` library. The `snappyHexMesh` [OpenFOAM, 2011] tool is unique even in comparison with commercial grid generators because it is capable of generating polyhedral volume meshes “snapped” to surfaces (including a refinement) of an arbitrary 3D geometry. However, it requires an external CAD tool to prepare the geometry and may skip some edges or corners during the snapping process. Therefore, it is not suitable for the geometries in the current work.

D.1.3. `GridGen3D`

One of the most comprehensive software utilities developed in this work is `GridGen3D`. It contains approximately 2000 lines in C++ programming language using procedural style. `GridGen3D` is a command-line tool for grid generation and Lorentz force interpolation for `OpenFOAM` calculations. Main capabilities of `GridGen3D` are as follows:

- Specification of geometry and interpolation parameters in a text file or partially as command-line options.

- Generation of a structured hexahedral grid with a single block and adjustable boundary layers. The grid actually consists of three axes with 1D point distributions (see below). Other steps of grid generation are included in the numbering algorithms for vertices and elements when saving the corresponding 3D grid. The z-coordinate can be deformed to form a deflected bottom surface.

- Lorentz force from a `GetDP` POS file containing a tetrahedral mesh can be imported. It can be averaged over several time steps and/or averaged at the nodes during the import (see Sec. 3.2). The values and the coordinates of the force distribution can be scaled, and the distribution is mapped onto the hexahedral grid using a linear interpolation inside the tetrahedrons (see below).

- Searching procedures for a tetrahedron to which a given point belongs or for a point which has identical coordinates as a given point were optimized by introducing a rough searching grid. A searching grid cell is assigned to each tetrahedron/point and the entities belonging to this cell are checked first. The processing time was significantly decreased in this manner.

- The grid together with the interpolated force distribution is saved to the `OpenFOAM` ASCII format.

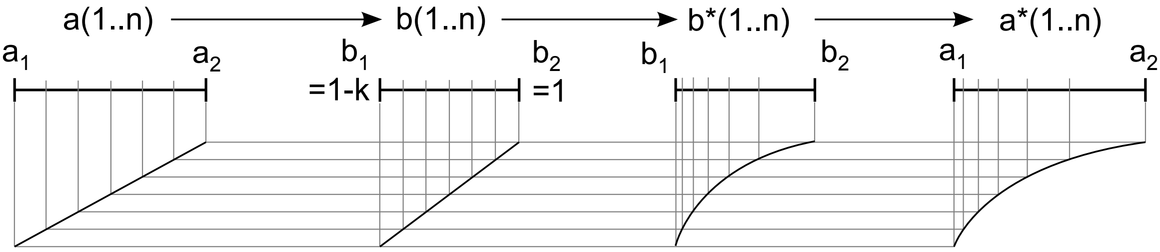

$$b = b_1 + \frac{b_2 - b_1}{a_2 - a_1}(a - a_1)$$

$$b^* = m \cdot b^p + s$$

$$m = \frac{b_2 - b_1}{b_2^p - b_1^p}$$

$$s = b_1 - m \cdot b_1^p$$

$$a^* = a_1 + \frac{a_2 - a_1}{b_2 - b_1}(b^* - b_1)$$

Figure D.1.: Algorithm for the calculation of node coordinates in a boundary layer in `GridGen3D`: transformation of a uniform node distribution $a(1 \ldots n)$ with a power function.

The algorithm for the calculation of node coordinates in a boundary layer is shown in Fig. D.1. The boundary layer thickness $d = a_2 - a_1$, number of elements n, power factor p (usually 3), and size distribution parameter k (usually about 0.7) are required as input parameters. The algorithm is based on a transformation of node coordinates $b(1 \ldots n) \rightarrow b^*(1 \ldots n)$ using a power function $b^* = m \cdot b^p + s$, with constants m and s.

Linear interpolation of a field ψ inside a tetrahedron with nodes 1, 2, 3, and 4 can be written as $\psi(x,y,z) = a + bx + cy + dz$, where the coefficients can be determined by solving a linear system with the known values of ψ_i at the 4 nodes [Jin, 2002, Sec. 5.3.2]. The following expressions are obtained for an arbitrary point p:

$$\begin{aligned}
&\psi(x_p,y_p,z_p) = \psi_1 \cdot N_1 + \psi_2 \cdot N_2 + \psi_3 \cdot N_3 + \psi_4 \cdot N_4 \\
&N_i = (a_i + b_i \cdot x_p + c_i \cdot y_p + d_i \cdot z_p)/6V_e, \quad i = 1,2,3,4 \\
&a_1 = +x_2(y_3 z_4 - y_4 z_3) - x_3(y_2 z_4 - y_4 z_2) + x_4(y_2 z_3 - y_3 z_2) \\
&a_2 = -x_1(y_3 z_4 - y_4 z_3) + x_3(y_1 z_4 - y_4 z_1) - x_4(y_1 z_3 - y_3 z_1) \\
&a_3 = +x_1(y_2 z_4 - y_4 z_2) - x_2(y_1 z_4 - y_4 z_1) + x_4(y_1 z_2 - y_2 z_1) \\
&a_4 = -x_1(y_2 z_3 - y_3 z_2) + x_2(y_1 z_3 - y_3 z_1) - x_3(y_1 z_2 - y_2 z_1) \\
&b_1 = +y_2(z_4 - z_3) - y_3(z_4 - z_2) + y_4(z_3 - z_2) \\
&b_2 = -y_1(z_4 - z_3) + y_3(z_4 - z_1) - y_4(z_3 - z_1) \\
&b_3 = +y_1(z_4 - z_2) - y_2(z_4 - z_1) + y_4(z_2 - z_1) \\
&b_4 = -y_1(z_3 - z_2) + y_2(z_3 - z_1) - y_3(z_2 - z_1) \\
&c_i(y,z,x) \leftarrow b_i(x,y,z) \\
&d_i(z,x,y) \leftarrow b_i(x,y,z)
\end{aligned} \tag{D.2}$$

$V_e = (a_1 + a_2 + a_3 + a_4)/6$ is the volume of the tetrahedron. For a point inside the tetrahedron, all N_i are positive. This condition is used to find the mesh tetrahedron corresponding to an arbitrary point.

D.2. Utilities for electromagnetic calculations

D.2.1. Simplified 3D magnetic field calculation

Realistic three-dimensional inductor geometries can be very complex and contain many electric current elements. Full 3D modeling is not trivial in such cases, especially, if the parts are small but scattered over a relatively large volume. Geometric simplifications may be limited due to phase shifts between the separate inductor parts. In some cases, it may be sufficient only to estimate the resulting magnetic field of an inductor, neglecting eddy currents in the conducting parts. Such a model has been implemented in a command-line utility using the object oriented C++ programming language.

The basic assumption in the model states that all parts of the inductor can be described by thin straight wires with a specified time-dependent current. The geometry is defined in a text file, an automatic description of a circle or several parallel wires is possible. The magnetic field of a single wire follows from the expression for a current length element $d\vec{l}$ [Griffiths, 1999]:

$$d\vec{B} = \frac{\mu_0 I_0 d\vec{l} \times \vec{r}}{4\pi r^3}, \tag{D.3}$$

where I_0 denotes the current in the element and $\vec{r}$ denotes the vector from the current element to the reference point. The magnetic field of the entire wire can be calculated by a simple numerical integration over N wire segments $\vec{dl_i}$:

$$B_x = \frac{\mu_0 I_0}{4\pi} \sum_{i=1}^{N} (dl_y r_{zi} - dl_z r_{yi})/r_i^3, \tag{D.4}$$

$$B_y = \frac{\mu_0 I_0}{4\pi} \sum_{i=1}^{N} (dl_z r_{xi} - dl_x r_{zi})/r_i^3, \tag{D.5}$$

$$B_z = \frac{\mu_0 I_0}{4\pi} \sum_{i=1}^{N} (dl_x r_{yi} - dl_y r_{xi})/r_i^3. \tag{D.6}$$

Alternatively, an analytical expression for the entire wire with a length L can be used (see Tab. D.1):

$$\vec{B} = \frac{\mu_0 I_0}{4\pi} \frac{\cos\gamma_1 - \cos\gamma_2}{d} \frac{\vec{B}^*}{|\vec{B}^*|}, \quad \vec{B}^* = \vec{L} \times \vec{r}_1, \quad \cos\gamma_i = \frac{\vec{r}_i \vec{L}}{|\vec{r}_i||\vec{L}|}, \quad d = \frac{|\vec{B}^*|}{L}, \tag{D.7}$$

where $\vec{r}_{1,2}$ are vectors from both ends of the wire ($\vec{L}$ is directed from 1 to 2) to the reference point and $\gamma_{1,2}$ are the corresponding angles with the wire. The resulting magnetic field of the entire inductor is calculated by a superposition of the fields from the separate wires at chosen reference points. The model was verified using analytical expressions for the magnetic field of an infinitely long or a short wire and for the magnetic field on the axis of a circular loop (see Tab. D.1).

D.2.2. Analytical tools

Several tools on the basis of the office package `Excel` and its programming language Visual Basic have been developed for efficient data analysis and visualization. A simple tool allows the visualization of the time-dependent magnetic field resulting from up to 6 circular coils

Configuration	Sketch	Expression
Short wire	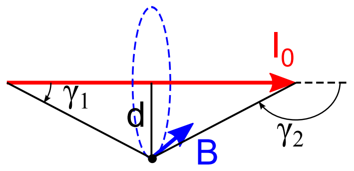	$B = \frac{\mu_0 I_0}{4\pi}\frac{\cos\gamma_1 - \cos\gamma_2}{d}$ (D.8)
Long wire ($\lvert\cos\gamma_{1,2}\rvert \approx 1$)	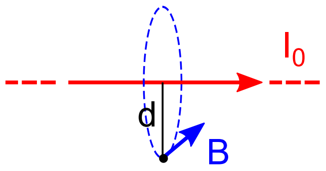	$B = \frac{\mu_0 I_0}{2\pi d}$ (D.9)
Circular loop	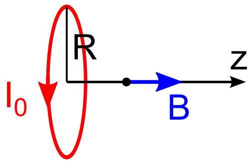	$B = \frac{\mu_0 I_0}{2}\frac{R^2}{(z^2+R^2)^{3/2}}$ (D.10) $B(z=0) = \frac{\mu_0 I_0}{2R}$ (D.11)
Short coil	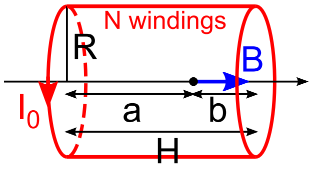	$B = \frac{\mu_0 N I_0}{2H}\left[\frac{a}{\sqrt{a^2+R^2}} + \frac{b}{\sqrt{b^2+R^2}}\right]$ (D.12) $B(a=b) = \frac{\mu_0 N I_0}{\sqrt{H^2+4R^2}}$ (D.13)
Long coil ($H \gg 2R$)	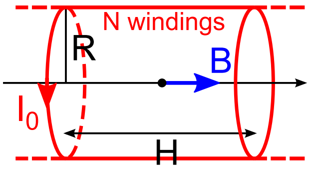	$B = \frac{\mu_0 N I_0}{H}$ (D.14)

Table D.1.: Analytical expressions for the magnetic field in various simple geometries. These expressions can be obtained by integrating the equation D.3. Most cases can be reduced to the integral $\int (a^2+x^2)^{-3/2}dx = \frac{x}{a^2\sqrt{a^2+x^2}}$ [Bronstein et al., 2008, p. 1087].

on their axis. The superposition of the separate fields shows how a TMF wave is formed and moves in dependence of phase shifts and other parameters.

Many analytical solutions including those for a cylinder in a TMF from Sec. 2.1.5 involve non-elementary Bessel functions. These are defined as infinite series and are not trivial to calculate, especially for complex numbers, and the support in `Excel` is very limited. Therefore, a Visual Basic script was developed for calculations of Bessel functions I_0, I_1, K_0, K_1, and their derivatives for complex arguments. They are used further to calculate the Kelvin functions Ber, Bei, Ker, Kei, and their derivatives for real arguments as well as Bessel functions J_0, J_1, Y_0, and Y_1 for complex arguments. The source code is mainly based on Fortran routines in [Zhang and Jin, 2009, mcik01.for] with improved asymptotic expansions for large arguments from [Abramowitz and Stegun, 1972, Sec. 9.7.1, 9.7.2]. The verification was done using the high precision online library [Keisan, 2009].

D.2.3. Various

The main results from a `GetDP` calculation are the magnetic field and Lorentz force density vectors in element centers. Both are constant over the element volume if linear finite elements are used. Therefore, the Lorentz force density is averaged in nodes when interpolating on the grid for flow calculations in `GridGen3D`. Since such averaging is relevant also for other fields, a C++ script has been written partly on the basis of `GridGen3D`. It reads a `GetDP` results file, performs the spatial averaging, and saves the results in the `GetDP` POS format, the `Paraview` VTK format, and also as values in a text file for selected points or lines.

It should be noted that this averaging introduces a numerical error in the Lorentz force density. This is important for the elements at the surface where a force gradient may be present because the space between element midpoints and the actual surface is not resolved in the calculation. Therefore, this region should be meshed carefully.

D.3. Utilities for flow calculations

D.3.1. `OpenFOAM` utilities

Utilities for processing the data from/for `OpenFOAM` are convenient to implement as `OpenFOAM` applications because of the possibility to access `OpenFOAM` data structures. Two simple post-processing utilities were developed. `volumeavr` calculates an volume average of a specified field, such as species concentration. `crysinter` adds a new field to the result files, with the field isolines corresponding to a predefined crystallization interface shape. This allows one to make cuts parallel to a deflected crystallization interface (with various distances from the boundary) in the post-processing with `Paraview`.

A further `OpenFOAM` utility `getdp2Foam` was developed for the interpolation of a 2D Lorentz force distribution from `GetDP` to an axisymmetric or three-dimensional mesh in `OpenFOAM` format. Such a mesh can be generated using `blockMesh` or `Gmsh`. The interpolation is carried out using linear expressions for the triangles of the `GetDP` mesh. The force distribution is rotated around a specified axis on the `OpenFOAM` mesh.

The ultimate result of the growth process – the silicon ingot – is described in the calculation by a time-dependent movement of the crystallization interface, with a definite species distribution for each time instant. The reconstruction of the resulting species distribution for the entire ingot requires an analysis of the fields for many time instants. Due to the high importance of this representation of results, which can be directly compared with experimental measurements, a special C++ command-line utility `conccrystal` has been developed. It takes a specified list of time instants and reads specified concentration fields on the boundary patch in VTK format (they can be written using the `OpenFOAM` `sample` utility). If the mesh points move only vertically, a 2D or 3D field with the resulting distribution can be easily generated. The results are saved in VTK format for `Paraview`.

D.3.2. Calculation of the spectrum of oscillations

The standard Fast Fourier Transform (FFT) is widely used for calculations of a frequency spectrum, but it is strictly applicable only to a signal with a constant time step. This is not always the case and a special class of methods has been developed in the literature, e.g., for applications to fluid dynamics or astrophysics as summarized in the reviews [Babu and

Stoica, 2010; Benedict et al., 2000]. The simplest method is a straightforward numerical integration of a time-function $h(t)$ in the Fourier integral with a non-constant time step to obtain the frequency function $g(\nu)$:

$$h(t) \to |g(\nu)| : \quad g(\nu) = \int_{-\infty}^{\infty} f(t) \exp(-2\pi i \nu t) dt. \tag{D.15}$$

The transform can be easily verified by the inverse transformation that should give the original signal. More advanced algorithms apply special methods to reduce the noise level for a better detection of the characteristic frequencies. The simple Fourier integral (D.15) as well as the algorithm for the Lomb periodogram method from [Press et al., 2007] have been implemented in a command-line C++ utility. Furthermore, a C++ interface has been developed for the `FFTW` library [FFTW, 2011] for FFT with an arbitrary number (not limited to the powers of 2) of data points.

D.4. Utilities for global thermal calculations

For thermal calculations with `Elmer`, only one additional tool was required. To evaluate the exact position of the crystallization interface ($T = T_m$) in dependence of time, the temperature profile on given lines was saved in each time step. A small C++ command-line utility was developed to extract the time-dependence from this data.

D.5. Post-processing

Many utilities for the analysis of calculation results from `GetDP` and `OpenFOAM` have been described in the previous sections. Here, we focus on the graphical visualization, which is an essential part of the evaluation of calculation results. Simple plots are needed for 1D calculations, 2D field distributions for 2D calculations, and usually a set of 2D field distributions for 3D calculations. If we add the time dimension, the amount of data continues to increase significantly. For the preparation of plots, mainly the office package `Excel` and the open source program `Gnuplot` [Gnuplot, 2011] were used in this work. The visualization of fields was carried out by the open source tools `Gmsh` and `Paraview` [ParaView, 2011].

For the number of 3D calculations on the order of 100 performed in this work, a complete evaluation of results requires a significant amount of technical work. Therefore, an automated reporting system has been developed for `OpenFOAM` calculations. It consists of the following main components/steps:

1. The main Python script is executed, which reads a list of calculations containing directory and file names, etc. All calculations are processed consecutively.

2. Main calculation parameters are extracted from the text files in the `OpenFOAM` case directory. These include such parameters as the number of mesh elements, execution time, program version, typical time step, Courant number, etc.

3. The `Paraview` component `pvpython` is called, which allows one to control `Paraview` using Python scripts. Data exchange with the main Python script is implemented using text files. Minimum and maximum values of various fields, such as Lorentz force,

temperature, and velocity, are extracted. Field distributions visualized with isolines or vectors on several 2D cuts and with 3D streamlines are exported to image files.

4. Input files are prepared for the plotting program `Gnuplot`. Then `Gnuplot` is called to generate various plots, such as the time-dependence of temperature, velocity components, or kinetic energy. Additionally, the distributions of Lorentz force, temperature, and velocity are plotted on several pre-defined lines, after automatically calling the `OpenFOAM` `sample` utility. All plots are saved as image files.

5. All generated images and extracted data are embedded in a HTML file. Such a file is generated for each calculation. After the script is finished, a special main HTML file can be opened in a web browser. It contains commands in the HTML and CSS languages, which allow one to browse all calculations and compare several calculations side by side.

Appendix E

Publication of results

E.1. Journal papers

E.1.1. Main publications

K. Dadzis, J. Ehrig, K. Niemietz, O. Pätzold, U. Wunderwald, J. Friedrich. Model experiments and numerical simulations for directional solidification of multicrystalline silicon in a traveling magnetic field. *Journal of Crystal Growth*, 333 (2011) 7–15.

K. Dadzis, J. Ehrig, K. Niemietz, O. Pätzold, U. Wunderwald, J. Friedrich. Non-isothermal model experiments and numerical simulations for directional solidification of multicrystalline silicon in a traveling magnetic field. *Journal of Crystal Growth*, 372 (2013) 145–156.

K. Dadzis, D. Vizman, J. Friedrich. Unsteady coupled 3D calculations of melt flow, interface shape, and species transport for directional solidification of silicon in a traveling magnetic field. *Journal of Crystal Growth*, 367 (2013) 77–87.

E.1.2. Significant contributions from this work

R. Nauber, M. Burger, M. Neumann, L. Büttner, K. Dadzis, K. Niemietz, O. Pätzold, J. Czarske. Dual-plane flow mapping in a liquid-metal model experiment with a square melt in a traveling magnetic field. *Experiments in Fluids*, 54 (2013) 1502.

D. Vizman, K. Dadzis, J. Friedrich. Numerical parameter studies of 3D melt flow and interface shape for directional solidification of silicon in a traveling magnetic field. Submitted to *Journal of Crystal Growth*.

E.2. Patent applications

M. Zschorsch, U. Wunderwald, T. Jung, J. Friedrich, K. Dadzis, G. Radel, J. Stenzenberger. Verfahren und Anordnung zur Beeinflussung der Schmelzkonvektion bei der Herstellung eines Festkörpers aus einer elektrisch leitfähigen Schmelze. Internationale Patentanmeldung WO002011076157A1.

E.3. Conferences

E.3.1. With a proceedings paper

M. Zschorsch, K. Dadzis, U. Wunderwald, T. Jung, J. Friedrich. Bridgman type solidification of multi-crystalline silicon influenced by a travelling magnetic field. In *3rd International Workshop on Crystalline Silicon Solar Cells*, Trondheim, Norway, June 3–5, 2009. Visual presentation.

U. Wunderwald, K. Dadzis, M. Zschorsch, T. Jung, J. Friedrich. Influence of traveling magnetic fields on melt convection during Bridgman type solidification of multi-crystalline silicon. In *24th European Photovoltaic Solar Energy Conference*, Hamburg, Germany, September 21–25, 2009. Oral presentation.

K. Dadzis, M. Zschorsch, U. Wunderwald, T. Jung, J. Friedrich. Use of travelling magnetic fields to influence melt convection during Bridgman type solidification of multi-crystalline silicon for photovoltaic applications. In *6th International Conference on Electromagnetic Processing of Materials*, Dresden, Germany, October 19–23, 2009. Oral presentation.

K. Dadzis, J. Ehrig, K. Niemietz, O. Pätzold, U. Wunderwald, J. Friedrich. Model experiments and numerical simulations for directional solidification in a traveling magnetic field. In *8th PAMIR International Conference on Fundamental and Applied MHD*, Borgo, France, September 5–9, 2011. Oral presentation.

E.3.2. Without a proceedings paper

K. Dadzis, M. Zschorsch, U. Wunderwald, T. Jung, J. Friedrich. Use of travelling magnetic fields to influence melt flow during solidification of multicrystalline solar silicon. In *Freiberger Silicon Days*, Freiberg, Germany, June 17–19, 2009. Oral presentation.

J. Friedrich, K. Dadzis, M. Zschorsch, U. Wunderwald, T. Jung. Traveling magnetic fields in directional solidification of multi-crystalline silicon. In *17th American Conference on Crystal Growth and Epitaxy*, Lake Geneva, U.S., August 9–14, 2009. Oral presentation.

U. Wunderwald, K. Dadzis, M. Zschorsch, T. Jung, J. Friedrich. Influence of traveling magnetic fields on melt convection in large melt volumes: time-dependent 3D simulation. In *DGKK Arbeitskreis – Massive Verbindungshalbleiter*, Freiberg, Germany, October 7–8, 2009. Oral presentation.

U. Wunderwald, K. Dadzis, M. Zschorsch, T. Jung, J. Friedrich. Use of magnetic fields to improve crystallization process during directional solidification of multi-crystalline silicon for photovoltaic applications. In *5. Silicon Saxony Day: Forum Photovoltaik*, Dresden, Germany, May 19, 2010. Oral presentation.

K. Dadzis, U. Wunderwald, M. Zschorsch, J. Friedrich. Melt flow and species distribution in directional solidification of large multi-crystalline silicon ingots with a traveling magnetic field. In *25th European Photovoltaic Solar Energy Conference*, Valencia, Spain, September 6–10, 2010. Visual presentation.

D. Vizman, K. Dadzis, J. Friedrich. Three dimensional modeling of melt flow and solid-liquid interface in directional solidification process under the influence of traveling magnetic fields. In *German Polish Conference on Crystal Growth*, Frankfurt (Oder)/ Slubice, March 14–18, 2011. Visual presentation.

K. Dadzis, J. Ehrig, K. Niemietz, O. Pätzold, U. Wunderwald, J. Friedrich. Model experiments and numerical simulations for directional solidification in a traveling magnetic field. In *DGKK Arbeitskreis – Herstellung und Charakterisierung von massiven Halbleitern*, Erlangen, Germany, October 5–6, 2011. Oral presentation.

K. Dadzis, J. Ehrig, K. Niemietz, O. Pätzold, U. Wunderwald, J. Friedrich. Model experiments and scaling laws for directional solidification of silicon in a traveling magnetic field. In *DGKK Jahrestagung*, Freiberg, Germany, March 7–9, 2012. Visual presentation.

K. Niemietz, O. Pätzold, M. Stelter, K. Dadzis, U. Wunderwald, J. Friedrich. Model experiments and numerical simulation for directional solidification of silicon in a traveling magnetic field In *4th European Conference on Crystal Growth*, Glasgow, Scotland, June 17–20, 2012. Visual presentation.

K. Niemietz, K. Dadzis, R. Nauber, M. Burger, O. Pätzold, U. Wunderwald, J. Czarske, J. Friedrich. Experimental and numerical modeling of melt flow for directional solidification of multicrystalline silicon in a travelling magnetic field. In *7th International Workshop on Modeling in Crystal Growth*, Taipei, Taiwan, October 28–31, 2012. Oral presentation.

Bibliography

Abramowitz, M. and Stegun, I. A. (1972). *Handbook of mathematical functions with formulas, graphs, and mathematical tables*. National Bureau of Standards, Washington, D.C. 10th print., with corr.

Abricka, M., Gelfgat, Y., and Krumins, J. (2002). Influence of combined electromagnetic fields on the heat/mass transfer in the Bridgman process. *Energy Conversion and Management*, 43:327–333.

Agrawal, L., Mandal, J. C., and Marathe, A. G. (2001). Computations of laminar and turbulent mixed convection in a driven cavity using pseudo-compressibility approach. *Computers and Fluids*, 30:607–620.

Alexiades, V. and Solomon, A. D. (1993). *Mathematical modeling of melting and freezing processes*. Hemisphere publishing corporation, Washington.

Ammon, W. v., Gelfgat, Y., Gorbunov, L., Virbulis, J., Weber, M., and Schmidt, H. (2008). Verfahren und Vorrichtung zur Herstellung eines Einkristalls aus Silicium. Patentschrift DE10259588B4.

Ammon, W. v., Virbulis, J., Tomzig, E., Gelfgat, Y., and Gorbunov, L. (2002). Verfahren und Vorrichtung zum Herstellen eines Einkristalls aus Silicium. Offenlegungsschrift DE10102126A1.

Appapillai, A. and Sachs, E. (2010). The effect of substrate material on nucleation behavior of molten silicon for photovoltaics. *Journal of Crystal Growth*, 312:1297–1300.

Arens, M. (2007). Berechnung des konvektiven Stofftransports bei der gerichteten Erstarrung von Solarsilizium. Diplomarbeit, Technische Universität Dresden.

Asbeck, F. H. (2009). *Eine solare Welt*. Kiepenheuer & Witsch, Köln.

Azizi, M., Meissner, E., and Friedrich, J. (2010). Ultrasound measurement of the position of the growing interface during directional solidification of silicon. In *25th European Photovoltaic Solar Energy Conference*, pages 1520–1523, Valencia, Spain.

Babu, P. and Stoica, P. (2010). Spectral analysis of nonuniformly sampled data – a review. *Digital Signal Processing*, 20:359–378.

Baehr, H. D. and Stephan, K. (2010). *Wärme- und Stoffübertragung*. Springer, 7. edition.

Bähr, T., Behnken, H., Henker, J., and Müller, A. (2007). Integrated simulation model for a newly developed silicon ingot casting unit: Temperatures, stresses, dislocations, impurity segregation and diffusion. In *22nd European Photovoltaic Solar Energy Conference*, pages 984–988, Milan, Italy.

Barvinschi, F., Stelian, C., Delannoy, Y., Mangelinck, N., and Duffar, T. (2003). Modeling the multi-crystalline silicon ingot solidification process in a vertical square furnace. *Journal of Optoelectronics and Advanced Materials*, 5:293–300.

Baumgartl, J. (1992). *Numerische und experimentelle Untersuchungen zur Wirkung magnetischer Felder in Kristallzüchtungsanordnungen*. PhD thesis, Universität Erlangen-Nürnberg.

Beatty, K. M. and Jackson, K. A. (2000). Monte Carlo modeling of silicon crystal growth. *Journal of Crystal Growth*, 211:13–17.

Beaudhuin, M., Duffar, T., Lemiti, M., and Zaidat, K. (2011). One-dimensional model of the equiaxed grain formation in multi-crystalline silicon. *Journal of Crystal Growth*, 319:106–113.

Behnken, H. (2009). Simulation of the development of dislocation density in multi-crystalline silicon during crystallisation processes. In *24th European Photovoltaic Solar Energy Conference*, pages 1281–1285, Hamburg, Germany.

Bellmann, M. P. and Meese, E. A. (2011). Effect of steady crucible rotation on the segregation of impurities in vertical Bridgman growth of multi-crystalline silicon. *Journal of Crystal Growth*, 333:1–6.

Bellmann, M. P., Meese, E. A., and Arnberg, L. (2010). Impurity segregation in directional solidified multi-crystalline silicon. *Journal of Crystal Growth*, 312:3091–3095.

Bellmann, M. P., Meese, E. A., and Arnberg, L. (2011a). Effect of accelerated crucible rotation on the segregation of impurities in vertical Bridgman growth of multi-crystalline silicon. *Journal of Crystal Growth*, 318:239–243.

Bellmann, M. P., Meese, E. A., Solheim, A., Sørheim, H., and Arnberg, L. (2008). Influence of crucible thermal properties on the solidification of multi-crystalline silicon in a Bridgman pilot scale furnace. In *23rd European Photovoltaic Solar Energy Conference*, pages 1243–1246, Valencia, Spain.

Bellmann, M. P., Meese, E. A., Syvertsen, M., Solheim, A., Sørheim, H., and Arnberg, L. (2011b). Silica versus silicon nitride crucible: Influence of thermophysical properties on the solidification of multi-crystalline silicon by Bridgman technique. *Journal of Crystal Growth*, 318:265–268.

Bellmann, M. P., M'Hamdi, M., Ellingsen, K., Solheim, A., Sørheim, H., and Arnberg, L. (2009). Analysis of the impact of crucible properties on thermally induced stresses in directionally solidified multi-crystalline silicon ingots. In *24th European Photovoltaic Solar Energy Conference*, pages 1244–1247, Hamburg, Germany.

Benedict, L. H., Nobach, H., and Tropea, C. (2000). Estimation of turbulent velocity spectra from laser Doppler data. *Measurement Science and Technology*, 11:1089–1104.

Bondeson, A., Rylander, T., and Ingelström, P. (2005). *Computational Electromagnetics*, volume 51 of *Texts in Applied Mathematics*. Springer.

Botella, O. and Peyret, R. (1998). Benchmark spectral results on the lid-driven cavity flow. *Computers and Fluids*, 27:421–433.

Boulfrad, Y., Øvrelid, E., M'Hamdi, M., and Arnberg, L. (2010). Modeling of iron distribution in a MC-Si ingot based on thermal history. In *25th European Photovoltaic Solar Energy Conference*, pages 1538–1542, Valencia, Spain.

BPEnergyStatistics (2011). BP statistical review of world energy/ June 2011.

Breitenstein, O., Rakotoniaina, J. P., Rifai, M. H. A., and Werner, M. (2004). Shunt types in crystalline silicon solar cells. *Progress in Photovoltaics: Research and Applications*, 12:529–538.

Bronstein, I. N., Semendjajew, K. A., Musiol, G., and Mühlig, H. (2008). *Taschenbuch der Mathematik*. Harri Deutsch, Frankfurt am Main, 7. edition.

Büllesfeld, F., Sahr, U., Miller, W., Rudolph, P., Rehse, U., and Dropka, N. (2010). Verfahren zum Erstarren einer Nichtmetall-Schmelze. Offenlegungsschrift DE102008059521A1.

Burton, J. A., Prim, R. C., and Slichter, W. P. (1953). The distribution of solute in crystals grown from the melt. Part I. Theoretical. *The Journal of Chemical Physics*, 21:1987–1991.

Chapin, D. M., Fuller, C. S., and Pearson, G. L. (1954). A new silicon p-n junction photocell for converting solar radiation into electrical power. *Journal of Applied Physics*, 25:676–677.

Chen, J.-C., Teng, Y.-Y., Lu, C.-W., and Chen, C.-Y. (2011). Numerical investigation of the oxygen impurity distribution during the multicrystalline silicon crystal growth under a gas flow guiding device. In *5th International Workshop on Crystal Growth Technology*, pages 19–20, Berlin, Germany.

Chen, X., Nakano, S., and Kakimoto, K. (2010a). Three-dimensional global analysis of thermal stress and dislocations in a silicon ingot during a unidirectional solidification process with a square crucible. *Journal of Crystal Growth*, 312:3261–3266.

Chen, X. J., Nakano, S., Liu, L. J., and Kakimoto, K. (2008). Study on thermal stress in a silicon ingot during a unidirectional solidification process. *Journal of Crystal Growth*, 310:4330–4335.

Chen, X. J., Nakano, S., Liu, L. J., and Kakimoto, K. (2010b). Gedanken experiment on point defects in unidirectional solidified single crystalline silicon with no dislocations. *Journal of Crystal Growth*, 312:192–197.

Chunduri, S. K. (2011a). Preparing for bigger loads. *Photon International*, 06:236–259.

Chunduri, S. K. (2011b). The quest for quasi. *Photon International*, 06:260–264.

Coletti, G., Kvande, R., Mihailetchi, V. D., Geerligs, L. J., Arnberg, L., and Øvrelid, E. J. (2008). Effect of iron in silicon feedstock on p- and n-type multicrystalline silicon solar cells. *Journal of Applied Physics*, 104:104913–1–104913–11.

Coriell, S. R. and McFadden, G. B. (1993). Morphological stability. In Hurle, D. T. J., editor, *Handbook of crystal growth*, volume 1: Fundamentals, part B: Transport and stability, pages 785–853. North-Holland.

Cramer, A., Eckert, S., Galindo, V., Gerbeth, G., Willers, B., and Witke, W. (2004a). Liquid metal model experiments on casting and solidification processes. *Journal of Materials Science*, 39:7285–7294.

Cramer, A., Pal, J., and Gerbeth, G. (2007a). Experimental investigation of a flow driven by a combination of a rotating and a traveling magnetic field. *Physics of Fluids*, 19:118109–1–118109–4.

Cramer, A., Pal, J., Koal, K., Tschisgale, S., Stiller, J., and Gerbeth, G. (2011). The sensitivity of a travelling magnetic field driven flow to axial alignment. *Journal of Crystal Growth*, 321:142–150.

Cramer, A., Pal, J., Zhang, C., Eckert, S., and Gerbeth, G. (2007b). Experimental investigation of time-dependent flow driven by a travelling magnetic field. *Springer Proceedings in Physics: Advances in Turbulence XI*, 117:750–750.

Cramer, A., Zhang, C., and Eckert, S. (2004b). Local flow structures in liquid metals measured by ultrasonic Doppler velocimetry. *Flow Measurement and Instrumentation*, 15:145–153.

Czupalla, M., Kießling, F.-M., Klein, O., Lange, R.-P., Lux, B., Miller, W., Rudolph, P., Ziem, M., and Kirscht, F. (2011). Verfahren und Vorrichtung zur Züchtung von Kristallen aus elektrisch leitenden Schmelzen, die in der Diamant- oder Zinkblendestruktur kristallisieren. Offenlegungsschrift DE102009027436A1.

Dagner, J., Hainke, M., Friedrich, J., and Müller, G. (2003). Effects of time-dependent magnetic fields on directional solidification of AlSi7 alloys. In *4th International Conference of Electromagnetic Processing of Materials*, Lyon, France.

Danaila, L. and Antonia, R. A. (2009). Spectrum of a passive scalar in moderate Reynolds number homogeneous isotropic turbulence. *Physics of Fluids*, 21:111702–1–111702–4.

Davidson, P. A. (1999). Magnetohydrodynamics in materials processing. *Annual Review of Fluid Mechanics*, 31:273–300.

Davidson, P. A. (2001). *An introduction to magnetohydrodynamics*. Cambridge University Press.

Davidson, P. A. (2004). *Turbulence. An introduction for scientists and engineers*. Oxford University Press.

Delannoy, Y., Barvinschi, F., and Duffar, T. (2007). 3D dynamic mesh numerical model for multi-crystalline silicon furnaces. *Journal of Crystal Growth*, 303:170–174.

Dietrich, M., Freudenberg, B., Müller, A., Seidel, J., and Stenzenberger, J. (2007). Ofen für Nichtmetall-Schmelzen. Offenlegungsschrift DE102006020234A1.

DOP2000Manual (2006). DOP2000. Model 2125/2032. User's manual. Signal Processing S. A.

Drikakis, D., Hahn, M., Mosedale, A., and Thornber, B. (2009). Large eddy simulation using high-resolution and high-order methods. *Philosophical Transactions of the Royal Society A*, 367:2985–2997.

Dropka, N., Miller, W., Menzel, R., and Rehse, U. (2010). Numerical study on transport phenomena in a directional solidification process in the presence of travelling magnetic fields. *Journal of Crystal Growth*, 312:1407–1410.

Dropka, N., Miller, W., Rehse, U., Rudolph, P., Büllesfeld, F., Sahr, U., Klein, O., and Reinhardt, D. (2011). Numerical study on improved mixing in silicon melts by double-frequency TMF. *Journal of Crystal Growth*, 318:275–279.

Dular, P. and Geuzaine, C. (2011). GetDP: a general environment for the treatment of discrete problems. `http://www.geuz.org/getdp`. Versions 1.2.1, 2.1.0, 2.1.1.

Dupret, F., Nicodeme, P., Ryckmans, Y., Wouters, P., and Crochet, M. J. (1990). Global modelling of heat transfer in crystal growth furnaces. *International Journal of Heat and Mass Transfer*, 33:1849–1871.

Eckert, S., Cramer, A., and Gerbeth, G. (2007). Velocity measurement techniques for liquid metal flows. In Molokov, S., Moreau, R., and Moffatt, K., editors, *Magnetohydrodynamics – Historical Evolution and Trends*, pages 275–294. Springer.

Eckert, S., Nikrityuk, P. A., Räbiger, D., Willers, B., and Eckert, K. (2009). Use of time-modulated AC magnetic fields for melt flow control during unidirectional solidification. *International Journal of Cast Metals Research*, 22:78–81.

Eichler, S., Seidl, A., Börner, F., Kretzer, U., and Weinert, B. (2003). A combined carbon and oxygen segregation model for the LEC growth of SI GaAs. *Journal of Crystal Growth*, 247:69–76.

Ellingsen, K., M'Hamdi, M., and Mortensen, D. (2010). Analysis of the effect of melt flow on impurity segregation during directional crystallization of silicon in a small scale furnace. In *25th European Photovoltaic Solar Energy Conference*, pages 1562–1565, Valencia, Spain.

Elmer (2011). Elmer: open source finite element software for multiphysical problems. `http://www.csc.fi/english/pages/elmer`. Versions 6.1, 6.2.

Emery, A. F., Johansson, O., Lobo, M., and Abrous, A. (1991). A comparative study of methods for computing the diffuse radiation viewfactors for complex structures. *Journal of Heat Transfer*, 113:413–422.

EPIAreport (2011). Solar generation 6: Solar photovoltaic electricity empowering the world. Report, The European Photovoltaic Industry Association and Greenpeace International.

ExpINEMET (2010). The magnetic, UDV and related measurements were carried out by Kathrin Niemietz, Jan Ehrig, and several technical assistants at INEMET under the supervision by Dr. Olf Pätzold, under the guidance and with the participation of the author in the time period 2010–2011.

ExpTHMelectric (2010). The electric and/or magnetic measurements were carried out by several colleagues from Fraunhofer THM under the guidance of the author in the time period 2010–2011.

ExpTHMfurnace (2011). The crystallization experiments as well as the characterization of the ingots were carried out by Iven Kupa and several other colleagues from Fraunhofer THM under the supervision by Dr. Ulrike Wunderwald in the time period 2011–2012.

Felten, F., Fautrelle, Y., Terrail, Y. D., and Metais, O. (2004). Numerical modelling of electromagnetically-driven turbulent flows using LES methods. *Applied Mathematical Modelling*, 28:15–27.

Ferziger, J. H. and Peric, M. (2002). *Computational methods for fluid dynamics*. Springer, 3. edition.

FFTW (2011). FFTW: a C subroutine library for computing the discrete Fourier transform. `http://www.fftw.org/`.

Fischer, B. (2001). *Modellierung zeitabhängiger Magnetfelder in Kristallzüchtungsanordnungen*. PhD thesis, Universität Erlangen-Nürnberg.

Frank-Rotsch, C., Jockel, D., Ziem, M., and Rudolph, P. (2008). Numerical optimization of the interface shape at the VGF growth of semiconductor crystals in a traveling magnetic field. *Journal of Crystal Growth*, 310:1505–1510.

Frank-Rotsch, C., P. Rudolph, P., Klein, O., Lange, R.-P., and Nacke, B. (2009a). Vorrichtung und Verfahren zur Herstellung von Kristallen aus elektrisch leitenden Schmelzen. Patentschrift DE102007028548B4.

Frank-Rotsch, C. and Rudolph, P. (2009). Vertical gradient freeze of 4 inch Ge crystals in a heater-magnet module. *Journal of Crystal Growth*, 311:2294–2299.

Frank-Rotsch, C. and Rudolph, P. (2010). Vorrichtung und Verfahren zur Züchtung von Kristallen aus elektrisch leitenden Schmelzen in Mehrtiegelanordnungen. Offenlegungsschrift DE102008034029A1.

Frank-Rotsch, C., Rudolph, P., Ziehm, M., Rehse, U., and Miller, W. (2009b). Verfahren zur intensiven Durchmischung von elektrisch leitenden Schmelzen in Kristallisations- und Erstarrungsprozessen. Offenlegungsschrift DE102008027359A1.

Franke, D. (2000). *Numerische Simulation der Versetzungsmultiplikation in multikristallinem Silicium aus der gerichteten Blockkristallisation*. PhD thesis, Technische Hochschule Aachen.

Franke, D., Rettelbach, T., Häßler, C., Koch, W., and Müller, A. (2002). Silicon ingot casting: Process development by numerical simulations. *Solar Energy Materials and Solar Cells*, 72:83–92.

Franke, S., Büttner, L., Czarske, J., Räbiger, D., and Eckert, S. (2010). Ultrasound Doppler system for two-dimensional flow mapping in liquid metals. *Flow Measurement and Instrumentation*, 21:402–409.

FreeCAD (2011). FreeCAD: a general purpose open source 3D CAD/ MCAD/ CAx /CAE /PLM modeler. `http://sourceforge.net/projects/free-cad`.

Fröhlich, J. (2006). *Large Eddy Simulation turbulenter Strömungen*. Teubner, Wiesbaden.

Friedrich, J. (2007). Control of melt convection in VGF and CZ crystal growth configurations by using magnetic fields: Theory and examples. In Dost, S. and Okano, Y., editors, *Crystal growth under applied fields*, pages 31–59. Transworld Research Network, Trivandrum, Kerala, India.

Fulkerson, W., Moore, J. P., Williams, R. K., Graves, R. S., and McElroy, D. L. (1968). Thermal conductivity, electrical resistivity, and Seebeck coefficient of silicon from 100 to 1300 K. *Physical Review*, 167:765–782.

Galindo, V., Grants, I., Lantzsch, R., Pätzold, O., and Gerbeth, G. (2007). Numerical and experimental modeling of the melt flow in a traveling magnetic field for vertical gradient freeze crystal growth. *Journal of Crystal Growth*, 303:258–261.

Gao, B., Chen, X. J., Nakano, S., and Kakimoto, K. (2010). Crystal growth of high-purity multicrystalline silicon using a unidirectional solidification furnace for solar cells. *Journal of Crystal Growth*, 312:1572–1576.

Gelfgat, A. Y. (2005). On three-dimensional instability of a traveling magnetic field driven flow in a cylindrical container. *Journal of Crystal Growth*, 279:276–288.

Gelfgat, A. Y. and Kit, E. (2005). Scin-effect influence on three-dimensional instability of a traveling magnetic field driven flow in a cylindrical container. In *The 15th Riga and 6th PAMIR Conference on Fundamental and Applied MHD*, pages 155–156, Riga, Jurmala, Latvia.

Gelfgat, Y., Abricka, M., and Krumins, J. (2001). Influence of alternating magnetic field on the hydrodynamics and heat/mass transfer in the processes of bulk single crystal growth. *Magnetohydrodynamics*, 37(4):337–347.

Gelfgat, Y., Krumins, J., and Abricka, M. (2003a). On a possibility to use travelling magnetic fields for concurrent heating and stirring of the melt in crystal growth. In *International Scientific Colloquium, Modelling for Electromagnetic Processing*, pages 211–218, Hannover, Germany.

Gelfgat, Y., Krumins, J., and Abricka, M. (2003b). On possible simultaneous heating and stirring of the melt at single crystal growth by one inductor of electromagnetic field. *Magnetohydrodynamics*, 39(2):201–210.

Gelfgat, Y. M., Krumins, Y., and Abricka, M. (1999). Motion of an electrically conducting fluid in a cylindrical volume acted on by superimposed rotating and travelling magnetic fields. *Magnetohydrodynamics*, 35(1):1–12.

Geuzaine, C. (2001). *High order hybrid finite element schemes for Maxwell's equations taking thin structures and global quantities into account*. PhD thesis, University of Liege.

Geuzaine, C. and Remacle, J.-F. (2009). Gmsh: a three-dimensional finite element mesh generator with built-in pre- and post-processing facilities. *International Journal for Numerical Methods in Engineering*, 79:1309–1331.

Geuzaine, C. and Remacle, J.-F. (2011). Gmsh: a three-dimensional finite element mesh generator with built-in pre- and post-processing facilities. `http://www.geuz.org/gmsh`. Versions 2.2.3–2.5.0.

Gibbings, J. C. (2011). *Dimensional analysis*. Springer.

Glassbrenner, C. J. and Slack, G. A. (1964). Thermal conductivity of silicon and germanium from 3K to the melting point. *Physical Review*, 134:A1058–A1069.

Glazov, V. M., Chizhevskaya, S. N., and Glagoleva, N. N. (1967). *Liquid Semiconductors*. Nauka, Moskwa. In Russian: В. М. Глазов, С. Н. Чижевская, Н. Н. Глаголева, *Жидкие полупроводники*, Наука, Москва.

Glazov, V. M. and Pashinkin, A. S. (2001). The thermophysical properties (heat capacity and thermal expansion) of single-crystal silicon. *High Temperature*, 39:413–419. Translated from Teplofizika Vysokikh Temperatur.

Gnuplot (2011). Gnuplot: portable command-line driven graphing utility. `http://www.gnuplot.info`. Versions 4.2.3–4.4.2.

Goetzberger, A., Voß, B., and Knobloch, J. (1997). *Sonnenenergie: Photovoltaik*. B.G. Teubner, Stuttgart, 2. edition.

Gräbner, O., Mühe, A., Müller, G., Tomzig, E., Virbulis, J., and von Ammon, W. (2000). Analysis of turbulent flow in silicon melts by optical temperature measurement. *Materials Science and Engineering B*, 73:130–133.

Grants, I. and Gerbeth, G. (2001). Stability of axially symmetric flow driven by a rotating magnetic field in a cylindrical cavity. *Journal of Fluid Mechanics*, 431:407–426.

Grants, I. and Gerbeth, G. (2002). Linear three-dimensional instability of a magnetically driven rotating flow. *Journal of Fluid Mechanics*, 463:229–239.

Grants, I. and Gerbeth, G. (2004). Stability of melt flow due to a traveling magnetic field in a closed ampoule. *Journal of Crystal Growth*, 269:630–638.

Grants, I. and Gerbeth, G. (2008). Use of a traveling magnetic field in VGF growth: Flow reversal and resulting dopant distribution. *Journal of Crystal Growth*, 310:3699–3705.

Grants, I., Klyukin, A., and Gerbeth, G. (2009a). Instability of the melt flow in VGF growth with a traveling magnetic field. *Journal of Crystal Growth*, 311:4255–4264.

Grants, I., Zhang, C., Eckert, S., and Gerbeth, G. (2008). Experimental observation of swirl accumulation in a magnetically driven flow. *Journal of Fluid Mechanics*, 616:135–152.

Grants, I., Zhang, C., Eckert, S., and Gerbeth, G. (2009b). Liquid metal tornado. In *6th International Conference on Electromagnetic Processing of Materials*, Dresden, Germany.

Gray, D. D. and Giorgini, A. (1976). The validity of the Boussinesq approximation for liquids and gases. *Journal of Heat and Mass Transfer*, 19:545–551.

Gresho, P. M. and Derby, J. J. (1987). A finite element model for induction heating of a metal crucible. *Journal of Crystal Growth*, 85:40–48.

Griffiths, D. J. (1999). *Introduction to Electrodynamics*. Prentice Hall, 3. edition.

Guo, Z., Maruyama, S., and Togawa, S. (1998). Combined heat transfer in floating zone growth of large silicon crystals with radiation on diffuse and specular surfaces. *Journal of Crystal Growth*, 194:321–330.

Hainke, M., Dagner, J., Friedrich, J., and Müller, G. (2005). Macrosegregation in binary AlSi7 alloys resulting from the application of time dependent magnetic fields. *Microgravity Science and Technology*, 16:59–63.

Häßler, C., Reisner, E.-U., Koch, W., Müller, A., Franke, D., and Rettelbach, T. (1999). Low dislocation density multicrystalline silicon for photovoltaic applications. *Solid State Phenomena*, 67-68:447–452.

Hatton, L. (1997). The T-experiments: Errors in scientific software. *Computational Science and Engineering, IEEE*, 4(2):27–38.

Helmreich, D. (1987). The Wacker ingot casting process. In Khattak, C. P. and Ravi, K. V., editors, *Silicon processing for photovoltaics II*, pages 99–151. North-Holland.

Hibiya, T., Fukuyama, H., Tsukada, T., and Watanabe, M. (2008). Thermophysical properties of molten silicon. In Scheel, H. K. and Capper, P., editors, *Crystal growth technology: From fundamentals and simulation to large-scale production*, pages 103–136. Wiley-VCH, Weinheim.

Hisamatsu, S., Matsuo, H., Nakano, S., and Kakimoto, K. (2009). Numerical analysis of the formation of Si_3N_4 and Si_2N_2O during a directional solidification process in multicrystalline silicon for solar cells. *Journal of Crystal Growth*, 311:2615–2620.

Hofstetter, J., Fenning, D. P., Bertoni, M. I., Lelievre, J. F., del Canizo, C., and Buonassisi, T. (2011). Impurity-to-efficiency simulator: Predictive simulation of silicon solar cell performance based on iron content and distribution. *Progress in Photovoltaics: Research and Applications*, 19:487–497.

Holmberg, M. T. (1998). *Three-dimensional finite element computation of eddy currents in synchronous machines*. PhD thesis, Chalmers University of Technology.

Hughes, W. F. and Young, F. J. (1989). *The Electrodynamics of Fluids*. Robert E. Krieger Publishing Company, Malabar, Florida.

Hurle, D. T. J. and Series, R. W. (1994). Use of magnetic fields in melt growth. In Hurle, D. T. J., editor, *Handbook of crystal growth*, volume 2: Bulk crystal growth, Part A: Basic techniques, pages 259–285. North-Holland.

IEAEnergyStatistics (2010). IEA key world energy statistics.

Iuga, M. (2003). Study of the influence of travelling magnetic fields on melt convection. Diploma thesis, Universität Erlangen-Nürnberg.

Iwatsu, R. and Hyun, J. M. (1995). Three-dimensional driven-cavity flows with a vertical temperature gradient. *International Journal of Heat and Mass Transfer*, 38:3319–3328.

Iwatsu, R., Hyun, J. M., and Kuwahara, K. (1993). Mixed convection in a driven cavity with a stable vertical temperature gradient. *International Journal of Heat and Mass Transfer*, 36:1601–1608.

Jasak, H. (1996). *Error analysis and estimation for the finite volume method with applications to fluid flows*. PhD thesis, University of London.

Jin, J. (2002). *The finite element method in electromagnetics*. Wiley, 2. edition.

Jockel, D., Frank-Rotsch, C., Rudolph, P., and Lange, R.-P. (2009). Vorrichtung zur Herstellung von Kristallen aus elektrisch leitenden Schmelzen. Patentschrift DE102007046409B4.

Julsrud, S. and Rudshaug, M. (2007). Crystallization furnace. International patent application WO2007148988A1.

Jung, T. and Friedrich, J. (2007). Kopplung verschiedener Softwareprogramme für die 3D – Simulation mit Hilfe von ORCAN. In *DGKK Arbeitskreis "Angewandte Simulation in der Kristallzüchtung"*, Iphofen, Germany.

Kaden, T., Schönwälder, S., Kreßner-Kiel, D., Gründig-Wendrock, B., Lüdemann, R., and Möller, H.-J. (2008). Incorporation and distribution of impurities in mc-Si ingots of increased mass and reduced process time: Simulations and measurements. In *23rd European Photovoltaic Solar Energy Conference*, pages 1075–1079, Valencia, Spain.

Kaiser, T. (1998). *Magnetohydrodynamische Effekte bei der Halbleiterzüchtung*. PhD thesis, Albert-Ludwigs-Universität Freiburg.

Kakimoto, K., Eguchi, M., Watanabe, H., and Hibiya, T. (1988). Direct observation by X-ray radiography of convection of molten silicon in the Czochralski growth method. *Journal of Crystal Growth*, 88:365–370.

Kakimoto, K., Liu, L., and Nakano, S. (2006). Analysis of temperature and impurity distributions in a unidirectional-solidification process for multi-crystalline silicon of solar cells by a global model. *Materials Science and Engineering B*, 134:269–272.

Kaneda, Y. and Ishihara, T. (2006). High-resolution direct numerical simulation of turbulence. *Journal of Turbulence*, 7:N20.

Kärrholm, F. P. (2006). Rhie-Chow interpolation in OpenFOAM. Lecture notes, Chalmers University of Technology.

Kasjanow, H., Nacke, B., Eichler, S., Jockel, D., Frank-Rotsch, C., Lange, P., Kießling, F.-M., and Rudolph, P. (2008). Investigation of asymmetry effects in a heater-magnet module for TMF VGF and LEC growth by three-dimensional numerical modeling. *Journal of Crystal Growth*, 310:1540–1545.

Keisan (2009). Keisan: calculation library by Casio. `http://keisan.casio.com`.

Kiessling, F. M. (2011). Neue Entwicklungen in der Kristallzüchtung von Solarsilicium. In *Freiberger Siliciumtage*, Freiberg, Germany.

Kiessling, F.-M., Büllesfeld, F., Dropka, N., Frank-Rotsch, C., Müller, M., and Rudolph, P. (2012). Characterization of mc-Si directionally solidified in travelling magnetic fields. *Journal of Crystal Growth*, 360:81–86.

Kiessling, F.-M., Dropka, N., Frank-Rotsch, C., Juda, U., Lüdge, A., Müller, M., Naumann, M., and Rudolph, P. (2011). Directional solidification of solar-grade silicon in travelling magnetic fields. In *German Polish Conference on Crystal Growth*, Frankfurt (Oder)/ Slubice, Germany/ Poland.

Kimura, S. and Terashima, K. (1997). A review of measurement of thermophysical properties of silicon melt. *Journal of Crystal Growth*, 180:323–333.

Kirpo, M. (2008). *Modeling of turbulence properties and particle transport in recirculated flows*. PhD thesis, University of Latvia.

Klein, O., Lechner, C., Druet, P.-E., Philip, P., Sprekels, J., Frank-Rotsch, C., Kießling, F.-M., Miller, W., Rehse, U., and Rudolph, P. (2008). Numerical simulation of Czochralski crystal growth under the influence of a traveling magnetic field generated by an internal heater-magnet module (HMM). *Journal of Crystal Growth*, 310:1523–1532.

Klein, O., Lechner, C., Druet, P.-E., Philip, P., Sprekels, J., Frank-Rotsch, C., Kießling, F.-M., Miller, W., Rehse, U., and Rudolph, P. (2009). Numerical simulations of the influence of a traveling magnetic field, generated by an internal heater-magnet module on liquid encapsulated Czochralski crystal growth. *Magnetohydrodynamics*, 45(4):557–567.

Klyukin, A., Grants, I., and Gerbeth, G. (2008). Experimental study of traveling magnetic field driven instability in a thermally stratified liquid gallium cylinder. In *7th PAMIR International Conference on Fundamental and Applied MHD*, Presqu'ile de Giens, France.

Koal, K. (2011). *Strömungsbeeinflussung in Flüssigmetallen durch rotierende und wandernde Magnetfelder*. PhD thesis, Technische Universität Dresden.

Koal, K., Grünberg, T., and Stiller, J. (2009). Scalar transport in liquid metal flows driven by rotating and travelling magnetic fields. In *6th International Conference on Electromagnetic Processing of Materials*, Dresden, Germany.

Koch, W., Hässler, C., Höfs, H.-U., Müller, A., and Schwirtlich, I. A. (1997). Planar solidification of multicrystalline silicon for photovoltaic applications. *Solid State Phenomena*, 57-58:401–412.

Krauze, A. (2005). *Mathematical modelling of turbulent melt flow under the influence of AC and DC magnetic fields in CZ crystal growth system*. PhD thesis, University of Latvia.

Krauze, A., Jekabsons, N., Muiznieks, A., Sabanskis, A., and Lacis, U. (2010). Applicability of LES turbulence modeling for CZ silicon crystal growth systems with traveling magnetic field. *Journal of Crystal Growth*, 312:3225–3234.

Krauze, A., Muiznieks, A., Mühlbauer, A., Wetzel, T., Gorbunov, L., Pedchenko, A., and Virbulis, J. (2004). Numerical 2D modelling of turbulent melt flow in CZ system with dynamic magnetic fields. *Journal of Crystal Growth*, 266:40–47.

Krauze, A., Rudevics, A., Muiznieks, A., Sabanskis, A., Jekabsons, N., and Nacke, B. (2008). Unsteady 3D LES modeling of turbulent melt flow with AC traveling EM fields for a laboratory model of the CZ silicon crystal growth system. In *International Scientific Colloquium Modelling for Electromagnetic Processing*, pages 85–90, Hannover, Germany.

Krauze, A., Rudevics, A., Muiznieks, A., Sabanskis, A., Jekabsons, N., and Nacke, B. (2009). Unsteady 3D LES modeling of turbulent melt flow with AC travelling EM fields for a laboratory model of the CZ crystal silicon crystal growth system. *Magnetohydrodynamics*, 45(4):605–611.

Krumin, Y. K. (1969). *Interaction of a traveling magnetic field with a conductiong medium.* Zinatne, Riga. In Russian: Ю. К. Круминь, *Взаимодействие бегущего магнитного поля с проводящей средой*, Зинатне, Рига.

Krumin, Y. K. (1983). *Fundamentals of theory and calculation for devices with a travelling magnetic field.* Zinatne, Riga. In Russian: Ю. К. Круминь, *Основы теории и расчета устройств с бегущим магнитным полем*, Зинатне, Рига.

Kuliev, A. T., Durnev, N. V., and Kalaev, V. V. (2007). Analysis of 3D unsteady melt flow and crystallization front geometry during a casting process for silicon solar cells. *Journal of Crystal Growth*, 303:236–240.

Kumar, V. (2005). *Modeling and numerical simulations of complex transport phenomena in crystal growth processes.* PhD thesis, Universität Erlangen-Nürnberg.

Kurz, M. (1998). *Development of CrysVUN++, a software system for numerical modelling and control of industrial crystal growth processes.* PhD thesis, Universität Erlangen-Nürnberg.

Lange, R.-P., Jockel, D., Ziem, M., Rudolph, P., Kießling, F., Frank-Rotsch, C., Czupalla, M., Nacke, B., and H. Kasjanow, H. (2009). Vorrichtung zur Herstellung von Kristallen aus elektrisch leitenden Schmelzen. Patentschrift DE102007028547B4.

Lange, R.-P., Ziem, M., and Rudolph, P. (2011). Vorrichtung und Verfahren zur Herstellung von Siliziumblöcken aus der Schmelze durch gerichtete Erstarrung. Offenlegungsschrift DE102009045680A1.

Lantzsch, R. (2009). *VGF-Kristallzüchtung unter dem Einfluss externer Magnetfelder.* PhD thesis, Technische Universität Bergakademie Freiberg.

Lantzsch, R., Galindo, V., Grants, I., Zhang, C., Pätzold, O., Gerbeth, G., and Stelter, M. (2007). Experimental and numerical results on the fluid flow driven by a traveling magnetic field. *Journal of Crystal Growth*, 305:249–256.

Lantzsch, R., Grants, I., Galindo, V., Pätzold, O., Gerbeth, G., Stelter, M., and Cröll, A. (2006). Fluid flow analysis and vertical gradient freeze crystal growth in a travelling magnetic field. *Magnetohydrodynamics*, 42(4):445–449.

Lantzsch, R., Grants, I., Pätzold, O., Stelter, M., and Gerbeth, G. (2008). Vertical gradient freeze growth with external magnetic fields. *Journal of Crystal Growth*, 310:1518–1522.

Lechner, C., Klein, O., and Druet, P.-E. (2007). Development of a software for the numerical simulation of VCz growth under the influence of a traveling magnetic field. *Journal of Crystal Growth*, 303:161–164.

Li, X., Fautrelle, Y., Ren, Z., Gagnoud, A., Zhang, Y., and Esling, C. (2011a). Morphological instability of interface, cell and dendrite during directional solidification under strong magnetic field. *Journal of Crystal Growth*, 318:23–27.

Li, Z., Liu, L., Ma, W., and Kakimoto, K. (2011b). Effects of argon flow on heat transfer in a directional solidification process for silicon solar cells. *Journal of Crystal Growth*, 318:298–303.

Li, Z., Liu, L., Ma, W., and Kakimoto, K. (2011c). Effects of argon flow on impurities transport in a directional solidification furnace for silicon solar cells. *Journal of Crystal Growth*, 318:304–312.

Liu, J. S., Kuan, C.-H., Cha, S.-C., Chuang, W.-L., Gau, G. J., and Jeng, J.-Y. (2011a). Photovoltaic technology development: A perspective from patent growth analysis. *Solar Energy Materials and Solar Cells*, 95:3130–3136.

Liu, L., Li, Z., Liu, X., Zhang, Y., and Xiong, J. (2011b). Effects of argon flow on melt convection and interface shape at different growth stages in a directional solidification process for solar silicon ingot of industrial size. In *5th International Workshop on Crystal Growth Technology*, pages 81–82, Berlin, Germany.

Liu, L., Nakano, S., and Kakimoto, K. (2006). Dynamic simulation of temperature and iron distributions in a casting process for crystalline silicon solar cells with a global model. *Journal of Crystal Growth*, 292:515–518.

Liu, L., Nakano, S., and Kakimoto, K. (2007). Three-dimensional global modeling of a unidirectional solidification furnace with square crucibles. *Journal of Crystal Growth*, 303:165–169.

Liu, L., Nakano, S., and Kakimoto, K. (2008). Carbon concentration and particle precipitation during directional solidification of multicrystalline silicon for solar cells. *Journal of Crystal Growth*, 310:2192–2197.

Lyubimova, T. P., Croell, A., Dold, P., Khlybov, O. A., and Fayzrakhmanova, I. S. (2004). Time-dependent magnetic field influence on GaAs crystal growth by vertical Bridgman method. *Journal of Crystal Growth*, 266:404–410.

Matsuo, H., Ganesh, R. B., Nakano, S., Liu, L., Arafune, K., Ohshita, Y., Yamaguchi, M., and Kakimoto, K. (2008a). Analysis of oxygen incorporation in unidirectionally solidified multicrystalline silicon for solar cells. *Journal of Crystal Growth*, 310:2204–2208.

Matsuo, H., Ganesh, R. B., Nakano, S., Liu, L., Arafune, K., Ohshita, Y., Yamaguchi, M., and Kakimoto, K. (2009). Effect of crucible rotation on oxygen concentration during unidirectional solidification process of multicrystalline silicon for solar cells. *Journal of Crystal Growth*, 311:1123–1128.

Matsuo, H., Ganesh, R. B., Nakano, S., Liu, L., Kangawa, Y., Arafune, K., Ohshita, Y., Yamaguchi, M., and Kakimoto, K. (2008b). Thermodynamical analysis of oxygen incorporation from a quartz crucible during solidification of multicrystalline silicon for solar cell. *Journal of Crystal Growth*, 310:4666–4671.

Mazuruk, K. (2002). Control of melt convection using traveling magnetic fields. *Advances in Space Research*, 29(4):541–548.

Meese, E. A. and Westermoen, A. (2007). High accuracy predictive furnace model for directional growth of multicrystalline silicon. In *22nd European Photovoltaic Solar Energy Conference*, pages 1141–1144, Milan, Italy.

Menzel, R. (2008). Dreidimensionale Simulation der Konvektionsströmung bei der Erstarrung von Solarsilizium. Diplomarbeit, Technische Universität Berlin.

Messer, M. and Aidun, C. K. (2009). Main effects on the accuracy of Pulsed-Ultrasound-Doppler-Velocimetry in the presence of rigid impermeable walls. *Flow Measurement and Instrumentation*, 20:85–94.

M'Hamdi, M. and Gouttebroze, S. (2009). Analysis of the residual stress field associated with particles in multi-crystalline silicon. In *24th European Photovoltaic Solar Energy Conference*, pages 1265–1268, Hamburg, Germany.

Mühe, A., Altekrüger, B., and Vonhoff, A. (2005). Kristallzüchtungsanlage. Offenlegungsschrift, DE 10349339 A1.

MillenniumPrize (2011). The millennium prize problems. Clay Mathematics Institute of Cambridge, `http://www.claymath.org/millennium/`.

Miller, W., Frank-Rotsch, C., and Rudolph, P. (2011). Numerical studies of flow patterns during Czochralski growth of square-shaped Si crystals. *Journal of Crystal Growth*, 318:244–248.

Miyazawa, H., Liu, L., Hisamatsu, S., and Kakimoto, K. (2008a). Numerical analysis of the influence of tilt of crucibles on interface shape and fields of temperature and velocity in the unidirectional solidification process. *Journal of Crystal Growth*, 310:1034–1039.

Miyazawa, H., Liu, L., and Kakimoto, K. (2008b). Numerical analysis of influence of crucible shape on interface shape in a unidirectional solidification process. *Journal of Crystal Growth*, 310:1142–1147.

Müller, A., Schwichtenberg, G., Leistner, J., and Seidel, J. (2004). Vorrichtung sowie Verfahren zur Überwachung der Kristallisation eines Mediums, insbesondere von Silizium. Offenlegungsschrift DE10234250A1.

Müller, U. and Bühler, L. (2001). *Magnetofluiddynamics in Channels and Containers*. Springer.

Möller, H. J. (1993). *Semiconductors for Solar Cells*. Artech House, Boston, London.

Möller, H. J., Long, L., Werner, M., and Yang, D. (1999). Oxygen and carbon precipitation in multicrystalline solar silicon. *Physica Status Solidi A*, 171:175–189.

Moreau, R. (1990). *Magnetohydrodynamics*. Kluwer Academic Publishers.

Moreau, R. (1999). The fundamentals of MHD related to crystal growth. *Progress in Crystal Growth and Characterization of Materials*, 38:161–194.

Muiznieks, A., Krauze, A., and Nacke, B. (2007). Convective phenomena in large melts including magnetic fields. *Journal of Crystal Growth*, 303:211–220.

Mukai, K., Yuan, Z., Nogi, K., and Hibiya, T. (2000). Effect of the oxygen partial pressure on the surface tension of molten silicon and its temperature coefficient. *ISIJ International*, 40:S148–S152.

Mullins, W. W. and Sekerka, R. F. (1964). Stability of a planar interface during solidification of a dilute binary alloy. *Journal of Applied Physics*, 35:444–451.

Nacke, B., Kasjanow, H., Krause, A., Muiznieks, A., Kiessling, F.-M., Rehse, U., and Rudolph, P. (2009). Three-dimensional transient modeling of the melt flow in a TMF VCZ system for GaAs crystal growth. *Magnetohydrodynamics*, 45(3):317–324.

Nakajima, K., Fujiwara, K., and Usami, N. (2008). High-quality Si multicrystals with same grain orientation and large grain size by the newly developed dendritic casting method for high-efficiency solar cell applications. In Fujikawa, Y., Nakajima, K., and Sakurai, T., editors, *Frontiers in Materials Research*, volume 10 of *Advances in Materials Research*, pages 123–140. Springer.

Nakano, S., Liu, L. J., Chen, X. J., Matsuo, H., and Kakimoto, K. (2009). Effect of crucible rotation on oxygen concentration in the polycrystalline silicon grown by the unidirectional solidification method. *Journal of Crystal Growth*, 311:1051–1055.

Narayanan, M. and Ciszek, T. (2010). Silicon solar cells: Materials, devices, and manufacturing. In Dhanaraj, G., Byrappa, K., Prasad, V., and Dudley, M., editors, *Springer Handbook of Crystal Growth*, chapter 51, pages 1701–1718. Springer.

Niemietz, K., Galindo, V., Pätzold, O., Gerbeth, G., and Stelter, M. (2011). Flow modelling with relevance to vertical gradient freeze crystal growth under the influence of a travelling magnetic field. *Journal of Crystal Growth*, 318:150–155.

Noeppel, A., Budenkova, O., and Fautrelle, Y. (2009). Numerical investigation of the influence of forced convection induced by a travelling magnetic field during solidification of metallic alloys. *Magnetohydrodynamics*, 45(4):497–503.

Ono, N. and Trapaga, G. (1997). A numerical study of the effects of electromagnetic stirring on the distributions of temperature and oxygen concentration in silicon double-crucible Czochralski processing. *Journal of The Electrochemical Society*, 144:764–772.

OpenFOAM (2011). OpenFOAM: the open source Computational Fluid Dynamics toolbox. `http://www.openfoam.com`. Versions 1.4.1, 1.5, 1.6.x, 1.7.1, 2.0.1, 2.1.0.

Pal, J., Cramer, A., Gundrum, T., and Gerbeth, G. (2009). MULTIMAG – A MULTIpurpose MAGnetic system for physical modelling in magnetohydrodynamics. *Flow Measurement and Instrumentation*, 20:241–251.

ParaView (2011). ParaView: open source scientific visualization. `http://www.paraview.org`. Versions 3.2.1–3.14.0.

Pope, S. B. (2004). Ten questions concerning the large-eddy simulation of turbulent flows. *New Journal of Physics*, 6:1–24.

Press, W. H., Teukolsky, S. A., Vetterling, W. T., and Flannery, B. P. (2007). *Numerical Recipes. The Art of Scientific Computing*. Cambridge University Press, 3. edition.

Priede, J. and Gerbeth, G. (2005). Breakdown of Burton-Prim-Slichter approach and lateral solute segregation in radially converging flows. *Journal of Crystal Growth*, 285:261–269.

Ramachandran, N., Mazuruk, K., and Volz, M. P. (2000). Use of traveling magnetic fields to control melt convection. *Journal of the Japan Society of Microgravity Application*, 17:98–103.

Reimann, C., Jung, T., Trempa, M., and Friedrich, J. (2008). Modeling of convective heat and mass transfer processes in crystal growth of silicon for photovoltaic applications. In *23rd European Photovoltaic Solar Energy Conference*, pages 1233–1238, Valencia, Spain.

Reimann, C., Trempa, M., Jung, T., Friedrich, J., and Müller, G. (2010). Modeling of incorporation of O, N, C and formation of related precipitates during directional solidification of silicon under consideration of variable processing parameters. *Journal of Crystal Growth*, 312:878–885.

Reimann, C. R. (2010). *Einbau von O, N und C bei der gerichteten Erstarrung von multikristallinem Silicium für die Photovoltaik*. PhD thesis, Universität Erlangen-Nürnberg.

Roache, P. J. (1998). *Verification and Validation in Computational Science and Engineering*. Hermosa, Albuquerque, NM.

Rudolph, P. (2008). Travelling magnetic fields applied to bulk crystal growth from the melt: The step from basic research to industrial scale. *Journal of Crystal Growth*, 310:1298–1306.

Rudolph, P., Czupalla, M., Dropka, N., Frank-Rotsch, C., Kießling, F.-M., Klein, O., Lux, B., Miller, W., Rehse, U., and Root, O. (2009a). Crystal growth from melt in combined heater-magnet modules. *Journal of the Korean Crystal Growth and Crystal Technology*, 19:215–222.

Rudolph, P., Czupalla, M., and Lux, B. (2009b). LEC growth of semi-insulating GaAs crystals in traveling magnetic field generated in a heater-magnet module. *Journal of Crystal Growth*, 311:4543–4548.

Rudolph, P., Czupalla, M., Lux, B., Kirscht, F., Frank-Rotsch, C., Miller, W., and Albrecht, M. (2011). The use of heater-magnet module for Czochralski growth of PV silicon crystals with quadratic cross section. *Journal of Crystal Growth*, 318:249–254.

Rudolph, P. and Kakimoto, K. (2009). Crystal growth from the melt under external force fields. *MRS Bulletin*, 34:1–8.

Ruzicka, M. C. (2008). On dimensionless numbers. *Chemical Engineering Research and Design*, 86:835–868.

Saitoh, T., Dhamrin, M., Kamisako, K., Hirasawa, T., Eguchi, T., and Yamaga, I. (2005). Numerical simulation of directional solidification process for high-quality silicon ingots. In *15th International Photovoltaic Science & Engineering Conference (PVSEC-15)*, pages 110–113, Shanghai, China.

Scheil, E. (1942). Bemerkungen zur Schichtkristallbildung. *Zeitschrift für Metallkunde*, 34:70–72.

Schwesig, P., Hainke, M., Friedrich, J., and Mueller, G. (2004). Comparative numerical study of the effects of rotating and travelling magnetic fields on the interface shape and thermal stress in the VGF growth of InP crystals. *Journal of Crystal Growth*, 266:224–228.

Shockley, W. and Queisser, H. J. (1961). Detailed balance limit of efficiency of p-n junction solar cells. *Journal of Applied Physics*, 32:510–519.

SignalProcessingUDV (2011). Ultrasonic doppler velocimetry. `http://www.signal-processing.com`.

Smith, V. G., Tiller, W. A., and Rutter, J. W. (1955). A mathematical analysis of solute redistribution during solidification. *Canadian Journal of Physics*, 33:723–745.

Socoliuc, V., Vizman, D., Fischer, B., Friedrich, J., and Müller, G. (2003). 3D numerical simulation of Rayleigh-Benard convection in an electrically conducting melt acted on by a travelling magetic field. *Magnetohydrodynamics*, 39(2):187–200.

Soiland, A.-K. (2004). *Silicon for Solar Cells*. PhD thesis, Norwegian University of Science and Technology.

Steinbach, I., Apel, M., Rettelbach, T., and Franke, D. (2002). Numerical simulations for silicon crystallization processes: Examples from ingot and ribbon casting. *Solar Energy Materials and Solar Cells*, 72:59–68.

Stiller, J. and Koal, K. (2009). A numerical study of the turbulent flow driven by rotating and travelling magnetic fields in a cylindrical cavity. *Journal of Turbulence*, 10:N44.

Stiller, J., Koal, K., and Blackburn, H. M. (2008). Turbulence in electrically conducting fluids driven by rotating and travelling magnetic fields. In Peinke, J., Oberlack, M., and Talamelli, A., editors, *Progress in Turbulence III*, volume 131 of *Springer Proceedings in Physics*, pages 215–218. Springer.

Stiller, J., Koal, K., Frana, K., and Grundmann, R. (2006). Stirring of melts using rotating and travelling magnetic fields. In *5th International Conference on CFD in the Process Industries*, CSIRO, Melbourne, Australia.

Stoddard, N., Wu, B., Witting, I., Wagener, M., Park, Y., Rozgonyi, G., and Clark, R. (2008). Casting single crystal silicon: Novel defect profiles from BP Solar's Mono$^{2\,\mathrm{TM}}$ wafers. *Solid State Phenomena*, 131-133:1–8.

Syvertsen, M., Juel, M., and Bellmann, M. P. (2010). Effect of better insulation in crystalox DS 250 furnace during melting and solidification on the furnace operation. In *25th European Photovoltaic Solar Energy Conference*, pages 1543–1545, Valencia, Spain.

Tanasie, C., Vizman, D., and Friedrich, J. (2011). Numerical study of the influence of different types of magnetic fields on the interface shape in directional solidification of multicrystalline silicon ingots. *Journal of Crystal Growth*, 318:293–297.

Teng, Y.-Y., Chen, J.-C., Lu, C.-W., and Chen, C.-Y. (2010). The carbon distribution in multicrystalline silicon ingots grown using the directional solidification process. *Journal of Crystal Growth*, 312:1282–1290.

Teng, Y. Y., Chen, J. C., Lu, C. W., Chen, C. Y., Kalaev, V. V., and Demina, S. E. (2009). Crystalline front control of growing multicrystalline Si ingots during the directional solidification process. In *18th PVSEC Conference*, Kolkata, India.

Teng, Y.-Y., Chen, J.-C., Lu, C.-W., Chen, H.-I., Hsu, C., and Chen, C.-Y. (2011). Effects of the furnace pressure on oxygen and silicon oxide distributions during the growth of multicrystalline silicon ingots by the directional solidification process. *Journal of Crystal Growth*, 318:224–229.

Tiller, W. A., Jackson, K. A., Rutter, J. W., and Chalmers, B. (1953). The redistribution of solute atoms during the solidification of metals. *Acta Metallurgica*, 1:428–437.

TOP500 (2012). TOP500 list of the world's top supercomputers. `http://www.top500.org`.

Trempa, M., Reimann, C., Friedrich, J., and Müller, G. (2010). The influence of growth rate on the formation and avoidance of C and N related precipitates during directional solidification of multi crystalline silicon. *Journal of Crystal Growth*, 312:1517–1524.

Tukovic, Z. and Jasak, H. (2007). Updated lagrangian finite volume solver for large deformation dynamic response of elastic body. *Transactions of FAMENA*, 31:1–16.

Umbrashko, A., Baake, E., Nacke, B., and Jakovics, A. (2006). Modeling of the turbulent flow in induction furnaces. *Metallurgical and Materials Transactions B*, 37B:831–838.

VDI-Waermeatlas (2006). *VDI-Wärmeatlas*. Springer, 10. edition. Herausgeber: Verein Deutscher Ingenieure, VDI-Gesellschaft Verfahrenstechnik und Chemieingenieurwesen (GVC).

Versteeg, H. K. and Malalasekera, W. (2007). *An Introduction to Computational Fluid Dynamics. The Finite Volume Method*. Pearson/ Prentice Hall, Harlow, 2. edition.

Villiers, E. d. (2006). *The potential of large eddy simulation for the modeling of wall bounded flows*. PhD thesis, University of London.

Vizman, D., Friedrich, J., and Mueller, G. (2007). 3D time-dependent numerical study of the influence of the melt flow on the interface shape in a silicon ingot casting process. *Journal of Crystal Growth*, 303:231–235.

Voller, V. R., Swaminathan, C. R., and Thomas, B. G. (1990). Fixed grid techniques for phase change problems: A review. *International Journal for Numerical Methods in Engineering*, 30:875–898.

Volz, M. P. and Mazuruk, K. (2004). Lorentz body force induced by travelling magnetic fields. *Magnetohydrodynamics*, 40(2):117–126.

Wang, X., Fautrelle, Y., Etay, J., and Moreau, R. (2009). A periodically reversed flow driven by a modulated traveling magnetic field: Part I: Experiments with GaInSn. *Metallurgical and Materials Transactions B*, 40B:82–90.

Wei, J., Zhang, H., Zheng, L., Wang, C., and Zhao, B. (2009). Modeling and improvement of silicon ingot directional solidification for industrial production systems. *Solar Energy Materials and Solar Cells*, 93:1531–1539.

Wilke, K.-T. and Bohm, J. (1988). *Kristallzüchtung*. Harri Deutsch, Thun, Frankfurt am Main, 2. edition.

Wu, B. and Clark, R. (2011). Influence of inclusion on nucleation of silicon casting for photovoltaic (PV) application. *Journal of Crystal Growth*, 318:200–207.

Wu, B., Stoddard, N., Ma, R., and Clark, R. (2008). Bulk multicrystalline silicon growth for photovoltaic (PV) application. *Journal of Crystal Growth*, 310:2178–2184.

Würzner, S., Helbig, R., Funke, C., and Möller, H. J. (2010). The relationship between microstructure and dislocation density distribution in multicrystalline silicon. *Journal of Applied Physics*, 108:083516–1–083516–5.

Yeh, K. M., Hseih, C. K., Hsu, W. C., and Lan, C. W. (2010). High-quality multi-crystalline silicon growth for solar cells by grain-controlled directional solidification. *Progress in Photovoltaics: Research and Applications*, 18:265–271.

Yesilyurt, S., Motakef, S., Grugel, R., and Mazuruk, K. (2004). The effect of the traveling magnetic field (TMF) on the buoyancy-induced convection in the vertical Bridgman growth of semiconductors. *Journal of Crystal Growth*, 263:80–89.

Yoshimoto, N., Ikeda, M., Yoshizawa, M., and Kimura, S. (1996). Sound velocity of molten silicon. *Physica B*, 219-220:623–625.

Zaidat, K. (2005). *Influence of a travelling magnetic field on directional solidification of binary metallic alloys*. PhD thesis, Institut National Polytechnique de Grenoble. In French.

Zaidat, K., Mangelinck-Noel, N., and Moreau, R. (2007). Control of melt convection by a travelling magnetic field during the directional solidification of Al-Ni alloys. *Comptes Rendus Mecanique*, 335:330–335.

Zaidat, K., Ouled-Khachroum, T., Vian, G., Garnier, C., Mangelinck-Noel, N., Dupouy, M. D., and Moreau, R. (2005). Directional solidification of refined Al-3.5wt% Ni under natural convection and under a forced flow driven by a travelling magnetic field. *Journal of Crystal Growth*, 275:e1501–e1505.

Zeytounian, R. K. (2009). *Convection in fluids. A rational analysis and asymptotic modelling*, volume 90 of *Fluid mechanics and its applications*. Springer.

Zhang, S. and Jin, J. M. (2009). Computation of special functions. `http://jin.ece.uiuc.edu/routines/routines.html`.

Ziem, M., Lange, R.-P., and Rudolph, P. (2010). Vorrichtung zur Herstellung von Kristallen aus elektrisch leitenden Schmelzen. Offenlegungsschrift DE102008035439A1.

Ziem, M., Rudolph, P., and Lange, R.-P. (2009). Vorrichtung zur Herstellung von Kristallen aus elektrisch leitfähigen Schmelzen. Patentschrift DE102007020239B4.

Zikanov, O. (2010). *Essential computational fluid dynamics*. Wiley.

Acknowledgments

First of all I would like to thank Dr. Jochen Friedrich from Fraunhofer IISB, who invited me to Freiberg and set up a challenging PhD position with great opportunities: between Freiberg and Erlangen and between 4 different institutions – Fraunhofer IISB in Erlangen, Fraunhofer THM in Freiberg, TU Bergakademie Freiberg, and SolarWorld in Freiberg. For the following years Dr. Jochen Friedrich became the supervisor and the motivator of my work and was an interested participant in many discussions and an especially careful reader of my writings.

Prof. H.-J. Möller from TU Bergakademie Freiberg accepted the academic supervision of the complex topic spanning from crystal growth and solid state physics to magnetohydrodynamics. I am also grateful to him for the academic freedom he granted me and for the interesting discussions about the physics of crystal growth. With the kind support of Prof. Möller, Romy Rietzschel from the Institut für Experimentelle Physik of TU Bergakademie Freiberg carried out thermographic measurements for the model experiments.

I would like to express my gratitude to Dr. Bernhard Freudenberg, Dr. Thomas Richter, Dr. Marc Dietrich, Dr. Olaf Perner, Dr. Matthias Reinecke, and Dr. Lamine Sylla of SolarWorld – they not only accepted but also supported my additional occupation with a more academic work despite of the industrial environment. As my internal supervisor, Dr. Marc Dietrich supported and encouraged me in complicated situations and was an interested reader of the manuscript, with much fun and pleasant time in our conversations.

My colleagues at Fraunhofer THM, Dr. Markus Zschorsch and Dr. Ulrike Wunderwald in particular, supported me in many practical problems during my initial time in Germany and provided an inspiring environment for my academic work in the following years. The development team of the crystallization furnace at Fraunhofer THM under the supervision by Dr. Ulrike Wunderwald gave the practical motivation of this work and enriched it in many interesting discussion. I am especially indebted to Iven Kupka who carried out the crystallization experiments and the characterization of the ingots. Dr. Ulrike Wunderwald and Iven Kupka as well as two other colleagues, Stefan Chromik and Konrad Domes, carried out several electrical measurements for model experiments.

The group of Dr. Olf Pätzold at the Institut für Nichteisen-Metallurgie und Reinststoffe of TU Bergakademie Freiberg helped me to reach new scientific goals in this work. Kathrin Niemietz and Jan Ehrig supported by several technical assistants carried out very comprehensive model experiments over several years with an extraordinary commitment. I thankfully appreciate this very fruitful scientific cooperation which allowed me to validate the numerical models and fill the gap between the theoretical simulations and the reality.

I am grateful to Dr. Thomas Jung from Fraunhofer IISB and Dr. Markus Zschorsch from Fraunhofer THM who introduced me to the world of open-source software und supported in many technical problems. Dr. Thomas Jung provided me with the solvers for electromagnetic and flow calculations developed previously at Fraunhofer IISB, which were the basis for further software development in this work. The simulation group at Fraunhofer IISB and THM discussed with a great patience and interest my extensive progress reports.

Prof. Daniel Vizman from the West University of Timisoara (Romania) carried out a large number of coupled flow calculations with the `STHAMAS3D` code. Our many discussions about

the physical and numerical aspects greatly improved my understanding of the interaction between melt flow and crystallization interface and supported further software development in this work.

Many colleagues at SolarWorld, in the groups of crystallization development at Deutsche Solar and SolarWorld Innovations in particular, gave me a unique insight into the topics of industrial production and research in an inspiring and pleasant working environment. I would like to thank all of them and apologize for not mentioning all the names explicitly.

Last but not least, a successful completion of this work would have not been possible without the kind and prompt accept from Prof. André Thess from TU Ilmenau to review this work.

Finally, I would like to thank Prof. Andris Muižnieks from the University of Latvia who opened for me the worlds of science and numerical simulation and also supported this work with useful comments and discussions.

This work was partly carried out within the HiQuaSil (12416/2025) and VolKris (70766/1921) projects funded by the European Regional Development Fund and by the Saxon State Ministry for Economic Affairs, Labour and Transport.

Versicherung

Hiermit versichere ich, dass ich die vorliegende Arbeit ohne unzulässige Hilfe Dritter und ohne Benutzung anderer als der angegebenen Hilfsmittel angefertigt habe; die aus fremden Quellen direkt oder indirekt übernommenen Gedanken sind als solche kenntlich gemacht.

Die Hilfe eines Promotionsberaters habe ich nicht in Anspruch genommen. Weitere Personen haben von mir keine geldwerten Leistungen für Arbeiten erhalten, die nicht als solche kenntlich gemacht worden sind.

Die Arbeit wurde bisher weder im Inland noch im Ausland in gleicher oder ähnlicher Form einer anderen Prüfungsbehörde vorgelegt.

Freiberg, den 3. Juli 2012 Kaspars Dadzis